HYDRODYNAMIC AND WATER QUALITY MODELLING OF CHICAGO AREA WATERWAY SYSTEM (CAWS)

BY

SUMIT SINHA

DISSERTATION

Submitted in partial fulfillment of the requirements
for the degree of Doctor of Philosophy in Civil Engineering
in the Graduate College of the
University of Illinois at Urbana-Champaign, 2012

Urbana, Illinois

Doctoral Committee:

Professor Marcelo H. García, Chair
Professor Gary Parker
Professor Albert J. Valocchi
Adjunct Associate Professor Nahil A. Sobh
Asst. Professor Xiaofeng Liu

ABSTRACT

Chicago Area Waterway System (CAWS) is a highly branched network of natural rivers and man-made canals. The total length of CAWS including rivers and canals is about 250 kms (156 miles). Although not very long CAWS is famous for the engineering feat that reversed the flow of Chicago River (CR), an integral part of CAWS, westward away from lake Michigan into which it previously drained. The flow in CAWS is regulated with the help of controlling structures existing at the extremities of the system. Also present at the banks of CAWS are four waste water treatment plants (WWTP's). Discharge from these four WWTP's account for the 75 percent of the flow in CAWS. CAWS also serve as an important link between Mississippi River basin and the Great Lakes. Although the dry-weather flow discharge in CAWS is as low as 15-20 m^3/s; the wet-weather flow discharge can be as high as 400 m^3/s. The normal dry-weather flow pattern in CAWS is from north to south and quite unidirectional. During the wet-weather condition with inflows from numerous CSO outlets, pumping station and WWTP's the flow becomes entirely three-dimensional.

In this research two and three dimensional numerical models are developed and applied to gain insights into the flow structure of CAWS under both dry and wet weather conditions. Numerical models based on different methodologies are used to study the flow physics in CAWS. For the two dimensional modelling two different models are used. A finite-difference model capable of solving shallow water equations (SWE) on generalised curvilinear coordinates on structured mesh is developed and applied to a portion of CAWS. Also used for the two dimensional modelling is a finite-element model, TELEMAC-2D, for the same portion of the river. TELEMAC suite of models are open-source and freely downloadable and have been developed by EDF *(Laboratoire National D'hydraulique Et Environment)*. Furthermore

the parallelized version of TELEMAC-2D is used for larger spatial domain of CAWS and temporally longer simulations are conducted. The results from hydrodynamic simulations are validated with the help of observed data obtained from the United States Geological Survey (USGS) located inside the computational domain.

As regards to three-dimensional modelling again combination of numerical models are used. EPA (Environmental Protection Agency) approved three-dimensional model EFDC (Environmental Fluid Dynamics Code) is used for the three-dimensional modelling of CAWS. For longer term simulation of CAWS, EFDC model has been parallelized using Open-MP paradigm leading to ***I-EFDC*** model. EFDC model solves the three dimensional vertically hydrostatic, free surface, turbulent averaged equations of motions for a variable density fluid. EFDC uses a stretched sigma or vertical coordinates and curvilinear orthogonal horizontal coordinates and is applied on structured mesh. The results obtained by the EFDC model were again validated with the help of observed data from various USGS gauging stations. After having applied and calibrated the hydrodynamic model; the water quality modelling of CAWS as a whole and it's various portions are conducted in a piecewise manner. For the water quality simulation simplistic DO-BOD (dissolved oxygen - biochemical oxygen demand) models is developed under Open-MP paradigm and joined with the hydrodynamic kernel of EFDC. Furthermore for portions of CAWS another three-dimensional model TELEMAC-3D is used. Once again for simulating range of flow conditions on a fine mesh, the MPI (message passing interface) parallelized version of TELEMAC-3D is used. Both with 2D and 3D models very good agreement between the observed and modelling results are obtained.

As CAWS criss-crosses through the city of Chicago and adjoining areas; its importance from aesthetic, environmental, social and economic point of view can not be over emphasized. The insights gained from the numerical modelling effort presented here will finally help in better management and upkeep of CAWS.

For Shishir who always inspired me and for Talia who always makes me smile

ACKNOWLEDGMENTS

This dissertation work would not have been possible without the guidance of my advisor Professor Marcelo H. Garcia, hence first and foremost I would like to thank him. During my term as a graduate student he constantly encouraged me to learn and try new things and consistently taught me that in both success and failures there are lessons to be learnt which improves us as a researcher. My special thanks are also extended towards my committee members comprising of Dr. Gary Parker, Dr. Albert J. Valocchi, Dr. Nahil Sobh and Dr. Xiaofeng Liu. All of them have been a source of a very valuable guidance to me and have constantly inspired me. I would also like to extend my gratitude towards Nils Oberg and Andrew Waratuke who have been most helpful on numerous occasions that has eventually helped in progressing this research forward. Gratitudes are also extended towards J.J. Duncker, P.R. Jackson and numerous other USGS researchers who were instrumental in providing the field data for the model validation and calibration. Finally starting with my office mates namely Davide Motta, Zhenduo Zhu and Talia E. Tokyay, I am most thankful to all my group mates as well as lab mates for providing me with an atmosphere that has been most conducive both for work and fun. The financial support of the Metropolitan Water Reclamation District of Greater Chicago (MWRD) through several grants is gratefully acknowledged. In conclusion I would also like to thank my family in India and Turkey without whose support I would not have embarked on this journey.

TABLE OF CONTENTS

LIST OF TABLES viii

LIST OF FIGURES ix

CHAPTER 1 INTRODUCTION 1
1.1 Motivation 1
1.2 Research objectives 4
1.3 Methodology 5
1.4 Dissertation Outline 6

CHAPTER 2 LITERATURE REVIEW: NUMERICAL MODELLING OF SURFACE FLOW PROBLEMS 8
2.1 Introduction 8
2.2 One Dimensional Modelling 11
2.3 Two Dimensional Modelling 16
2.4 Three Dimensional Modelling 19
2.5 Conclusion 21

CHAPTER 3 DEVELOPMENT AND APPLICATION OF 2D MODELS 23
3.1 Introduction 23
3.2 Depth-averaged Models used and Developed 25
3.3 Test Cases for Validation of 2D Models 32
3.4 Conclusion 39

CHAPTER 4 THEORETICAL AND NUMERICAL FORMULATION OF THREE-DIMENSIONAL HYDRODYNAMIC AND WATER-QUALITY MODEL 41
4.1 Introduction 41
4.2 Hydrodynamic Model 43
4.3 Numerical Model for Hydrodynamic Equations 48
4.4 Boundary Conditions for the Hydrodynamic Model 50
4.5 Water Quality Model 52
4.6 Conclusion 60

CHAPTER 5 APPLICATION OF THREE-DIMENSIONAL MODELS TO CAWS 61
5.1 Introduction 61
5.2 Wet-weather Simulation 62
5.3 Long Term Simulation 80
5.4 Dye Study Simulation 91
5.5 Water Quality simulation 99
5.6 Conclusion 121

CHAPTER 6 DEVELOPING INDEX-VELOCITY RATING CURVE FOR THE CHICAGO RIVER: INSIGHTS FROM MULTIDIMENSIONAL NUMERICAL MODELS 123
6.1 Introduction 123
6.2 Domain Description and Modelling Methodology 126
6.3 Numerical Models Used 131
6.4 Computational Grid and Boundary Conditions for the Simulated Storm 134
6.5 Simulation Results and Discussion 136
6.6 Conclusion 156

CHAPTER 7 PARALLELIZATION AND SCALE-UP OF I-EFDC MODEL 157
7.1 Introduction 157
7.2 Domain Description 158
7.3 Numerical Discretization of the Governing Equations 159
7.4 Model Setup and Mesh Resolutions 162
7.5 Results and Conclusion 165

CHAPTER 8 CONCLUSION AND FUTURE WORK 185
8.1 Summary of Main Results 185
8.2 Technical Contributions 187
8.3 Future Work 189

APPENDIX A DERIVATION OF SHALLOW WATER EQUATIONS 190

REFERENCES 199

LIST OF TABLES

4.1 EFDC model water quality state variables 54

5.1 Length, Width and Depth of various segments of CAWS modeled 80
5.2 Distance of Fluorometers from Lemont Street 96
5.3 DO, BOD and Suspended Sediment Concentration in RAPS CSO's for May 2009 108
5.4 DO, BOD and Suspended Sediment Concentration from WWTPs for May 2009 109

LIST OF FIGURES

1.1 Chicago Area Waterway System 2

3.1 Staggered arrangement of variables 28
3.2 Boundary-fitted mesh for T-channel for FinFlow-2D 32
3.3 Boundary-fitted mesh for T-channel for TELEMAC 33
3.4 Flow configuration for T-channel 33
3.5 Flow field at steady state a) From TELEMAC-2D b) From FinFlow-2D 34
3.6 Bubbly Creek, South Fork of South Branch of Chicago River . 35
3.7 Boundary-fitted Mesh for Bubbly Creek 36
3.8 Unstructured Mesh for Bubbly Creek 36
3.9 CSO event in Bubbly Creek a) Flow velocity at steady state from FinFlow-2D near turning basin b) Flow velocity at steady state from TELEMAC-2D near turning basin 37
3.10 CSO event in Bubbly Creek a) Flow velocity at steady state from FinFlow-2D near RAPS b) Flow velocity at steady state from TELEMAC-2D near RAPS 37
3.11 Streamlines at steady state a)At z = 0.002 m from the bottom b) At z = 0.04 m from the bottom 39

4.1 Free surface displacement centred horizontal grid 49
4.2 Schematic showing interaction between bed and water column 58

5.1 Portion of CAWS modeled for wet-weather simulation 63
5.2 Flow through Grand Avenue between Sep 10th and Sep 18th . 64
5.3 Stage Variation at Stickney Avenue between Sep 10th and Sep 18th, 2008 65
5.4 Discharge from RAPS between Sep 10th and Sep 18th, 2008 . 65
5.5 Controlling structures modeled on the Main Branch 66
5.6 Flow through North and South sluice gates between Sep 10th and Sep 18th, 2008 66
5.7 Bathymetry data for the portion of domain modeled 67
5.8 3D computational grid with 4273 cells in horizontal and 8 layers in vertical 68

5.9 Stage elevations at Columbus drive for various outflow through Chicago Lock 69
5.10 Flow velocity in Bubbly Creek, 40 hours after the start of simulation 69
5.11 Flow velocity in Main Branch, 40 hours after the start of simulation 70
5.12 Flow velocity in Bubbly Creek, 80 hours after the start of simulation 71
5.13 Flow velocity in Main Branch, 80 hours after the start of simulation 72
5.14 Flow velocity in Bubbly Creek, 110 hours after the start of simulation 72
5.15 Flow velocity in Main Branch, 110 hours after the start of simulation 73
5.16 Flow velocity in Bubbly Creek, 150 hours after the start of simulation 74
5.17 Flow velocity in Main Branch, 150 hours after the start of simulation 74
5.18 (a)Dye concentration 92 hours,(b)108 hours after start of simulation 76
5.19 (c)Dye concentration 116 hours, (d) 120 hours after start of simulation 76
5.20 Flow velocity in Bubbly Creek, 40 hours after the start of simulation with no discharge from RAPS 77
5.21 Flow velocity in Bubbly Creek, 80 hours after the start of simulation with no discharge from RAPS 78
5.22 Flow velocity in Bubbly Creek, 110 hours after the start of simulation with no discharge from RAPS 79
5.23 Flow velocity in Main Branch, 110 hours after the start of simulation with no discharge from RAPS 79
5.24 Schematic of CAWS 81
5.25 Computational mesh for Chicago Area Waterway System (CAWS) 83
5.26 Outflow through various WWTPs for May-2009 84
5.27 CSO's from RAPSfor May-2009 84
5.28 Location of USGS gauging station inside the computational domain 85
5.29 Comparison between observed and simulated stage at Grand Avenue for May-2009 86
5.30 Comparison between observed and simulated stage at Columbus Drive for May-2009 86
5.31 Comparison between observed and simulated stage at Stickney Avenue for May-2009 87

5.32 Velocity magnitude a) 3^{rd}, b) 7^{th} c) 11^{th} and d) 14^{th} day after start of the simulation near Goose Island on North Branch, Chicago River 88
5.33 Velocity magnitude a) 17^{th}, b) 21^{st} c) 24^{th} and d) 28^{th} day after start of the simulation near Goose Island on North Branch, Chicago River 88
5.34 Velocity magnitude a) 3^{rd}, b) 7^{th} c) 11^{th} and d) 14^{th} day after start of the simulation on Main Branch, Chicago River . 89
5.35 Velocity magnitude a) 17^{th}, b) 21^{st} c) 24^{th} and d) 28^{th} day after start of the simulation on Main Branch, Chicago River . 89
5.36 Velocity magnitude a) 3^{rd}, b) 7^{th} c) 11^{th} and d) 14^{th} day after start of the simulation in Bubbly Creek 90
5.37 Velocity magnitude a) 17^{th}, b) 21^{st} c) 24^{th} and d) 28^{th} day after start of the simulation in Bubbly Creek 90
5.38 Portion of CAWS where the dye-dispersal campaign was carried out in Dec. 2009 91
5.39 End of computational domain at Lockport power plant 92
5.40 Location of power-plant intake and outfall inside the modeled domain 93
5.41 Computational mesh for dye simulation 94
5.42 Computational mesh near power plant 95
5.43 Computational mesh with side-slip structures incorporated . . 95
5.44 Position of dye-probe placed by USGS along the length of the domain 96
5.45 Comparison between simulated and observed dye concentration, FL-291 and FL-292 97
5.46 Comparison between simulated and observed dye concentration, FL-293 and Fl-294 97
5.47 Dye Concentration near power plant, 10 hours after injection . 98
5.48 Snapshot of velocity magnitude 42 and 50 hours after the start of simulation 98
5.49 Velocity magnitude in Bubbly Creek 4 hours after the start of the simulation 101
5.50 Velocity magnitude in Bubbly Creek 8 hours after the start of the simulation 101
5.51 Velocity magnitude in Bubbly Creek 12 hours after the start of the simulation 102
5.52 DO levels in the creek 4 hours after the start of the simulation 103
5.53 DO levels in the creek 8 hours after the start of the simulation 103
5.54 DO levels in the creek 10 hours after the start of the simulation 104
5.55 DO levels in the creek 12 hours after the start of the simulation 104
5.56 Compairison between observed and simulated DO at 36th street and I55 105

5.57 Suspended sediment concentration 2 and 4 hours after the start of the simulation . . . 106
5.58 Suspended sediment concentration 6 and 8 hours after the start of the simulation . . . 106
5.59 Suspended sediment concentration 10 and 12 hours after the start of the simulation . . . 107
5.60 Location of water quality monitoring station on the computational grid of CAWS . . . 109
5.61 Variation of DO at 36^{th} street in Bubbly Creek for May-2009 . 110
5.62 Variation of DO at I-55 in Bubbly Creek for May-2009 110
5.63 DO concentration a) 3^{rd}, b) 7^{th} c) 11^{th} and d) 14^{th} day after start of the simulation in Bubbly Creek . . . 112
5.64 DO concentration a) 17^{th}, b) 21^{st} c) 24^{th} and d) 28^{th} day after start of the simulation in Bubbly Creek . . . 112
5.65 DO variation along the water column at 36^{th} street on Bubbly Creek . . . 113
5.66 DO variation along the water column at I-55 on Bubbly Creek 114
5.67 BOD concentration 5.3, 5.69, 12.91 and 13.12 days after start of simulation in Bubbly Creek . . . 114
5.68 BOD concentration 14.73, 14.79, 25.92 and 26.04 days after start of simulation in Bubbly Creek . . . 115
5.69 DO variation at Loomis street . . . 116
5.70 DO variation at Kinzie Avenue . . . 116
5.71 DO variation along water column at Loomis Street . . . 117
5.72 DO variation along water column at Kinzie Avenue . . . 118
5.73 DO concentration a) 3^{rd}, b) 7^{th} c) 11^{th} and d) 14^{th} day after start of the simulation near Goose Island . . . 118
5.74 DO concentration a) 17^{th}, b) 21^{st} c) 24^{th} and d) 28^{th} day after start of the simulation near Goose Island . . . 119
5.75 DO concentration a) 3^{rd}, b) 7^{th} c) 11^{th} and d) 14^{th} day after start of the simulation in Main Branch Chicago River . . 119
5.76 DO concentration a) 17^{th}, b) 21^{st} c) 24^{th} and d) 28^{th} day after start of the simulation in Main Branch Chicago River . . 120

6.1 Chicago Area Waterway System . . . 127
6.2 Lockport power house at the southern end of the domain . . . 128
6.3 AVM and H-ADCP path near Lemont looking from top, adapted from Jackson et al. (2012) . . . 129
6.4 Elevations from AVM and H-ADCP, adapted from Jackson et al. (2012) . . . 130
6.5 Combination of inflow conditions tried . . . 134
6.6 Computational mesh generated through Bluekenue . . . 135
6.7 Stage variation at Romeoville for the period of simulated storm 136
6.8 Computational mesh for the extended domain . . . 137

6.9 Computational mesh for the extended domain 137
6.10 Depth averaged velocity plots from TELEMAC-2D after 9 and 50 hours start of the simulation 139
6.11 Depth averaged velocity plots from TELEMAC-2D after 72 and 84 hours start of the simulation 140
6.12 Depth averaged velocity plots from TELEMAC-2D after 108 and 120 hours start of the simulation 141
6.13 Results from TELEMAC-3D 12 hours after the start of the simulation 142
6.14 Results from TELEMAC-3D 48 hours after the start of the simulation 142
6.15 Results from TELEMAC-3D 72 hours after the start of the simulation 143
6.16 Results from TELEMAC-3D 84 hours after the start of the simulation 143
6.17 Results from TELEMAC-3D 108 hours after the start of the simulation 144
6.18 Results from TELEMAC-3D 120 hours after the start of the simulation 145
6.19 AVM Index velocity developed by numerical models 146
6.20 H-ADCP Index velocity developed by numerical models 147
6.21 Velocity magnitude, 3, 12 and 24 hours after the start of the simulation 147
6.22 Velocity magnitude, 36, 48 and 60 hours after the start of the simulation 148
6.23 Velocity magnitude, 72, 84 and 96 hours after the start of the simulation 148
6.24 Comparison between modeled and observed stage at Lemont . 149
6.25 Comparison between modeled and observed discharge at Lemont 150
6.26 Froude number at Romeoville 151
6.27 Froude number at Lemont 151
6.28 Froude number at the upstream end on CSSC stretch 152
6.29 Froude number at the upstream end Cal-Sag stretch 152
6.30 Extended domain ending at Lockport and including Controlling Works 153
6.31 Free surface elevation between July, 22nd and 27th, 2010 at Romeoville and Lockport 154
6.32 Simulated and observed stage at Romeoville and Lemont in the extended domain 155
6.33 Upstream propagating surface wave near controlling works 2.25 hours after the start of the simulation 155

7.1 Domain for studying the parallel speed up of I-EFDC model . 158

7.2 Mesh-1 with 4000 control volumes in horizontal and 8 layers in vertical . . . 163
7.3 Mesh-2 with 8000 control volumes in horizontal and 8 layers in vertical . . . 164
7.4 Velocity magnitude 114 hrs after the start of simulation on Mesh-1, near Turning Basin . . . 166
7.5 Velocity magnitude 114 hrs after the start of simulation on Mesh-2, near Turning Basin . . . 166
7.6 Velocity magnitude 114 hrs after the start of simulation on Mesh-1, on Main Branch . . . 167
7.7 Velocity magnitude 114 hrs after the start of simulation on Mesh-2, on Main Branch . . . 167
7.8 Velocity magnitude 120 hrs after the start of simulation on Mesh-1, on Main Branch . . . 168
7.9 Velocity magnitude 120 hrs after the start of simulation on Mesh-2, on Main Branch . . . 168
7.10 Velocity magnitude 120 hrs after the start of simulation on Mesh-1, in Bubbly Creek . . . 169
7.11 Velocity magnitude 120 hrs after the start of simulation on Mesh-1, near Turning Basin . . . 170
7.12 Velocity magnitude 120 hrs after the start of simulation on Mesh-2, in Bubbly Creek . . . 170
7.13 Velocity magnitude 120 hrs after the start of simulation on Mesh-2, near Turning Basin . . . 171
7.14 Free surface elevation with Mesh1 and Mesh2 near Columbus drive on Main Branch, Chicago River . . . 171
7.15 Velocity magnitude 102 hrs after the start of the simulation near Bubbly Creek with 4 layers in vertical on Mesh-1 . . . 172
7.16 Velocity magnitude 102 hrs after the start of the simulation near Bubbly Creek with 8 layers in vertical on Mesh-1 . . . 173
7.17 Velocity magnitude 102 hrs after the start of the simulation near Bubbly Creek with 12 layers in vertical on Mesh-1 . . . 173
7.18 Velocity magnitude 144 hrs after the start of the simulation near Bubbly Creek with 4 layers in vertical on Mesh-1 . . . 174
7.19 Velocity magnitude 144 hrs after the start of the simulation near Bubbly Creek with 8 layers in vertical on Mesh-1 . . . 174
7.20 Velocity magnitude 144 hrs after the start of the simulation near Bubbly Creek with 12 layers in vertical on Mesh-1 . . . 175
7.21 Velocity magnitude 102 hrs after the start of the simulation near Main Branch with 4 layers in vertical on Mesh-1 . . . 175
7.22 Velocity magnitude 102 hrs after the start of the simulation near Main Branch with 8 layers in vertical on Mesh-1 . . . 176
7.23 Velocity magnitude 102 hrs after the start of the simulation near Main Branch with 12 layers in vertical on Mesh-1 . . . 176

7.24 Velocity magnitude 144 hrs after the start of the simulation near Main Branch with 4 layers in vertical on Mesh-1 177
7.25 Velocity magnitude 144 hrs after the start of the simulation near Main Branch with 8 layers in vertical on Mesh-1 177
7.26 Velocity magnitude 144 hrs after the start of the simulation near Main Branch with 12 layers in vertical on Mesh-1 178
7.27 Variation of water surface elevation at Columbus Ave Mesh-1 with different numbers of layer in the vertical 179
7.28 Velocity magnitude 102 hrs after the start of the simulation through a section in turning-basin near Bubbly Creek with 4 layers in vertical on Mesh-1 180
7.29 Velocity magnitude 102 hrs after the start of the simulation through a section in turning-basin near Bubbly Creek with 8 layers in vertical on Mesh-1 180
7.30 Velocity magnitude 102 hrs after the start of the simulation through a section in turning-basin near Bubbly Creek with 12 layers in vertical on Mesh-1 181
7.31 Computational time consumed by Mesh-1 with different number of processors 183
7.32 Computational time consumed by Mesh-2 with different number of processors 183
7.33 Speed-Up obtained on Mesh-1 and Mesh-2 with different number of processors 184

CHAPTER 1

INTRODUCTION

1.1 Motivation

Chicago is the largest city in both Illinois and Midwest, it's the third most populated city in the United states with population around 3 million. Chicago Area Waterway System (CAWS) is a highly branched network of natural rivers and man-made canals. Although CAWS is not distinctly long, it is of vital importance from aesthetic, environmental, social and economic point of view. CAWS also serve as an important link between Mississippi River basin and the Great Lakes. CAWS is made up of the following reaches.

a) West Fork of the North Branch of the Chicago River

b) Middle Fork of the North Branch of the Chicago River

c) East Fork (Skokie River)

d) North Branch of the Chicago River (North Branch)

e) North Shore Channel

f) South Branch of the Chicago River(South Branch)

g) South fork of South Branch of the Chicago River (Bubbly Creek)

h) Chicago Sanitary and Ship Canal (CSSC)

i) Calumet Sag Channel

Chicago River (CR) which is an integral part of CAWS. CR is famous for 19^{th} century civil engineering feat that directed its flow south away from the lake Michigan into which it previously drained. The flow orientation in CR is shown in Figure (1.1). The aforementioned flow reversal of the CR was

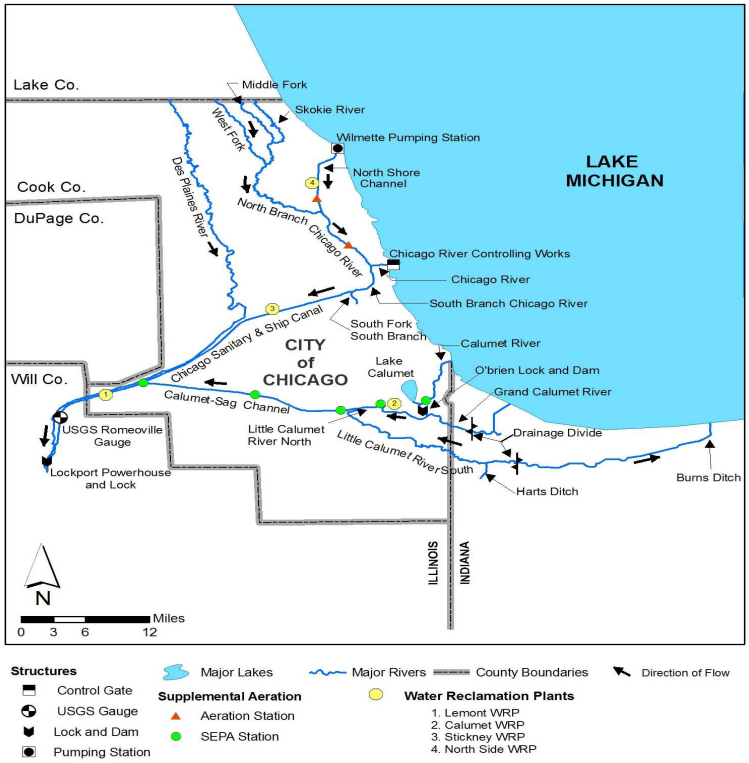

Figure 1.1: Chicago Area Waterway System

accomplished by construction of three man-made channels namely Chicago Sanitary and Ship Canal (CSSC), North Shore Channel and Calumet Sag Channel (Figure 1.1) by the early 20th century. In the present day, the CR flows west away from the Lake Michigan and joins the Chicago River North Branch (NB) and together they flow southwards as Chicago River South Branch (SB). Also present on the banks of CAWS are four Waste Water Treatment Plants (WWTPs), operated and owned by Metropolitan Water Reclamation District of Greater Chicago (MWRDGC). The four WWTP's present on the banks of CAWS are as follows.

i) Lemont Water Reclamation Plan (LWRP)

ii) Calumet Water Reclamation Plant (CWRP)

iii) Stickney Water Reclamation Plant (SWRP)

iv) North-Side Water Reclamation Plant (NSWRP)

The outflow from these four WWTP's account for the 70 percent of flow in CAWS (USACE, 2001). Flow in CAWS is regulated with the help of control-

ling structures located at the extremities of the domain. These controlling structures comprise of locks and gates and help in releasing or withdrawing water from Lake Michigan. Racine Avenue Pumping Station (RAPS) situated towards the south end of the Bubbly Creek is responsible for conveying the rainfall-runoff flow collected from the adjoining area after a storm event to the water treatment plant at Stickney (Figure 1.1). During the episodes of intense storm leading to combine sewer overflow (CSO), as the conveyance capacity of RAPS is exceeded and the excessive water is discharged into Bubbly Creek. Although the flow in CAWS is almost unidirectional, from north to south, during dry weather condition. During CSO events as the flow from RAPS heads towards the south branch and meets the flow coming from the north branch, it acquires a completely three-dimensional nature.Jackson et al. (2008) also showed the existence of density current and bi-directional flow on the main branch of the Chicago River. Also existing on the extremities of the domain (Figure 1.1) are various controlling structures that regulate the flow in the Chicago River. Due to the combined effect of the controlling structures, pumping station and outflow from various water treatment plant the flow in CAWS can be highly unsteady and completely three-dimensional in nature. The first objective of this research work is to come up with a validated and calibrated three dimensional hydrodynamic model for CAWS in a piecewise manner.

It is a well known fact that the health of any river system is generally gauged by the level of dissolved oxygen (DO) in it. In case of the Chicago River and CAWS in general, the DO levels in various parts of the system has been found to be at levels less than the standard set by Illinois Pollution Control Board (IPCB). As water quality state variables are of paramount importance the second objective of this research work is to come up with calibrated and validated three-dimensional water quality model for CAWS. As regards with water quality modeling extensive 1D water quality modeling has been conducted by Alp and Melching (2006), 2D water quality modeling of Bubbly Creek was conducted by Motta et al. (2010). But to the best of the authors knowledge a complete three-dimensional water quality model for CAWS has not been presented till date

The completion of the flow reversal of the Chicago River helped Chicago to prosper as a city. In the present day the withdrawal of water from Lake Michigan through various controlling structures is limited and restricted by

US Supreme court decree. The flow accounting to that end is carried out at the USGS gauging station located near Lemont on Illinois and Michigan canal portion of CAWS. This flow accounting makes the aforementioned USGS gauging station [USGS-05536890] as one of the most scrutinized gauging station in the country. It is a well known fact that a gauging station located in unsteady flow domain exhibit hysterisis in stage discharge rating curve, to combat the problem of loop there is a paradigm shift toward index-velocity plot for obtaining a single valued bankable discharge through a given cross-section. The third objective of this research is to construct index velocity plot at Lemont gauging station with help of multidimensional models.

1.2 Research objectives

The primary objective of this research work is to successfully model the three-dimensional hydrodynamic and water quality phenomenon and processes associated with CAWS. Some of the specific questions and tasks that is undertaken through this research are as follows.

1. How will the impaired water being discharged from the RAPS during a CSO event will affect the overall water quality of Bubbly creek and Chicago Area Waterways (CAWS) in general?

2. During an intense CSO event what is the final fate of the dissolved and suspended constituents coming through the Racine Avenue Pumping Station (RAPS)?

3. With outflows from various water treatment plants and CSO's from pumping station, how does water quality characteristics of CAWS evolve over a sustained period of time ?

4. Is it possible to verify the veracity of index-velocity relationship developed for Chicago River, near Lemont on $I\&M$ canal with help of multidimensional models ?

Although the hydrodynamic and water quality processes associated with CAWS is essentially three-dimensional in nature, to get a sense in depth-averaged mode, a two-dimensional model based on shallow water equations

is also developed. The developed model is validated with help of laboratory set ups and then finally applied to the portion of CAWS, Bubbly Creek.

1.3 Methodology

As the main aim of this project is to model three-dimensional hydrodynamic and water quality phenomenon in CAWS, to that end an EPA approved model EFDC (Environmental Fluid Dynamics Code) is used. EFDC model solves three dimensional vertically hydrostatic, free surface, turbulent averaged equations of motions for a variable density fluid. Model uses a stretched sigma or vertical coordinates and curvilinear orthogonal horizontal coordinates. Dynamically coupled transport equations for turbulent kinetic energy, turbulent length scale, salinity and temperature are also solved. The specific task of this research can be presented as follows. It was initially developed at Virginia Institute of Marine Science (VIMS) and has been under constant development at Ven-Te-Chow hydrosystems lab. There are number of reasons for choosing EFDC for the numerical modeling of CAWS, some of them are listed here.

- EFDC model can be made to work for multiblock river system, which very much is the case of Chicago river with existence of various creeks and slips.
- The model being in three dimension facilitates more realistic incorporation of water quality source/sink terms like SOD and reaeration, where SOD is only made active for the bottom layer and reaeration is made valid only for the top layer.
- As the governing equations in vertical are recast into the sigma coordinate system, it's able to incorporate the real bathymetry of the river system in the numerical simulations.
- As the model has the capability of simulating free surface, it helps in modeling the stage variation during the wet weather event which can be significant.
- Access to the source code, enables the improvement and addition of newer modules to the existing kernel of EFDC.

- Last but not the least EFDC is an EPA approved code for modeling of surface flow problems in USA.

To simulate the larger portions of CAWS over longer period of time EFDC model is parallelized using Open-MP paradigm. Another important objective of this research was to examine and study the parallel speed up of EFDC model by constructing meshes of different resolutions and running it on different number of processors. All the simulations presented as a part of this research are carried out on Hydrosystem cluster, which is a 7 node, 56-core Intel Xeon cluster. Each node has 8 cores and 32 GB of RAM. The nodes are connected to each other with an Ethernet interconnect and share a network file system (NFS).

For studying the veracity of index-velocity plot at USGS gauging station [USGS-05536890] near Lemont open source (www.opentelemac.org) finite-element based TELEMAC suite of models would be used. TELEMAC suite of models are chosen because they are based on unstructured mesh and are parallelized with MPI (Message Passing Interface) paradigm which enables the use of more number of processors than just the one associated with a given node. In case of the hydrosystem cluster as mentioned before each node has 8 core or processors. TELEMAC suite of models were ported on the hydrosystem cluster, a numerical code based on three-dimensional shallow water equations implemented with MPI was essential because multiple simulations for long period of time were conducted to obtain index velocity plot.

1.4 Dissertation Outline

This dissertation is structured as follows. In **Chapter 2** literature review in regards with surface flow problem is presented, **Chapter 3** details the development and application of two-dimensional model. In **Chapter 4** the details about the hydrodynamic and water quality model is presented, **Chapter 5** presents the various hydrodynamic and water quality application of the parallelized EFDC model. In **Chapter 6** the index velocity plots are constructed through multi-dimensional TELEMAC suite of models, **Chapter 7** presents the detail study on the speed-up of parallized EFDC model and finally in

Chapter 8 conclusions are drawn. In Appendix-A a detail derivation of shallow water equations that are used for developing the 2D model is presented, these equations are the basis of finite-difference 2D model (FinFlow-2D) developed as a part of this research.

CHAPTER 2

LITERATURE REVIEW: NUMERICAL MODELLING OF SURFACE FLOW PROBLEMS

2.1 Introduction

Before starting to describe the tools and techniques used for numerical modelling of surface flow problems, it is imperative to revisit the fundamental equations of motion that various numerical models aim to solve. Perhaps a bit of discussion on the theoretical history of the fundamental equations is also warranted. As discussed by Rouse and Ince (1957) the advent of hydrodynamics can be chiefly attributed to three mathematicians of the 18^{th} century; namely Daniel Bernoulli (1700-1782), Leonhard Euler (1707-1783) and Jean le Rond d'Alembert (1717-1783). It was Bernoulli who coined the term *Hydrodynamics* in a document published in 1738. D'Alembert main contribution to hydrodynamics was unifying the principles of momentum and energy and their application to fluid motion. Despite making significant contribution to the field of hydrodynamics, it somehow missed the rightful acclaim. This can be attributed to the fact that in 1755 Euler published a series of analysis that accomplished most of the things that D'Alembert, if not Bernoulli, had thought of doing. Although the earlier work of D'Alembert and Bernoulli formed more or less the starting point in the work of Euler, but the extent of his contributions were so enormous that the equations of motion for non-viscous motion differ a little from those he presented in the 18^{th} century. Perhaps it won't be an exaggeration to say he was the first scientist to establish the area of hydrodynamics, the way we know it today. Such were the challenges and problems posed by the field of hydrodynamics that Bernouli remarked.

> *"Admittedly, as useful a matter as the motion of fluid and related sciences has always been an object of thought. Yet until this day neither our knowledge of pure mathematics nor our command of*

the mathematical principles of nature have permitted a successful treatment"(Daniel Bernoulli, September 1734)

The next significant breakthrough in hydrodynamics happened in 19^{th} century. Louis Marie Henri Navier (1785-1836) who was an engineer who analysed motion of fluid from purely mathematical point of view and presented the same in his 1827 paper, "Memoire sur les lois du mouvement des fluides". His analysis was somewhat similar to Euler albeit the consideration of an extra force term which represented the hypothetical attraction or repulsion between adjacent fluid molecules. Although a breakthrough, Navier was only able to explain this force term as an unknown function of the spacing between the moving fluid molecules. He was not able to interpret from his deduction the general theory behind the internal mechanism of fluid resistance. Finally it was the British mathematician Sir George Gabriel Stokes (1819-1903) whose name became interminably and inextricably linked with that of Navier, who chose to work on the same problem. In his 1845 paper, "On the Theories of the Internal Friction of Fluids in Motion and of the Equilibrium and Motion of Elastic Solids", contained the derivation of Navier-Stokes equation which is followed till this day. In his paper Stokes replaced Navier's more general coefficient with the coefficient of dynamic viscosity.

Two other researchers with very high accomplishments and to whom the field of hydrodynamics owes a great deal of gratitude were Joseph Boussinesq (1842-1929) and Osborne Reynolds (1842-1912). Boussinesq was more of a theoretician and Reynolds was an engineer by training and profession. In his 1894 high-impact paper entitled, "On the Dynamical Theory of Incompressible Viscous Fluids and the Determination of the Criterion", he extended the basic equations of fluid motion to the case of turbulent flow. The essence of his approach was to decompose the instantaneous fluid velocity as the sum of mean and fluctuating components and then finally retaining only those values which had temporal mean other than zero. Reynold's primary aim was to investigate the onset of turbulence, despite being only partially successful in this, his lasting contribution was what is now famously known as, Reynolds Average Navier-Stokes (RANS) equations for turbulent flow. As regards to Boussinesq he undertook a rigorous research in turbulence and its affect on the mixing processes. As a result of his research he was able to relate the

mixing phenomenon to the mean velocity distribution. Because of the lack of a solution for the turbulence problem, the theories proposed by Reynolds and Boussinesq are still used in a rigorous manner in both engineering and theoretical studies. Finally the three-dimensional Navier-Stokes equations in cartesian coordinate system which forms the starting point of any kind of numerical modelling effort is presented here.

$$\frac{\partial u}{\partial x} + \frac{\partial v}{\partial y} + \frac{\partial w}{\partial z} = 0 \tag{2.1}$$

$$\frac{\partial u}{\partial t} + \frac{\partial uu}{\partial x} + \frac{\partial uv}{\partial y} + \frac{\partial uw}{\partial z} = \frac{1}{\rho}F_x - \frac{1}{\rho}\frac{\partial p}{\partial x} + \nu\left[\frac{\partial^2 u}{\partial x^2} + \frac{\partial^2 u}{\partial y^2} + \frac{\partial^2 u}{\partial z^2}\right] \tag{2.2}$$

$$\frac{\partial v}{\partial t} + \frac{\partial vu}{\partial x} + \frac{\partial vv}{\partial y} + \frac{\partial vw}{\partial z} = \frac{1}{\rho}F_y - \frac{1}{\rho}\frac{\partial p}{\partial y} + \nu\left[\frac{\partial^2 v}{\partial x^2} + \frac{\partial^2 v}{\partial y^2} + \frac{\partial^2 v}{\partial z^2}\right] \tag{2.3}$$

$$\frac{\partial w}{\partial t} + \frac{\partial wu}{\partial x} + \frac{\partial wv}{\partial y} + \frac{\partial ww}{\partial z} = \frac{1}{\rho}F_z - \frac{1}{\rho}\frac{\partial p}{\partial z} + \nu\left[\frac{\partial^2 w}{\partial x^2} + \frac{\partial^2 w}{\partial y^2} + \frac{\partial^2 w}{\partial z^2}\right] \tag{2.4}$$

The mass conservation or the continuity equation is given by (2.1) and the momentum equations in three directions is given by (2.2), (2.3) and (2.4). In the aforementioned equations u, v and w denotes the velocity component in x, y and z direction respectively. The density of the fluid is denoted by ρ, p is the pressure, F_x is the external force e.g. gravity and ν is the dynamic viscosity. The formulation of three-dimensional RANS equations were of such a high impact that the famous German mathematician made the following statement about it.

> *"As far as I can see, there is today no reason not to regard the hydrodynamic equations of [Navier and Stokes] as the exact expression of the laws that rule the motion of real fluids"(Hermann Helmholtz 1873)*

2.2 One Dimensional Modelling

Flow in an open channel is as example of gradually varied, unsteady, non uniform, free surface flow (Henderson, 1966; Chow, 1973).The one-dimensional mathematical model for the surface flow problems is based on some form of Saint-Venant equations. Saint-Venant equations appear in multiple forms in literature and can be either written in differential or integral form. These equations are fundamentally derived from the section-averaging of the depth-averaged three-dimensional RANS equations. The derivations of these equations are based on certain underlying assumptions presented here.

- In one dimensional modelling the velocity distribution and water depth is uniform across the section.
- The vertical acceleration of the fluid under consideration is negligible implying that the pressure variation along the depth is hydrostatic resulting in a small streamline curvature.
- The average channel bed slope is small so that the cosine of the angle between the bed slope angle and the horizontal can be replaced by unity.
- The boundary friction and resistance can be replaced by the same laws that govern the steady flow.

The continuity and momentum equation for 1D Saint-Venant equations is as follows.

$$\frac{\partial A}{\partial t} + \frac{\partial Q}{\partial x} = q_l \tag{2.5}$$

$$\frac{\partial Q}{\partial t} + \frac{\partial \left(\frac{\beta Q^2}{A}\right)}{\partial x} + gA\frac{\partial z_s}{\partial x} + gAS_f = q_l v_x \tag{2.6}$$

In the aforementioned equations x is the spatial coordinate representing the streamwise distance; A is the flow area; Q is the flow discharge, defined as Q = AU, with U being the flow velocity averaged over the cross-section;

z_s is the water stage; β is the correction factor for the momentum due to the non-uniformity of the streamwise velocity over the cross-section; q_l is the side flow discharge per channel unit length; v_x is the velocity of the side flows in the direction of the x-coordinate; S_f is friction slope given by the following equation.

$$S_f = \frac{Q|Q|}{K^2} \tag{2.7}$$

where K is the conveyance. For a simple cross-section, $K = AR^{2/3}/n$, with R being the hydraulic radius and n the Manning roughness coefficient of the channel. The equations (2.5) and (2.6) constitutes what is commonly known as one-dimensional Saint-Venant equations. The one-dimensional momentum equation can be presented in numerous different forms with the help of little algebraic manipulation. For example the water surface elevation can be expressed as the sum of water depth and bed elevation.

$$z_s = z_b + h \tag{2.8}$$

Therefore, $\frac{\partial z_s}{\partial x} = \frac{\partial z_b}{\partial x} + \frac{\partial h}{\partial x}$, where h is the water depth, also $-S_o = \frac{\partial z_b}{\partial x}$ denotes the bed slope. Incorporating these representations and ignoring the side flow,q_l, the momentum equation in 1D Saint-Venant equation can be reformulated as

$$\frac{1}{A}\frac{\partial Q}{\partial t} + \frac{1}{A}\frac{\partial}{\partial x}\left(\frac{Q^2}{A}\right) + g\frac{\partial h}{\partial x} - g(S_o - S_f) = 0 \tag{2.9}$$

Depending on the scenario and case being simulated, the one dimensional governing equations as given by (2.5) and (2.9) can be further simplified. For example neglecting the local acceleration term $\frac{1}{A}\frac{\partial Q}{\partial t}$, convective acceleration term $\frac{1}{A}\frac{\partial}{\partial x}\left(\frac{Q^2}{A}\right)$, pressure force term $g\frac{\partial h}{\partial x}$ one arrives at what is commonly known as, Kinematic wave model, where the momentum equation reduces to

$$S_o = S_f \tag{2.10}$$

which implies a balance between the friction and gravity force. This over-simplification is applicable in the cases where the variations in the flow velocity and depth are negligible in comparison with the channel bed. Another kind of common simplification used in regards with 1D Saint-Venant equation, (2.9), is neglecting the local and convective acceleration term which reduces the momentum equation to the following form.

$$\frac{\partial h}{\partial x} - g(S_o - S_f) = 0 \tag{2.11}$$

Together with the continuity equation (2.5) and the reduced momentum equation (2.11) we obtain what is commonly known as the, diffusion-wave model. Considering all the terms in the 1D Saint-Venant equations gives us the dynamic wave model. It is a well known fact that in a sub-critical flow when the water level or the flow rate is changed at a particular point, the effect of these changes propagate back upstream. To capture these backwater effects it is essential to use full-blown dynamic wave model. Unfortunately because of the non-linear nature of 1D Saint-Venant equation, the analytical solution of these equations are possible for only very few select cases. It is because of this reason that one needs to resort to numerical models. The numerical modeling of 1D Saint-Venant equations can be accomplished by couple of different methods, listed here.

- Finite Difference Method (FDM)
- Finite Volume Method (FVM)
- Finite Element Method (FEM)
- Method of Characteristics (MOC)

The early attempts to solve non-linear 1D Saint-Venant equation started with advances made in finite-difference technique. The history of finite-difference technique can be traced back to the the seminal work of A. Thom in 1920s under the title, "the method of squares" to solve non-linear hydrodynamic equations. In (FDM) method the governing equations are solved on a given set of nodes in what is known as the computational domain. For each node, the unknown function values or state variables are found, replacing the differential equations by difference or discretized equations with

truncated Taylor series expansions. Perhaps it can be said without exaggeration that finite-difference method is conceptually and intuitively the easiest method to implement. A FDM scheme can be either explicit or implicit. In the area of Computational Fluid Dynamics (CFD) lot of difference methods were based on the work of Lax and Wendroff (1960) and its variation provided by MacCormack (1969). Moretti (1979) provided an explicit scheme, this was further analysed and improved by Gabutti (1983). As mentioned before the governing 1D Saint-Venant equations can be written in number of different forms. Beam and Warming (1976) developed implicit finite difference scheme for hyperbolic system in conservation form. In regards with implicit scheme, a very important piece of work was presented by Preissmann (1961) which was particularly for river hydraulics problem. The Delft hydraulics Laboratory scheme Vreugdenhil (1973) and the Abott scheme Cunge et al. (1980) were also developed for the basic one-dimensional flow equations. The contribution of Preissmann (1961) can be comprehended from the fact that it became the underlying kernel behind the rampantly used 1D model HEC-RAS (Brunner, 2001). As mentioned before, because of the ease of implementation and comprehension, FDM technique became the guiding engine behind host of 1D models which are still quite popular today e.g. (HEC-RAS, DWOPER, ISIS, MIKE-11, etc). All these models utilized the same assumptions of constant velocity across a section, hydrostatic pressure distribution over the depth and small bed slope.

(McDonald, 1971) and (MacCormack and Paullay, 1972) were two of the first researchers who applied FVM technique in the field of fluid dynamics by trying to solve two dimensional time dependent Euler equations (Hirsch, 1988). The FVM technique starts with decomposing the domain in number of non-overlapping smaller control volumes. It is on these control volumes that the integral form of the governing equations are solved. As the FVM technique is based on the integral form, it has shown better conservation characteristics than the other techniques. Because of this inherent property of conservation on each control volume level, FVM has gained widespread acceptance with the researchers trying to solve fluid flow problems. Numerous researchers have utilized finite-volume technique for the solution of 1D Saint-Venant equations. Some of the examples are Alcrudo et al. (1992), Ambrossi (1995), Delis and Skeels (1998), Glaister (1988) and Goutal and Maurel (2002).

Although many ideas are common to both finite difference and finite element method, because of FEM's applicability to complicated domains and systematic use of variational approach has led to its increased popularity. The basic idea behind the FEM technique is again to decompose the modelling domain into number of smaller elements, these elements can be triangular or quadrilateral in shape. The solution at any point or node of the element is then obtained by the series expansion of the nodal values within the vicinity of the node. One of the key ideas behind the FEM which defines the variant of the method being used is the selection of the basis function, also known as the trial or the shape function. This basis function is multiplied by the nodal contribution in the FEM scheme. Finally the implementation of FEM for fluid flow problems can be listed as a set of the following distinct steps.

- Discretize domain into elements, triangular or quadrilateral
- Select basis functions
- Formulate the integral equations for each element
- Calculate element matrices and vectors
- Incorporate boundary conditions
- Solve system of simultaneous linear equations for the unknown state variables

Hicks and Steffler (1992) and Keuning (1976) applied FEM to open channel flow problem. As a computational technique FEM originated in engineering literature when in mid 1950s structural engineers had connected the well established framework analysis with variational methods in continum mechanics into a discretization method in which a structure is thought of as divided into elements with locally defined stresses or strains.

As far as the method of characteristic is concerned (MOC), it dates back to 1789 when Monge developed a graphical procedure to solve hyperbolic partial differential equations which later on became famous as MOC Chaudhry (1994). For the detail methodology of the technique the reader may refer to (Abbott, 1979) and (Yen et al., 1986) among many others. In essence the technique comprise of defining the characteristic lines along which the disturbance propagates. These lines are special in a sense because certain

characteristic properties tend to stay constant on these lines. The method can be thought of a technique in which we construct lines in space and time on which the characteristic values are assigned on the boundary where it enters the domain or region of interest. The application of this technique to the hydrodynamic equations can be found in detail in Chaudhry (1994), Abbott (1979) and Stoker (1957). Although the method is primarily designed for the solution of hyperbolic partial differential equation (PDE); if the solution to the hyperbolic PDE is discontinuous the method might fail. Only if the solution variable has a constant value on the either side of the shock Rankine-Hugoniot condition may be applied other wise it might be tough to come up with a closed form of solution.

2.3 Two Dimensional Modelling

Although 1D models are simple to develop and use it fails to provide the detailed information about the flow physics. This becomes more relevant if the domain being modeled is not very straight and the direction of the flow is not always aligned with the direction of the main channel. The governing equations for the fluid motion in two-dimension is obtained by depth-averaging of 3D RANS equation. These equations were first presented by Saint-Venant in 1871 in a paper titled, *"Theorie du mouvement non-permanent des eaux, avec application aux crues des rivieres et a l'introduction des marees dans leur lit"*. Compte-Rendu a l'Academie des Sciences de Paris, 73, 147-154. The key idea behind or rather restrictive hypotheses behind these equations is that the wavelength should be much greater than the depth of of the flow. These equations are of extreme importance in maritime or fluvial hydraulics and govern free surface flows in shallow waters, hence also commonly known as, "shallow water equations".

$$\frac{\partial h}{\partial t} + \frac{\partial \left(hU_x\right)}{\partial x} + \frac{\partial \left(hU_y\right)}{\partial y} = 0 \tag{2.12}$$

$$\frac{(\partial hU_x)}{\partial t} + \frac{\partial\left(hU_x^2\right)}{\partial x} + \frac{\partial\left(hU_xU_y\right)}{\partial y} = -gh\frac{\partial z_s}{\partial x} + \frac{1}{\rho}\frac{\partial\left[h\left(T_{xx}+D_{xx}\right)\right]}{\partial x} + \frac{1}{\rho}\frac{\partial\left[h\left(T_{xy}+D_{xy}\right)\right]}{\partial y} + \frac{1}{\rho}\left(\tau_{sx}-\tau_{bx}\right) \tag{2.13}$$

$$\frac{(\partial hU_y)}{\partial t} + \frac{\partial\left(hU_xU_y\right)}{\partial x} + \frac{\partial\left(hU_y^2\right)}{\partial y} = -gh\frac{\partial z_s}{\partial y} + \frac{1}{\rho}\frac{\partial\left[h\left(T_{yx}+D_{yx}\right)\right]}{\partial x} + \frac{1}{\rho}\frac{\partial\left[h\left(T_{yy}+D_{yy}\right)\right]}{\partial y} + \frac{1}{\rho}\left(\tau_{sy}-\tau_{by}\right) \tag{2.14}$$

The aforementioned (2.12), (2.13) and (2.14) represents the continuity and momentum equations in x and y coordinate direction respectively. T_{xx} and T_{yy} are the depth-averaged normal and shear stresses; D_{xx} and D_{xy} account for the dispersion of momentum transport due to the vertical non-uniformity of velocity defined as $D_{xx} = \frac{-\rho}{h}\int_{z_b}^{z_s}\left(u_x - U_x\right)^2 dz$, $D_{yy} = \frac{-\rho}{h}\int_{z_b}^{z_s}\left(u_y - U_y\right)^2 dz$ and $D_{xy} = \frac{-\rho}{h}\int_{z_b}^{z_s}\left(u_x - U_x\right)\left(u_y - U_y\right) dz$; τ_{sx} is the x-component of shear force per unit horizontal area; usually due to the wind driven forces at the water surface, defined as $\tau_{sx} = \tau_{xz,s} - \tau_{xx,s}\partial z_s/\partial x - \tau_{xy,s}\partial z_s/\partial y$ and τ_{bx} is the x-component of bed shear force per unit horizontal area, defined as $\tau_{bx} = \tau_{xz,b} - \tau_{xx,b}\partial z_b/\partial x - \tau_{xy,b}\partial z_b/\partial y$. It is worth noting that the dispersion momentum tensor $D_{xy} = D_{yx}$. The closure for depth-averaged stresses can be provided by following the Boussinesq assumption of relating the gradient of depth-averaged velocities to the depth-averaged stresses. Rastogi and Rodi (1978) provided a depth-averaged $\kappa-\epsilon$ models for closure of depth-averaged stresses. However it is the dispersion terms D_{ij} that lacks a general method for their handling in the depth-averaged shallow water equations. In nearly straight channels the dispersion transports is usually combined with the turbulent stresses. In curved channels, secondary flows plays an important role and hence they should be taken in account while formulating numerical models through additional closures.

As regards to the numerical modelling of 2D shallow water equations; the same methodologies i.e. Finite Difference Method (FDM), Finite Volume Method (FVM) and Finite Element Method (FEM) are commonly used. The development of numerical models for 2D shallow water equations historically started with the usage of finite-difference technique. Although FDM schemes

are intuitively easy to understand and apply, there popularity has some what diminished because of its limited applicability in the area of complex domains. However, one can bypass this limitation to some extent by the usage of multi-block technique and using the grid transformation methodology Molls and Chaudhry (1995). The ease of implementation of this methodology is amply demonstrated by its numerous application, some of the examples among many others are Fennema and Chaudhry (1990), Vukovic and Sopta (2002) and Molls and Chaudhry (1995). There are good number of examples of usage of both FEM and FVM technique for the solution 2D shallow water equations. As regards to FEM some of the examples among many others are Katapodes (1984), Akanbi and Katapodes (1988) and Tucciarelli and Termini (2000). Although lot of researchers have devoted their time for the application and development of FEM solvers for the surface flow problems, one that has been widely cited is TELEMAC-2D, Bates et al. (1999), Bates and DeRoo (2000), Horritt and Bates (2001). In regards with the application of 2D numerical models to the real rivers Bates and Anderson (1993) developed a finite element model for river flow inundation. The model considered the depth averaged Reynolds equations along with a simplistic turbulence model for the shear stress. The model developed covered 11 km reach of River Culm, Devon, UK and its adjoining floodplains. The spatial domain was covered with quadrilateral and triangular control volume. Good agreement was obtained between the modelled and observed data. In regards with FVM (Zhao et al., 1994) developed a model RVFVM-2D. There model was also equipped with wetting and drying algorithm. First the model investigated a case of hypothetical dam break which was followed by the application of the model in an experimental area of Kissimmee River basin, Florida. Although the modelling performed in this research work only considered steady state simulations, different upstream discharges at were considered for various set of simulations. Good agreement between the modelled and observed flow velocities at the designated gauges were obtained. A significant and a novel contribution in the area of FVM was made by Anastasiou and Chan (1997), they solved the shallow water equations using Godunov-type second-order upwind finite volume formulation. One of the special contribution in this work was to deal with the two-dimensional problem as a series of local one-dimensional problem. The spatial domain was discretized with the help of triangular cells. The flux at the control volume faces were computed

by solving one-dimenisonal local Riemann problem. Finally the model was applied to benchmark problems and the discrepancy between the modelled and observed data were very marginal. Over the years due to the continuous efforts of various researchers number of commercial codes for solving surface flow problems have also cropped up, common examples are MIKE21 by Danish Hydraulic Institute (DHI), HYDRO2DE Beffa and Connel (2001) among others.

2.4 Three Dimensional Modelling

In regards with three-dimensional modelling of the governing equations (2.1) to (2.4) are solved numerically without any further simplifying assumptions. Although these equations are arrived by RANS approximation of three-dimensional Navier-Stokes equation, the numerical solution of these equations can be computationally very expensive. Deardoff (1970) was one of the first researchers to delve into three-dimensional numerical modeling at large Reynolds numbers. The application of three-dimensional model for river and ocean scale almost always made use of hydrostatic pressure assumption in the vertical, such an assumption felicitated in bringing down the computational cost by an order of magnitude. Blumberg and Mellor (1987) were first in developing a three-dimensional model with hydrostatic pressure assumption, they successfully applied their model to capture ocean related phenomenon. Their model became famous as Princeton Ocean Model (POM). In this model the gradients of baroclinic and barotropic pressures are separated into two distinct modes. Casulli and Cheng (1992) develop another three-dimensional model based on three-dimensional and two-dimensional SWE which became famous as TRIM (Tidal Residual and Intertidal Mudflat) model,(Casulli et al., 1993),(Casulli and Cattani, 1994). The Trim3D model combines a semi-implicit formulation and a Lagrangian-Eulerian model for transport equations. The pressure and velocity nodes are staggered. Based on finite-difference methodology Hydraulics (1999) developed a three-dimensional SWE model where the equations of motion in the horizontal plane was recast into Orthogonal Curvilinear Coordinate System (OCCS). The advantage of transforming the equations of motion from Cartesian grid to curvilinear grid was that it could follow the realistic

boundary lines of the domain in a better manner. Although the transformation of equations results in metrics which complicates the computation of spatial derivatives, this can be somewhat minimized by keeping the curvilinear grids orthogonal. All the aforementioned model cited here used sigma transformation in the vertical. As far as fully three-dimensional modelling of natural rivers are concerned (Sinha et al., 1998) were one of the first researchers to develop completely three-dimensional model for a 4-km stretch of the Columbia River downstream of the Wanapum Dam in the pacific north-west of USA without any hydrostatic pressure assumption . Their model solved RANS equations closed with the standard $\kappa - \epsilon$ turbulence model. Multiple islands in the domain were resolved by applying boundary fitted curvilinear coordinates in conjunction with multiblock approach. Small scale bed-roughness was accounted by incorporating the wall-function concept in the model. Model was calibrated with help of detailed field and laboratory measurements collected for range of power plant operations. The model developed was successfully able to capture various three dimensional flow characteristics. Although a remarkable piece of work the model was only able to simulate 4 kms of the river-reach. In regards with 3D modelling another problem that is ubiquitously encountered is the handling of free-surface. As the position of free-surface keeps on changing with the changing velocity of fluid particles, the position of this free surface should become a part of the computational procedure. Number of methods have been developed to circumvent this problem, Volume of Fluids (Hirt and Nichols, 1981) and Marker in Cell (MAC) (Welch et al., 1966) have gained considerable popularity. In another three-dimensional modelling effort Ye and McCorquodale (1998) developed a 3D model based again on finite-difference technique, in their model in horizontal plane a boundary-fitted curvilinear coordinate was used. But in the vertical direction σ transformation was used which helped in keeping the track of the changing free-surface and variable bed topography. A modified form of $\kappa - \epsilon$ model was incorporated in their work and finally the model was applied to the various experimental set-ups and good agreement was obtained between the modelled and observed data. It must be noted once again that the model was successfully applied to laboratory set-ups.

2.5 Conclusion

There are numerous techniques and packages for the numerical modelling of surface water flow. The decision to use 1, 2 or 3D numerical model is always governed by the problem one is trying to solve. As mentioned in the chapter-1 of this thesis the numerical modelling performed as a part of this research is finally meant for gaining insights into the prevailing flow physics of CAWS. In regards with CAWS, extensive one-dimensional hydrodynamic and water quality modelling of the waterways (CAWS) has been performed by Alp and Melching (2006). Although 1D model gives a good idea of flow characteristics, its limitations can not be ignored. In respect to CAWS with existence of WWTPs, pumping station, slips and other small tributaries the flow feature in CAWS is not always uni-directional. Especially during wet weather conditions when Racine Avenue Pumping Station (RAPS) discharge into the Bubbly Creek, as the flow in the creek travels northward and meets the flow from the south branch it becomes completely three-dimensional in nature. In another location of CAWS, during the winter months when the city of Chicago puts salt on the roads to combat the snow problem, as this salt finds its way in the river, there is a potential for the formation of density currents in the main branch of the Chicago river. Jackson et al. (2008) showed the existence of such density current with the help of the observed flow velocity in the main branch of the Chicago river. In regards with water quality modeling, Motta et al. (2010) have done two-dimensional modeling of portions of CAWS namely Bubbly Creek. But due to the degraded nature of the bed of Bubbly Creek, a three-dimensional model which captures the effect of SOD and DO depletion due to resuspended sediment Waterman et al. (2011) would be more viable. keeping all these consideration in mind it was decided to use a public domain model EFDC for three-dimensional modeling of CAWS. EFDC (Environmental Fluid Dynamics Code) is an EPA approved three-dimensional model, based on finite difference methodology, capable of simulating free-surface hydrodynamics in riverine and estaurine environments. In this research work the three-dimensional hydrodynamic modeling of CAWS is carried out using EFDC, to reduce to computational time taken to simulate various storms the hydrodynamic kernel is parallelized using Open-MP paradigm. Water quality models that can work in conjunction with the hydrodynamic kernel of EFDC are also developed and

are applied to small and large stretches of CAWS. Also as a part of this research another open source code TELEMAC suite of models based on finite element methodology are used for developing index velocity relationship in Illinois and Michigan canal branch of CAWS. Finally to get a sense in depth-averaged mode a two-dimensional model based on finite difference methodology is developed and applied to the portions of CAWS.

CHAPTER 3

DEVELOPMENT AND APPLICATION OF 2D MODELS

3.1 Introduction

One dimensional numerical model based on some form of Saint-Venant equations are ubiquitous and commonly applied for long term simulations and large spatial domains, encompassing real rivers, some examples are (Brunner (2001) DHI (2005) Wu and Vieira (2001)) among many others. One dimensional models are computationally least expensive and easy to set up and use, however, the limitations offered by such models cannot be ignored. In one dimensional models the flow is supposed to be unidirectional, generally following the direction parallel to that of the main channel. In cases where there is a formation of recirculation zones, 1D model would grossly overestimate the conveyance. 1D models can certainly not be used in the vicinity of hydraulic structures. Furthermore 1D models are apt for the cases where the flow path of the river being modeled is well defined. With the increasing speed of desktop computers and advent of cluster computers there has been a paradigm shift in the numerical modelling of surface flow problems, considerable research has been done in developing numerical models based on two dimensional Saint-Venant equations. Two dimensional Saint-Venant equations are also commonly known as 2D shallow water equations (2D-SWE) these are derived from depth averaging of three dimensional Navier-Stokes equations (3D-NSE) under a simplifying assumption of hydrostatic pressure distribution in the vertical. This assumption of hydrostatic pressure distribution in vertical direction is often used by numerical modellers and is a plausible assumption for modelling environmental flows characterized by horizontal length scales which are orders of magnitude greater than their vertical counterparts. Over the past number of years considerable amount of research has been done for developing numerical methods for solving 2D-SWE. Three

most commonly used techniques are finite difference, finite volume and finite element methods.

As already explained Finite difference method (FDM) is based on the differential form of governing equations and in this method the solutions are computed on a given set of nodes also known as the computational domain, the unknown variables are solved for by replacing the differential equations with their discretized form which are obtained by truncated Taylor series expansion. (Chow and Ben-Zvi, 1973) were one of the pioneers in development of numerical models based of finite difference methodology for solution of 2D-SWE. A lot of other researchers have contributed significantly in the development of finite difference algorithm for the solution of 2D Saint-Venant equations, some of the examples among many other are (Aureli et al. (2000) Hervouet and Petitjean (1999) Molls and Chaudhry (1995) Fennema and Chaudhry (1990)).

In case of Finite volume methods (FVM) are based on the integral form of governing equations and has the advantage of incorporating the discontinuities in the solution which might occur due to the hyperbolic nature of the governing equations. Finite volume methods can be implemented on both structure and unstructured meshes. The method essentially comprises of decomposing the computational domain in smaller number of control volume and it is on these control volumes that the integral forms of the governing equations are solved. Some of the examples among many others pertaining to the application of finite volume method for the solution of 2D-SWE are (Abad et al. (2008) Anastasiou and Chan (1997) Brufau et al. (2002)).

Finite element methods (FEM) is commonly used in conjunction with unstructured meshes. The computational domain is decomposed into smaller sub-domains which may be triangular or quadrilateral in shape. The solution at any point is then represented by a series expansion of the nodal values with in the local vicinity of that point. The nodal contributions are multiplied by basis function (also known as shape, interpolation or trial functions) and the representation of basis function defines the finite element method being used. Number of researchers have contributed in development and application of FEM to 2D-SWE. Some of the examples among many others are (Bates et al. (1992) Berger and Stockstill (1995) Akanbi and Katapodes (1988) Hervouet and Petitjean (1999)). As mentioned lot of researchers have contributed in the development of FEM algorithms as applied to 2D-SWE but one of the

most cited model is TELEMAC-2D Bates et al. (1992) Hervouet and Petitjean (1999). The has been an increased interest in the development and application of TELEMAC suite of models especially after it went open-source (www.opentelemac.org).

In this research work first a finite-difference model based on body fitted generalized curvilinear coordinate form of 2D-SWE (FinFlow-2D) is developed and applied to physical models and a real world case of Bubbly Creek, south fork of the South Branch of the Chicago River Sinha et al. (2010). The same cases are also simulated with the FEM model TELEMAC-2D. TELEMAC-2D was developed by the National Hydraulics and Environment Laboratory of the Research and Development Directorate of the French Electricity Board (EDF-R&D) in collaboration with other research institutes. TELEMAC-2D is based on finite-element methodology Hervouet (2007) and offers the significant advantage of accommodating irregular boundaries. The hydrodynamic simulation results obtained from both the models are studied and presented in a comparative fashion.

3.2 Depth-averaged Models used and Developed

In the following subsections depth-averaged model used and developed are described in detail. This is followed by the application of depth-averaged model for various lab set-ups and different portions of CAWS.

3.2.1 Description of FinFlow-2D Model

The finite difference model FinFlow-2D developed as part of this research is based on the non-conservative form of 2D-SWE. These equations are transformed to generalised curvilinear form to accommodate the irregular boundaries. The equations of motion solved by FinFlow-2D model are as follows.

$$\frac{\partial \zeta}{\partial t} + \frac{\partial (Uh)}{\partial x} + \frac{(Vh)}{\partial y} = 0 \tag{3.1}$$

$$\frac{\partial U}{\partial t}+U\frac{\partial U}{\partial x}+V\frac{\partial U}{\partial y}=fV-g\frac{\partial \eta}{\partial x}+\frac{\tau_{wx}-\tau_{bx}}{\rho h}+\nu_t\left[2\frac{\partial^2 U}{\partial x^2}+\frac{\partial^2 V}{\partial x\partial y}+\frac{\partial^2 U}{\partial x^2}\right] \quad (3.2)$$

$$\frac{\partial V}{\partial t}+U\frac{\partial V}{\partial x}+V\frac{\partial V}{\partial y}=fU-g\frac{\partial \eta}{\partial y}+\frac{\tau_{wy}-\tau_{by}}{\rho h}+\nu_t\left[2\frac{\partial^2 V}{\partial x^2}+\frac{\partial^2 U}{\partial x\partial y}+\frac{\partial^2 V}{\partial y^2}\right] \quad (3.3)$$

In the above equations, Eq.(3.1), (3.2) and (3.3) denotes the continuity and momentum equation in x and y direction respectively. ζ denotes the water surface elevation, U is the depth-averaged velocity in the x direction, V is the depth-averaged velocity in Y direction, h is the depth of the water column, f is the Coriolis force, g is the acceleration due to gravity, ν_t is the turbulent eddy viscosity, τ_{wx} and τ_{wy} is the wind shear stress on the surface of water in x and y direction respectively and finally τ_{bx} and τ_{by} is the bed shear stress again in x and y direction respectively. Before the governing equations for FinFlow-2D model can be solved numerically they are transformed to non-orthogonal boundary fitted coordinate system. The transformed equations in boundary-fitted curvilinear coordinate is given by the following equations

$$\frac{\partial \zeta}{\partial t}+\frac{1}{J}\left[y_\eta\frac{\partial (UD)}{\partial \xi}-y_\xi\frac{\partial (UD)}{\partial \eta}+x_\xi\frac{\partial (VD)}{\partial \eta}-x_\eta\frac{\partial (VD)}{\partial \xi}\right]=0 \quad (3.4)$$

$$\begin{aligned}\frac{\partial U}{\partial t}+\frac{[y_\eta U-x_\eta V]}{J}\frac{\partial U}{\partial \xi}+\frac{[x_\xi V-y_\xi U]}{J}\frac{\partial U}{\partial \eta}-fV+\frac{g}{J}\left[y_\eta\frac{\partial \zeta}{\partial \xi}-y_\xi\frac{\partial \zeta}{\partial \eta}\right]\\ -\frac{\tau_{wx}-\tau_{bx}}{\rho h}-\nu_t TRANSFORM\left[2\frac{\partial^2 U}{\partial x^2}+\frac{\partial^2 V}{\partial x\partial y}+\frac{\partial^2 V}{\partial x^2}\right]=0\end{aligned} \quad (3.5)$$

$$\begin{aligned}\frac{\partial V}{\partial t}+\frac{[y_\eta U-x_\eta V]}{J}\frac{\partial V}{\partial \xi}+\frac{[x_\xi V-y_\xi U]}{J}\frac{\partial V}{\partial \eta}+fU+\frac{g}{J}\left[x_\xi\frac{\partial \zeta}{\partial \eta}-x_\eta\frac{\partial \zeta}{\partial \xi}\right]\\ -\frac{\tau_{wy}-\tau_{by}}{\rho h}-\nu_t TRANSFORM\left[2\frac{\partial^2 V}{\partial x^2}+\frac{\partial^2 U}{\partial x\partial y}+\frac{\partial^2 V}{\partial y^2}\right]=0\end{aligned} \quad (3.6)$$

In the equations, Eq. (3.4), (3.5) and (3.6) ξ and η shows the two curvilinear coordinate direction, the function TRANSFORM denotes that the argument in the bracket needs to be transformed before the model imple-

mentation. The argument in the TRANSFORM function corresponds to the diffusion term in Eq.(3.2) and (3.3). As the diffusion terms is second order in nature, the transformation leads to the generation of several terms. The basic transformation technique from cartesian coordinates to curvilinear coordinates for the first and second order derivative is governed by the following rules.

$$f_x = \frac{1}{J}\left[f_\xi y_\eta - f_\eta y_\xi\right] \tag{3.7}$$

$$f_y = \frac{1}{J}\left[f_\eta x_\xi - f_\xi x_\eta\right] \tag{3.8}$$

In the equations, Eq.(3.7) and Eq.(3.8) x and y denotes the cartesian coordinates and ξ and η are the curvilinear ones. The jacobian of transformation is given by $J = x_\xi y_\eta - x_\eta y_\xi$. As regards to the second derivative terms the transformation expression can again be obtained by successive application of Eq.(3.7) and Eq.(3.8). For example the second derivative $f_x x$ in transformed curvilinear coordinates will be given as.

$$f_{xx} = \frac{\left[y_\eta^2 f_\xi \xi - 2y_\xi y_\eta f_\xi \eta + y_\xi^2 f_\eta \eta\right]}{J^2} + \frac{\left[y_\eta^2 y_\xi \xi - 2y_\xi y_\eta y_{\xi\eta} + y_\xi^2 y_{\eta\eta}\right]\left[x_\eta f_\xi - x_\xi f_\eta\right]}{J^3} + \frac{\left[y_\eta^2 x_\xi \xi - 2y_\xi y_\eta x_{\xi\eta} + y_\xi^2 x_{\eta\eta}\right]\left[y_\xi f_\eta - y_\eta f_\xi\right]}{J^3} \tag{3.9}$$

Similar formulation can be developed for f_{yy} and f_{xy}. It is these transformed equations,

FinFlow-2D solves generalized curvilinear coordinate form of 2D-SWE as represented by equations Eqs.(3.4),(3.5) and (3.6). The aforementioned governing equations are solved through mix of implicit and explicit technique. Continuity equation, Eq. (3.4)is solved through an implicit technique and momentum equations, Eqs.(3.5) and (3.6) are solved through an explicit technique. The hydrodynamic variables, depth-averaged velocity components (U and V) and the water surface elevation are stored in a staggered manner on

the structured computational grid (Figure3.1). The staggered arrangement of variables helps in the implementation of higher order differencing scheme. As shown in (Figure3.1), in FinFlow-2D both components of depth averaged velocities are stored on both the horizontal and vertical edges of the control volume. This helps in successful implementation of higher-order discretization scheme for the cross derivative terms, for example $\frac{\partial(UD)}{\eta}$ in Eq.(3.5). The water surface elevation is stored in the center of the control volume. As is well known that the most troublesome term to model in 2D-SWE is the advective term. First-order implementation of the advective term despite being less dissipative, compromises on the accuracy. Second-order scheme generally give rise to spurious oscillations and in convection dominated flow may eventually destroy the solution. Hence, in the present work second order hybrid upwind-central scheme with the facility of ghost cell on the boundary was implemented for the advective term. The terms other than advective in nature were discretized using second-order central difference scheme.

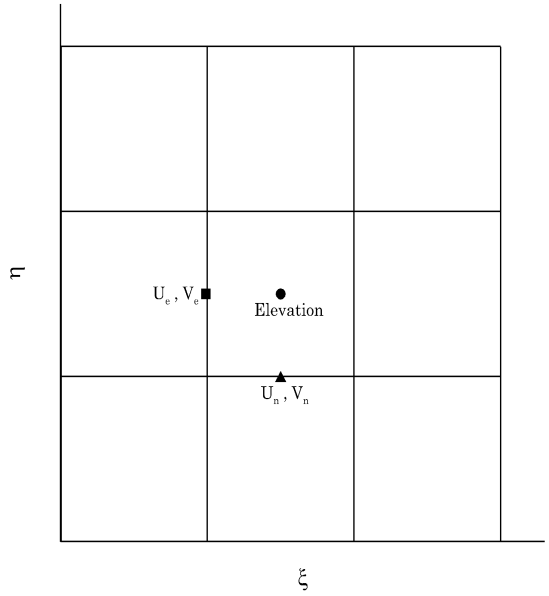

Figure 3.1: Staggered arrangement of variables

As already mentioned pure upwind scheme results in unwanted spurious oscillations, hence a hybrid scheme, a mixture of central and upwind scheme was used in the model developed. As shown in the Figure 3.1 the velocity both velocity components are located on north as well as the eastern edge of

the control volume. In regards to the advective term the hybrid second-order upwind scheme needs to be applied to the $\left[\frac{y_\eta U - x_\eta V}{J}\right]\frac{\partial U}{\partial \xi}$ in the x-momentum equation. The second order hybrid upwind-scheme is applied in the following manner. If $y_{\eta I,J}U^n_{E,i,j} - x_{\eta I,J}V^n_{E,i,j} \geq 0$ then

$$\frac{\partial U}{\partial \xi} \approx P1\left[\frac{3U^n_{E,i,j} - 4U^n_{E,i-1,j} + U^n_{E,i-2,j}}{2}\right] + P2\left[3U^n_{E,i,j} - 4UT1 + U^n_{E,i-1,j}\right] \tag{3.10}$$

P1 and P2 in the above equation are coefficients which work as the weighting factor given to the two-cell and one-cell derivative calculations and there sum should be equal to unity. As regards to UT1, it is given by the following expression $UT1 = \frac{U^n_{N,i,j}+U^n_{N,i,j-1}}{2}$. The subscript E and N denotes the variables located on the east and north edges of the control volume respectively. If $y_{\eta I,J}U^n_{E,i,j} - x_{\eta I,J}V^n_{E,i,j} < 0$ then

$$\frac{\partial U}{\partial \xi} \approx -P1\left[\frac{3U^n_{E,i,j} - 4U^n_{e,i+1,j} + U^n_{E,i+2,j}}{2}\right] - P2\left[3U^n_{E,i,j} - 4UT2 + U^n_{E,i+1,j}\right] \tag{3.11}$$

In the above expression $UT2 = \frac{U^n_{N,i+1,j}+U^n_{N,i+1,j-1}}{2}$. In the x-momentum equation the second-order hybrid upwind scheme also needs to be applied to the term $\left[\frac{y_\eta U - x_\eta V}{J}\right]\frac{\partial U}{\partial \xi}$. This is carried out in a somewhat similar manner. If $x_{\xi I,J}V^n_{E,i,j} - y_{\xi I,J}U^n_{E,i,j} \geq 0$ then

$$\frac{\partial U}{\partial \eta} \approx P1\left[\frac{3U^n_{E,i,j} - 4U^n_{E,i,j-1} + U^n_{E,i,j-2}}{2}\right] + P2\left[3U^n_{E,i,j} - 4UT1 + U^n_{E,i,j-1}\right] \tag{3.12}$$

where $UT1 = \frac{U^n_{N,i,j-1}+U^n_{N,i+1,j-1}}{2}$. Also if $x_{\xi I,J}V^n_{E,i,j} - y_{\xi I,J}U^n_{E,i,j} < 0$ then

$$\frac{\partial U}{\partial \eta} \approx -P1\left[\frac{3U^n_{E,i,j} - 4U^n_{E,i,j+1} + U^n_{E,i,j+2}}{2}\right] - P2\left[3U^n_{E,i,j} - 4UT2 + U^n_{E,i,j+1}\right] \tag{3.13}$$

where $UT2 = \frac{U^n_{N,i,j}+U^n_{N,i+1,j}}{2}$. The expressions given above correspond to the momentum equation in the x-direction, in a symmetrical manner the advective terms corresponding to the y momentum equation in generalised curvilinear coordinate can be discretized. As regards to the rest of the terms in both x and y momentum equation second order central difference scheme was utilized.

3.2.2 Description of TELEMAC-2D

The governing equation solved by TELEMAC-2D are as follows

$$\frac{\partial U}{\partial t}+U\frac{\partial U}{\partial x}+V\frac{\partial U}{\partial y} = -g\frac{\partial \eta}{\partial x}+\frac{\tau_{wx}-\tau_{bx}}{\rho h}+\frac{1}{h}\left[\frac{\partial}{\partial x}\left(h\nu_t\frac{\partial U}{\partial x}\right)+\frac{\partial}{\partial y}\left(h\nu_t\frac{\partial U}{\partial y}\right)\right]+S_x \tag{3.14}$$

$$\frac{\partial V}{\partial t}+U\frac{\partial V}{\partial x}+V\frac{\partial V}{\partial y} = -g\frac{\partial \eta}{\partial y}+\frac{\tau_{wx}-\tau_{bx}}{\rho h}+\frac{1}{h}\left[\frac{\partial}{\partial x}\left(h\nu_t\frac{\partial V}{\partial x}\right)+\frac{\partial}{\partial y}\left(h\nu_t\frac{\partial V}{\partial y}\right)\right]+S_y \tag{3.15}$$

The equations solved by TELEMAC-2D are again based on 2D Saint-Venant equations but the way it is represented is a bit different. In equations Eq.(3.14) and Eq.(3.15) U and V once again denotes the depth average velocity in x and y direction, ν_t is the turbulent eddy viscosity

The governing equations solved by TELEMAC-2D are presented in equations Eqs.(3.14) and (3.15). The numerical solution of these equations are obtained by adopting the fractional-step method. In the first step the advective part of the governing equations are solved by the method of characteristics. Due to the hyperbolic nature of the advection equation method of characteristics is a suitable choice. The variables solved for are depth-averaged velocity components (U and V) and water depth (h), also if $\kappa - \epsilon$ model is used for the eddy viscosity computation, they are also advected with the method of characteristics. In the second step the solution from the first step is used as the initial values for the hydrodynamic variables. In this step rest of terms i.e. diffusion, source terms and propagation is considered. These terms are resolved with the help of finite-element methodology. Variational

formulation and dicretization in space and time then transform continuous equations into discrete linear system whose unknown are the values of physical quantities, U, V and h at the nodes of the computational mesh. The linear system thus obtained is then resolved by an iterative method of the conjugate gradient type.

3.2.3 Grid Generation and Boundary Conditions

FinFlow-2D has been developed for multiblock structured mesh. The preprocessor used for generating grids for FinFlow-2D is Gridgen. Although model is developed for genralized curvilinear from of Shallow Water Equations, while constructing the grids it is attempted to keep it as orthogonal as possible. As the end purpose of model development is its application to portions of CAWS, the multiblock ability of the model helps in incorporating various side slip structures while simulating portions of CAWS. As regards to TELEMAC suite of models, it works with unstructured mesh. The ability to work on unstructured mesh helps in accommodating highly irregular boundaries. The preprocessor used for generating grids for TELEMAC is Bluekenue. The mesh generator, Bluekenue, is developed by Canadian Hydraulic Center (CHC) and is freely available from there website, $http : //www.nrc - cnrc.gc.ca/eng/ibp/chc/software/kenue/blue - kenue.html.$

As regards to the boundary conditions. At the open boundaries FinFlow-2D has been programmed to handle prescribed discharge or free surface elevation. These values can be either fixed in time or can be given as a time-series. On the solid boundaries for the faster code development all the velocity components are made zero. In TELEMAC-2D the open boundaries can be specified in identical manner to FinFlow-2D that is the user can specify either a fixed or a time series of discharge or free-surface elevation. At the solid boundaries the normal component to the wall is made zero, for the tangential component wall-function methodology is implemented.

3.3 Test Cases for Validation of 2D Models

3.3.1 Flow in a T-shape Channel

Flow in a branched T-shape flume has been investigated by many researchers. Shettar and Muruthy (1997) conducted both physical and numerical modelling of the flow features in the T-shaped flume, more recently Lai (2010) also investigated the same test case with their finite volume model. The T-shaped flume consist of 3 m long horizontal channel with a perpendicular side channel again of 3 m in length. The width of both the main channel and the side channel in 0.3 m in width.

The structured mesh used for FinFlow-2D had a resolution 120 X 30 cells for the main channel and 40 X 30 cells for the side channel. The resolution in the zone of confluence between the side and the main channel was increased in such a fashion that Δ x = Δ y = 0.01 m.

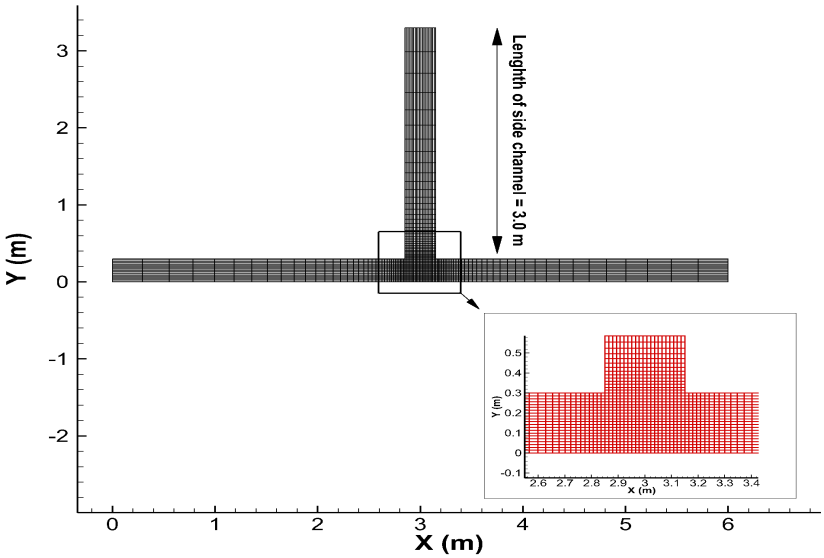

Figure 3.2: Boundary-fitted mesh for T-channel for FinFlow-2D

In the aforementioned flume the same flow configuration as simulated by Shettar and Muruthy (1997) is simulated. The boundary condition for the simulation is appropriately shown in Figure 3.4. An inflow value of 0.00567 m^3/s in the main channel and boundary stage elevation of 0.0465 m is simulated. The flume is initialized with constant water depth of 0.0555 m.

As the flow reaches a steady state both in TELEMAC-2D and FinFlow-2D

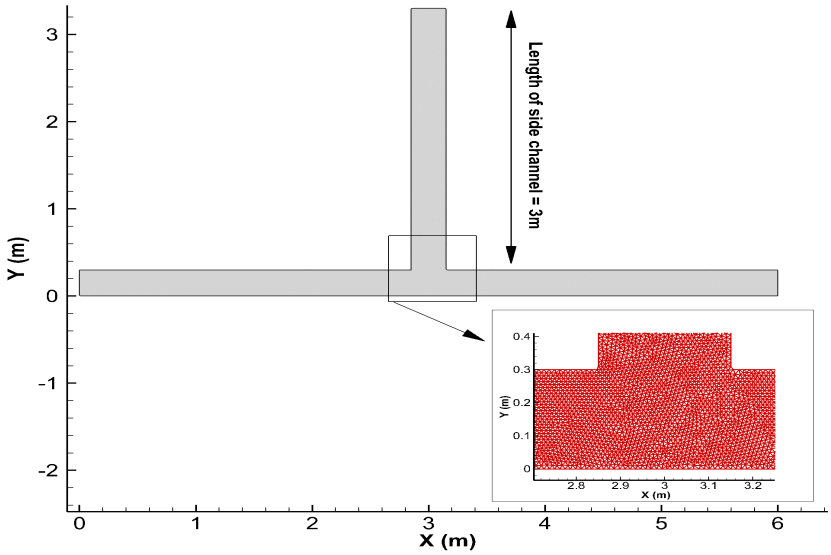

Figure 3.3: Boundary-fitted mesh for T-channel for TELEMAC

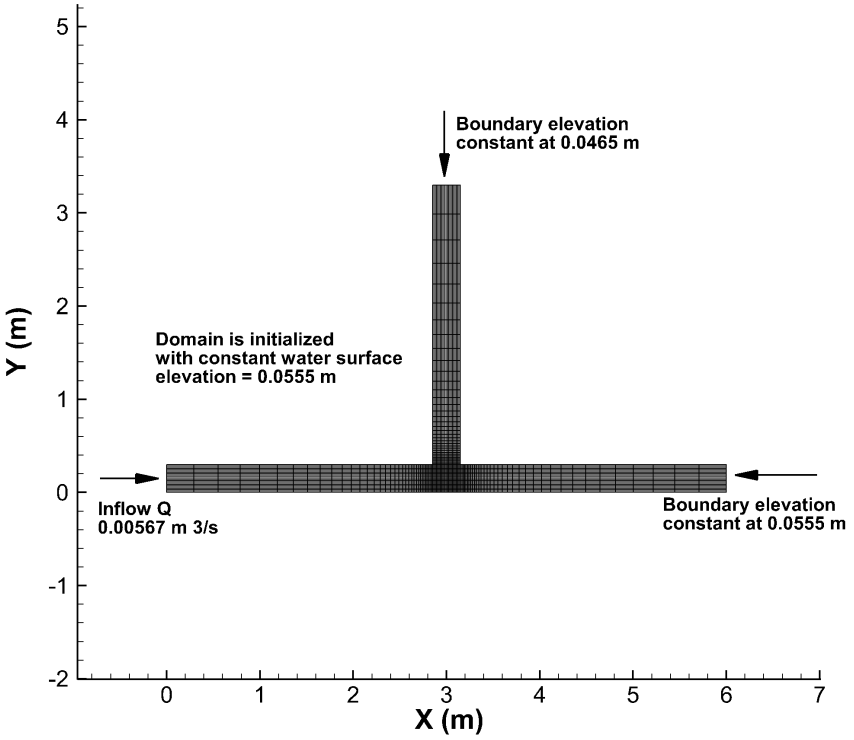

Figure 3.4: Flow configuration for T-channel

a circulation zone is formed in the side channel, this is shown in 3.5. The flow velocity reaches as high as 0.5 m/s in the side channel. A second separation zone is observed in the main channel in FinFlow-2D simulation (Figure 3.5b)

because of the absence of wall function implementation.

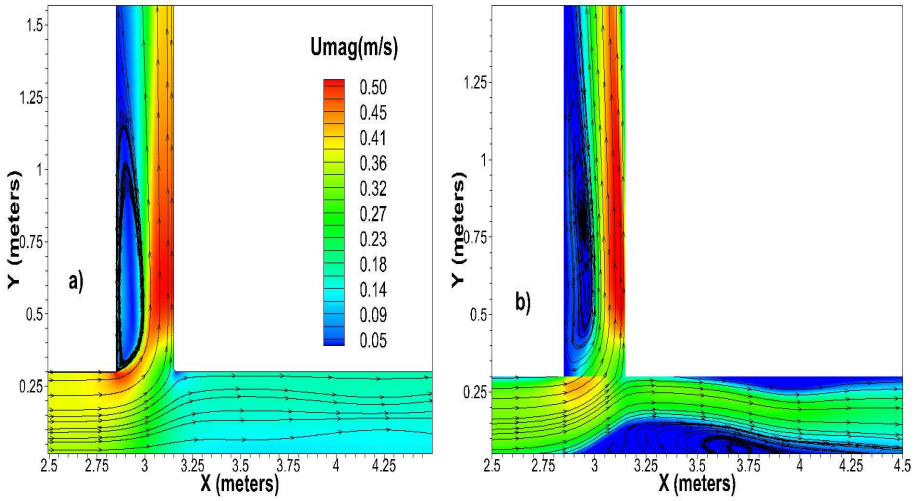

Figure 3.5: Flow field at steady state a) From TELEMAC-2D b) From FinFlow-2D

3.3.2 Flow in Bubbly Creek: Portion of CAWS

As mentioned before, models developed and used as a part of this research is finally applied for simulating the flow physics in portions of the Chicago Area Waterways System (CAWS). Bubbly creek is a 2200 meters long channel that forms the South Fork of the South Branch of CAWS. As shown in Figure3.6 towards the southern end of the creek RAPS is located. During the wet weather conditions when the conveyance capacity of RAPS to transport the rainfall-run-off water to the treatment plant at Stickney (Figure3.6) is overwhelmed, it leads to CSO discharge into the creek. In this research a typical CSO event is simulated both with FinFlow-2D and TELEMAC-2D. The grids used by FinFlow-2D and TELEMAC-2D is shown in Figure3.7 and Figure3.8 respectively.

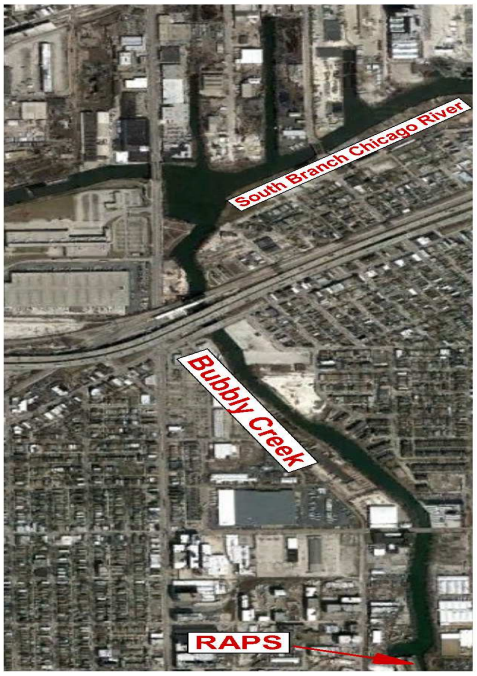

Figure 3.6: Bubbly Creek, South Fork of South Branch of Chicago River

The bed-elevation of Bubbly creek is at a higher level than the adjoining South Branch (SB). The water depth in Bubbly Creek varies between 1.5 m - 3.0 m. During a CSO event the inflow from RAPS leads to higher flow velocities inside the creek. As the flow makes its way to the SB it finds a deeper area and there is a significant reduction in the flow velocity. The CSO event simulated as a part of this research had a flow magnitude of 45 m^3/s from RAPS and 25 m^3/s in the SB flowing from east to west. The water

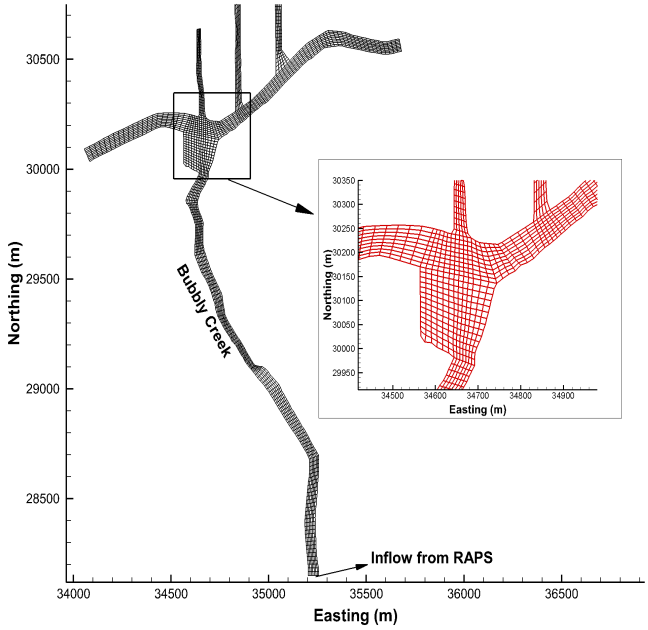

Figure 3.7: Boundary-fitted Mesh for Bubbly Creek

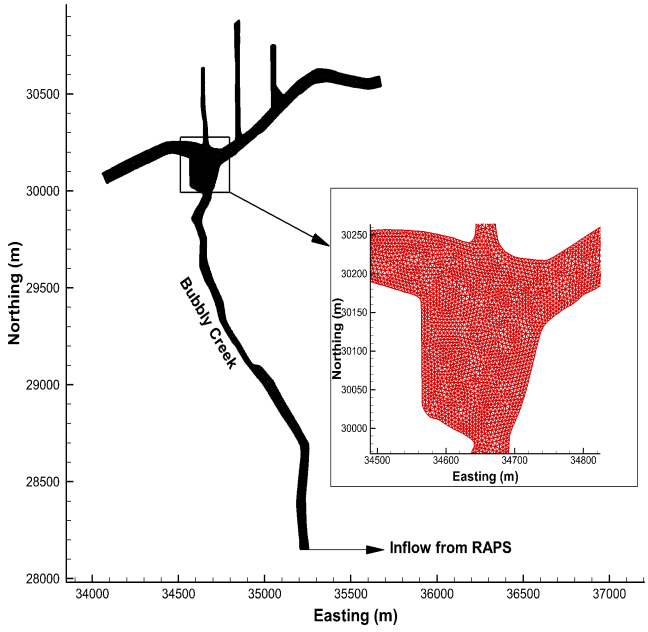

Figure 3.8: Unstructured Mesh for Bubbly Creek

surface elevation at the west end of computational domain was held constant at -0.66 m with Chicago City Datum (CCD). CCD is situated at the 176.63 m above sea level. The simulation results at steady state is shown in Figure

3.9 and 3.10

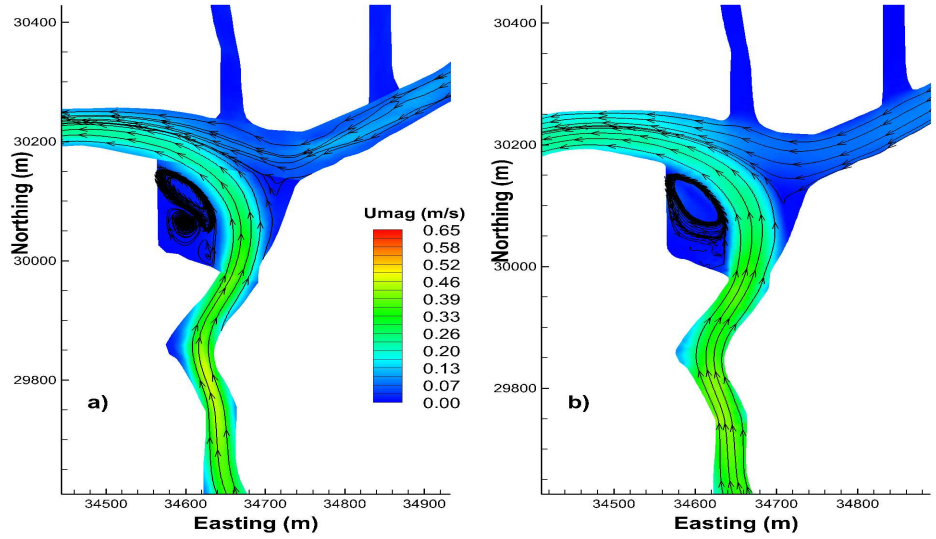

Figure 3.9: CSO event in Bubbly Creek a) Flow velocity at steady state from FinFlow-2D near turning basin b) Flow velocity at steady state from TELEMAC-2D near turning basin

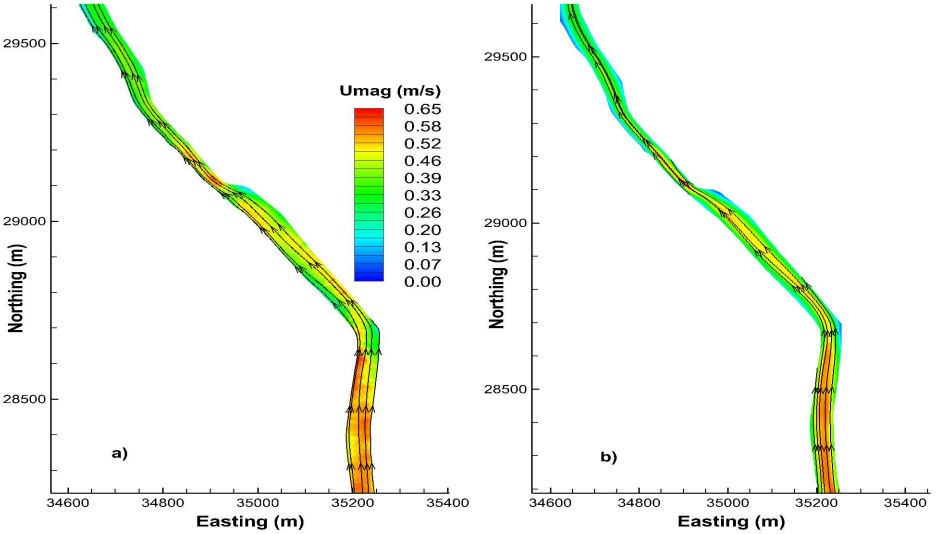

Figure 3.10: CSO event in Bubbly Creek a) Flow velocity at steady state from FinFlow-2D near RAPS b) Flow velocity at steady state from TELEMAC-2D near RAPS

Both TELEMAC-2D and FinFlow-2D converge at about same velocity magnitude values, the flow velocities in Bubbly Creek reaches 0.45 m/s as it

nears the turning basin and is at even higher level near RAPS at around 0.65 m/s in both FinFlow-2D and TELEMAC simulation. Also noticeable from Figures 3.9 and 3.10 is that as the flow exits from the creek it flows towards the west, which is the normal flow orientation in the SB of the Chicago River.

3.4 Conclusion

In this chapter a 2D model based on depth-averaged shallow water equations implemented on generalised curvilinear coordinate is presented. The governing equations are transformed from cartesian coordinate to curvilinear coordinate before the numerical implementation. The 2D model developed as a part of this research captured the extent of recirculation zone in the branched channel, Figure , in a satisfactory manner. The extent of recirculation zone is quite similar to what was obtained by Shettar and Muruthy (1997) and more recently by Lai (2010) . As explained Shettar and Muruthy (1997), one of the best ways to study the flow pattern in a branched channel is through stream lines. The flow at the junction in the case of T-Channel can be divided in two regions; the region from which the branched channel abstracts the water and region where the flow continues in the main channel. The dividing streamline can be seen in Figure 3.5. Its worth mentioning that the flow in a T-Channel presented here is inherently three-dimensional in nature. The same flume with identical boundary condition was also simulated with a three-dimensional model EFDC. The details about the EFDC model is presented in the next chapter. The streamlines when plotted with 3D model, EFDC, at the steady state showed a little different pattern.

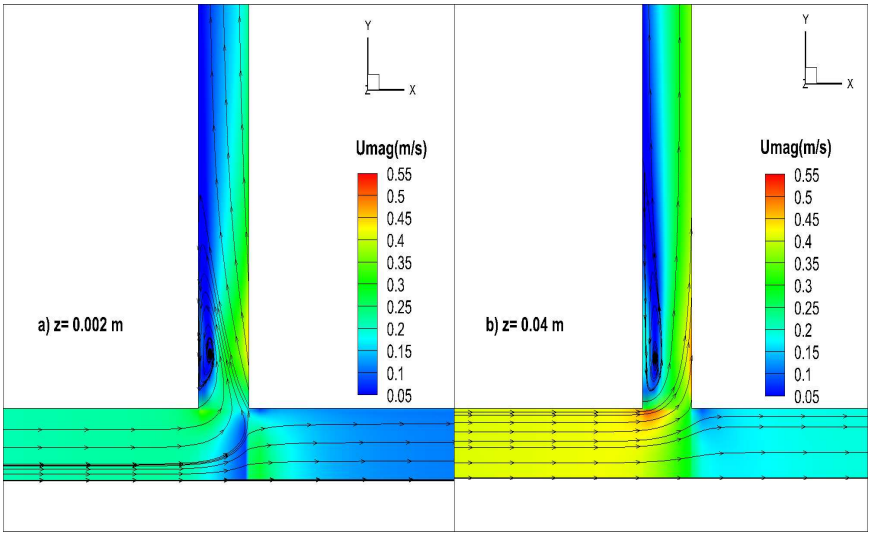

Figure 3.11: Streamlines at steady state a)At z = 0.002 m from the bottom b) At z = 0.04 m from the bottom

Presented Figure 3.11a are streamlines in the T-Channel at an elevation of z = 0.002 m and 3.11b shows the pattern at an elevation of z = 0.4 m

obtained by EFDC model. The diving stream line between two regions of flow extends further into the main channel in the slice near the bed (z = 0.002 m) as shown in Figure 3.11a. This is due to the fact that slower moving fluid near the bed is abstracted and turned into the side channel with greater ease as compared to the flow near the surface. This is further elucidated from the zone of higher velocity in the main channel beyond the location of branched channel; this is again due to the fact that faster moving fluid near the surface is comparatively tougher to be moved into the side channel. As regards to the simulation conducted through TELEMAC-2D as shown in Figure3.5 the flow magnitude is quite similar to the one obtained by FinFlow-2D and they tally in a satisfactory manner with the results obtained from (Shettar and Muruthy, 1997).

As far as the simulation in the Bubbly Creek is concerned as mentioned before both FinFlow-2D and TELEMAC-2D produced identical flow velocity plot at steady state, please see Figures 3.9 and 3.10. The zone of higher velocity in both the simulation is located near RAPS and a distinct decrease in the velocity magnitude is noticed as the flow reaches towards the turning basing and eventually into the South Branch. This is explained by the fact that the South Branch of the Chicago River is distinctly deeper than Bubbly Creek.

Finally in conclusion although 2D model is easier to set up and demands less computational resources, there are cases which need application of a fully three-dimensional model. Also in real world situations where water quality conditions are of prime importance, as in the case of Chicago Waterway System, using 3D model helps in incorporating sink and source terms like sediment oxygen demand (SOD) and reaeration in more realistic manner , with SOD term being limited to the bottom layer and reaeration term acting on the top layer Sinha et al. (2010). As a future work authors would like to develop water quality modules for the 2D model which can be connected with the developed hydrodynamic model and parallelize the code either through Open-MP or MPI technique.

CHAPTER 4

THEORETICAL AND NUMERICAL FORMULATION OF THREE-DIMENSIONAL HYDRODYNAMIC AND WATER-QUALITY MODEL

4.1 Introduction

This chapter presents an overview of the basic theoretical and numerical concepts associated with the EFDC model. Environmental Fluid Dynamics Code (EFDC) is an EPA (Environmental Protection Agency) approved public domain code that can model both hydrodynamics and water quality for surface water systems. Although a full three-dimensional numerical model capable of simulating surface flow phenomenon can be very expensive computationally, but with emergence of cluster computers and powerful desktop machines, application and development of three-dimensional models for surface flow problems is becoming increasingly common. Numerous models have been developed in the past decades. Many of them are actually based on similar theories and numerical schemes, even though the way they accept the inputs and the nature in which they output the results might look completely different. Some of the examples of the models sharing the same underlying philosophy are Estuarine, Coastal and Ocean Model (ECOM) Hydroqual (1991),Hydroqual (1995), EFDC, both have hydrodynamic theories similar to the Princeton Ocean Model (POM) Blumberg and Mellor (1987). The application 3D or rather quasi-3D model started after the pioneering work done with Princeton Ocean Model. POM, ECOM, EFDC and CH3D models all use the sigma coordinate in the vertical and orthogonal curvilinear grid in the horizontal, xy-plane. The aforementioned models have been applied to rivers, estuaries and even oceans. The original EFDC model was developed at the Virginia Institute of Marine Science.

A good approximation while describing and subsequently modeling surface water systems is to assume that the flows are incompressible, which implies that the water density does not change with the pressure. The buoyancy ef-

fect in such an incompressible fluid is accounted by what is commonly known as ***Boussinesq Approximation***. In Boussinesq approximation, variations in the water density is ignored, except for the gravitational term where the acceleration due to gravity is multiplied by modified density which incorporates the change in density due to various dissolved constituents or the temperature effects. The hydrodynamic kernel of EFDC incorporates Boussinesq approximation and is capable of capturing stratification effect.

All the three-dimensional models mentioned before namely, POM, ECOM, CH3D, also Delft3D and finally EFDC assumes the pressure to be hydrostatic along the water column. This is a very common assumption made while modeling the water bodies whose horizontal length scales are order of magnitude greater than there vertical counterparts. This assumption leads in simplifying the three-dimensional Navier-Stokes equations and leads to what is commonly known as ***Three-dimensional Shallow Water Equation***. The hydrostatic approximation assumes that the vertical pressure gradient is almost balanced by the forcing due to buoyancy excess. The vertical acceleration term is much smaller and can be omitted. The hydrostatic assumption proves out to be immensely helpful in the numerical solution of the governing equation. The hydrostatic assumption reduces the vertical momentum equation to the following form.

$$\frac{1}{\rho}\frac{\partial p}{\partial z} = -g \tag{4.1}$$

The hydrostatic approximation equation relates the vertical pressure gradient to the vertical distribution of the density. This hydrostatic pressure assumption along the water column is also made in EFDC. Although hydrostatic assumption for pressure distribution works well in most of the cases, this assumption breaks down when the horizontal length scale reaches the vertical length scale, at these points in the water body the pressure becomes the function of the velocity. An alternative to constructing a fully 3D model is to treat the system as a set of horizontal layers that interact via source-sink terms representing the water exchanges with overlying and underlying layers. This approach allows for eliminating the momentum equations in vertical direction. For the most surface water applications, the ***quasi-3D*** application ensures computational efficiency and model accuracy. EFDC also utilizes this approximation while solving the equation in 3-dimensional framework. Al-

though the quasi-3d approximation helps in solving the 3-dimensional equation in computational efficient manner, this kind of assumption in the model prevents the model from being used for the near field problem, where a high degree of turbulence occurs. For example, a model that does not include a vertical momentum equation cannot resolve momentum transfer due to submerged jet.

As mentioned before that overall goal of this research is to apply EFDC model to various small and large segments of Chicago Area Waterways System (CAWS). In Chapter 5 results from application and validation of EFDC model for various segments of CAWS is presented. Before going into the application, perhaps a detail discussion about the theoretical and numerical formulation of EFDC model is warranted. Also presented in this Chapter is the description of EFDC water quality models and water quality models developed as a part of this research which are applied concomitantly with the hydrodynamic kernel of EFDC. EFDC comes with it's own 21 state variable water quality model, but for present research purposes a simpler DO-BOD model was developed and used in conjunction with the available data sets. Although the 21 state variable water quality model encompasses more physics and processes but such a complicated model would need a lot more input parameters and calibration of such a model could be a very time consuming task. Even with hydrostatic pressure assumption and quasi-3D approximation the computational time consumed by the model to run real time simulation can be quite significant. Hence, as a part of this research the hydrodynamic kernel of EFDC was parallelized on the Open-MP paradigm. EFDC also comes with transport solver for conservative and non-conservative scalars, such as salinity,temperature, dye, shell fish larva and suspended sediment.

4.2 Hydrodynamic Model

The formulation of the governing equations used for the flow simulation of CAWS starts with vertically hydrostatic, boundary layer form of the turbulent equations of motions . As mentioned previously hydrostatic assumption is a reasonable approximation for CAWS and in general a preferred modeling assumption by numerical modelers, while attempting to model rivers,estuaries, bays and other water bodies, where the horizontal length

scales are order of magnitudes larger than the vertical length scale. In the case of Bubbly Creek and CAWS as a whole, this seems to be a fitting and a valid assumption. Furthermore to accommodate the realistic boundary conditions, the governing equations in the horizontal plane are recast in the Orthogonal Curvilinear Coordinate System (OCCS). In order to provide a uniform resolution in the vertical direction a stretching or mapping function is used. The computational domain is bounded by the domain bathymetry at the bottom and free surface at the top, which is dynamic in time and space. The stretching function used to obtain uniformity in the vertical or z direction is given by equation 4.2.

$$z = \frac{(z^* + h)}{(\zeta + h)} \tag{4.2}$$

The * denotes the original physical coordinates, -h and ζ are the physical vertical coordinates of the bottom topography and the free surface respectively. After making the required transformations for the OCCS and implementing the stretching function in the vertical according to equation (4.2), and using the Boussinesq approximation for the variable density fluid, we obtain the desired form of the governing equations. The partial differential equations for continuity, momentum, salinity and temperature forms the governing set of equations of motion for the model. The governing set of equations that are eventually discretized and solved numerically by the model are presented in the equations below.

$$\begin{aligned} &\frac{\partial(mHu)}{\partial t} + \frac{\partial(m_y Huu)}{\partial x} + \frac{\partial(m_x Hvu)}{\partial y} + \frac{\partial(mwu)}{\partial z} - \\ &(mf + v\frac{\partial m_y}{\partial x} - u\frac{\partial m_x}{\partial y})Hv = -m_y H\frac{\partial(g\zeta + p)}{\partial x} \\ &-m_y(\frac{\partial h}{\partial x} - z\frac{\partial H}{\partial x})\frac{\partial p}{\partial z} + \frac{\partial(mH^{-1}A_v\frac{\partial u}{\partial z})}{\partial z} + Q_u \end{aligned} \tag{4.3}$$

$$\frac{\partial(mHv)}{\partial t}+\frac{\partial(m_yHuv)}{\partial x}+\frac{\partial(m_xHvv)}{\partial y}+\frac{\partial(mwv)}{\partial z}-$$
$$(mf+v\frac{\partial m_y}{\partial x}-u\frac{\partial m_x}{\partial y})Hu=-m_xH\frac{\partial(g\zeta+p)}{\partial y} \tag{4.4}$$
$$-m_y(\frac{\partial h}{\partial y}-z\frac{\partial H}{\partial y})\frac{\partial p}{\partial z}+\frac{\partial(mH^{-1}A_v\frac{\partial v}{\partial z})}{\partial z}+Q_v$$

$$\frac{\partial p}{\partial z}=-gH(\rho-\rho_o)\rho_o^{-1}=-ghb \tag{4.5}$$

$$\frac{\partial(m\zeta)}{\partial t}+\frac{\partial(m_yHu)}{\partial x}+\frac{\partial(m_xHv)}{\partial y}+\frac{\partial(mw)}{\partial z}=0 \tag{4.6}$$

$$\frac{\partial(m\zeta)}{\partial t}+\frac{\partial(m_yH\int_0^1 udz)}{\partial x}+\frac{\partial(m_xH\int_0^1 v)}{\partial y}=0 \tag{4.7}$$

$$\rho=\rho(S,T) \tag{4.8}$$

$$\frac{\partial(mHS)}{\partial t}+\frac{\partial(m_yHuS)}{\partial x}+\frac{\partial(m_xHvS)}{\partial y}$$
$$+\frac{\partial(mwS)}{\partial z}=\frac{\partial(mH^{-1}A_b\partial_zS)}{\partial z}+Q_S \tag{4.9}$$

$$\frac{\partial(mHT)}{\partial t}+\frac{\partial(m_yHuT)}{\partial x}+\frac{\partial(m_xHvT)}{\partial y}$$
$$+\frac{\partial(mwT)}{\partial z}=\frac{\partial(mH^{-1}A_b\partial_zT)}{\partial z}+Q_T \tag{4.10}$$

In the equations from (4.3) to (4.10), u and v are the horizontal velocity components in the curvilinear horizontal orthogonal coordinates x and y, m_x and m_y are the square roots of the diagonal components of the metric tensor,

$m = m_x m_y$ is the jacobian or square root of the metric tensor determinant. As mentioned, to impart uniformity in the vertical z direction the depth is mapped using the stretching function given by equation (4.2). The velocity in the stretched vertical dimensionless coordinate z is denoted by w, the equation which relates it to the dimensioned velocity w^* is as follows.

$$w = w^* - z(\frac{\partial \zeta}{\partial t} + um_x^{-1}\frac{\partial \zeta}{\partial x} + vm_y^{-1}\frac{\partial \zeta}{\partial y}) + (1-z)(um_x^{-1}\frac{\partial h}{\partial x} + vm_y^{-1}\frac{\partial h}{\partial y}) \quad (4.11)$$

In computing the total depth (H), we start with placing the origin at undisturbed physical vertical coordinate represented by $z^* = 0$. The total depth (H) is taken as the sum of depth (h) below the undisturbed free surface and the surface elevation (ζ) above the free surface. Hence the total depth becomes $H = h + \zeta$. p represents the amount of physical pressure above the reference density hydrostatic pressure normalized by the reference density ρ_o, hence the expression for p is finally given by $p = \frac{\rho_o g H(1-z)}{\rho_o}$. In the momentum equations (4.3) and (4.4) f is the coriolis parameter, A_v is the vertical turbulent or eddy viscosity, Q_u and Q_v are momentum source and sink terms which are eventually modeled as subgrid-scale horizontal diffusion Smagorinsky (1963). In equation (4.5) b denotes the buoyancy, which is taken as the deviation of density ρ from the reference density ρ_o, normalized by the reference density. The density at different point in the domain is a function of temperature and salinity as shown by the equation (4.8). The equation of state used by the model is given by the following expression.

$$\begin{aligned}\rho(T) = \rho_o + 6.793952 * 10^{-2}T - 9.0952 * 10^{-3}T^2 + 1.001685 * 10^{-4}T^3 \\ -1.120083 * 10^{-6}T^4 + 6.536332 * 10^{-9}T^5\end{aligned} \quad (4.12)$$

Furthermore, the salinity dependence of density is given by the following expression.

$$\begin{aligned}\Delta\rho(S) = S[&0.824493 - 4.0899 * 10^{-3}T + 7.6438 * 10^{-5}T^2 \\ &-8.2467 * 10^{-7}T^3 + 5.3875 * 10^{-9}T^4] \\ +S^{1.5}[&-5.72466 * 10^{-3} + 1.0227 * 10^{-4}T - 1.65646 * 10^{-6}T^2] \\ &+S^2[4.8314 * 10^{-4}]\end{aligned} \tag{4.13}$$

In equations (4.12) and (4.13) T is the temperature in centigrade and S denotes the salinity in PSU (practical salinity units). Integrating the continuity equation (4.6) from the bottom z = 0 to top, z = 1 using the familiar kinematic boundary condition of w = 0 at the top and the bottom we end up with equation (4.7). In transport equations for salinity (4.9) and temperature (4.10), Q_s and Q_t represent the source and sink terms for salinity and temperature respectively. These terms are again modeled as subgrid-scale horizontal diffusion terms. The equations starting from (4.3) to (4.10) form a close system for variables u, v, w, p, ζ, ρ, S and T, provided the vertical turbulent viscosity and diffusivity and source and sink terms are specified. The vertical turbulent viscosity and diffusivity are provided by second moment turbulent closure model developed by Mellor and Yamada (1982), and modified by Galperin et al. (1988). Mellor -Yamada model relates turbulent viscosity A_v and diffusivity A_b to turbulent intensity, qq, a turbulent length scale, l and a Richardson number R_q in the following manner.

$$A_v = \phi_v ql = 0.4(l + 36R_q)^{-1}(1 + 6R_q)^{-1}(1 + 8R_q)ql \tag{4.14}$$

$$A_b = \phi_b ql = 0.5(l + 36R_q)^{-1}ql \tag{4.15}$$

$$R_q = \frac{gh\partial_z b}{q^2}\frac{l^2}{H^2} \tag{4.16}$$

In the equations (4.14) and (4.15) ϕ_v and ϕ_b account for reduced or enhanced vertical mixing or transport in stable and unstable vertically density stratified environments, respectively.

4.3 Numerical Model for Hydrodynamic Equations

The governing partial differential equations presented from (4.3) to (4.10) are discretized and eventually solved for a computational cells enclosed by six faces. In the vertical plane (x,z) or (y,z) the cells are bounded by same non-dimensional constant z height. The governing equations from (4.3) to (4.10) involve free surface dynamics and assumption of rigid lid is not made. The numerical solution for the above equations proceed by adopting a technique of mode splitting Madala. and Piacsek (1977). In the mode splitting technique we solve the fast moving surface wave (external mode) and slow moving internal gravity wave (internal mode) separately, which results in speeding up the simulation by orders of magnitude. The external mode or the volume transport equations are obtained by integrating the internal mode equations over the depth, thereby eliminating all the vertical structure. The depth integration of the equation (4.7) gives us an expression for the variation of free surface in time, which is presented below.

$$\frac{\partial \zeta}{\partial t} + \frac{1}{m}\left(\frac{\partial \overline{U}}{\partial x} + \frac{\partial \overline{V}}{\partial y}\right) = 0 \tag{4.17}$$

The numerical implementation of external mode equations starts with adopting the staggered arrangement of variables on Arikawa or C grid. The staggered arrangement of variable helps in implementing the second order difference scheme for all the spatial derivatives. The staggered arrangement of variables is shown in Figure 4.1.

Finally the solution of internal mode equations gives us the detail velocity structure in vertical and completes the three dimensional picture. The depth-averaged equations (External mode) are not independent of the vertically varying equations (Internal mode). They are coupled through the interfacial stress terms. EFDC model's time integration employs a second order accurate three time level finite difference scheme. The discretized version of external mode equations are solved through semi-implicit scheme which is simultaneously solved by preconditioned conjugate gradient method to yield new surface elevation. The external mode solution is finally completed by calculation of the depth average velocity using new surface elevation. The advantage of semi-implicit in the external model is that it allows for larger

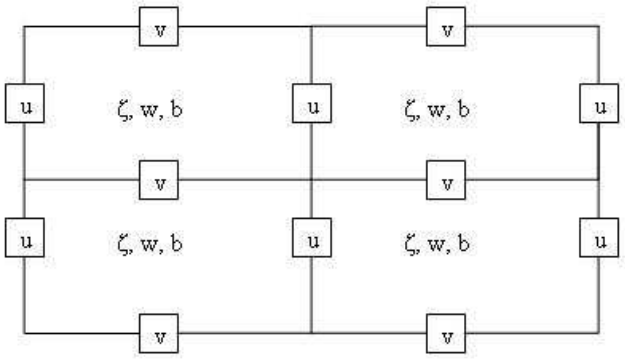

Figure 4.1: Free surface displacement centred horizontal grid

time steps constrained only by the stability criteria of the explicit central difference or upwind advection scheme used for the non liner acceleration term. The detail implementation of the numerical model is presented in Hamrick (1992).

At the risk of reiterating and re-emphasizing the numerical solution of the governing equations for EFDC uses a finite volume-finite difference spatial discretization with an MAC or C grid staggering of the discrete variables. As shown in Figure 4.1 the velocity components are located on the faces of the primary or continuity control volume, with the depth, buoyancy, and concentration of transported constituents located at the centroid. As regrads to the excess pressure it is defined on the top face of the continuity control volume. Horizontally staggered control volumes are defined for the horizontal momentum equations, with advective momentum fluxes located on the faces and shear stresses located on the top faces. An additional set of control volumes, staggered vertically, are used for the transport equations for the turbulence parameters. Finite volume spatial integration over the four sets of control volumes combined with finite difference approximations of horizontal depth, excess pressure, and bottom elevation gradients results in centred, second-order-accurate spatial discretizations. The Coriolis and curvature accelerations in the momentum equations are discretized using a second-order accurate, energy-conserving scheme Arakawa and Lamb (1977). The temporal integration of the momentum and continuity equations uses a second-order-accurate, semiimplicit, three-time-level, leapfrog trapezoidal

scheme, with the period insertion of a two-time-level trapezoidal step to suppress the computational mode generated by the three-time-level scheme. An externalinternal mode splitting scheme is also utilized to give partial decoupling of the external or barotropic model solution (which is implicit in the horizontal) from the internal, baroclinic or shear stress solution (which is implicit in the vertical).

4.4 Boundary Conditions for the Hydrodynamic Model

The boundary conditions for the numerical model can be primarily divided into the categories of vertical and lateral boundary. The flow being modeled needs to satisfy certain boundary conditions at the top (the free surface), bottom (the river bed). The free surface is a material surface and hence there can not be any flow across it; hence we end up with the kinematic boundary condition for the bed and the surface of the river as $w = 0$ at $z = (0, 1)$. Vertical boundary condition for the momentum equations are kinematic shear stresses at the surface $z = 1$ and the bottom $z = 0$. Shear stresses at the top and bottom is given by the following equation.

$$A_v H^{-1} \partial_z (u, v)_{z=0} = (\tau_{bx}, \tau_{by}) = C_B \sqrt{u_{bl}^2 + u_{bl}^2} (u_{bl}, v_{bl}) \tag{4.18}$$

$$A_v H^{-1} \partial_z (u, v)_{z=1} = (\tau_{sx}, \tau_{sy}) = C_D \sqrt{U_w^2 + V_w^2} (U_w, V_w) \tag{4.19}$$

In the above equations τ_{bx} and τ_{by} corresponds to the shear stresses at the bottom (z=0), τ_{sx} and τ_{sy} = shear stresses at the surface (z=1), U_w and V_w corresponds to the wind velocity components at 10 m above the water surface, C_B is the bottom drag coefficient, C_D is the wind stress coefficient and finally the subscript bl refers to the velocity at the bottom sigma layer. In sigma coordinate system, the bottom drag coefficient is usually calculated using Mellor (1988).

$$C_B = \frac{\kappa^2}{(ln(\Delta z_b / 2 z_o))^2} \tag{4.20}$$

where $\kappa = 0.4$ is Karman constant, Δz_b is the dimensionless thickness of the bottom layer, $z_o = z_o^*/H$ is the dimensionless roughness height and z_o^* is the bottom roughness height.
The wind stress coefficient, C_D is given by the following expression.

$$C_D = 1.2 * 10^{-6}(0.8 + 0.065\sqrt{U_w^2 + V_w^2}) \tag{4.21}$$

where U_w and V_w are wind velocity components in meters per second (m/s) at 10 meters above the water surface. The vertical boundary condition would also be needed for the solution of equations (4.9) and (4.10), which governs the solution of salt and temperature in the domain. As mentioned earlier the bottom boundary corresponding to $(z = 0)$ represents a non permeable boundary, hence the boundary condition for salt and temperatures takes the following form.

$$\frac{A_v}{H}(\frac{\partial T}{\partial z}, \frac{\partial S}{\partial z}) = 0 \tag{4.22}$$

But at the surface,$(z = 1)$ the gradient of temperature and salt corresponds to the inward flux, which is again given as follows.

$$\frac{A_v}{H}(\frac{\partial T}{\partial z}, \frac{\partial S}{\partial z}) = -(< wT(1) >, < wS(1) >) \tag{4.23}$$

where $< wT(1) >$ corresponds to the temperature flux at the surface (m/s^oC), and $< wS(1) >$ corresponds to the salinity flux at the surface (m/s ppt).

As far as the lateral boundary condition is concerned it can again be divided into two categories, the wall boundary and the open boundary condition (OBC). The wall boundary condition is easy to implement and can be taken care of by implementing no flux condition at those boundaries in momentum equation. It is the OBC that has been the subject of much research see Sommerfeld (1949), Orlanski (1976). The open boundary condition (OBC) can be taken care of in more than one ways, an ideal OBC should be transmissive and should allow the phenomenon generated in the interior of the domain to pass through the boundary without undergoing significant distortion and without influencing the solution in the interior of the domain. Hence, we can say that the primary goal of OBC is to allow the waves and disturbances originating with in the domain, such as water surface elevation

and velocity to freely leave the domain. Because of it's detrimental ability to contaminate the solution within the domain, the usual practice is to specify the OBC at a farther and a safe distance from the domain of interest, the general rule is that the farther away the OBC is from the area of interest, the less OBC errors will affect the model results. EFDC model has more than one way of taking care of OBC.

- Radiation Boundary Condition: The radiation boundary condition is the simplest and is based on the simple and stable extrapolation of the boundary values from the interior of the domain.
- Specified Boundary Condition: Boundary condition on the open boundary can also be specified mainly as a time series of observed data, which can be the time series of surface elevation.
- Periodic Boundary Condition: This type of boundary condition is often valid for channel flow. It's based on the hypothesis that what goes out on one side, comes back in from the other side.

The boundary condition to be applied at on open boundary is often guided by the availability of the data. Also the boundary condition in for a three dimensional modeling can be obtained from 2D or 1D model, where the end result can be variation of discharge or water surface elevation. The inflow and outflow boundary condition in EFDC is applied through and external input file, 'QSER.INP', the file contains the time varying or steady amount of flow coming in or going out from the computational domain. For the modeling of CAWS, this was the procedure adopted.

4.5 Water Quality Model

The numerical solution of hydrodynamic variables are logically followed by an effort to model the water quality state variables. A lot of development has been made in the field of water quality modeling for which primarily civil engineers have been responsible, Chapra (1997). The health of any natural water body like rivers, lake, estuary etc are determined by ascertaining the levels of some key water quality state variables. A healthy water body forms an integral component of a vibrant ecosystem. EPA came up with a clean

water act in 1972, which became the cornerstone of surface water quality protection in the United States. The purpose of water quality modeling undertaken in regards with CAWS has been primarily to understand and isolate the reasons behind the impaired nature of some of the tributaries of CAWS. The enhanced understanding of processes affecting the water quality condition of various portions of CAWS will eventually help in suggesting remedial measures to improve the water quality conditions of CAWS.

4.5.1 EFDC Water Quality Model Description

EFDC comes with a very detailed water quality model, which has the capacity to simulate 21 water quality state variables. The kinetic processes included in the water quality models are derived from the CE-QUAL-ICM water quality model Cerco and Cole (1995). As oppose to water quality models such as WASP, that uses Biochemical Oxygen Demand (BOD) to represent oxygen demanding organic material, EFDC water quality model is carbon based. EFDC can model up to four species of algae, all represented in carbon units. The three organic carbon plays the equivalent role of BOD. State variables like Organic Carbon, Phosphorus and Nitrogen can be represented by up to three reactive sub classes which are refractory, particulate and labile. The 21 different state variables that EFDC can model are presented in the following table. EFDC water quality model is referred as EFDC-WQM here on in this thesis.

The governing mass-balance equation for each of the water quality state variables may be expressed as:

$$\begin{aligned} &\frac{\partial(m_x m_y HC)}{\partial t} + \frac{\partial(m_y HuC)}{\partial x} + \frac{\partial(m_x HvC)}{\partial y} + \frac{\partial(m_x m_y wC)}{\partial z} \\ &= \frac{\partial}{\partial x}(\frac{m_y H A_x}{m_x}\frac{\partial C}{\partial x}) + \frac{\partial}{\partial y}(\frac{m_x H A_y}{m_y}\frac{\partial C}{\partial y}) + \frac{\partial}{\partial z}(m_x m_y \frac{A_z}{H}\frac{\partial C}{\partial z}) + m_x m_y H S_c \end{aligned} \tag{4.24}$$

where

C = concentration of a water quality state variable.

u, v, w = velocity components in the cuvilinear sigma, x, y and z directions,respectively.

Table 4.1: EFDC model water quality state variables

(1) cyanobacteria	(12) refractory particulate organic nitrogen
(2) diatom algae	(13) labile particulate organic nitrogen
(3) green algae	(14) dissolved organic nitrogen
(4) stationary algae	(15) ammonia nitrogen
(5) refractory particulate organic carbon	(16) nitrate nitrogen
(6) labile particulate organic carbon	(17) particulate biogenic silica
(7) dissolved organic carbon	(18) dissolved availbale silica
(8) refractory particulate organic phosphorus	(19) chemical oxygen demand
(9) labile particulate organic phosphorus	(20) dissolved oxygen
(10) dissolved organic phosphorus	(21) total active metal
(11) total phosphate	

A_x, A_y, A_z = turbulent diffusivities in the x, y and z directions respectively.
Sc = internal and external sources and sinks per unit volume.
H = water column depth.
m_x, m_y = horizontal curvilinear coordinate scale factors.

The equation (4.24) is an advection-diffusion equation with source-sink term included. The first three terms on the left hand side of the mentioned equation shows the transport due to advection of the water quality variable, where as the first three terms on the right hand side of the equation (4.24) shows the transport due to the diffusion. The last term in the equation represents the kinetic processes and external loads for each of the state variables. EFDC-WQM solves the equation (4.24) by fractional step procedure method. In this method the kinetic terms and the physical transport terms are decoupled and solved separate stages. The decoupled equations are presented here, the subscript p refers to physical process and k refers to the kinetic processes.

$$\frac{\partial(m_x m_y HC)}{\partial t_p} + \frac{\partial(m_y HuC)}{\partial x} + \frac{\partial(m_x HvC)}{\partial y} + \frac{\partial(m_x m_y wC)}{\partial z}$$
$$= \frac{\partial}{\partial x}(\frac{m_y HA_x}{m_x}\frac{\partial C}{\partial x}) + \frac{\partial}{\partial y}(\frac{m_x HA_y}{m_y}\frac{\partial C}{\partial y}) + \frac{\partial}{\partial z}(m_x m_y \frac{A_z}{H}\frac{\partial C}{\partial z}) + m_x m_y H S_{cp} \tag{4.25}$$

$$\frac{\partial C}{\partial t_k} = S_{ck} \tag{4.26}$$

with finally

$$\frac{\partial}{\partial t}(m_x m_y HC) = \frac{\partial}{\partial t_p}(m_x m_y HC) + (m_x m_y H)\frac{\partial C}{\partial t_k} \tag{4.27}$$

The physical sources and sinks, which are associated with the volumetric inflows and outflows are already dealt with in the transport equation (4.25). The kinetic step is made at a constant water column depth at the end of the physical transport step. This allows the depth and the scale factors to be eliminated from the kinetic processes and which in turn can be further split into reactive and internal sources and sinks given by the following equation.

$$\frac{\partial C_k}{\partial t} = K.C + R \tag{4.28}$$

where K is the kinetic rate ($time^{-1}$) and R represents internal source/sink term (mass $volume^{-1}$ $time^{-1}$). Equation (4.28) is obtained by linearizing some terms in the kinetic equations, mostly Monod type expressions. The solution scheme for both the physical transport and the kinetic equations is second-order accurate.

4.5.2 Development of Three-dimensional DO-BOD Model

It is easy to realize that using comprehensive 21-state variable water quality model can be a gigantic undertaking. Some of the problems that can crop up immediately while trying to use such a model is the availability of data. Such a comprehensive water quality model will require much larger amount of observed data which will form the part of initial and boundary conditions

for all the state variables being simulated. Even if all the data is available the calibration of model will be a time consuming and a daunting exercise. Keeping all these considerations in perspective a simplified DO-BOD model was developed to work in conjunction with three-dimensional EFDC model. The two-dimensional implementation of the same model can be found in Motta et al. (2010). The DO-BOD model developed forms kinetic part of the water quality model, as discussed before the transport of a constituent in a water body can be defined by advection-dispersion-reaction equation. The advection and diffusion procedure is taken care by the transport module of the EFDC and for the reaction terms a new simplified water quality model is introduced. The governing equations for the DO-BOD model developed without the interaction of the bed with the water column can be presented as follows.

$$\frac{\partial C_{DO}}{\partial t} = \alpha k_r(C_s - C_{DO}) - k_d\theta_d^{(T-20)}\left(\frac{C_{DO}}{K_{BOD}+C_{DO}}\right)C_{BOD} - \frac{SOD}{\Delta z}\theta_s^{(T-20)} \tag{4.29}$$

$$\frac{\partial C_{BOD}}{\partial t} = -k_d\theta_D^{(T-20)}\left(\frac{C_{DO}}{K_{BOD}+C_{DO}}\right)C_{BOD} + W_{BOD} + \frac{F_{diff} - F_{sed} + F_{res}}{\Delta z_1} \tag{4.30}$$

where C_{BOD} and C_{DO} are BOD and DO concentrations (mg/l), k_d is the deoxygenation rate at $20°C$, θ_d is the deoxygenation temperature coefficient, K_{BOD} is the half saturation constant for oxygen limitation, SOD is the sediment oxygen demand, Δz is the thickness of the mesh cell, θ_s is the SOD temperature coefficient, k_r is the reaeration rate at $20°C$, θ_a is the reaeration temperature coefficient, C_s denotes the concentration of DO at saturated condition.

The reaeration rate of dissolved oxygen at the air-water interface is proportional to the oxygen gradient across the interface, $(C_s - C_{DO})$, when assuming the air is saturated with oxygen. The proportional coefficient k_r, also know as the reaeration coefficent, includes the effect of turbulence and surface wind. The reaeartion formulation used in EFDC is given O'Connor

Dobbins formulation which is given as follows.

$$k_r = \frac{1}{\Delta z}\left(k_{ro}\frac{U^{0.5}}{H^{0.5}} + W_{rea}\right) \times (KT_r)^{(T-20)} \tag{4.31}$$

The formula used here for the turbulence reaeration is the one proposed by O'Connor and Dobbins (1958). Here, k_{ro} is a constant with a value of 3.933, U is the velocity magnitude, H is the depth of the water column, KT_r is the constant for the temperature adjustment of dissolved oxygen reaeration rate, T is temperature, and Δz is the thickness of the surface layer cell. The wind effect on reaeration is given by the following formulation.

$$W_{rea} = 0.728U_w^0.5 - 0.317U_w + 0.0372U_w^2 \tag{4.32}$$

In equation 4.32, U_w is the wind speed (m/s) at the height of 10 m above water surface.

(Motta et al., 2010) showed the importance of interaction showed the importance of bed-water interaction while implementing DO-BOD model in conjunction with two-dimensional depth averaged hydrodynamic model, STREMR-HySedWq. The processes incorporated while extending and implementing the same model in a three-dimensional framework is shown schematically in Figure 4.2.

The right most term in the equation 4.30 represents the bed-water interaction in the implemented model. As explained in Motta et al. (2010) the bed is divided in two layers i.e. top and bottom. The thickness of these layers is kept constant in time. BOD simulated by the model can be present in both the water column as well as the top layer; as dissolved constituents or attached to the sediment particles. The dissolved (subscript d) BOD concentrations in the water column $CBOD_{,w,d}$ (subscript w) and in top bed layer $CBOD_{,b,d}$ are given by the following expression, where $C_{BOD,w}$ is the BOD concentration in the water column so far expressed at C_{BOD}, $C_{BOD,b}$ is the BOD concentration in the top layer, $f_{w,d}$ and $f_{b,d}$ are the dissolved fractions (between 0 and 1) in the water column and bed top layer respectively, n

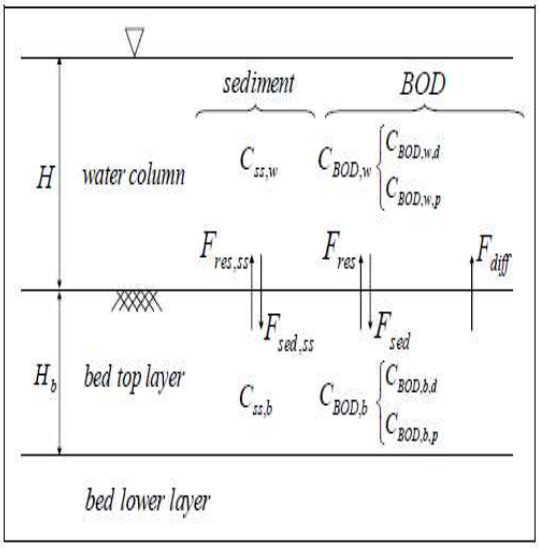

Figure 4.2: Schematic showing interaction between bed and water column

denotes the bed porosity.

$$C_{BOD,w,d} = f_{w,d} C_{BOD,w} \tag{4.33a}$$

$$C_{BOD,b,d} = f_{b,d} \frac{C_{BOD,b}}{n} \tag{4.33b}$$

The BOD concentration attached to the particles (subscript "p") in the water column $C_{BOD,w,p}$ and bed top layer $C_{BOD,b,p}$ are given by the following equations.

$$C_{BOD,w,p} = (1 - f_{w,d})\, C_{BOD,w} \tag{4.34a}$$

$$C_{BOD,b,p} = (1 - f_{b,d})\, \frac{C_{BOD,b}}{n} \tag{4.34b}$$

The total exchange of BOD between bed and the water column is given by the algebraic sum of three fluxes (please see Figure 4.2) diffusion flux (F_{diff}), sedimentation flux (F_{sed}) and resuspension flux (F_{res}). The diffusion

flux represents the exchange of dissolved BOD between the water column and the bed top layer; it is given by the following expression.

$$F_{diff} = \frac{E_{diff}}{H_b} \left(C_{BOD,b,d} - C_{BOD,w,d} \right) \tag{4.35}$$

The sedimentation flux represents the sum of settling of BOD attached to the sediments and the inclusion of pore water due to the bed aggradation caused by the sedimentation of the suspended sediments. It is given by the following expression.

$$F_{sed} = v_s \left(1 - n \right) \frac{C_{BOD,w,p}}{C_{ss,w}} + v_s n C_{BOD,w,d} \tag{4.36}$$

In equation 4.36,$C_{ss,w}$ is the concentration of the suspended sediment in the water column and v_s is the settling velocity of the sediment particles. Finally the re-suspension flux (F_{res}) is the sum of re-suspension of BOD attached to the sediment particles in the bed and release of pore water due to bed erosion caused by the sediment re-suspension. It is given by the following expression.

$$F_{res} = v_r \left(1 - n \right) \frac{C_{BOD,b,p}}{C_{ss,b}} + v_r n C_{BOD,b,d} \tag{4.37}$$

In equation 4.37, v_r denotes the erosion rate, $C_{ss,b}$ denotes the sediment volume concentration in the bed (m^3_{ss}/m^3). The erosion rate of the sediment particles v_r is given by entrainment function given by Smith and McLean (1977) for the non-cohesive sediment. The erosion rate v_r also known as the entrainment (E) function is given by equation 4.38.

$$E = 0.65 \frac{\gamma_o \left(\tau^*_s / \tau^*_c - 1 \right)}{1 + \gamma_o \left(\tau^*_s / \tau^*_c - 1 \right)} \tag{4.38}$$

Finally it must be reiterated that although the bed-water interaction is incorporated into the model, the bed level doesnt change in time. Hence essentially bed is taken as a source of organic sediment particles which when

resuspended exerts a sink effect on the dissolved oxygen in the water column.

4.6 Conclusion

In this chapter the details about the EFDC's hydrodynamic kernel and water quality model that was developed to work in conjunction with EFDC's hydrodynamic kernel is presented. As most of the flow and water quality phenomenon associated with CAWS are three-dimensional in nature, the decision to use EFDC as the hydrodynamic kernel is justified. As the main motivation of this research work has been three-dimensional hydrodynamic and water-quality simulation of CAWS, in order to cover larger spatial domain and longer temporal simulation EFDC model has been parallelized in an efficient manner the model is subsequently known as I-EFDC. The parallelization details of I-EFDC is presented in Chapter 7. Along with the description of the hydrodynamic kernel of EFDC, simplistic DO-BOD model was developed and applied to shorter and larger portion of CAWS. Its worth reiterating that the decision to develop simplistic DO-BOD model that can work in conjunction with EFDC model was made as anything more complicated would require lots of data for boundary and initial conditions, which are not always available. Moreover the usage of a water quality model with added complexity will have lot more parameters that will need calibration and will make the whole modeling effort much more time consuming. Finally in the following chapter, Chapter 5, number of simulation on shorter and larger portion of CAWS is presented which helps in elucidating the complexity associated with flow and water quality processes in CAWS.

CHAPTER 5

APPLICATION OF THREE-DIMENSIONAL MODELS TO CAWS

5.1 Introduction

In this chapter three-dimensional models are applied for various small and extended portions of CAWS. As mentioned before the flow orientation in CAWS is from north to south during dry weather conditions. During the normal course of flow in dry weather conditions the flow magnitude in most of CAWS is about 20-25 m^3/s.It is during wet weather conditions that the flow becomes entirely three dimensional in nature and the discharge in the river can increase significantly. During wet weather conditions, when the pumps at the Racine Avenue Pumping Station (RAPS) located at the headwaters of Bubbly Creek, a tributary to the South Branch of the Chicago River, are overwhelmed and are no longer able to transport the mixture of storm run-off and sewage to the water reclamation plant at Stickney near Cicero Avenue (see Figure 5.1), the untreated water is discharged into Bubbly Creek. As the flow generated in Bubbly Creek due to the action of RAPS progresses northwards and meets the turning basin, it acquires a complete three dimensional characteristics. Depending on its momentum, the flow emanating from Bubbly Creek can act as a barrier to the flow in the South Branch of the Chicago River.

Various research questions that has been addressed through this work and with help of three-dimensional models are as follows

1. Examine the variation of river stages and the flooding potential in the main branch and south branch of the Chicago River during a CSO event.

2. Examine the evolution of a conservative scalar discharged from RAPS through the system, during a wet weather condition.

3. Conduct a What-If analysis and examine how the flow field is affected if no flow discharge happened from RAPS during the simulated wet weather condition.

4. Conduct a long term simulation and track the evolution of effluent from the four waste water treatment plants located on banks of CAWS.

5. Demonstrate the application of three-dimensional model in reproducing the evolution of dye study through $I\&M$ canal done in Dec. 2009

5.2 Wet-weather Simulation

5.2.1 Description

In this section, Environmental Fluid Dynamics Code (EFDC), was used to simulate the intense storm which happened between 10th and 18th of September, 2008. The storm of September 2008 caused by torrential rains surpassed the capacity of Chicago's 32 flood control reservoir and 109 miles of deep tunnel system (TARP), designed to collect combined sewer overflow (CSO) from Chicago and 51 suburban municipalities. As a last resort to fight the threat of flood, the Metropolitan Water Reclamation District of Greater Chicago (MWRDGC) had to authorize the opening of three locks and gates on the MB of the CR so that the storm water could be discharged into Lake Michigan. In an official release MWRDGC stated that several billion gallons of water were discharged into Lake Michigan as a result of this exceptional storm. Lake Michigan forms the main source of drinking water for the city of Chicago and the surrounding areas, releasing the water from the Chicago River which is of impaired quality and more so in the case of a (CSO) event, is always the last and an undesirable option. The total length of the waterway numerically modeled and studied as a part of this research is about 21 kilometers (about 12.6 miles). The various segments that are included are Chicago River North Branch (NB) starting from Grand Avenue, Chicago River Main Branch (MB), Chicago River South Branch (SB) till Cicero Avenue, and Bubbly Creek. The model is validated against the stage observation s obtained from the US Geological Station (USGS) gauging station [Station No. 05536123] at Columbus Drive on the Main Branch of the

Chicago River. Model thus validated was further used to study the effect of flow on the dissolved constituent like dye which is used as a tracer for studying the effect of flow on dissolved constituents, which is crucial from water quality point of view for the whole Chicago Area Waterways System (CAWS). The domain modeled in this simulation is shown in Figure 5.1.

Figure 5.1: Portion of CAWS modeled for wet-weather simulation

5.2.2 Boundary Conditions and Computational Grid for the Simulation

The domain modeled numerically comprise of Bubbly Creek, South Branch, Main Branch and North Branch. Altogether 21 km of the CAWS was numerically modeled. The boundaries of the domain that drive the flow inside the domain are located at Grand Avenue, Racine Avenue Pumping Station (RAPS) and Chicago River Controlling Works (CRCW). These are appropriately marked in 5.1. The United States Geological Survey (USGS) maintains a gauging station at Grand Avenue [Station No. 05536118], which records both stage and discharge coming into the domain modeled here. The dis-

charge recorded at the gauging station, which forms the input to the system between Sep-10th and Sep-18th, 2008, starting at 12:00 am on Sep-10th and ending on 12:00 am on Sep-18th is presented in Figure 5.2. The SB of the

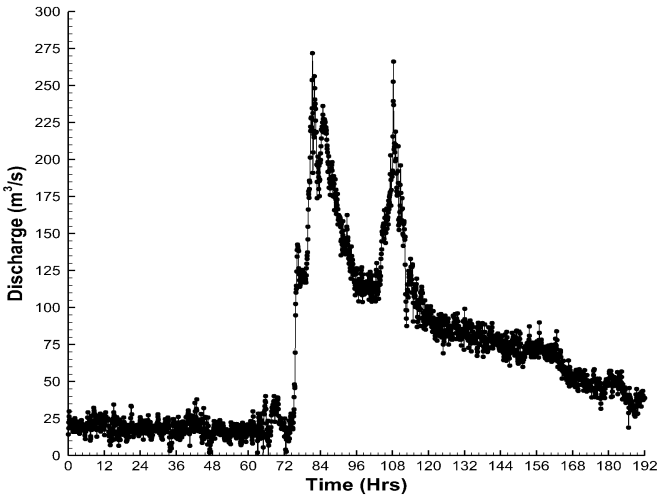

Figure 5.2: Flow through Grand Avenue between Sep 10th and Sep 18th

domain modeled here, ends at Stickney Avenue. Stickney Avenue forms an open boundary condition (OBC) for the segment under consideration, the stage elevation at this boundary was obtained from USGS gauging station [Station No 05536140] and used here as the outflow boundary condition for the flow. The variation of stage with respect to Chicago City Datum (CCD) as recorded by the (USGS) is presented in Figure 5.3. The Chicago city datum is marked at 176.63 m above the mean sea level. Due to the intense storm during the week of Sep-10 to Sep-18, 2008, the pumps at RAPS were switched on at 4:40 am on Sep-13th and were finally switched off at 9:20 am on Sep-15th. The amount of flow discharge by RAPS coming into Bubbly Creek is shown in Figure 5.27. The flow measurements from the Chicago River Controlling Works (CRCW) serve as the boundary condition for the part of the domain touching the Lake Michigan. The controlling structures which were incorporated in this study as a boundary condition for the numerical modeling is marked in Figure 5.5. The flow measurements for the north and south gates located on the lake front side on the main branch as shown in Figure5.5 were obtained by the Metropolitan Water Reclamation District (MWRD) of Chicago. Flow discharge through the north and south

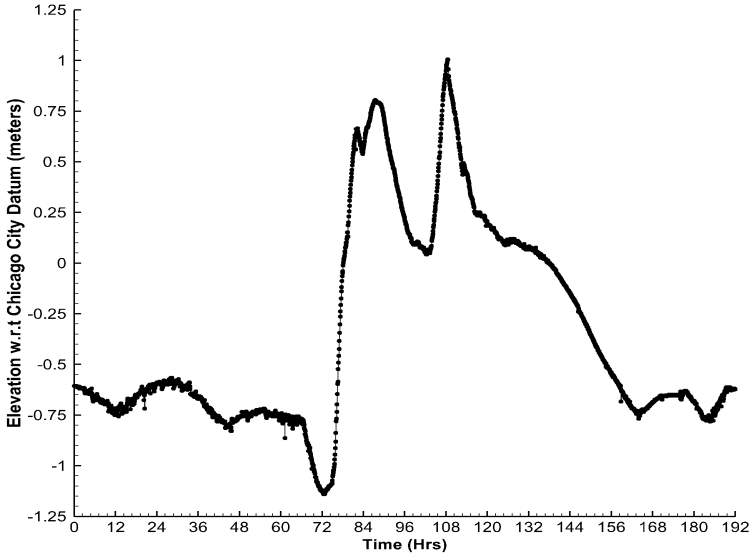

Figure 5.3: Stage Variation at Stickney Avenue between Sep 10th and Sep 18th, 2008

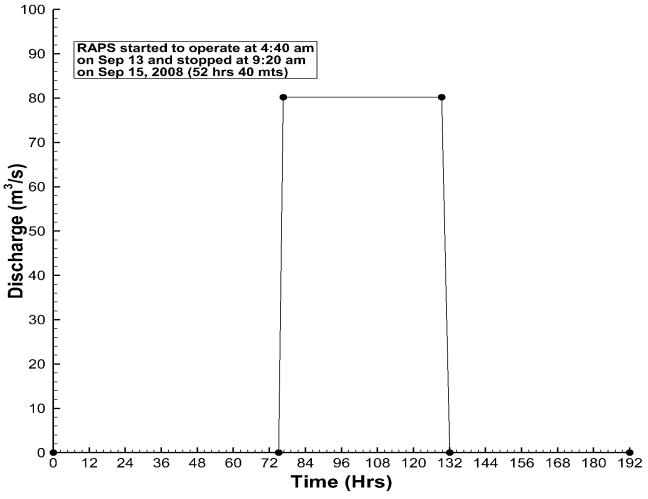

Figure 5.4: Discharge from RAPS between Sep 10th and Sep 18th, 2008

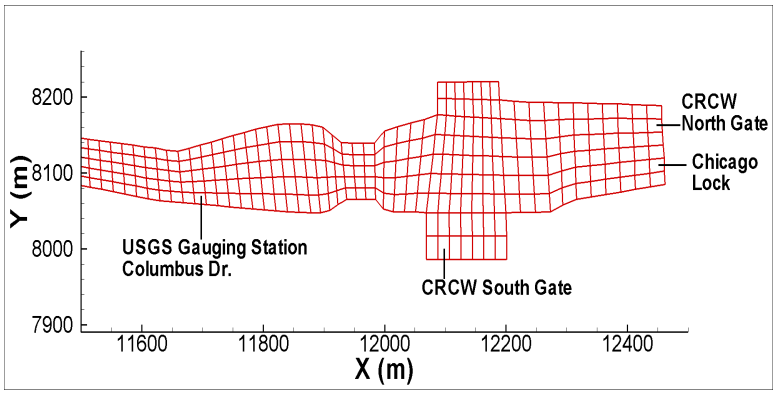

Figure 5.5: Controlling structures modeled on the Main Branch

gates are shown here in Figure 5.6. All the above boundary conditions were

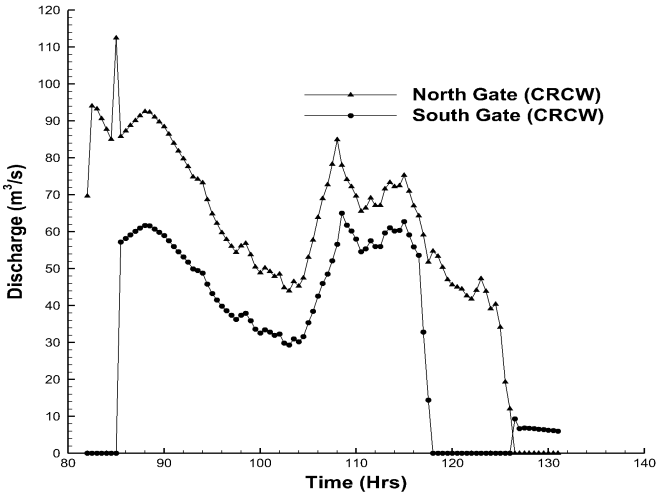

Figure 5.6: Flow through North and South sluice gates between Sep 10th and Sep 18th, 2008

utilized in setting up the model for the simulation period of eight days.

The first and most crucial step for the hydrodynamic simulation is the process of grid generation. In the present research the process of grid generation started with the bathymetry data available from the USGS field survey. The bathymetry data obtained from USGS is presented in Figure 5.7. As seen in Figure 5.7 the bed of Bubbly Creek is at higher elevation than the rest of the domain, which consequently makes Bubbly Creek shallower in terms of water depth when compared to the rest of the CR. From the given bathymetry data the boundary of the domain to be modeled was extracted

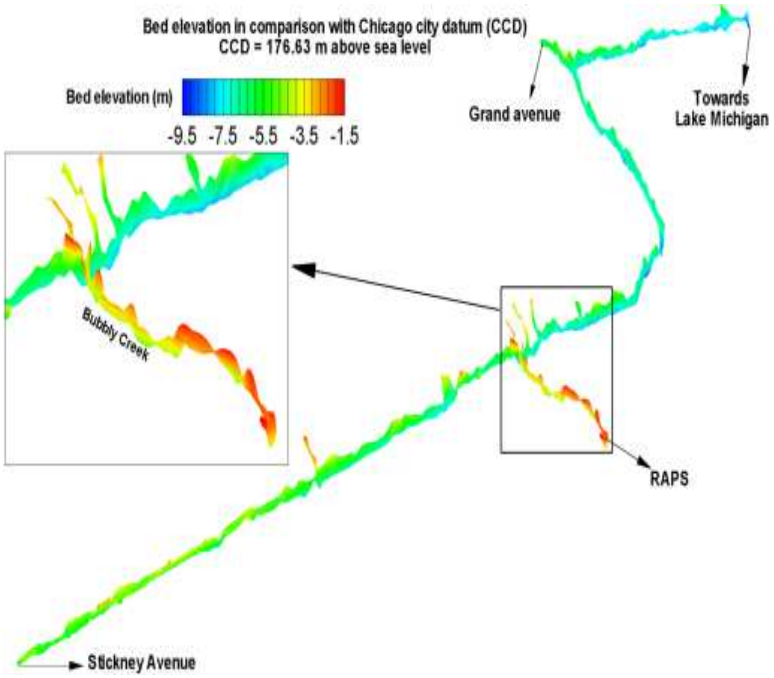

Figure 5.7: Bathymetry data for the portion of domain modeled

which was used in the generation of depth averaged grid using the software Gridgen . Finally as the water depth in the whole domain varied between 3 and 8 meters it was decided to have eight layers in vertical. In end the depth averaged planar grid along with sigma coordinates in vertical when plotted together resulted in Figure 5.8. The grid constructed had 4273 cells in horizontal and 8 layers in vertical. The average grid spacing in the direction of flow was kept at 40 meters and around 10 meters in the transverse direction. Eight layers in the vertical direction are of equal thickness and gave the vertical resolution of as low as 0.4 meter. The orthogonality of the depth averaged grid constructed was ensured by keeping the skewness of each control volume close to 0 with the help of the gridding software Gridgen. As the governing equations of motion are transformed from Cartesian coordinate system to Orthogonal Curvilinear Coordinate System (OCCS), it is imperative that the grid constructed are orthogonal in nature, the adverse effect of grid non-orthogonality on the solution of external mode equation or shallow water equation is presented in (Sankaranaryanan and Spauliding, 1984).

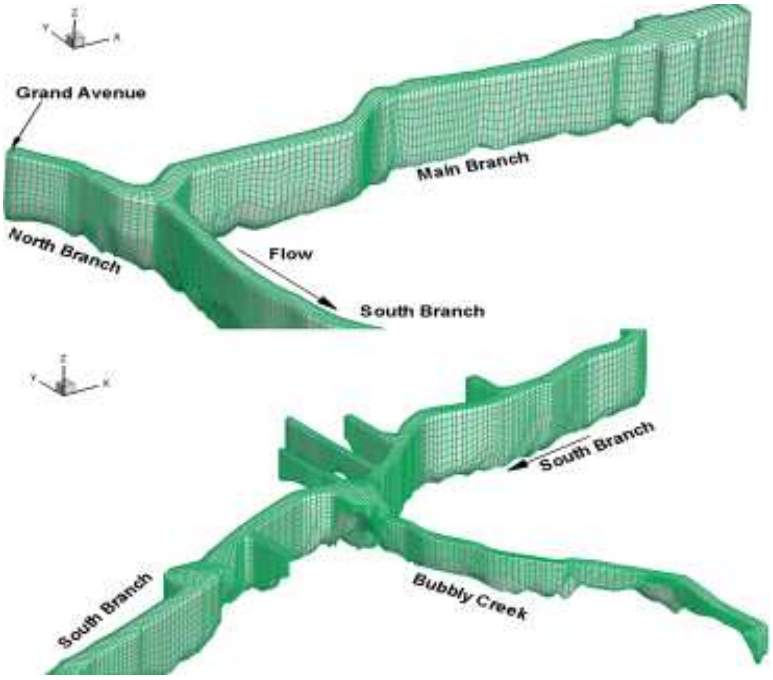

Figure 5.8: 3D computational grid with 4273 cells in horizontal and 8 layers in vertical

5.2.3 Hydrodynamic Simulation Results and Discussion

The result of hydrodynamic simulation is validated with the help of observed stage values at the Columbus Drive on the MB of the CR [Station No. 05536123]. It should be mentioned that the amount of outflow through the Chicago lock, Figure 5.5, was not available; hence the outflow through the lock was used as a calibration parameter for better matching of stage values at the Columbus Drive. Also, it is worth mentioning that the Chicago lock stayed opened only for the duration of 5 hours during the entire period of the simulated event. The lock was opened 108.5 hours after that start of the simulation (12:00 am on Sep-10th, 2008) and was closed 113.5 hours after the start of the simulation. The north and south gates, Figure 5.6, were opened 82 hours after the start of the simulation and they stayed opened till 130 hours after the start of the simulation. It can be clearly seen that as the amount of flow through the lock increases, the model captures the second peak in stage elevation in a better manner. We are concerned more with the second peak of the stage elevation (Figure 5.6) because it falls during the time frame when the gates and the lock on the MB of the CR were opened. Finally corresponding to the gate outflow of 168 m^3/s, the flow velocities in different

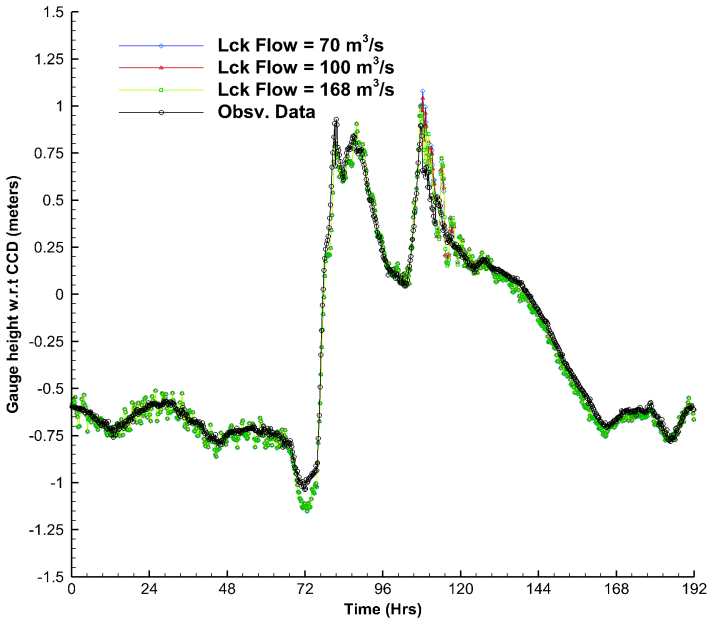

Figure 5.9: Stage elevations at Columbus drive for various outflow through Chicago Lock

areas of the CR are presented at different point in times. Flow velocity in

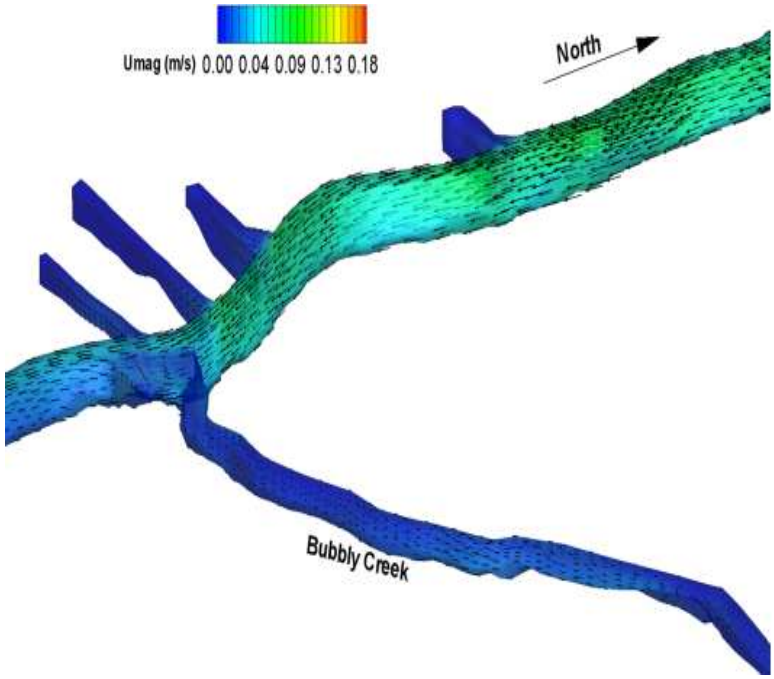

Figure 5.10: Flow velocity in Bubbly Creek, 40 hours after the start of simulation

Bubbly Creek area stays almost close to zero when RAPS is not pumping and any flow in Bubbly Creek during such times is due to the minimum flow that finds its way from the South Branch to Bubbly Creek. As far as the area of the Main Branch is concerned, the simulation shows the direction of flow coming from the NB makes its way towards the SB. Flow velocity in the Main Branch is also not significant; also its worth noticing that the locks and gates on the Lake Michigan side are closed at this point in the simulation. This can also be classified as the normal course of the flow, the flow coming through Grand Avenue, Figure 5.11, carries the most of the flow from the North Side Water Reclamation Plant (NSWRP) situated 16 km upstream from Grand Avenue. Typically the flow from the North Branch (NB) enters the South Branch (SB) and then flows into the Des Plaines River. As the water coming from the NB carries the effluent from NSWRP, the typical flow pattern of north to south is helpful in preserving the water quality condition of the MB of the CR. But, during extreme events, similar to one being modeled here, when gates and locks on the MB are opened, it has a suction effect which attracts the flow from the NB, which is certainly detrimental for the water quality condition of the MB and, eventually, of Lake Michigan The

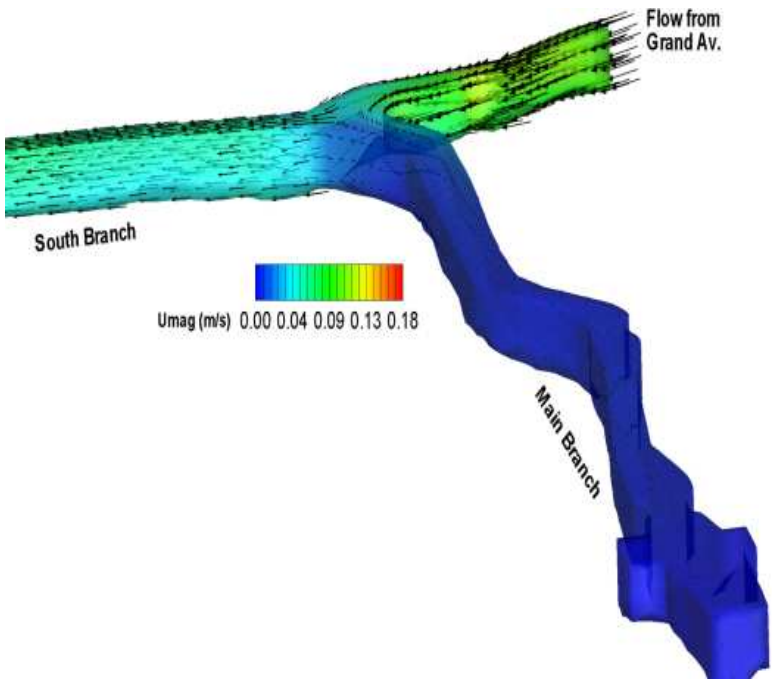

Figure 5.11: Flow velocity in Main Branch, 40 hours after the start of simulation

flow velocity after 80 hours from the start of the simulation is presented in Figure 5.12. The flow velocity in Bubbly Creek reaches as high as 0.8 m/s

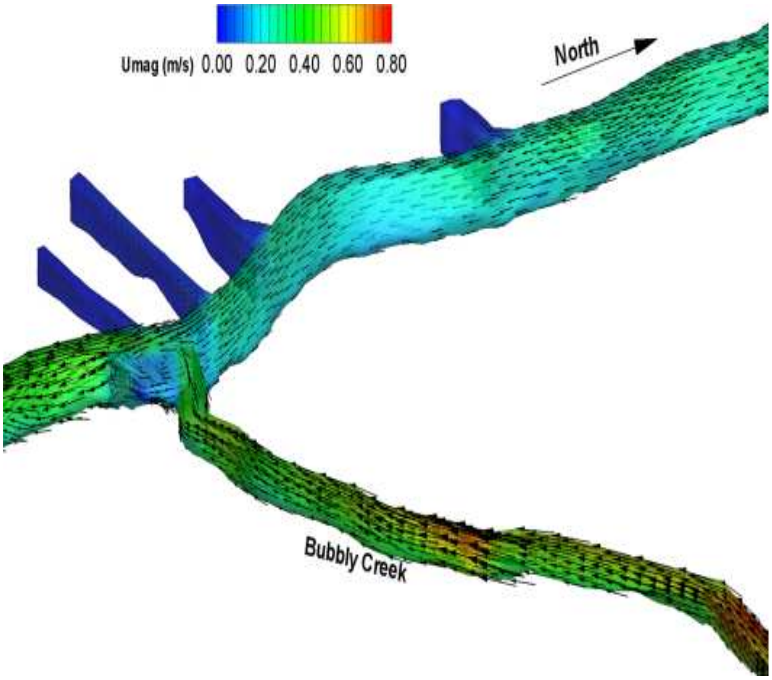

Figure 5.12: Flow velocity in Bubbly Creek, 80 hours after the start of simulation

due to the large flow coming from the RAPS. As regards to the flow in the SB is concerned it is still dictated by the flow coming from the Grand Avenue. The velocity in the MB and the junction of NB and MB is shown in Figure 5.13. It is worth reiterating that the lock and gates on the Lake Michigan side was still closed at this point in the simulation. As we go ahead in time, simulation results for the velocity plots 110 hours after the start of the simulation are presented in Figure 5.14. The direction of the flow in the SB of the Chicago River(CR) is now dictated by the flow coming from RAPS and overwhelms the flow coming south from Grand Avenue. The flow coming out of Bubbly Creek forms a natural barrier which backs up the water into the SB and starts to flow in the north direction. The velocity plots in the MB of CR are presented in Figure 5.15. At this point in time the lock and gates, whose positions are marked in Figure 5.5, are opened. As a result of this we can see that the flow coming from Grand Avenue makes it way to the MB towards Lake Michigan rather than continuing towards the south. Also, it can be seen in Figure5.15, that the flow in the SB is directed up towards the

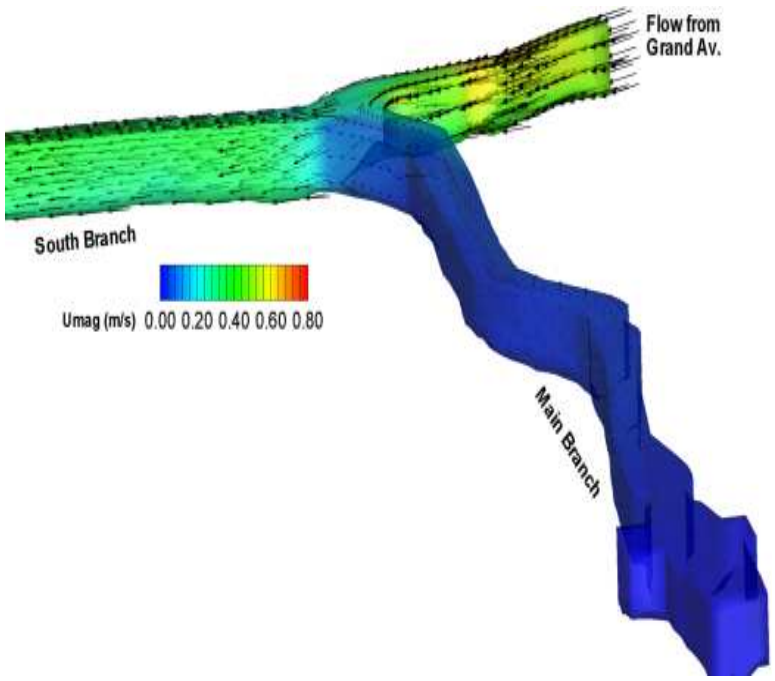

Figure 5.13: Flow velocity in Main Branch, 80 hours after the start of simulation

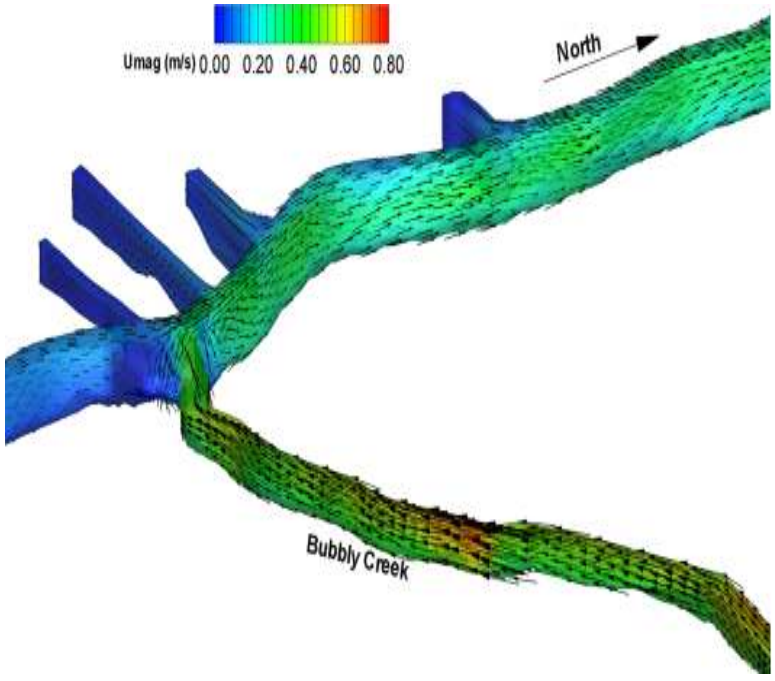

Figure 5.14: Flow velocity in Bubbly Creek, 110 hours after the start of simulation

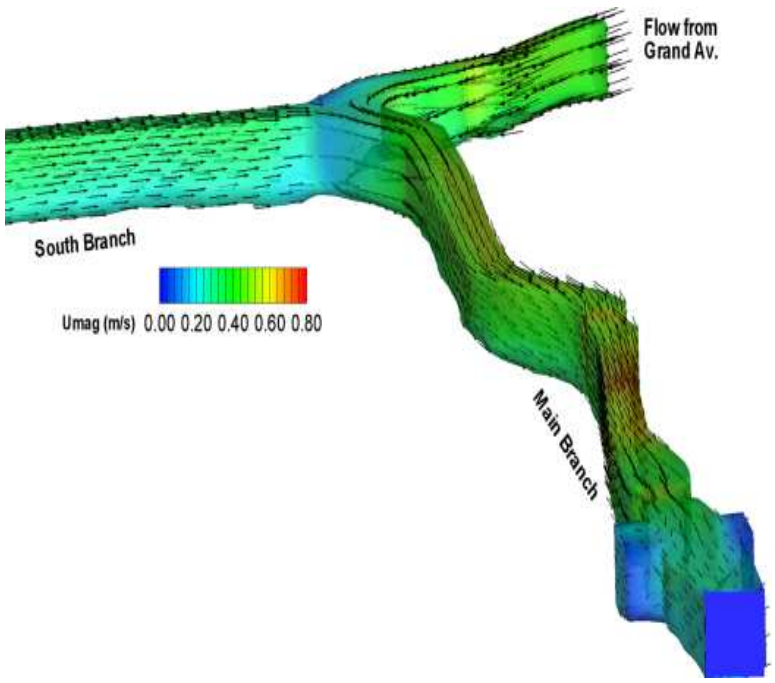

Figure 5.15: Flow velocity in Main Branch, 110 hours after the start of simulation

junction with the MB. Hence, the flow from both NB and SB finds its way in the MB of the CR. Finally when the gates are closed and the pumps at RAPS are turned off the flow characteristics revert to its normal course. The flow in Bubbly Creek 150 hours after the start of the simulation is presented in Figure 5.16. When the pumps at RAPS are turned off the flow velocity in Bubbly Creek reduces drastically and is almost close to zero. The flow velocity in the NB and MB of the CR also returns to its normal course and flows from north to south, which is shown in Figure 5.17. Although the normal pattern of the flow is from north to south, during an extreme event the flow pattern in CR is a result of complicated interaction between the flow coming from RAPS, the north branch through Grand Avenue and the operation of gates and lock on the MB of CR (CRCW), the flow pattern can very well exhibit a reverse trend, such trend is very well captured by the developed model.

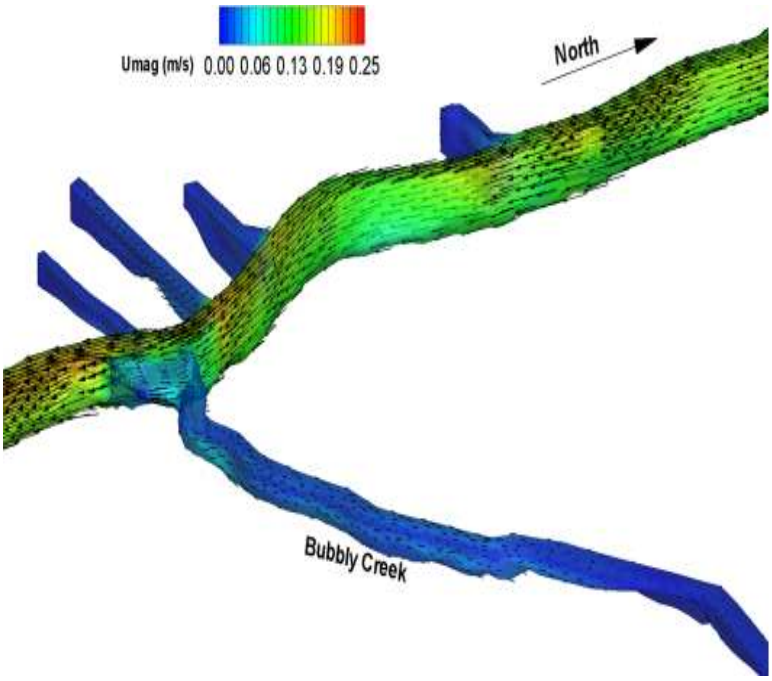

Figure 5.16: Flow velocity in Bubbly Creek, 150 hours after the start of simulation

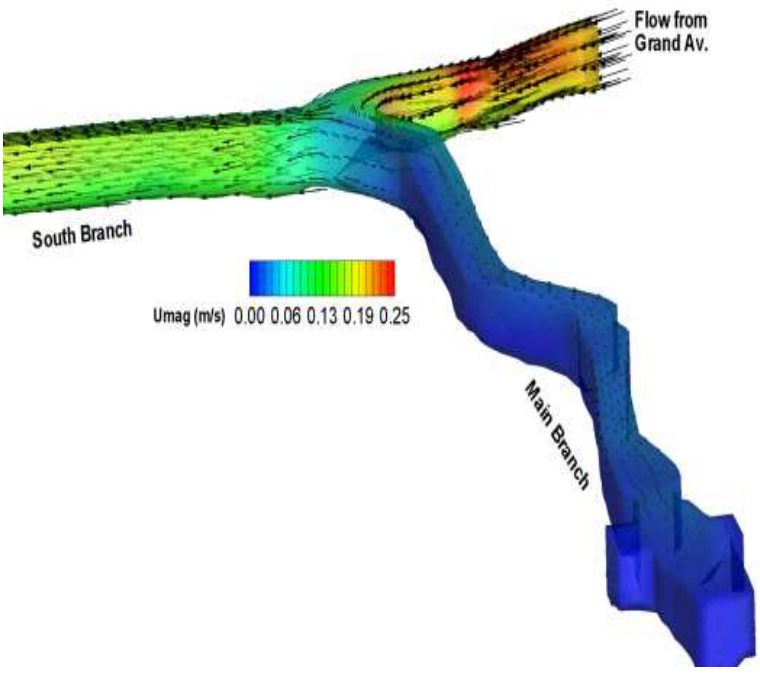

Figure 5.17: Flow velocity in Main Branch, 150 hours after the start of simulation

5.2.4 Dye used as a Tracer for Examining the Fate of Contaminant

Racine Avenue Pumping Station (RAPS) starts pumping water into Bubbly Creek when its capacity to transport water to the treatment plant at Stickney near Cicero Avenue, Figure 5.1, is overwhelmed. As stated in the introduction, one of the questions that has been tried to address through this modelling exercise is to examine the final fate of the contaminants coming from the RAPS during an extreme CSO event. Researchers have been suspicious for some time that during an extreme CSO event the contaminants coming from RAPS might flow upstream into the SB and finally may find their way to the MB of the CR and Lake Michigan. The storm event of September, 2008 that has been modeled here did produce a flow in the direction opposite to its normal course i.e. north to south as shown in Figures 5.14 and 5.15. The fate of any contaminants coming from RAPS was examined by using dye as a tracer. In the numerical simulation conducted, when RAPS started discharging water into Bubbly Creek, 25 g/l of dye was introduced with incoming flow from RAPS. The evolution of the dye concentration was tracked in the entire CR subsequently to its injection. The plot of the dye concentration after 92 and 108 hours after the start of the simulation is shown in Figure 5.18. The entire CR was initialized with a dye concentration of 0 g/l prior to the start of the simulation. As is marked by the arrow in the part (b) of Figure 5.19, the dye coming from the RAPS has a tendency to move upstream. The same plots at 116 and 120 hours after the start of the simulation are presented in Figure 5.19. A distinct positive dye concentration in the MB of CR is observed. This can be attributed to the incoming dye from RAPS as that is the only source in the numerical simulation conducted. Finally, this exercise confirms our concern that during an extreme CSO event any pollutants coming from RAPS might flow all the way up to the main branch of the CR and have a detrimental effect on the water quality of Lake Michigan. This could potentially lead to beach closings during the summer months if the levels of bacteria end up being too high in the coastal area of Lake Michigan.

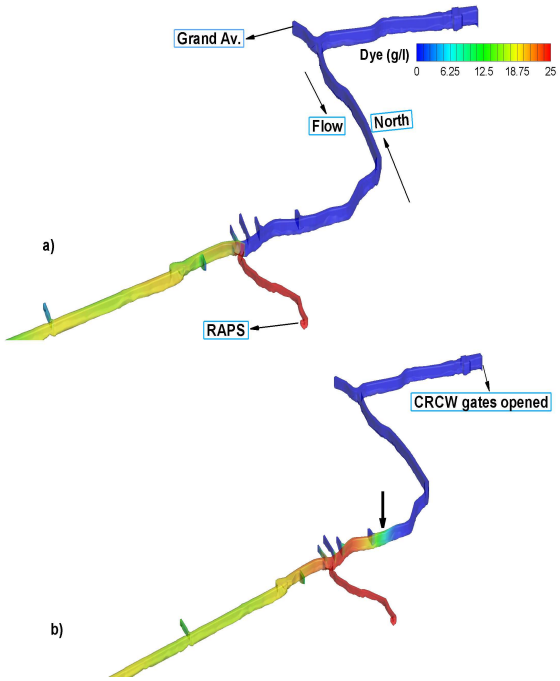

Figure 5.18: (a)Dye concentration 92 hours,(b)108 hours after start of simulation

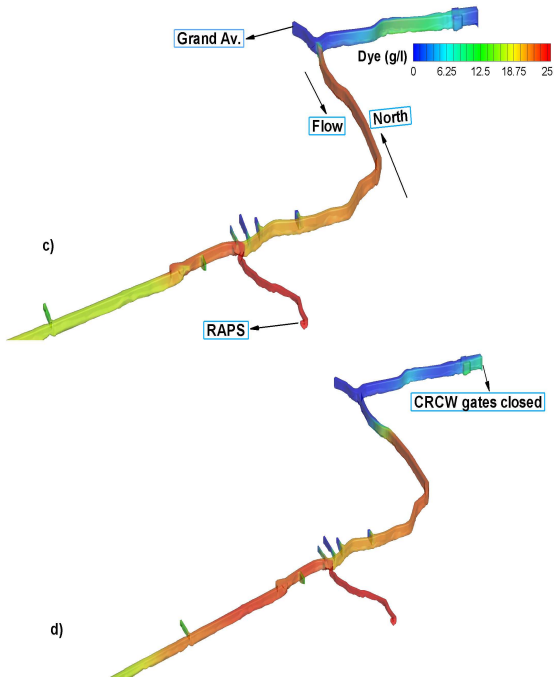

Figure 5.19: (c)Dye concentration 116 hours, (d) 120 hours after start of simulation

5.2.5 What-if Analysis: Simulation Results with No CSO Discharge from RAPS during the Wet-weather Event

In this section the same wet-weather event of September 2008 is simulated again with no CSO discharge from RAPS. The purpose of this simulation is to examine if the flow reversal occurs in absence of the CSO discharge from RAPS. For this simulation exercise the boundary condition is exactly same as before with only difference of having no discharge from RAPS. Velocity plots at different points in time are presented again for this simulation. As regards

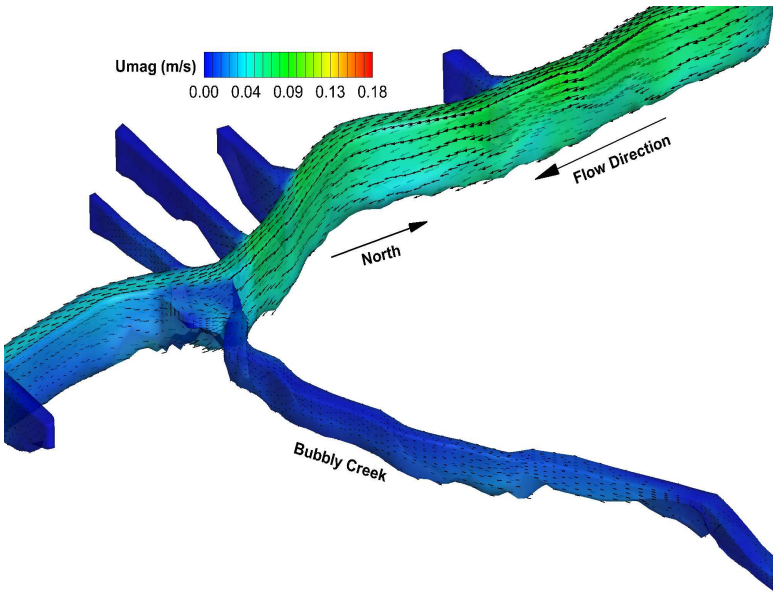

Figure 5.20: Flow velocity in Bubbly Creek, 40 hours after the start of simulation with no discharge from RAPS

to the velocity vector plots shown in Figure 5.20, it is very similar to the plot in Figure 5.10 as the boundary condition for this simulation is identical to the results presented before. Plot in Figure 5.20 shows the velocity vectors 40 hours after the start of the simulation, also noticeable is the minuscule disturbance and low velocities that are generated in Bubbly Creek as a result of the flow in the SB. As mentioned before discharge from RAPS starts 80 hrs after the start of the simulation and it is at this point in time that we need to examine the velocity vector plots in a comparative manner, when the discharge from RAPS is not considered.

As shown in Figure 5.21 in the absence of discharge from RAPS in this

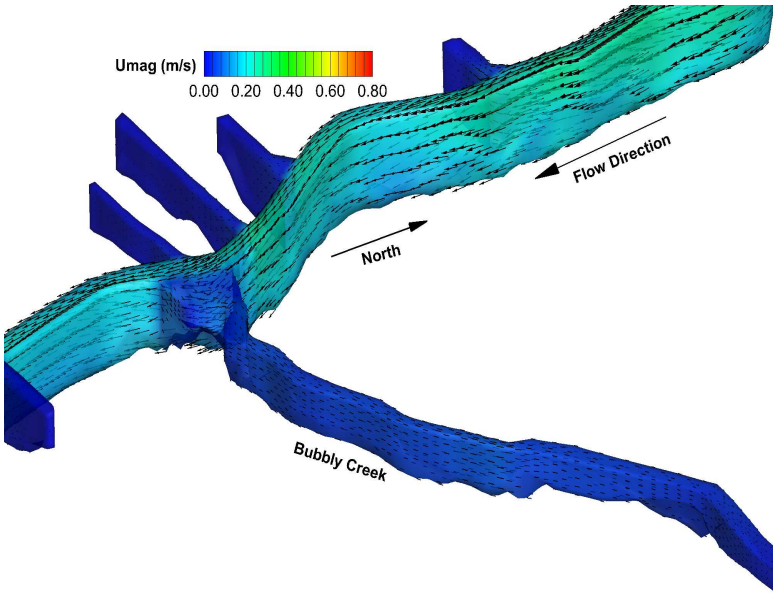

Figure 5.21: Flow velocity in Bubbly Creek, 80 hours after the start of simulation with no discharge from RAPS

simulation, the flow velocity in Bubbly Creek is very low and close to null. In comparison to Figure 5.12, the velocities observed in the SB on the south side of Bubbly Creek (see Figure 5.21) are significantly lower. It is worth reiterating that the flow velocities observed in Bubbly Creek, around the turning basin, are caused by the disturbance that propagates into the creek due to the velocities in the SB. As shown in before the flow reversal in the SB occurs as a result of opening the gates located at the mouth of Lake Michigan on the MB of CR. The purpose of this simulation was to investigate the possibility of flow-reversal in the SB in absence of RAPS discharge while incorporating the real time operation of CRCW lock and gates. Velocity plot 110 hours after the start of the simulation is presented in Bubbly Creek and MB of the CR.

As shown in Figure 5.22, the flow reversal still occurs but the velocity generated in the SB of the CR is significantly lower than observed in Figure 5.14. Discharge from RAPS along with the opening of gates definitely leads to the generation of higher velocities in the SB towards the main stem of the Chicago River.

As shown in Figure 5.23, the flow reversal still occurs but the northward

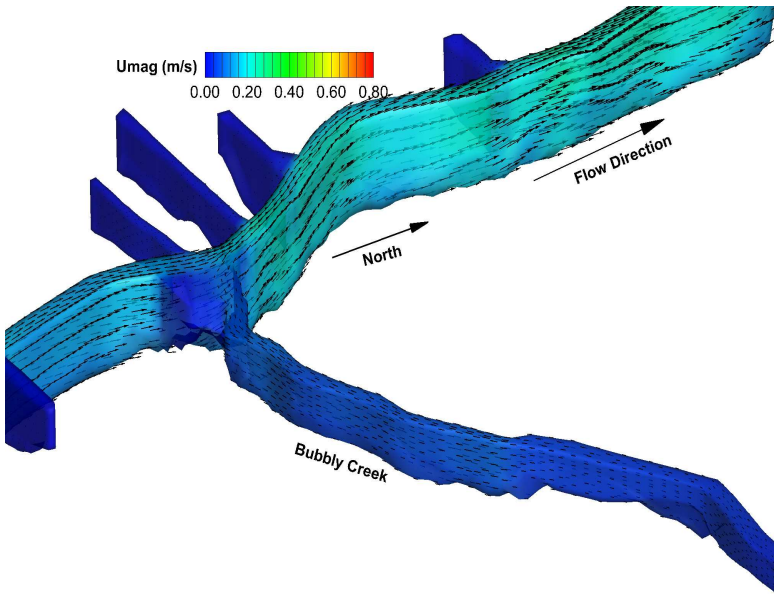

Figure 5.22: Flow velocity in Bubbly Creek, 110 hours after the start of simulation with no discharge from RAPS

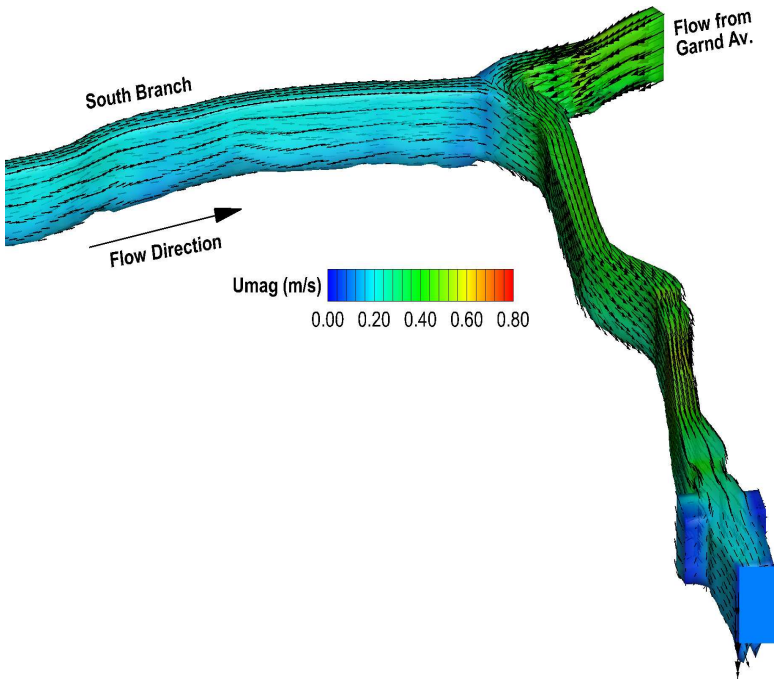

Figure 5.23: Flow velocity in Main Branch, 110 hours after the start of simulation with no discharge from RAPS

velocity created in the SB in absence of discharge from RAPS is significantly lower than observed in Figure 5.14 and Figure 5.16. Finally in absence of discharge from RAPS, flow reversals will still occur but only when both the CRCW gates and lock (see Figure 5.5) are all opened concomitantly. During the dry weather condition the controlling structures at CRCW are not opened simultaneously and it is only during extreme weather conditions (similar to one modeled here) that the lock and gates are opened simultaneously to circumvent the problem of flooding.

5.3 Long Term Simulation

5.3.1 Description

In the section the computational model for the CAWS is extended to include almost 120 kms of the navigable waterway system. The majority of the flow in CAWS is from the four Waste Water Treatment Plant (WWTP's) shown in Figure 5.24. The main segments of the CAWS modeled as a part of this research are shown in Table-1 along with their approximate length, width and depth. These segments are also appropriately marked in Figure 5.24. The total length of CAWS which is modeled as a part of this research is 100.0 kilometers. The CAWS is one of the major water transportation systems in the world. As shown in Figure 5.24, there are three northern tributaries namely the West Fork, the Middle Fork and the Skokie River.

Table 5.1: Length, Width and Depth of various segments of CAWS modeled

Waterways Branch	Lth. (kms)	Wth. (m)	Dth. (m)
Nth. Shore Channel	12.4 kms	27.5 m	0.61 - 3 m
Chicago Rvr.	2.4 kms	61-146 m	6 - 8 m
Sth. Brch. Chicago Rvr	7.2 kms	61-76 m	4 -6 m
Bubbly Creek	2.1 Kms	30.5-61 m	0.9 -3.95 m
Chicago San. and Shp. Canal	50 Kms	42-92 m	2.43 - 8.23 m
Cal-Sag Channel	26 Kms	92-137 m	1.22 - 3.66 m

These there tributaries flow southwards, parallel to each other and join to become what is known as the Chicago River North Branch(NB), the NB meets the man-made North Shore Channel as it flows east and together they

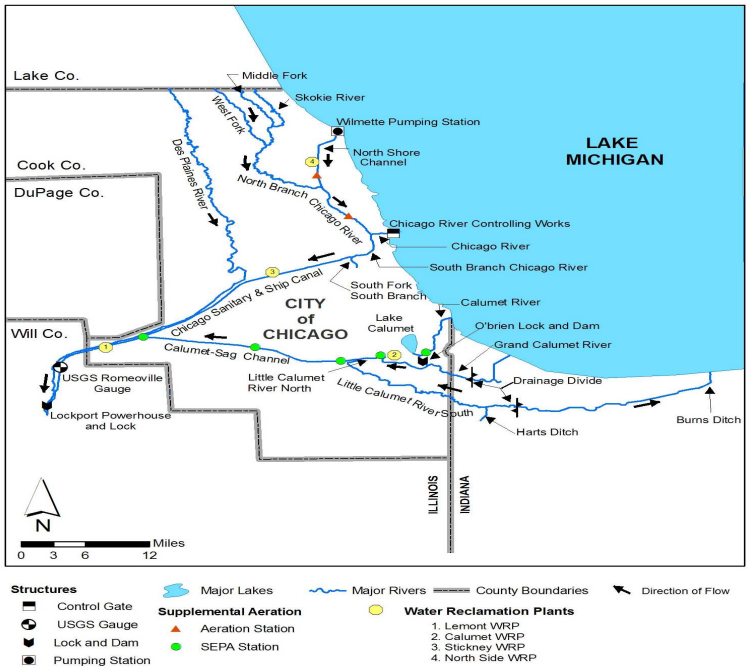

Figure 5.24: Schematic of CAWS

flow south as the NB. The main stem of Chicago River flows westward away from the Lake Michigan through the Chicago downtown and joins the NB and together they flow south as the Chicago River South Branch (SB). The SB is joined by the Bubbly Creek and together they flow south-west through a man-made channel known as Chicago Sanitary and Ship Canal (CSSC). CSSC is then met by another man-made channel which is known as Calumet-Sag Channel. The Calumet River System (CRS) is another part of the CWS. Although CRS itself is comprised of more than one tributary (Figure 5.24) for the modeling purposes only the Cal-Sag channel ending at OBrien Lock and Dam was considered. It is worth reiterating that all the four WWTPs were included as the point source in the modeling domain. These accounted for the major source of flow in the modeled portion of CWS. Also included in the modeling domain along with WWTPs is Racine Avenue Pumping Station (RAPS) situated at the south end of the Bubbly Creek. The pumps at RAPS collects and conveys the street and sewer flow from the adjoining area to the water treatment plant at Stickney marked as 3 in Figure 5.24. During the period of intense storm the pumps at RAPS might get overwhelmed which in turn leads to the generation of Combined Sewer Overflow (CSO) events wherein the excess flow generated is dumped into Bubbly Creek. This excess

flow rich in organic and suspended sediment has a detrimental effect on the water quality. The water quality impact of such CSO events is also examined as a part of this research. In this section the hydrodynamic simulation for the month of May-2009 is conducted. The choice of the month was based on the amount of available parameters for setting up the model and the quantity of observed data for finally calibrating and validating the model. The hydrodynamic model presented here was calibrated by changing the value of bottom roughness coefficient. As EFDC model is a three-dimensional model capable of simulating free surface, it was found that the bottom roughness did not have a huge impact on the hydrodynamics of the flow. The hydrodynamic model was calibrated to match the available stage elevation data from the USGS gauging station at Grand Avenue on the NB [USGS-05336118], Columbus drive at the Chicago River Main Branch (MB) [USGS-05536123] and Stickney Avenue on CSSC [USGS-05536140].

5.3.2 Boundary Conditions and Computational Grid for the Simulation

Once again the computational grid for the whole domain was constructed using the preprocessing tool Gridgen. It should be reiterated that this software was chosen because of its ability to construct multi-block orthogonal curvilinear grids. The mesh constructed is presented in Figure 5.25 and it covered approximately 100 kms of CAWS.

The three dimensional mesh had 18,000 cells in the horizontal direction and 8 layers in vertical. The resolution of the mesh was fixed after some trial simulations so that simulating one month did not take excessively long and mesh was fine enough to capture the pertinent flow and water quality characteristics. Eight layers in the vertical gave the resolution of the mesh in the vertical direction as low as 0.1-0.2 m in the shallower areas of, i.e. Bubbly Creek. The mesh resolution in horizontal direction along the flow varied between 8-12 m and 5-7 m in the transverse direction. Mesh resolution in the confluence areas of various segments were kept towards the finer side to capture more details of the flow physics.

The hydrodynamic model for CWS was initialized with zero velocity components and constant surface elevation of -0.66 m with respect to the Chicago

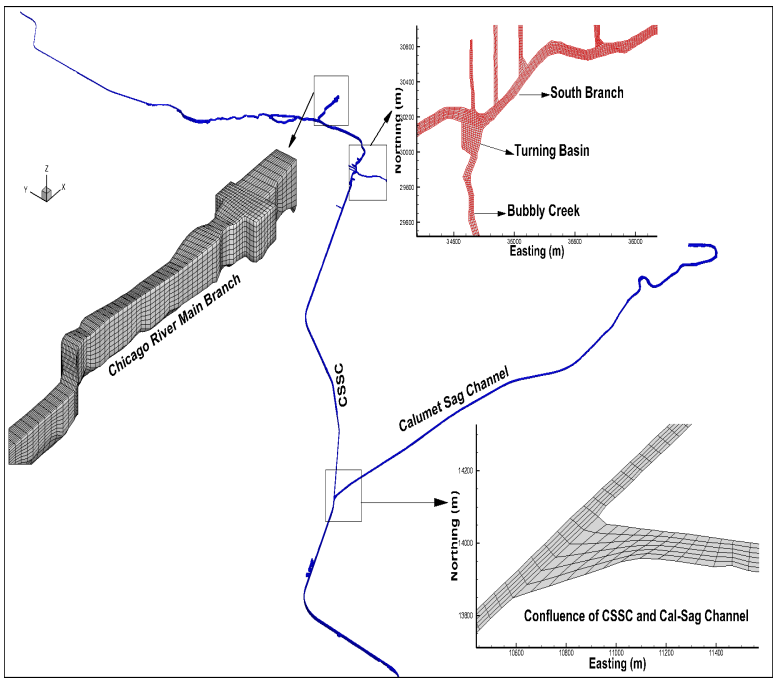

Figure 5.25: Computational mesh for Chicago Area Waterway System (CAWS)

City Datum (CCD), the value of -0.66 m is in accordance with the free surface elevation obtained from the USGS gauging station during dry-weather flow conditions. CCD is located 176.32 m above sea level. The hydrodynamic simulation for the month of May-2009 was setup using the flow inputs from the four WWTPs. Also included in the modeling effort were the flow diversions from the Chicago River Controlling Works (CRCW) on the MB. CRCW on the MB is comprised of two gates and a lock which opens towards the Lake Michigan. The amount flow coming in from these were obtained from MWGRDC records. During May-2009 there were four CSO events in the Bubbly Creek, the amount of flow through RAPS during these events were also incorporated in the simulation. The amounts of flow coming into the domain from three major WWTPs are shown in Figure 5.26. The water surface elevation was recorded at three points inside the computational domain as shown in Figure 5.28. These points corresponded to the area where USGS maintains gauging station.

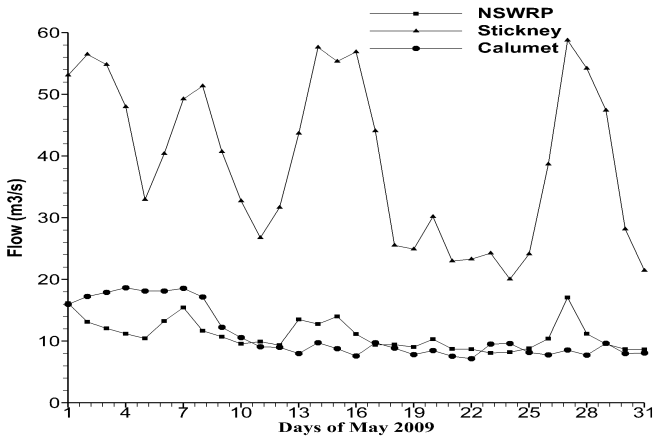

Figure 5.26: Outflow through various WWTPs for May-2009

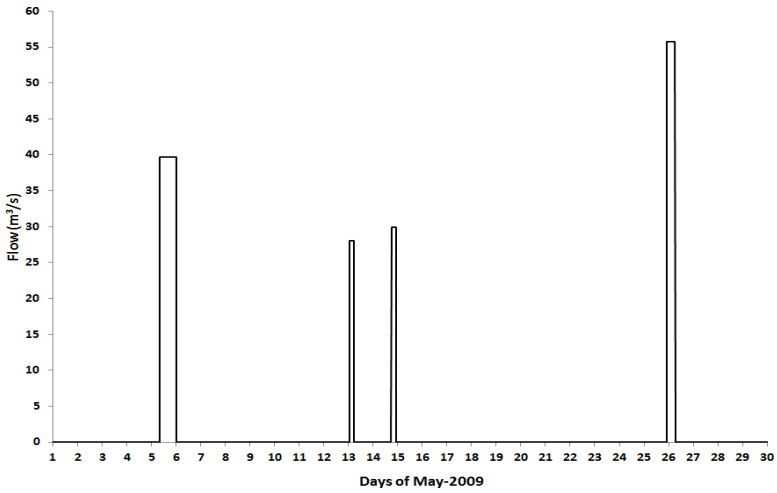

Figure 5.27: CSO's from RAPSfor May-2009

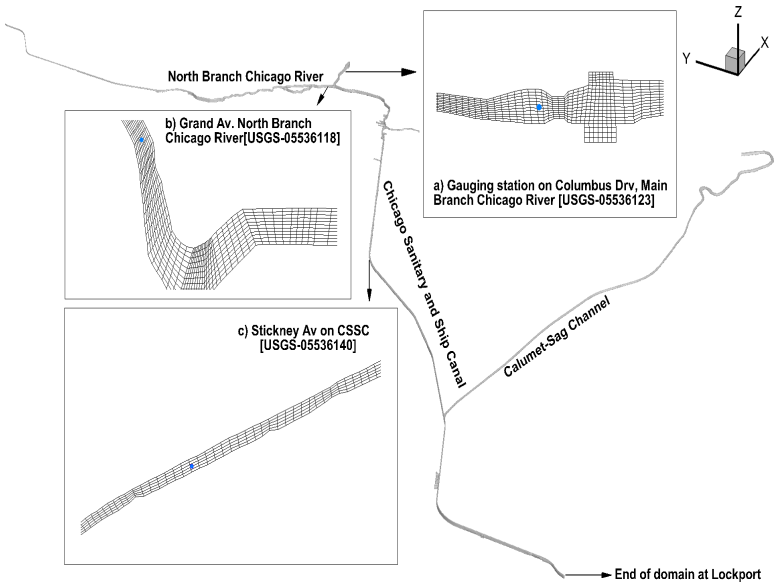

Figure 5.28: Location of USGS gauging station inside the computational domain

5.3.3 Hydrodynamic Simulation Results and Discussion

The hydrodynamic simulation for the month of May-2009 was started with what is commonly known as, "cold-start" wherein all the velocity components in the whole domain was initialized to null value.The comparison between the observed and simulated water surface elevation is presented in Figures 5.29. 5.30 and 5.31. The three-dimensional model satisfactorily replicated the variation in the stage elevation at the three gauging stations.

In regards with the velocity, the magnitude varied between 5 15 cm/ sec. The zone of high velocity was concentrated in the vicinity of WWTPs. A distinct increase in the velocity magnitude is noticed around the times of high outflow from WWTPs. The flow velocity magnitude in different portion of CAWS is presented in the following figures. It is worth mentioning that any significant flow velocity associated with the main branch of the Chicago River is as a result of the opening and closing of gates and lock on the main branch. Also worth reiterating is that any significant flow velocity in Bubbly Creek is as a outcome of CSO events generated from RAPS situated at the mouth of the Bubbly Creek. During the event of intense rain-storm when the conveyance capacity of RAPS to transport untreated water to the waste water treatment plant at Stickney (Figure 5.24) is overwhelmed, the excess water is discharged into Bubbly Creek leading to CSO events. It should be

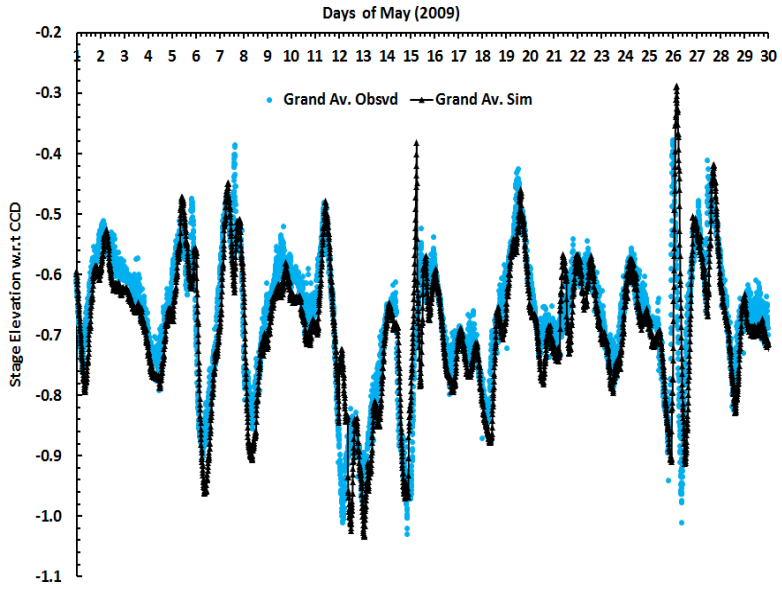

Figure 5.29: Comparison between observed and simulated stage at Grand Avenue for May-2009

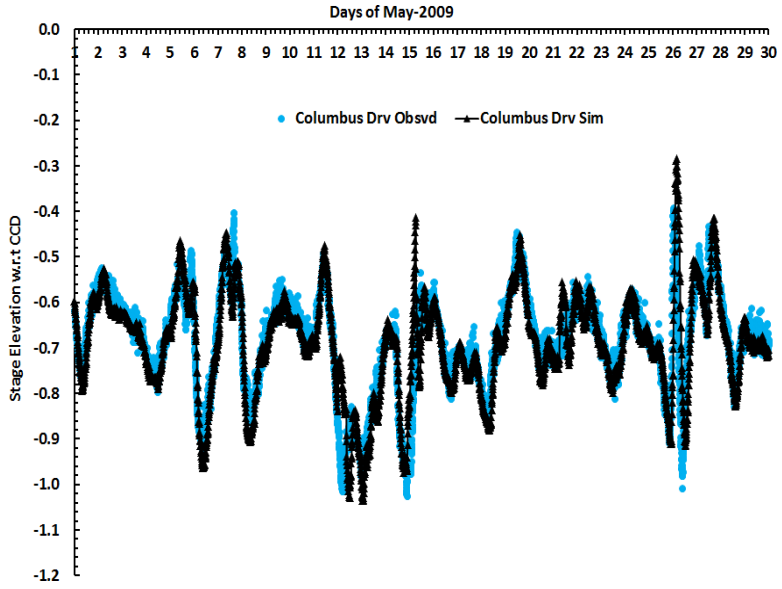

Figure 5.30: Comparison between observed and simulated stage at Columbus Drive for May-2009

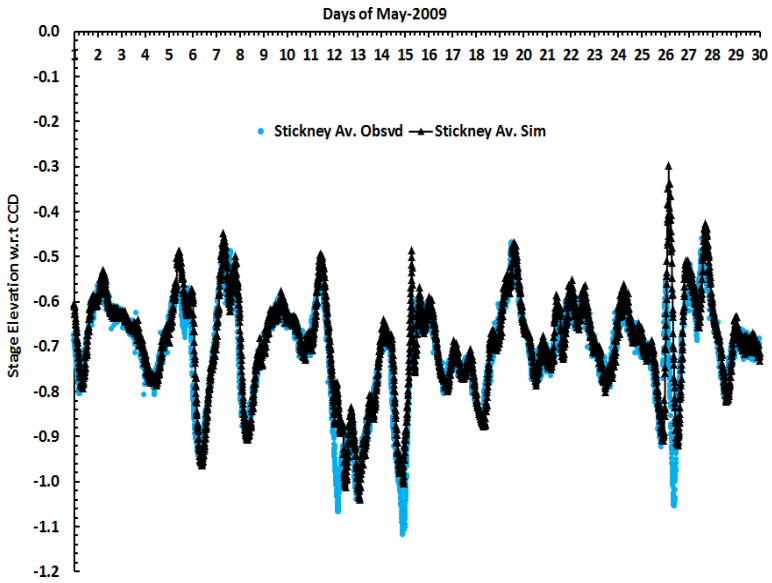

Figure 5.31: Comparison between observed and simulated stage at Stickney Avenue for May-2009

mentioned that the calibration procedure to capture the stage variation at Grand Avenue, Columbus Drive and Stickney Avenue entailed modification of bottom roughness height. But it's worth reiterating that as EFDC is a three-dimensional model with free-surface dynamics, changing of bottom roughness did not have a significant impact on either the stage or the flow magnitude in the case of CAWS. The simulation results presented here are conducted with fixed bottom roughness of 0.2 cms.

Notice that increased velocity in different portions of CAWS is usually associated with increased outflow from the four WWTPs or due to CSO events happening from RAPS.

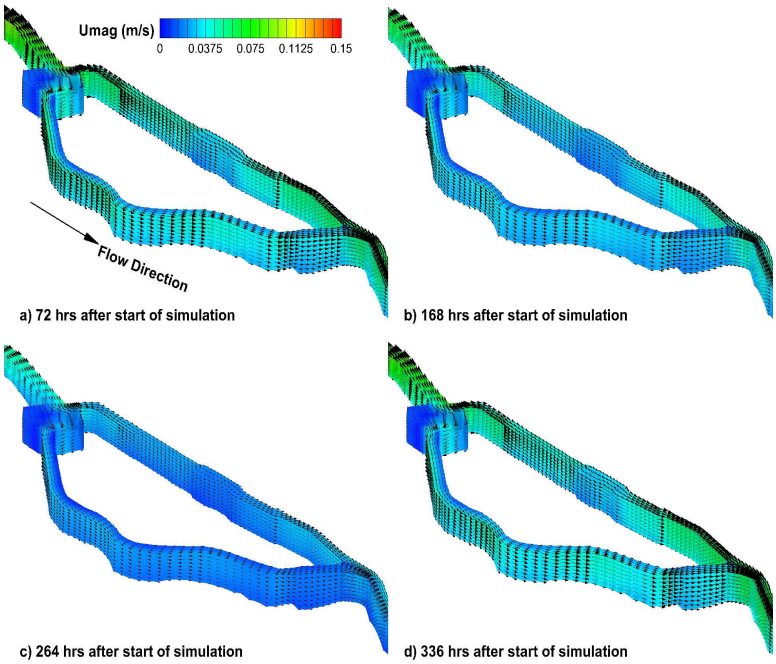

Figure 5.32: Velocity magnitude a) 3^{rd}, b) 7^{th} c) 11^{th} and d) 14^{th} day after start of the simulation near Goose Island on North Branch, Chicago River

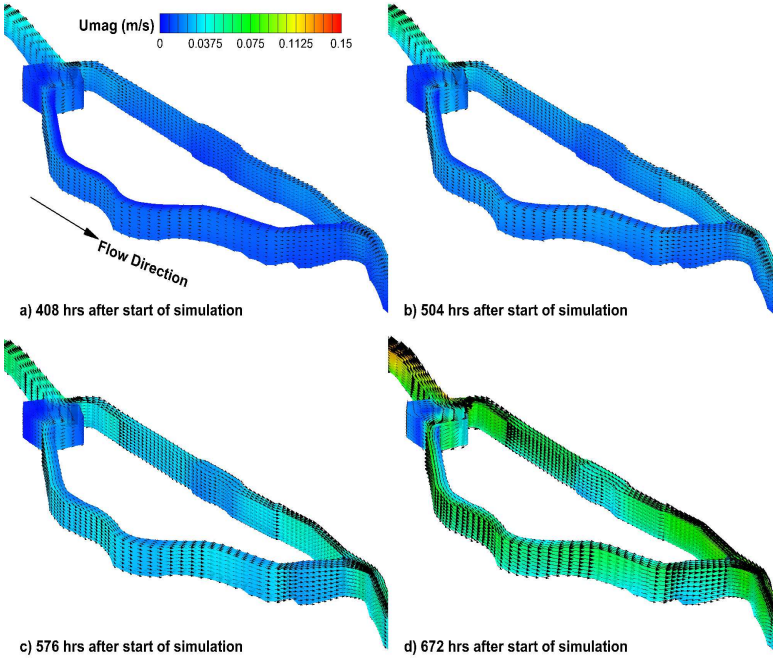

Figure 5.33: Velocity magnitude a) 17^{th}, b) 21^{st} c) 24^{th} and d) 28^{th} day after start of the simulation near Goose Island on North Branch, Chicago River

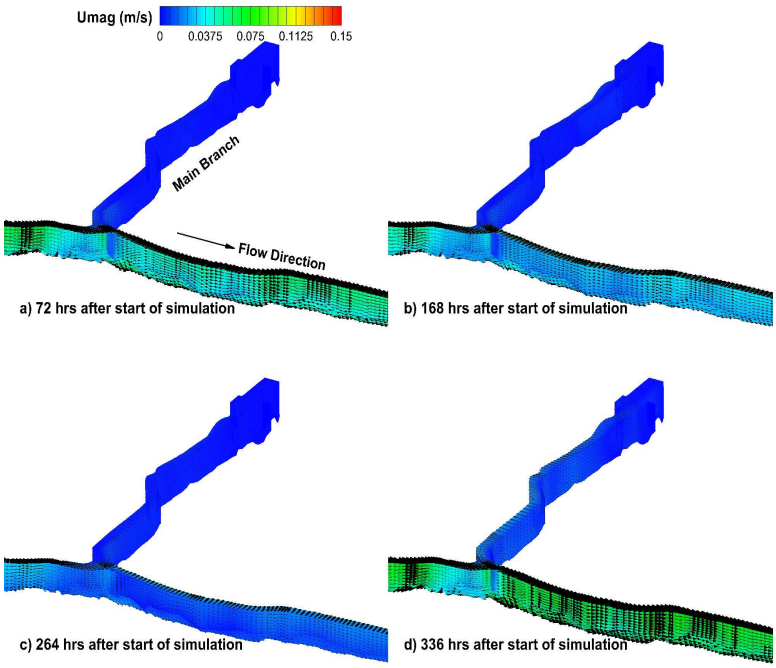

Figure 5.34: Velocity magnitude a) 3^{rd}, b) 7^{th} c) 11^{th} and d) 14^{th} day after start of the simulation on Main Branch, Chicago River

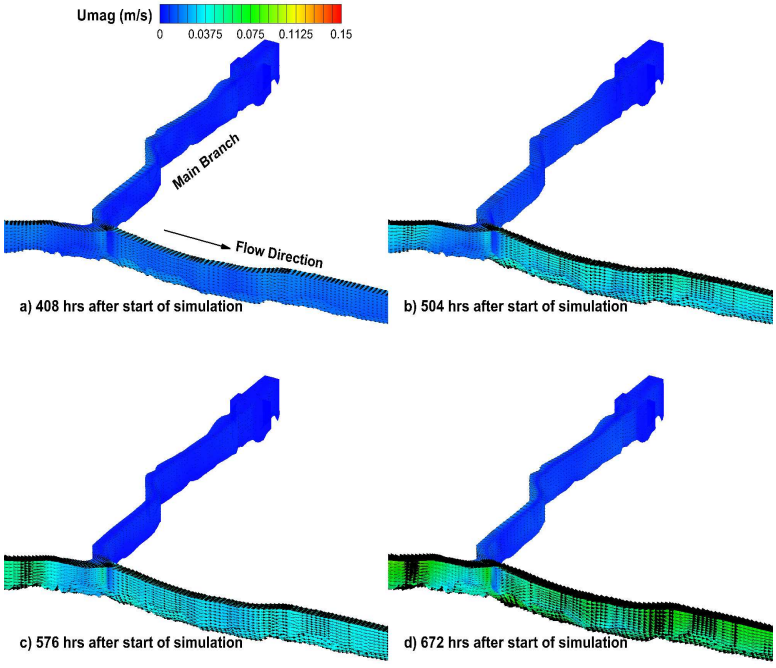

Figure 5.35: Velocity magnitude a) 17^{th}, b) 21^{st} c) 24^{th} and d) 28^{th} day after start of the simulation on Main Branch, Chicago River

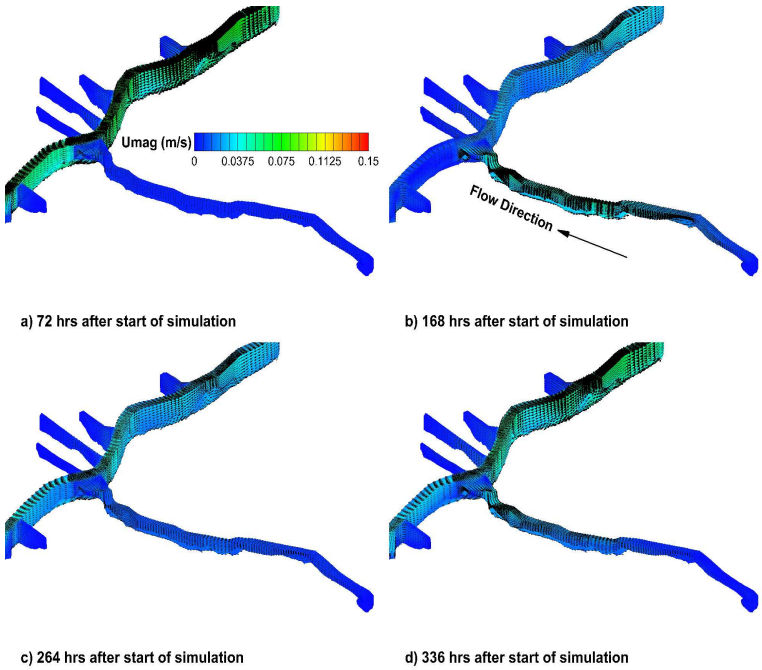

Figure 5.36: Velocity magnitude a) 3^{rd}, b) 7^{th} c) 11^{th} and d) 14^{th} day after start of the simulation in Bubbly Creek

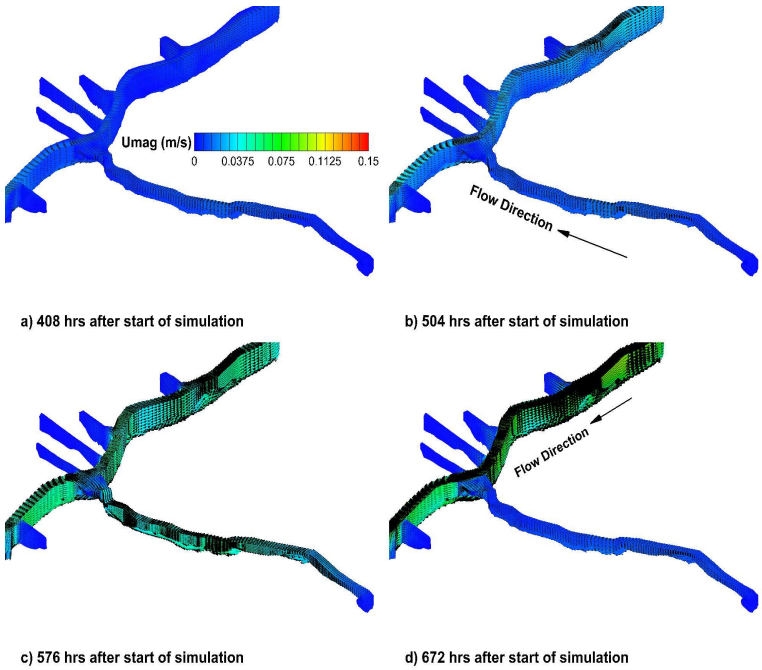

Figure 5.37: Velocity magnitude a) 17^{th}, b) 21^{st} c) 24^{th} and d) 28^{th} day after start of the simulation in Bubbly Creek

5.4 Dye Study Simulation

5.4.1 Description

Researchers have confirmed that a large number of non native Asian Carp has been steadily making their way up the Mississippi River basin. There is a clear and imminent danger of these invasive species making its way into Lake Michigan. Scientists fear that if Asian carp successfully migrate up into Lake Michigan it will endanger and hamper the ecological balance of the Great Lakes. As CAWS forms a vital link between the Great Lakes and Mississippi River basin, USGS conducted a fish-kill operation in December of 2009 in I&M canal portion of CAWS conducted by using piscicide Rotenone. Prior to releasing the poison to kill any Asian Carp USGS conducted a dye campaign is the southern portion of CAWS to get a sense of the dispersive characteristic of that portion of the river. The dye study gave USGS researchers a sense of timing and application of detoxifying agents after the piscicide had been used. The portion of the CAWS where the dye study was conducted is shown in the following figure.

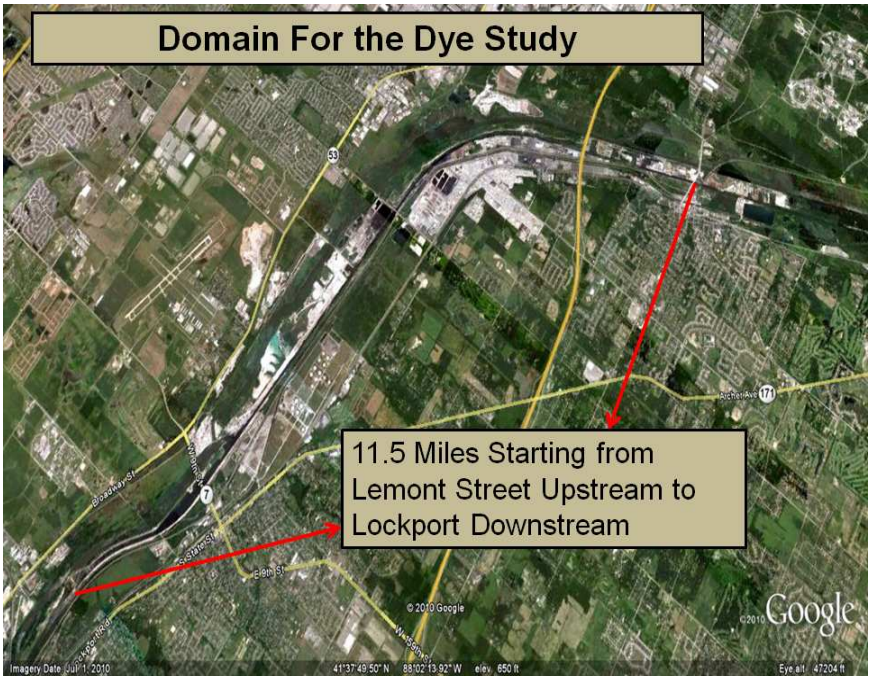

Figure 5.38: Portion of CAWS where the dye-dispersal campaign was carried out in Dec. 2009

As mentioned before Chicago Area Waterways System (CAWS) forms a vital link between two major water systems namely the Mississippi River basin and the Great lakes. In this section EFDC model was used to model the dye-dispersal study carried out in I&M canal portion of CAWS. As shown in Figure 5.38 the computational domain for the three-dimensional modeling ended at the Lockport power house and the downstream end of the modeled domain. A closer look at the Lockport end of the domain is presented in the Figure 5.39.

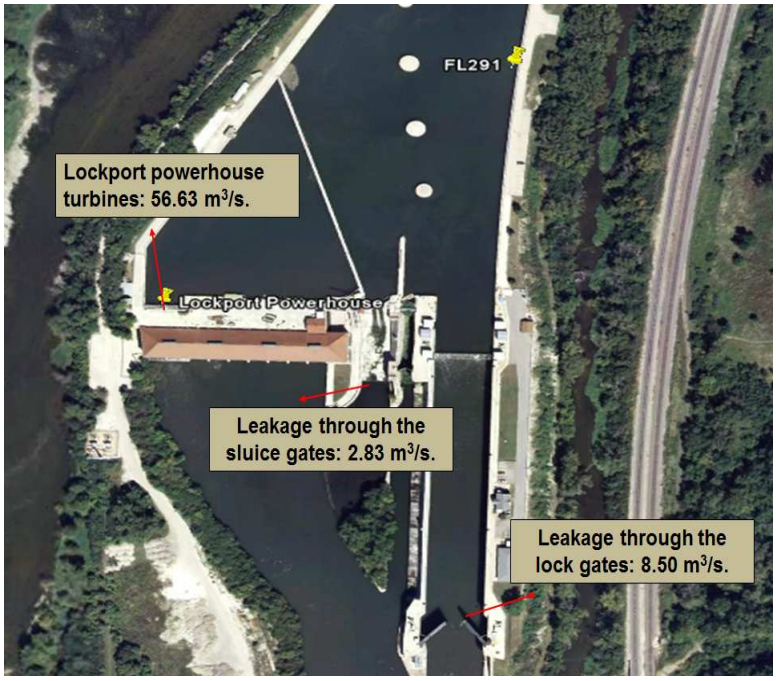

Figure 5.39: End of computational domain at Lockport power plant

It must be reiterated that the numerical modeling was carried out with the end purpose of getting a sense of dispersal characteristics of the flow in I&M canal during dry-weather condition. A well calibrated three-dimensional model will be very helpful in predicting the placement and timing of application of detoxifying agents, once the poisonous piscicide has been used to conduct the fish-kill operation. Although portion of CAWS modeled as a part of this research is very channel-like and straight in shape, the three-dimensionality of the flow can be attributed to the presence of outfalls and intake structures associated with the power plant, located three miles upstream from Lockport power house. The aforementioned power plant withdraws and returns water from I&M canal at the rate of 54.36 m^3/s, the

location of power plant intake and outfall is shown in Figure 5.40.

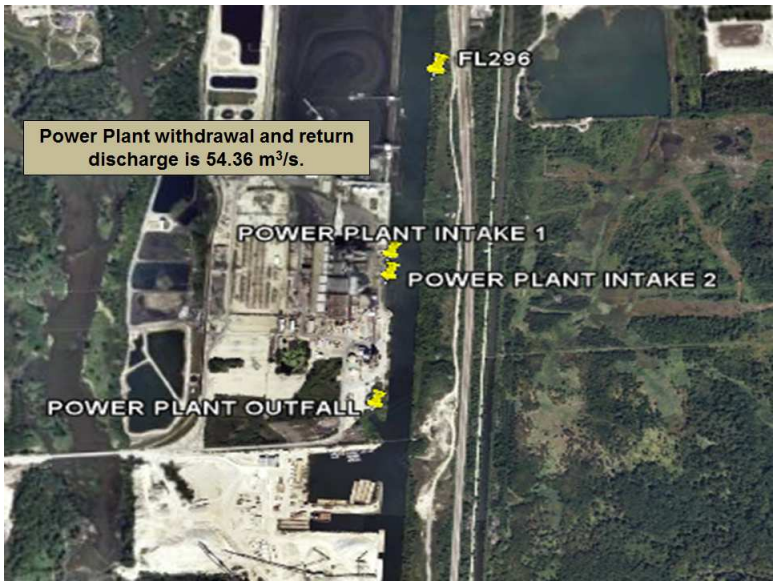

Figure 5.40: Location of power-plant intake and outfall inside the modeled domain

5.4.2 Boundary Conditions and Computational Grid for the Simulation

The total length of the portion of CAWS numerically modeled as a part of this research is 18.5 kms (see Figure 5.38). The boundary data used for setting up the simulation came from the USGS gauging stations. The outflow discharge boundary condition was used at the south end of the domain, the outflow and the leakages through various outfall structures are shown in the 5.39. The dye injection began at 19:51 hours on Dec 2, 2009, almost 20 hours after the start of the numerical simulation. The rate of dye injection was set at 2.955e-6 m^3/s and the concentration at the injection point was 2.3e8 ppb. Rhodamine dye was injected for 9 hours, 2.3 kms downstream from the Lemont Street. Finally, through the south end of the domain from various end points the constant outflow of 56.63, 2.83 and 8.50 m^3/s was set for the entire duration of the simulation. USGS maintains a gauging station at the Lemont Street and the inflow data used for the simulation was obtained from this gauging station. The dye concentration was initialized with 0 ppb in the whole domain before starting the numerical simulation. The only source of

the incoming dye was from the injection point 2.3 kms downstream from the Lemont Street. The numerical simulation was conducted for 72 hours. The simulation was carried out for the real time period, from 12:00 am on Dec 2, 2009 to 12:00 am on Dec 5, 2009. The computational grid used for the numerical simulation was again made with the help of the pointwise software Gridgen.

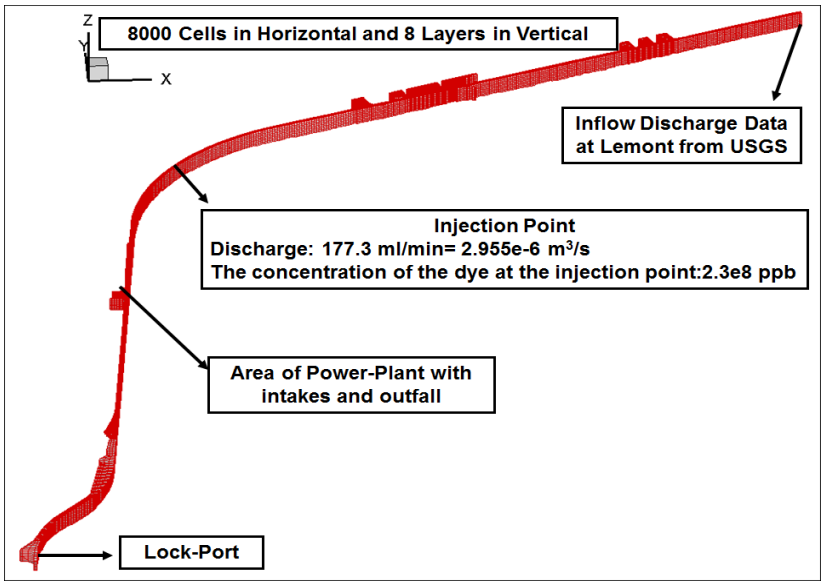

Figure 5.41: Computational mesh for dye simulation

As shown in Figure 5.41 the computational grid used for the simulation has 8000 cells in horizontal and 8 layers in vertical. As mentioned before because of the existence of side-slip structures and power plant outfalls and intakes the flow acquires a three-dimensional nature. A closer look on the computational grid near the locations of these structures are presented in Figures 5.42 and 5.43.

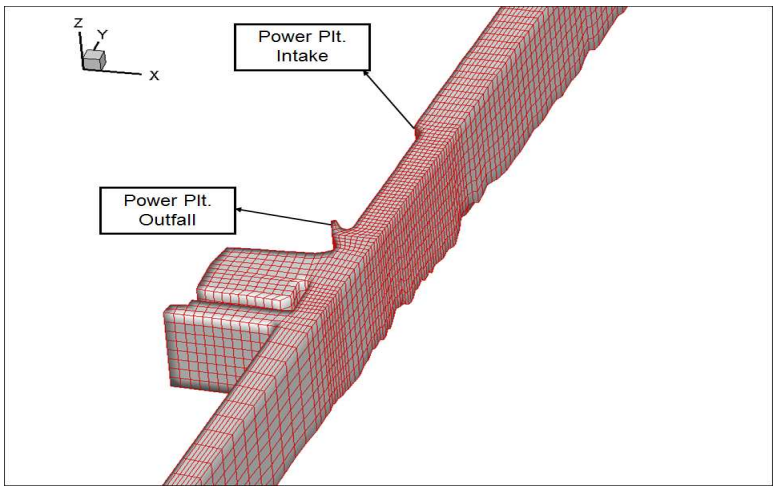

Figure 5.42: Computational mesh near power plant

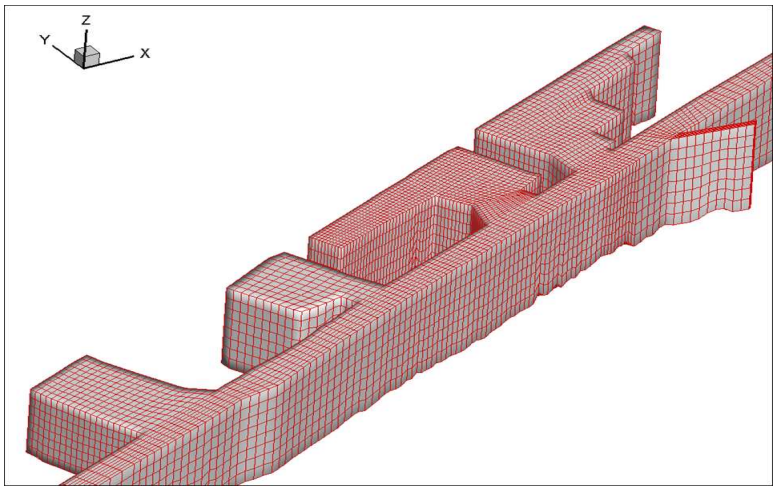

Figure 5.43: Computational mesh with side-slip structures incorporated

5.4.3 Simulation Results and Discussion

During the dye-dispersal campaign USGS placed probe at regular intervals. The location of these probes is shown in Figure 5.44.

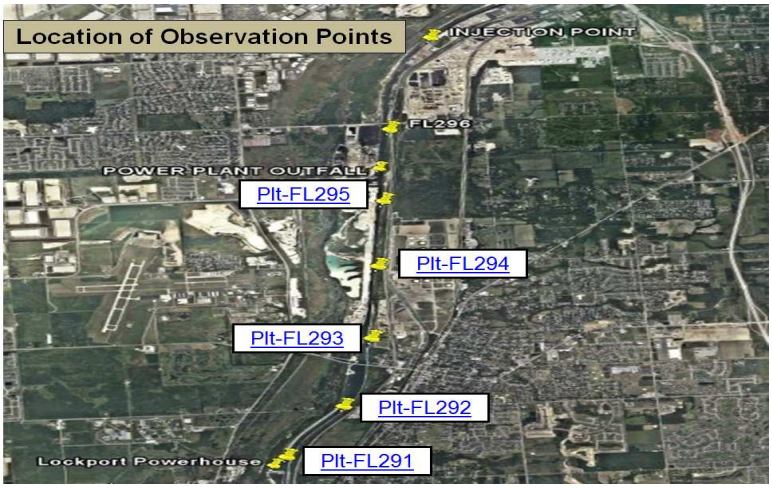

Figure 5.44: Position of dye-probe placed by USGS along the length of the domain

The distance of these probes from the injection point at the Lemont street is shown in Table 5.2.

Table 5.2: Distance of Fluorometers from Lemont Street

Station	Dis. from inj. point (m)
FL291	9929.1
FL292	8610.0
FL293	7032.8
FL294	5391.3
FL295	3910.7

A comparative plot between the simulated and observed dye concentration is presented in Figures 5.45 and 5.46. The numerical model is able to capture the evolution and variation of dye concentration in a satisfactory manner. Also it must be reiterated that during the entire period of simulation the power plant located inside the computational domain, withdrew and discharged water from the river at a rate of about $57 m^3/s$. As mentioned before, its near the outfall and intake structures associated with the power-plant that the augmented three-dimensionality of the flow is observed. The same is also demonstrated in a better manner in Figures 5.47 and **??**.

The streamline structure shown in Figure ?? distinctly demonstrates the multi-dimensionality of the flow near power plant intake and outfall structures. Finally the flow velocity in the entire modeled domain did not exceed the magnitude of 0.25 m/s as observed in field campaign as in numerical simulation as shown in Figure 5.48.

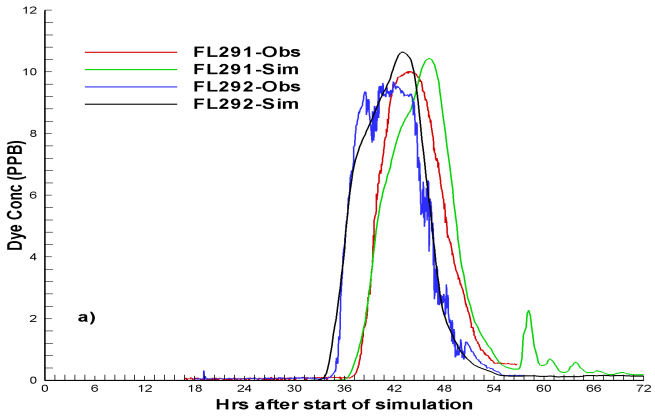

Figure 5.45: Comparison between simulated and observed dye concentration, FL-291 and FL-292

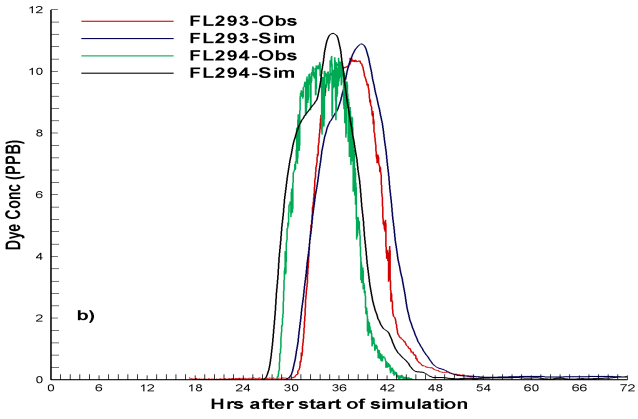

Figure 5.46: Comparison between simulated and observed dye concentration, FL-293 and Fl-294

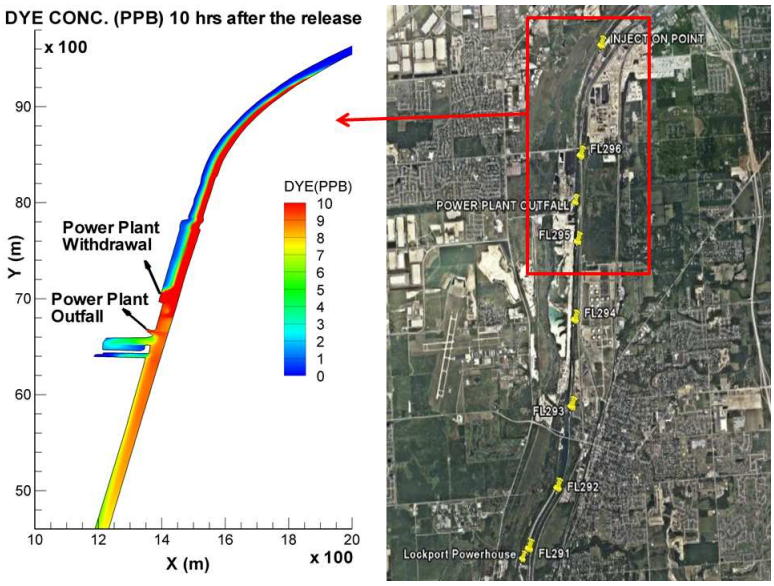

Figure 5.47: Dye Concentration near power plant, 10 hours after injection

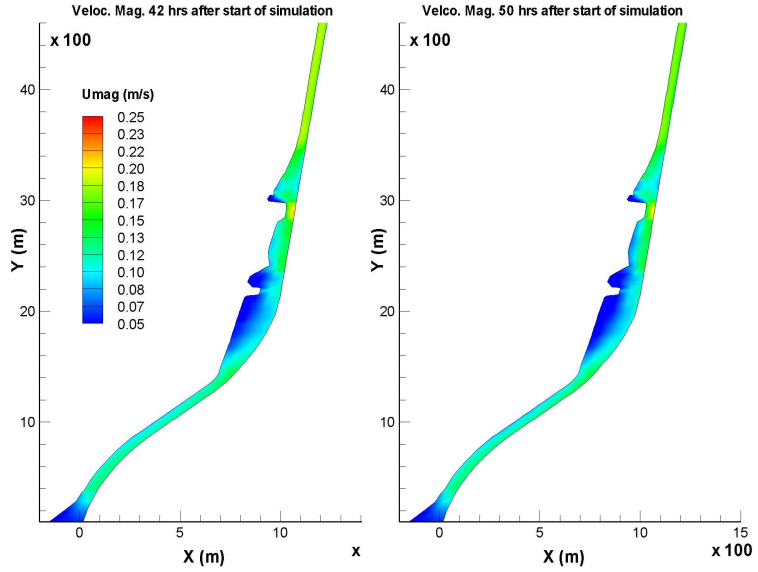

Figure 5.48: Snapshot of velocity magnitude 42 and 50 hours after the start of simulation

5.5 Water Quality simulation

5.5.1 Application of Three-dimensional DO-BOD Model for Bubbly Creek

In this subsection the first in the series of application of water quality models to various portion of CAWS is presented. The study area for this modeling exercise comprises of the entire 2200 meters long channel of the South Fork of the South Branch of Chicago River, colloquially referred as Bubbly Creek, along with various slips at the mouth of the Creek. Bubbly creek was once a pristine wetland system that provided natural aquatic and terrestrial habitat for fish, bird and other species. Bubbly Creek has undergone major physical changes, which includes deepening and widening of the channel, creation of sheet pile banks, severe hydrologic alteration, and introduction of polluted sediments and runoff. A mix of land uses are found along the banks of Bubbly Creek including industrial plants, trucking terminals, rail yards and construction material yards which are giving way to new commercial and residential development. In olden days there were number of meat packing plants situated along the banks of the Bubbly Creek. The channel was systematically widened and deepened to allow for drainage and disposal of waste from the nearby meat packing industries. Biochemical reactions caused by the decomposing animal waste continuously produce methane and hydrogen sulphide bubbles. To this day these bubbles constantly float to and break at the water surface, for which the name, Bubbly Creek is colloquially given. Today, Bubbly creek is a relatively straight 2200 meters long channel that originates at the Racine Avenue Pumping Station (RAPS) and flows north during the over flow events to its confluence with the south branch of the Chicago River. Bubbly Creek is relatively shallow with depth varying from 2 meters near RAPS and around 5 meters at the mouth where it meets the south branch of the Chicago River. The width of the creek varies between 40 and 65 meters. The major physical alterations caused by the development has severely degraded the natural ecosystem and eliminated most of the natural aquatic and terrestrial habitat. Due to gigantic man made changes, hydrologic alterations, combined sewer overflow (CSO), Bubbly creek remains a severely impaired ecosystem with vast opportunities for restoration. Bubbly creek faces complex series of problems which requires a very keen and close

examination, which hopefully would finally yield some pragmatic restoration procedures. Some of the challenges faces by the Bubbly Creek are explained in little more detail here.

Stagnant flow condition: During dry weather periods Bubbly Creek is stagnant, except for the occasional movement of water caused by the passing boats or the slight surge from the South Branch. Even during light to moderate rainfall the flows in Bubbly Creek is not severely affected as only a very small area adjacent to the channel directly drains into Bubbly Creek. It would not be a stretch to say that for most of the time Bubbly Creek behaves more like a lake system rather than a regular river. During the stagnant periods, severely degraded water quality in Bubbly Creek can be attributed to several factors, including biochemical activity between the sediment and the water column, residual water quality from CSOs and photosynthetic activity. Levels of dissolved oxygen (DO), which are indicators of water quality impairment in a stream, typically plummet during stagnant periods and often reaches zero.

Combined sewer overflow: During excessively heavy rainfall events, the combined sewer system that drains surface water runoff and sanitary waste by gravity to RAPS can become overwhelmed. During these times to avoid the problems of water accumulation in the related sewer shed, the pumps at RAPS are turned on which discharges directly into Bubbly Creek. As the quality of water coming into RAPS and getting discharges into Bubbly Creek is severely impaired it has an adverse effect on the overall water quality in Bubbly Creek. At maximum overflow capacity RAPS can discharge almost 170 cubic meters per second in Bubbly Creek. At such high discharge the water levels in Bubbly Creek can increase significantly, especially near the pumps the change in water levels has been observed to be as high as 1 meter. The flow velocity produced as a result of such massive discharge varies around 1 meter per second and some time even more. Such high velocities lead to increase bed shear stress which resuspends lot of undesired organic matter from the bed of Bubbly Creek, which again adversely affects the water quality.

The CSO event simulated and presented in this subsection occurred on September 13^{th}, 2006, the flow coming from RAPS was of the order of 70 m^3/s and the duration of CSO was about 7.66 hrs. The flow in the South Branch was kept at 20 m^3/s. First the results from the hydrodynamic simulations are presented in Figures 5.49 and 5.50.

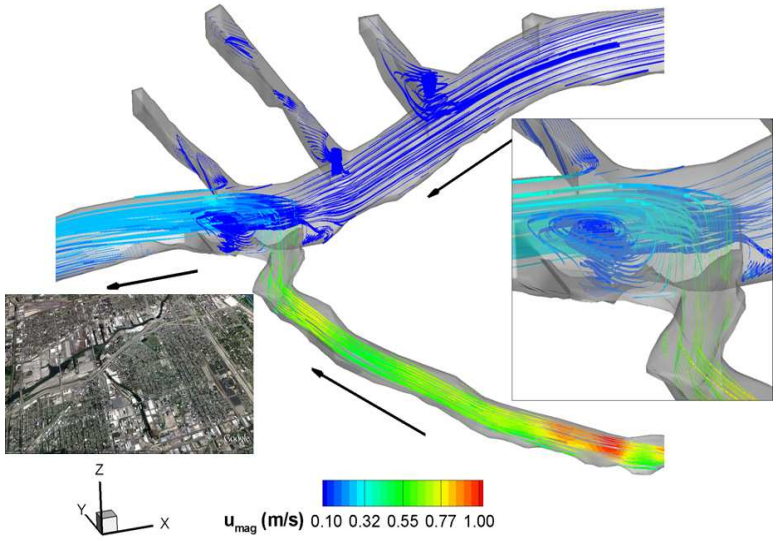

Figure 5.49: Velocity magnitude in Bubbly Creek 4 hours after the start of the simulation

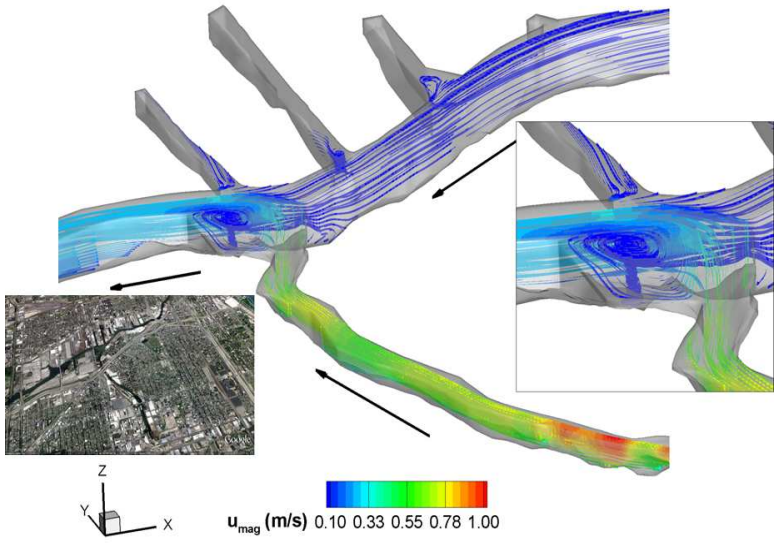

Figure 5.50: Velocity magnitude in Bubbly Creek 8 hours after the start of the simulation

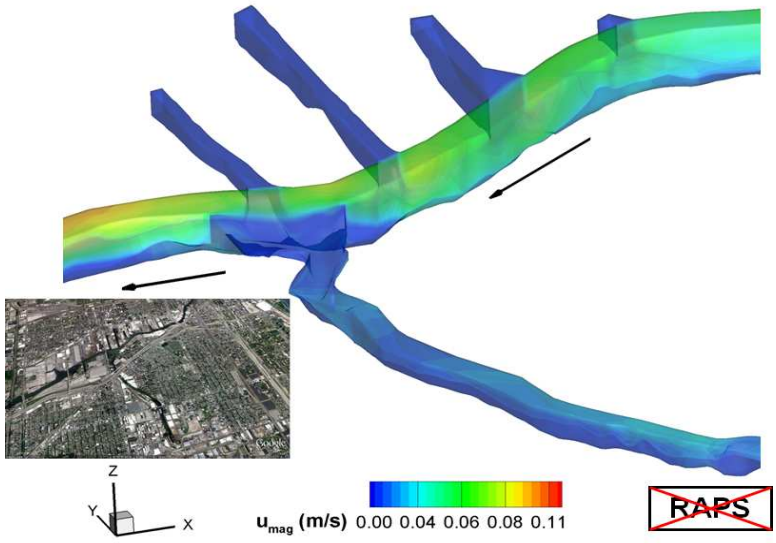

Figure 5.51: Velocity magnitude in Bubbly Creek 12 hours after the start of the simulation

Notice the formation of circulation zones around the area of turning basin, where the northward moving flow in Bubbly Creek meets the South Branch of the Chicago River. These vortices are observed in turning basin only during the CSO event. Also noticeable is the increased flow velocity in Bubbly Creek during the CSO event, the magnitude of flow velocity reaches as high as 1 m/s during the CSO. Also presented in Figure 5.51 is a plot that shows the hydrodynamic feature after the end of the CSO. After the end of the CSO the flow velocity in the creek returns to its usual levels of close to zero values.

As regards with water quality constituents, the incoming flow from the RAPS had saturated DO value of 9 mg/l, and BOD at 68.1 mg/l. The inflow from north in the main channel had incoming DO level of 6.86 mg/l and BOD of 5 mg/l. The SOD was taken constant at 3.3 gm/mt^2/day for Bubbly Creek. The entire computational domain was initialized with DO value at 1.2 mg/l. This value was obtained by taking the average of the observed DO values at 36th street and I-55 stations before the onset of the CSO event. The concentration of incoming suspended sediment from RAPS with the flow was set at 650 mg/l based on the data from MWRGDC. The evolution of DO in the domain through and after the CSO is presented in series of plots in Figures 5.52 to 5.55.

As shown in Figures 5.52 and 5.53 during the CSO event the DO levels in

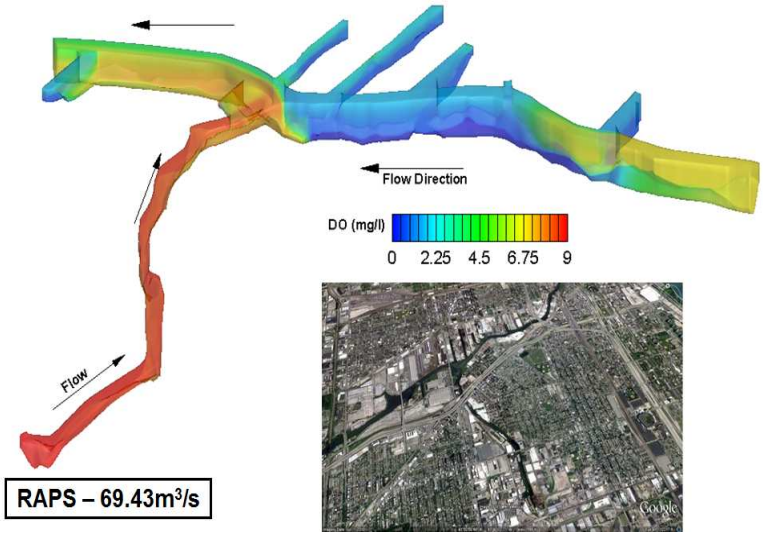

Figure 5.52: DO levels in the creek 4 hours after the start of the simulation

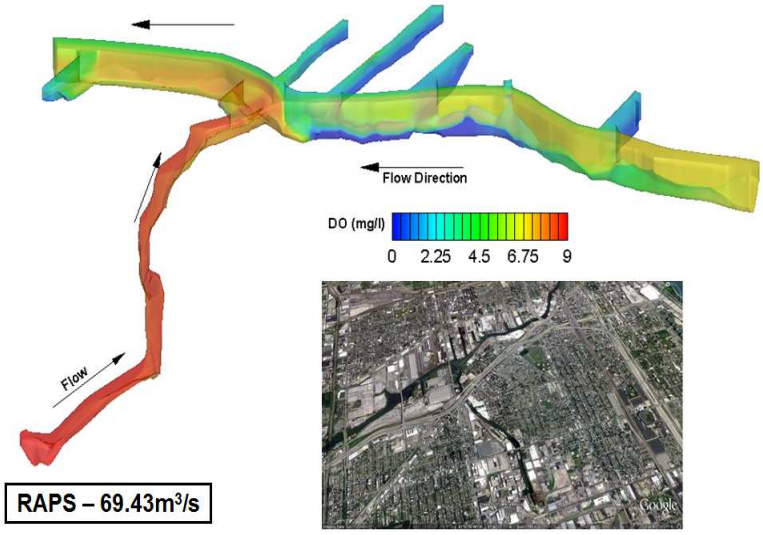

Figure 5.53: DO levels in the creek 8 hours after the start of the simulation

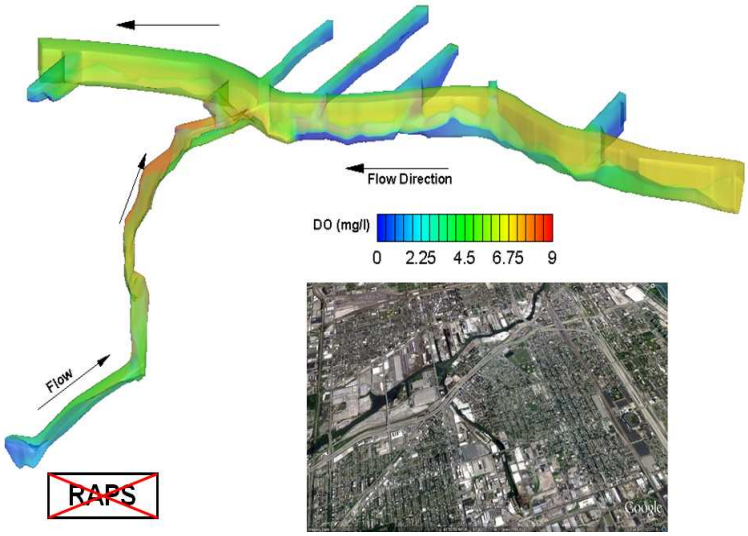

Figure 5.54: DO levels in the creek 10 hours after the start of the simulation

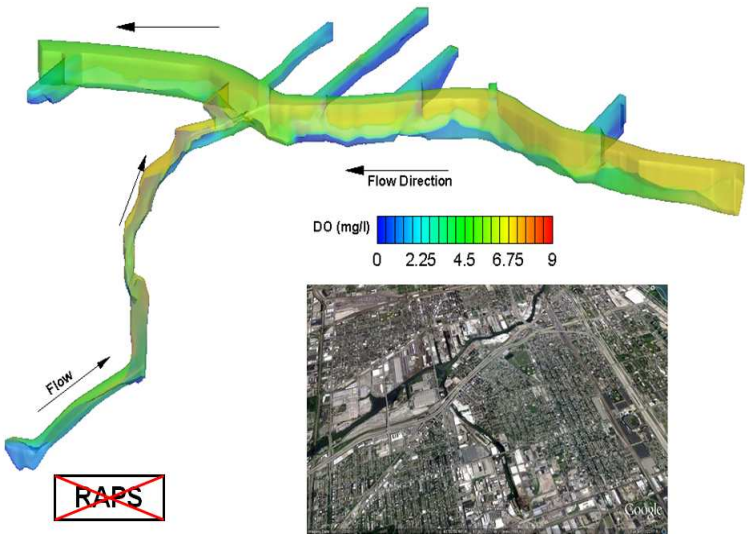

Figure 5.55: DO levels in the creek 12 hours after the start of the simulation

Bubbly Creek undergoes sharp and sudden increased because the water that comes through system of pipes and shafts is already saturated with DO and this high level of DO is advected with the flow along the length of the creek during a CSO event. As observed here and also shown by Motta et al. (2010) it is when the CSO event ends that once can see the changing and dynamic nature of DO variation. Notice in Figure 5.54 and 5.55 as time goes by the depletion of DO is observed and DO levels drop from its saturated value of 9 mg/l to values around 5 mg/l or even below. This can be explained by the fact that incoming CSO, although saturated with DO, is also high in BOD and suspended sediment concentration. Furthermore the increased velocity in the creek resuspends the organic matter from the bed and has a sink effect on the DO levels in the water column. There are two water-quality monitoring stations in Bubbly Creek located at 36th street and I-55. The probes located at these locations measure the DO levels 1 m below the free-surface elevation, the comparison between the observed and simulated DO level is shown in Figure 5.56.

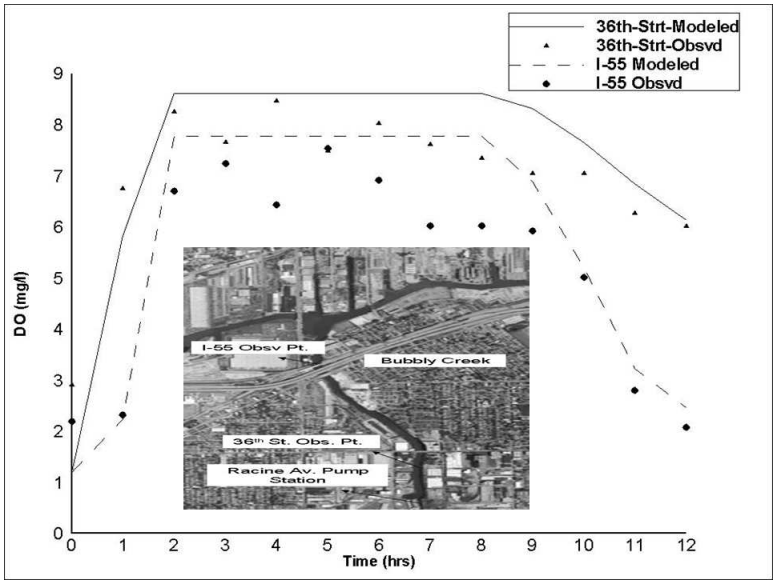

Figure 5.56: Compairison between observed and simulated DO at 36th street and I55

Finally also presented in series of plots is the variation of incoming suspended sediment from RAPS through the modeled domain. As shown in from Figures 5.57 to 5.59 the incoming suspended sediment concentration also exhibits the same trend, initially with the incoming CSO flow it gets

advected and intrudes into the side-slip and also propagates upstream. But after the end of the CSO we can see a settling nature of the suspended sediment particles (see Figure 5.59.

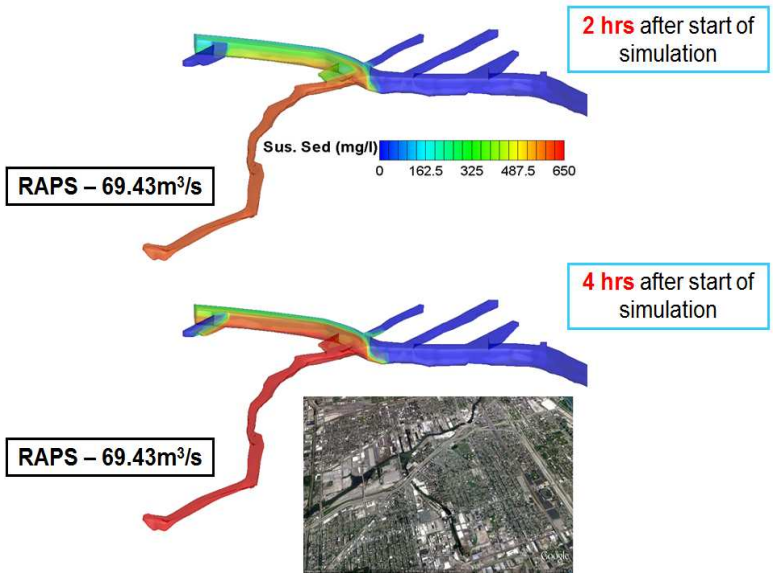

Figure 5.57: Suspended sediment concentration 2 and 4 hours after the start of the simulation

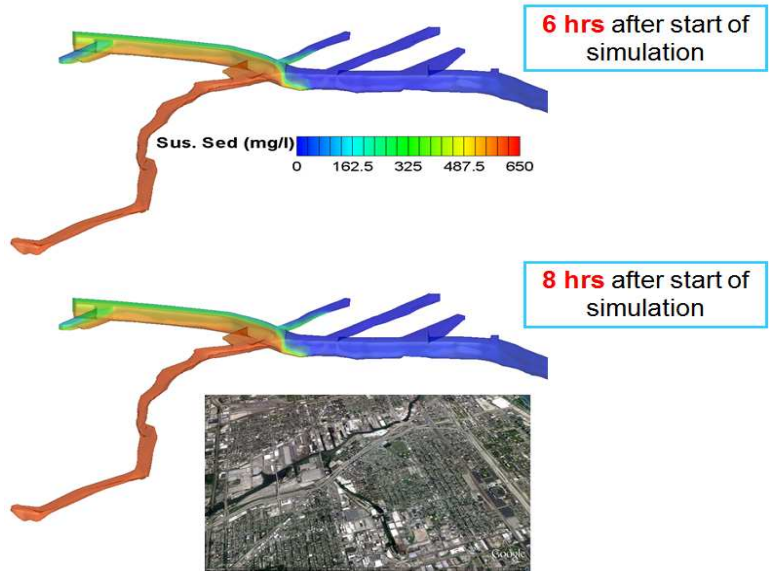

Figure 5.58: Suspended sediment concentration 6 and 8 hours after the start of the simulation

In conclusion it can be said that the DO levels in the creek experiences a surge when a CSO occurs but after the CSO is over the DO levels inside

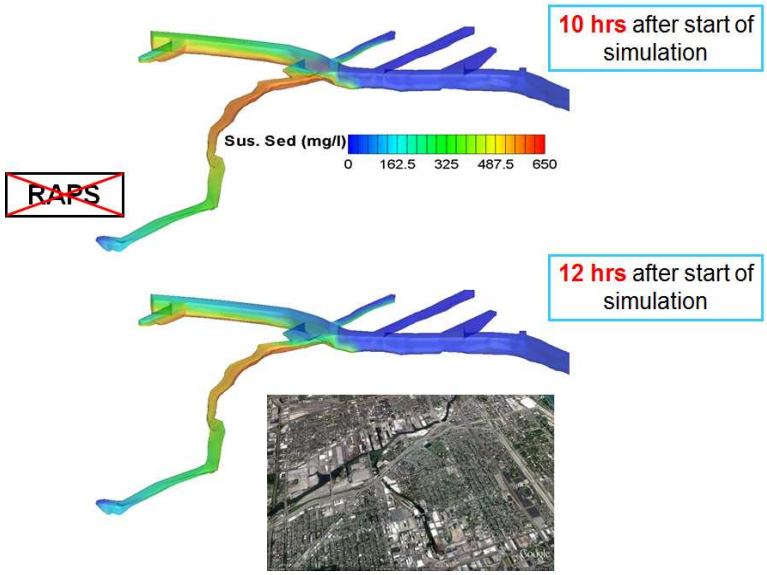

Figure 5.59: Suspended sediment concentration 10 and 12 hours after the start of the simulation

the creek is governed by two competing factors of Sediment Oxygen Demand (SOD) and reaeration. In the simulation results presented here SOD values used were fixed at levels of 3.3 gms/m^2/day. As mentioned and explained in Chapter 4, SOD values in this modeling effort acts more like a calibration parameter. But in light of Waterman et al. (2009) work perhaps it would be advisable to develop a physics based model which can capture the DO sink effect of resuspended sediment particles from the bed of the creek.

5.5.2 Application of Three-dimensional DO-BOD model for CAWS

In this section the simplistic DO-BOD model developed and described in chapter 4, as a part of this research is applied to the whole CAWS. The simulation is conducted for the month of May-2009. As is well known that Bubbly Creek is one of the most impaired section of CAWS. The DO levels in Bubbly Creek often reaches as low as 1 mg/l. Based on the data collected from monitoring stations at 36^{th} street and I-55 the DO values in Bubbly Creek were initialized with 0.2 mg/l near RAPS and linearly increasing to 8.0 mg/l near the turning basin where Bubbly Creek meets the South Branch of the Chicago River. The rest of the CAWS domain was initialized with DO

value of 8.0 mg/ l. BOD was initialized with a value of 5.0 mg/l in the whole CAWS domain. As explained in chapter 4 while incorporating the bed-water column interaction dynamics in the developed DO-BOD model, provision was made for modeling BOD both as dissolved and particulate form in the water column and the sediment layer. But due to lack of the date pertaining to the partition of BOD as dissolved and particulate form, the simulation presented here was done with the assumption that the BOD in the water column exist in dissolved form and in bed layer it is present in the particle format. Spatially and temporally constant value of bed SOD of $3.3gm/m^2/day$ was used in the simulation. The amount of BOD present in the bed is tough to estimate hence this was taken as a calibration parameter in accordance with Motta et al. (2010) and fixed at 5000 mg/l. This corresponded to a concentration over mass of sediments of 13.2 mg/g. Its also very tough to measure the settling velocity of the sediments, especially during the high flow condition, hence this was again taken as the calibration parameter and its value was fixed at 4.5 m/day. The thickness of bed top layer was fixed at 3 m. As mentioned before there were four CSOs during the month of May-2009 from RAPS. The observed values of various water quality constituents in the effluent CSO from RAPS is presented in the following table.

Table 5.3: DO, BOD and Suspended Sediment Concentration in RAPS CSO's for May 2009

CSO (mg/l)	St-DO	Ed-DO	St-BOD	Ed-BOD	St-SS	Ed-SS
1	2.2	2.2	60	60	641	641
2	6.4	6.4	88	88	506	506
3	4.9	2.3	61	60	224	120
4	4.1	7.2	206	60	532	350

Also incorporated in the water quality simulation presented here is water quality characteristics of the effluent from the four WWTPs. The average incoming levels of various water quality constituents coming from WWTP's are presented in the following table.

After having calibrated the hydrodynamic model for May-2009, the water quality model was run in conjunction with the hydrodynamic model for the same period. The incoming water quality characteristics from RAPS and WWTPs as presented above were incorporated into the model simulation.

Table 5.4: DO, BOD and Suspended Sediment Concentration from WWTPs for May 2009

WWTS	Avg. DO(mg/l)	Avg. BOD(mg/l)	Avg. SS(mg/l)
LWRP	7.875	7.918	8.344
CWRP	4.387	7.313	4.612
SWRP	4.645	8.987	4.000
NSWRP	3.320	7.264	3.096

The simulated values of the water quality characteristics were recorded from the numerical model at the same locations where MWRDGC maintains monitoring stations. These monitoring station records the water quality characteristics like DO and temperature at 0.8 - 1.0 m below the dry weather water surface elevation of CAWS. During the dry weather condition the water surface elevation in CAWS is maintained at -0.66 m below Chicago City Datum (CCD). The locations of the pertinent water quality monitoring station is shown in the following figure.

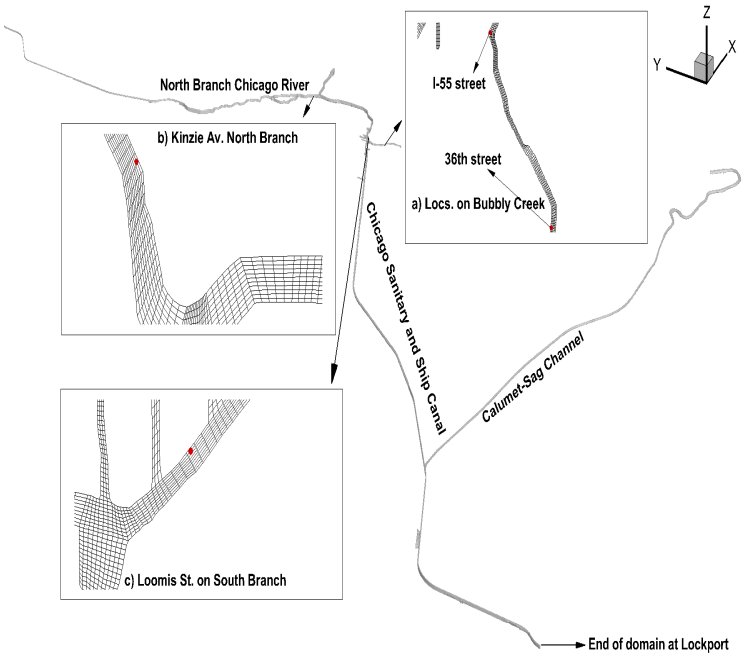

Figure 5.60: Location of water quality monitoring station on the computational grid of CAWS

The water quality characteristics were recorded at the locations shown in the above figure. As mentioned previously Bubbly Creek is one of the most impaired section of CAWS, the DO variation at the two monitoring stations

located in Bubbly Creek is shown in the following figures.

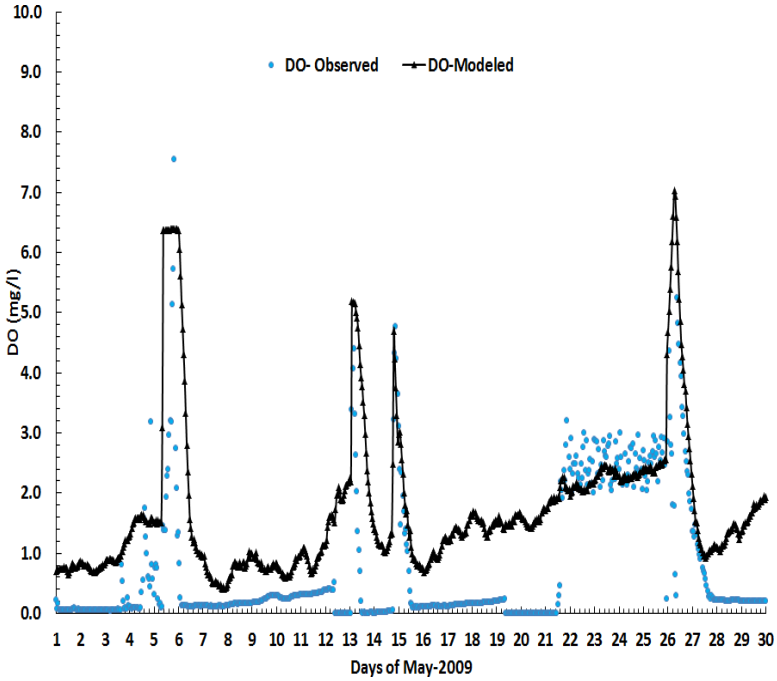

Figure 5.61: Variation of DO at 36^{th} street in Bubbly Creek for May-2009

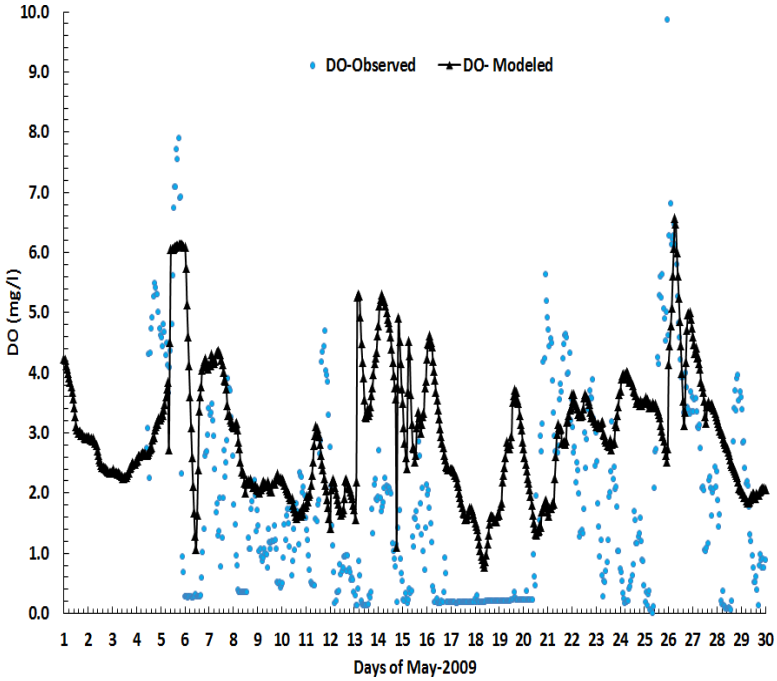

Figure 5.62: Variation of DO at I-55 in Bubbly Creek for May-2009

It can be seen from Figures 5.61 and 5.62 that the model developed replicated the DO variation trend for May-2009 in a satisfactory manner. Also

notice that there are stretches of time Figure 5.61 when the observed value of DO stays close to nil. The time-stretches of nil value of DO, especially around 36^{th} street, often happens after a CSO event. This can be explained as follows, during a CSO event when large volumes of water are discharged into Bubbly Creek, the high flow velocity especially in the shallower areas of the creek is able to re-suspend highly organic matter from the bed of the creek. The re-suspened organic matter stays in the water column and has a sink effect on the DO in the water column. Its worth reiterating that this process is distinctly and repeatedly observed towards the gauging station at 36^{th} street because the water depth in this area is between 1.5 - 2.5 m, hence during a CSO event when the degraded material is re-suspended from the bed, entire water column is able to feel the drawdown of DO. It is only through reaeartion that the DO is replenished in the water column which takes some time hours and some times even days. As far as the DO level near I-55 is concerned, although we do observe the decrease of DO to almost nil values following CSO events but the stretches of time for which the DO levels stays close to zero is much shorter in comparison with the 36^{th} street. One of the reasons for faster replenishment of DO I-55 station is its proximity to the South Branch of the Chicago River. During the dry weather conditions the flow velocity in the South Branch is always higher than the flow velocity in Bubbly Creek, which is more or less a stagnant backwater of South Branch of Chicago River. It can be hypothesise that due to the increased velocity and higher water depth in South Branch, diffusion of DO from South Branch to Bubbly Creek is facilitated and helps in improving the DO condition near I-55 on Bubbly Creek. Also presented in Figures 5.63 and 5.64 is DO contour in Bubbly Creek at different point in times during the month of May-2009.

Notice that the DO levels in Bubbly Creek is marginally low for most of the times. It is only during CSO events that the DO-saturated water that comes from RAPS brings up the DO level in the creek momentarily. But then this augmented DO is consumed by the organic matter which is generally resuspended from the bed of the creek. One of the distinct advantage of having a three-dimensional model is the ability to examine the variation of DO along the depth in the water column. With this end in mind and to study the variation of DO immediately following the CSO events, the DO values in the water column is recorded 1,2,3,4 and 5 hours after all the four

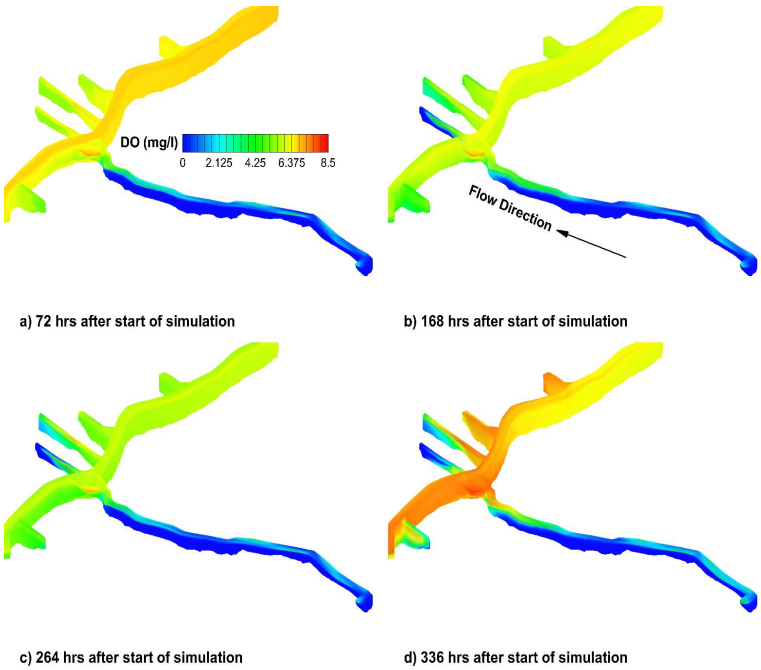

Figure 5.63: DO concentration a) 3^{rd}, b) 7^{th} c) 11^{th} and d) 14^{th} day after start of the simulation in Bubbly Creek

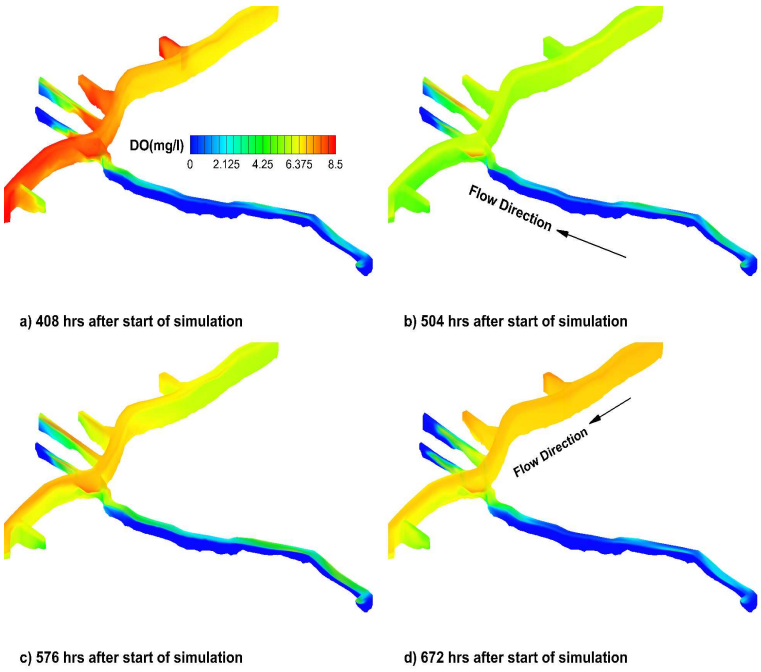

Figure 5.64: DO concentration a) 17^{th}, b) 21^{st} c) 24^{th} and d) 28^{th} day after start of the simulation in Bubbly Creek

CSOs at 36^{th} street and I-55 monitoring station. Plots for the variation of DO along the water column is presented in Figures 5.65 and 5.66

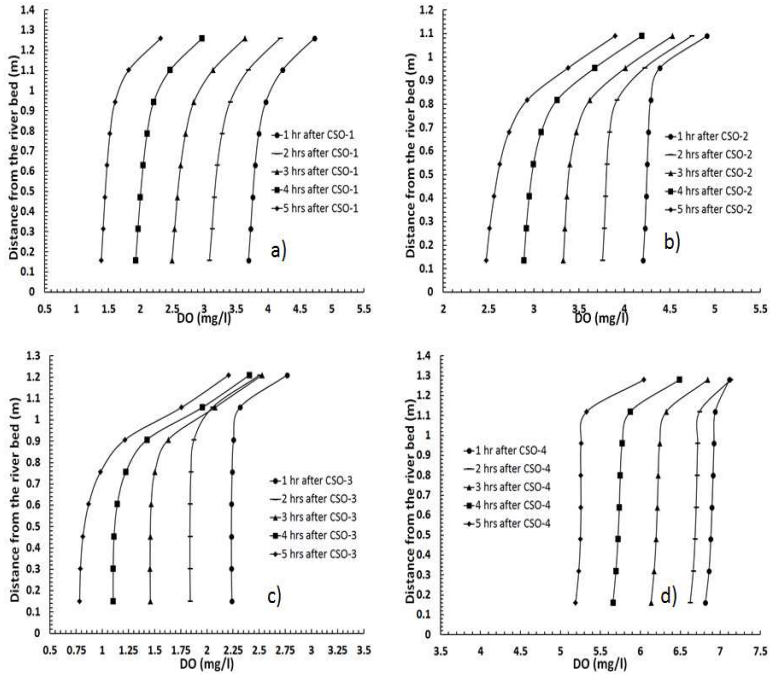

Figure 5.65: DO variation along the water column at 36^{th} street on Bubbly Creek

Both in the cases of 36^{th} street and I-55 on Bubbly Creek, it can be clearly seen that the DO levels is lowest near the bed and it keeps on depleting steadily after every CSO event. Also when examined in comparative manner we see that the level of DO is higher at I-55 in comparison to 36^{th} street, the reason for this is the shallower water depth around 36^{th} street in comparison to I-55. At this point perhaps it is warranted to present some BOD plots in Bubbly Creek area.

As shown in Figures 5.67 and 5.68 a sudden and a sharp increase in Bubbly Creeks BOD concentration is observed during CSO events, Figures 5.67(a), 5.67(c), 5.68(b) and 5.68(d). This is entirely guided by the effluent BOD concentration from RAPS. Also worth noticing is the vertical characterization of BOD concentration, it can be clearly seen from Figures 5.67(b) and 5.67(d) that the BOD concentration that is modeled as the sum total of dissolved and particulate form attached to the sediments in the bed, shows a distinct deposition characteristics after the end of every CSO when the flow velocity in Bubbly Creek subsides down. The model results also capture the upstream

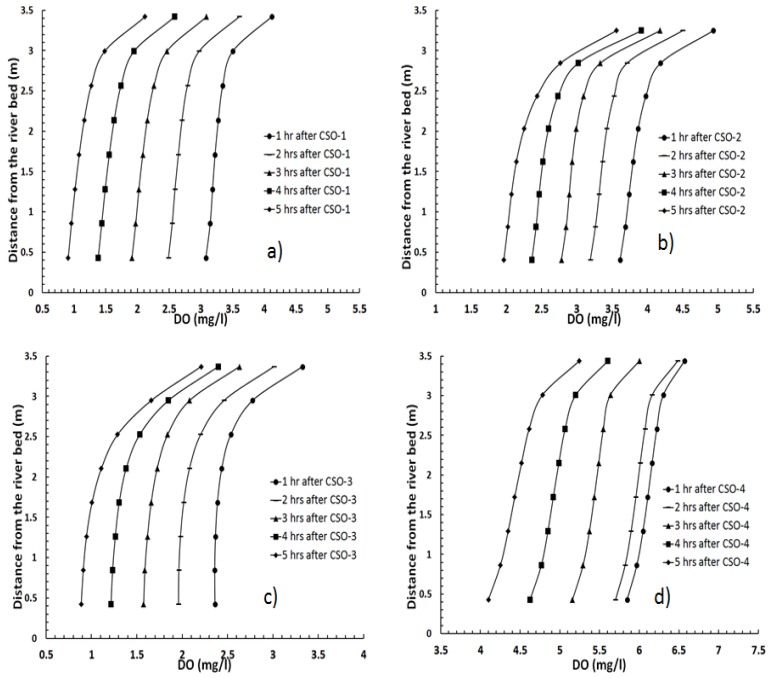

Figure 5.66: DO variation along the water column at I-55 on Bubbly Creek

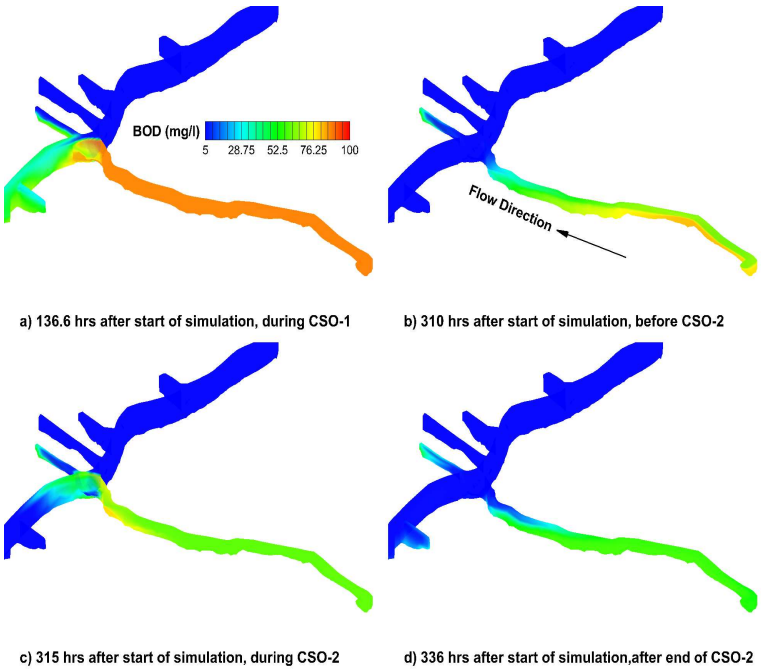

Figure 5.67: BOD concentration 5.3, 5.69, 12.91 and 13.12 days after start of simulation in Bubbly Creek

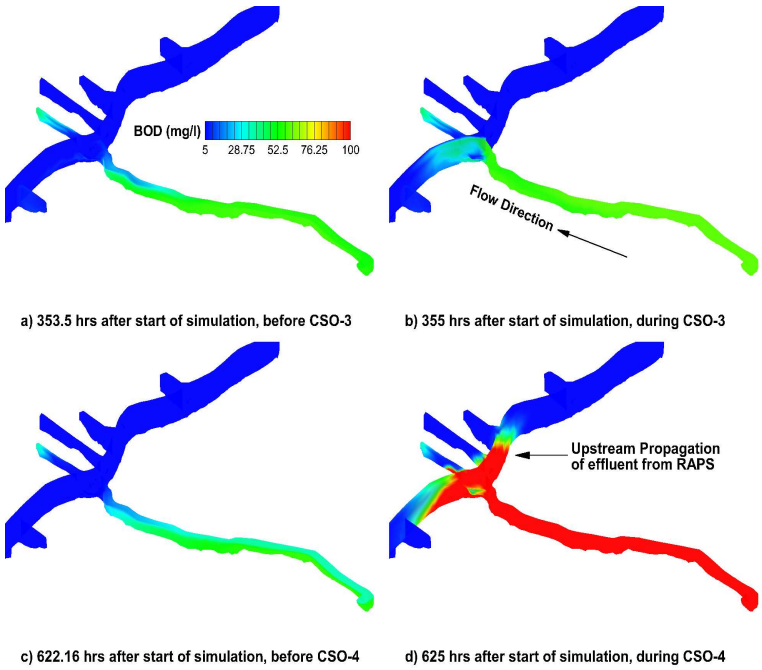

Figure 5.68: BOD concentration 14.73, 14.79, 25.92 and 26.04 days after start of simulation in Bubbly Creek

propagation of effluent from RAPS as shown in Figure 5.68(d). Although the flow in CAWS is from north to south, there can be scenarios in which both flow and dissolved constituents can traverse in opposite direction.

The other water quality monitoring stations as shown in Figure 5.60 are located near Kinzie Avenue on North Branch and Loomis Street on South Branch. The variation of DO for the month of May-2009 at Loomis street and Kinizie Avenue is presented in Figures 5.69 and 5.70. The DO-BOD model developed captures the trend in DO variation at Loomis Street is a very nice manner. As regards to Kinzie Avenue although there is a discrepancy betweeen the simulated and observed DO, the broad trend of DO variation is also captured by the model. The discrepancy between the observed and predicated DO at Kinzie Avenue can be partly attributed due to the influence of NWSRP which is located upstream of this location. As mentioned before, inputs for the DO-BOD model presented here were based on the monthly average effluent concentration values of DO, BOD and SS from NSWRP as well as other WWTPs. Using higher resolution effluent data for the water quality state variables might do a better job of capturing the DO trend at Kinzie Avenue.

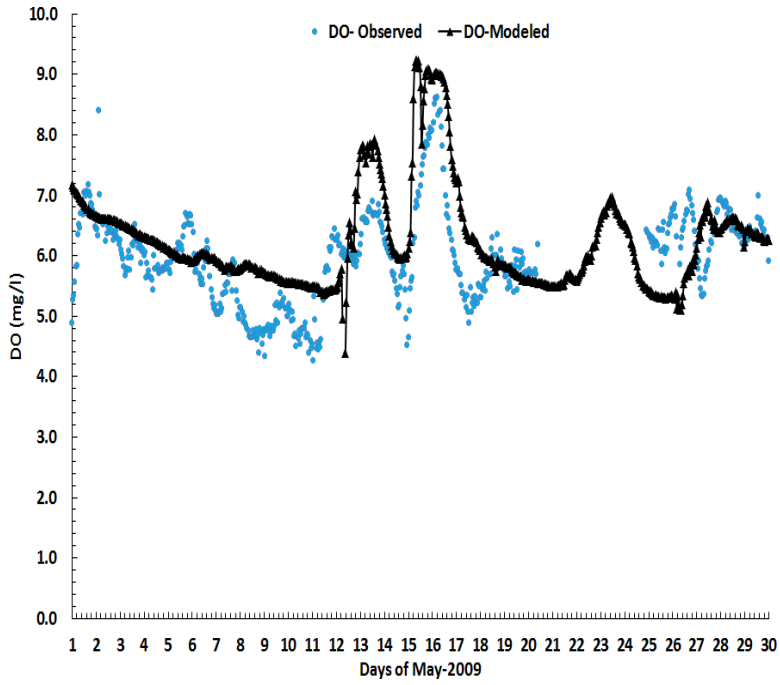

Figure 5.69: DO variation at Loomis street

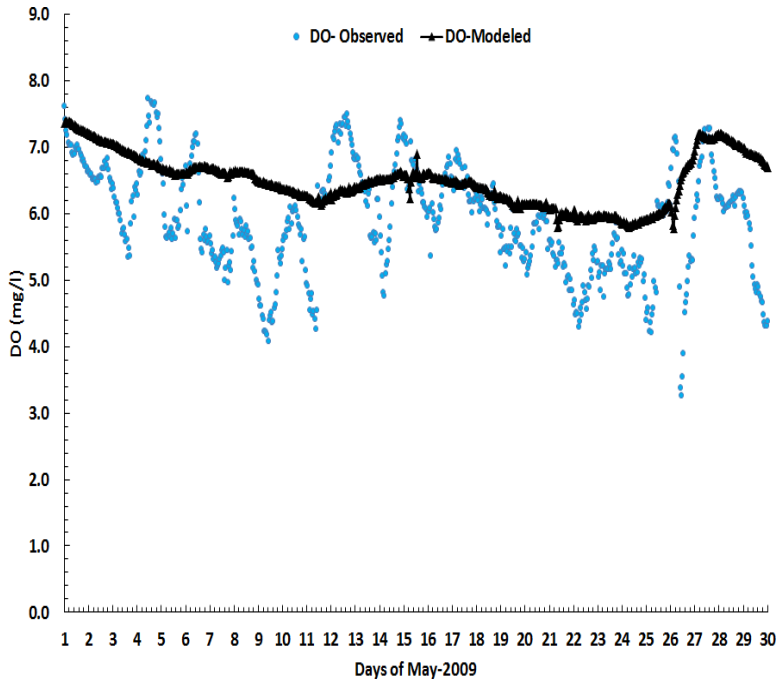

Figure 5.70: DO variation at Kinzie Avenue

As mentioned previously that after every CSO event a sharp and a sudden dip in DO levels in Bubbly Creek is observed at I-55 and 36th street, similar plots are made for Loomis Street and Kinzie Avenue.

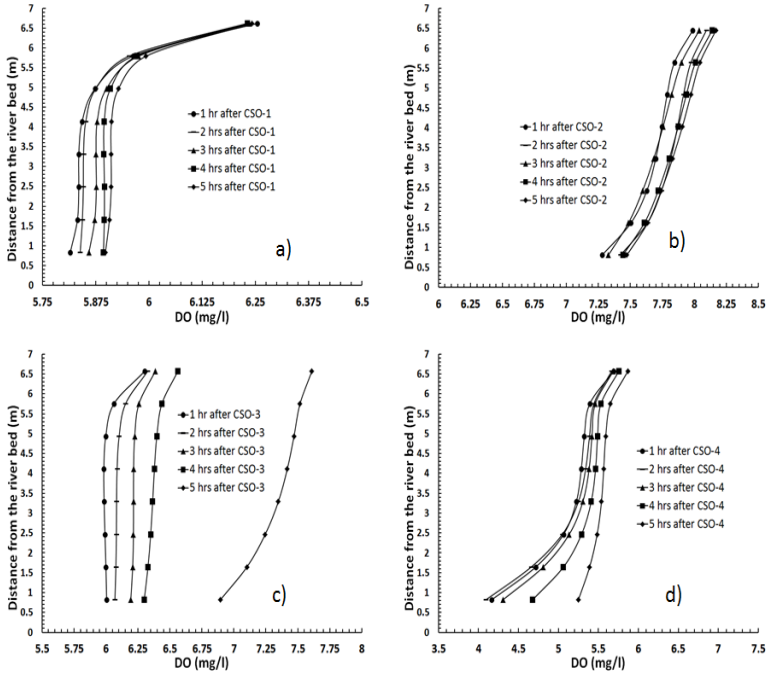

Figure 5.71: DO variation along water column at Loomis Street

As it can be observed in Figures 5.71 and 5.71 the depletion of DO near the bed is greater than the surface, the magnitude of the DO depletion both near the bed and the surface is not as high as in the case of Bubbly Creek. It must also be kept in mind that both at Loomis Avenue and Kinzie Avenue the water depth is significantly greater than that at Bubbly Creek; this implies that the effluent BOD coming from RAPS has more volume to get diluted and its effect on DO depletion is also decreased.

Finally the DO contour plots for the areas near Goose island on Chicago River North Branch and Chicago River Main Branch is presented in the following figures.

As shown in Figures 5.73, 5.74, 5.75 and 5.76 the minimum value of DO in other areas of CAWS usually doesn't go below 6.25 mg/l. A sudden increase in DO levels in the segments other than Bubbly Creek is usually associated and contingent upon the DO concentration of effluent from the four WWTPs. Also worth mentioning is that during summer months MWRDGC implements what is commonly known as discretionary-diversion and takes

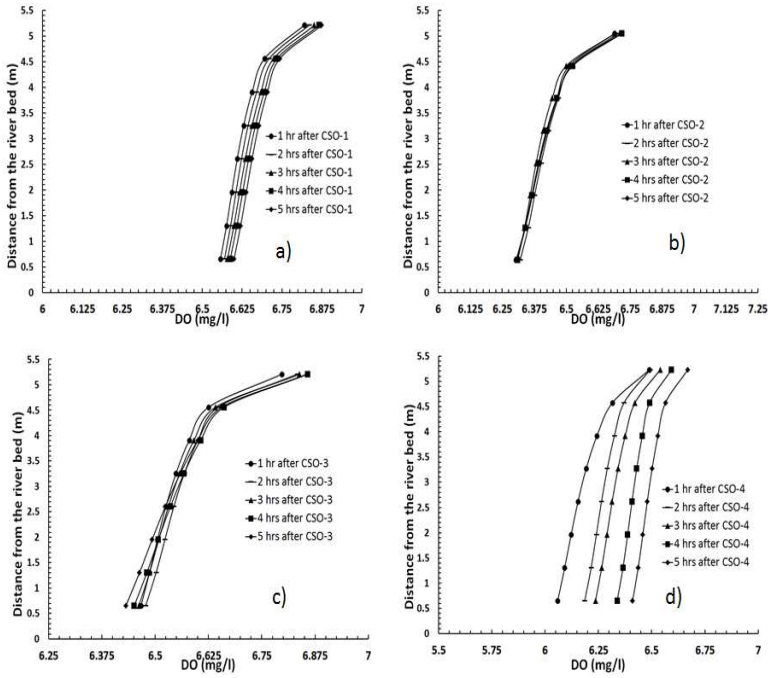

Figure 5.72: DO variation along water column at Kinzie Avenue

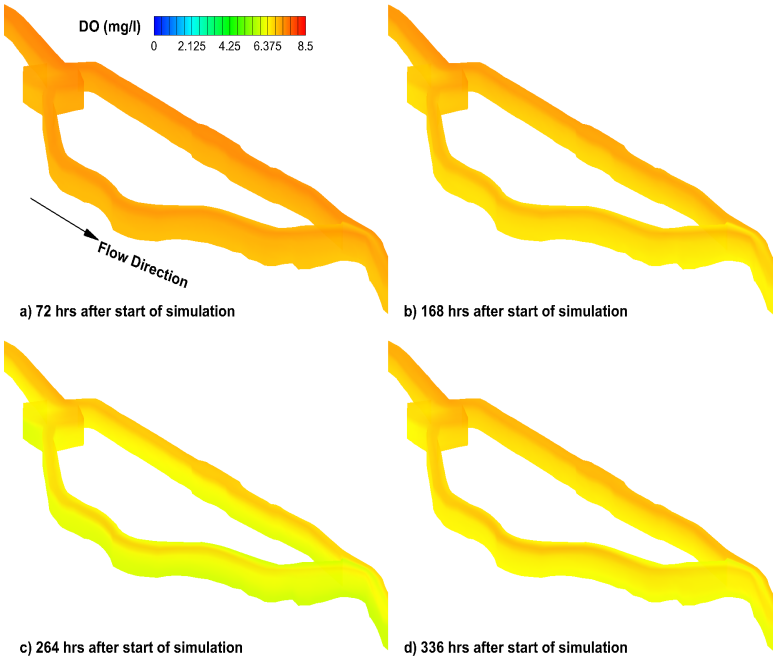

Figure 5.73: DO concentration a) 3^{rd}, b) 7^{th} c) 11^{th} and d) 14^{th} day after start of the simulation near Goose Island

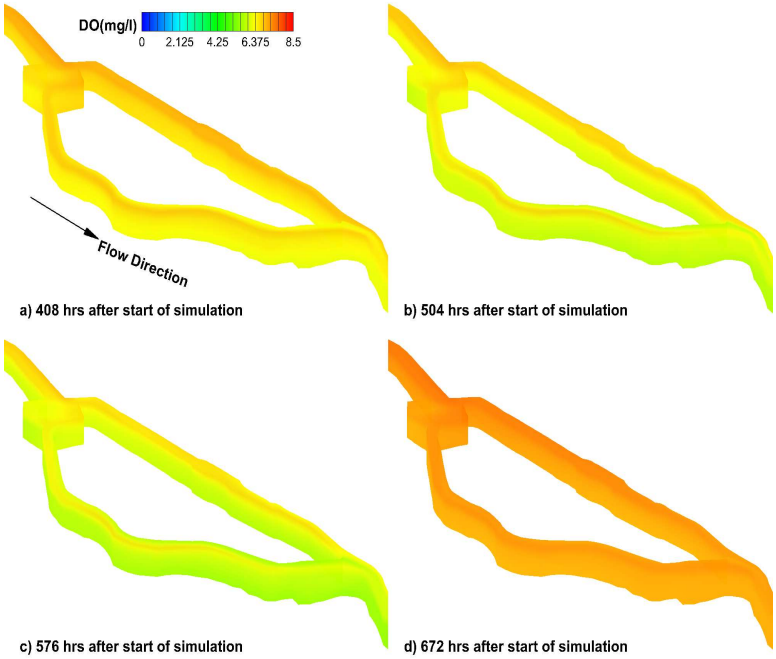

Figure 5.74: DO concentration a) 17^{th}, b) 21^{st} c) 24^{th} and d) 28^{th} day after start of the simulation near Goose Island

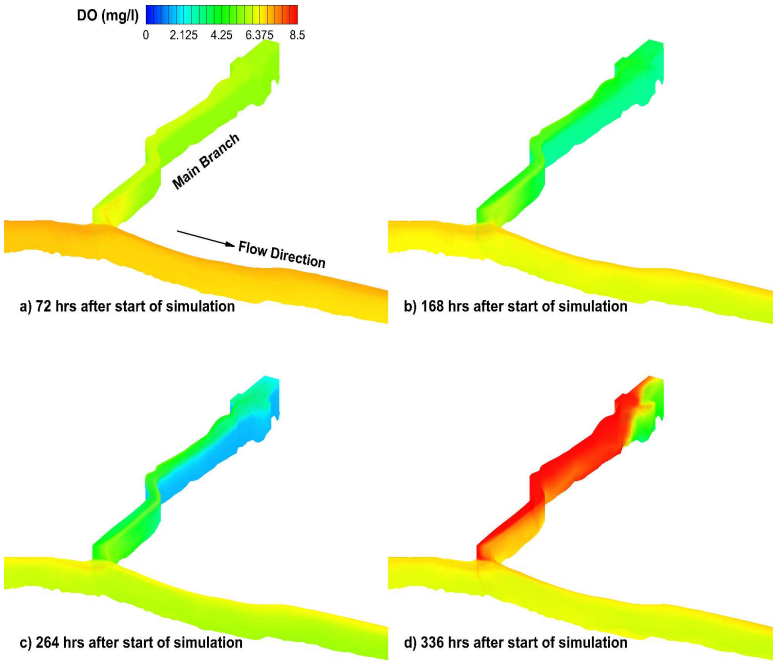

Figure 5.75: DO concentration a) 3^{rd}, b) 7^{th} c) 11^{th} and d) 14^{th} day after start of the simulation in Main Branch Chicago River

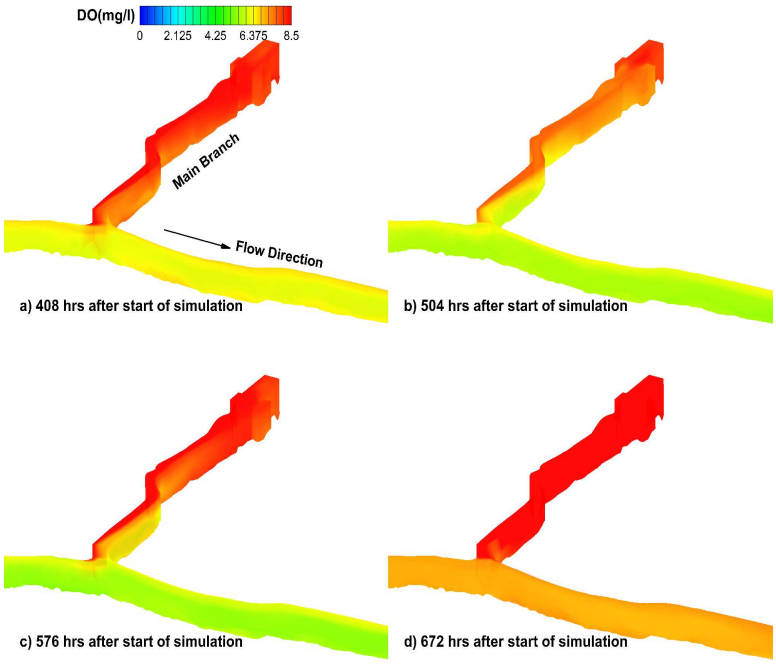

Figure 5.76: DO concentration a) 17^{th}, b) 21^{st} c) 24^{th} and d) 28^{th} day after start of the simulation in Main Branch Chicago River

water from the Lake Michigan, which is usually having higher DO content, to improvise the water quality condition of the Chicago River Main Branch.

5.6 Conclusion

In this chapter application and validation of a three dimensional hydrodynamic model for various portion of CAWS is presented. A storm event which led to an intense CSO event in September of 2008 has been modeled and several other application has been also presented. The model has been validated based on the stage elevation data from USGS gauging station on the main branch of the Chicago River near Columbus drive on the Main Branch [Station No. 05536123]. Although it would be ideal to get more data sets for the validation purposes, it is not always possible to get a lot of data in the real world, especially during wet weather conditions. Also as a part of this modeling exercise we have shown that any contaminants coming from RAPS during a CSO event can move upstream through the South Branch and may find their way up into the Main Branch of the Chicago River and into Lake Michigan. It is estimated that during the storm modeled (September 2008) herein, several billion gallons of water were discharged into Lake Michigan through the CRCW alone to prevent flooding. The flow pattern during a wet weather event can be exactly opposite to its nature during the dry weather conditions. Also during the wet weather condition upstream intrusion of contaminants coming from RAPS has been observed . As shown with a passive scalar in the modeling result presented herein, the passive scalar coming from RAPS has the potential to end up in Main Branch of the Chicago River during extreme wet weather conditions. Bubbly Creek is one of the most impaired segments of Chicago River in terms of water quality (Motta et al., 2010) (Waterman et al., 2011) the water quality conditions in the creek are further exacerbated by frequent CSO events from RAPS. Extensive 1D water quality model for the same system has been carried out, the reader may refer citeAP06. But as shown in the work presented herein the flow features in the CWS can be completely three-dimensional in nature during wet weather conditions which would have a significant consequence on various water quality state variables. Also in both 1D (Alp and Melching, 2006) and 2D (Motta et al., 2010) modeling of the system, there are certain assumptions made while simplifying the equations of motion that might not be true under wet weather conditions. For example in 2D water quality models (Motta et al., 2010) sink terms like Sediment Oxygen Demand (SOD) act on the whole water column as the model is based on depth-averaged equations. But from

three-dimensional modeling point of view it would be plausible and more realistic to let this sink term act only on the bottom most control volumes near the bed and let the dissolved oxygen diffuse through the water column. Finally the calibrated and validated hydro-environmental model for CAWS can be an immensely helpful tool in the upkeep of CAWS

CHAPTER 6

DEVELOPING INDEX-VELOCITY RATING CURVE FOR THE CHICAGO RIVER: INSIGHTS FROM MULTIDIMENSIONAL NUMERICAL MODELS

6.1 Introduction

The conventional method for measuring flow-discharge at a gauging-station in riverine-environment relies on the usage of stage-discharge rating curve. This process exclusively depends on continuous measurements of stage at the given section, which is subsequently converted into discharge values with the help of an estimated stage-discharge relationship. In situations where the gauging station is not affected by the flow-unsteadiness it is quite easy to derive bankable single-valued rating curve. This can be achieved by applying graphical methods Mander (1978); Fenton and Keller (2001) or conventional regression methods Moyeed and Clarke (2005); Asgeir (2006). However, if a variable backwater and unsteady flow exist at a gauging station single-valued stage-discharge rating curve becomes inaccurate. It is a well-known fact that under the usual subcritical flow condition in a riverine environment the stage at a given section is influenced by the downstream control. Due to the flow unsteadiness the conventional stage-discharge rating curve exhibits a loop. As explained by Fread (1975) this loop is the manifestation of the fact that the discharge at a given section, under the unsteady flow conditions, is not only the function of stage but also of the energy slope. A typical unsteady flow pattern in a river system is associated with the propagation of flood wave. Mander (1978) explained that when a flood wave passes down the river channel through a given cross-section, the effect of the wave front when upstream of the cross-section is to increase the approach velocity at the cross-section. As the flood peak passes downstream of the cross-section, the rear of the wave enhances the backwater affect at the cross-section and hence reduces the velocity at the cross-section. The consequence of the flood-peak passage through the section is such that for the same stage, the discharge is higher

during the rising stage than the falling stage. This phenomenon eventually results in hysteretic effect in stage-discharge rating curve. Simply put due to this hysteretic effect one can get obtain multiple values of discharge for the same stage in the river, depending on if the considered stage is associated with the rising limb or the falling limb of the passing flood wave.

To combat the problem of hysteresis in the stage-discharge curve, a family of rating methods that use the velocity measured for the subsection of the flow area (index velocity) as a second parameter to estimate discharge is rapidly becoming popular. This technique is commonly known as the, Index-velocity method Simpson and Rodger (1999),Morlock et al. (2001). The index velocity method incorporates the velocity data into the discharge calculation. In this method a relationship between the index velocity and cross-section mean velocity is developed. Index-velocity ratings are obtained by measuring the velocity at a subsection of the flow cross-section (V_{index}) and the water level. This index-velocity is then related with the mean velocity in the cross-section through an empirical relationship. The mean-velocities across the cross-section are usually obtained by boat-mounted, Acoustic Doppler Current Profiler (ADCP) campaigns. After having established an empirical relationship between the mean velocity (V_{mean}) and index velocity, this along with a relation between the stage and cross-section area finally felicitates the computation of discharge through the cross-section under consideration. It must be stated that the Index-Velocity ratings require a stage-area rating curve to transform the measured stage with respect to a pre-defined datum into the cross-sectional flow area. This index-velocity method for the measurement of discharge has gained considerable popularity in recent times as a viable alternative for the computation of single-valued discharge through a given cross-section in a riverine environment.

Chicago Area Waterway System (CAWS) forms a vital link between two major water systems namely the Mississippi River basin and the Great Lakes, please see Figure 6.1. As documented in Jackson et al. (2012) the State of Illinois' annual withdrawal from Lake Michigan is limited by a U.S. Supreme Court decree, and the U.S. Geological Survey (USGS) is responsible for monitoring flows in the Chicago Sanitary and Ship Canal (CSSC) near Lemont, Illinois as a part of the Lake Michigan Diversion Accounting overseen by the U.S. Army Corps of Engineers, Chicago District. One of the integral component of Lake Michigan Diversion Accounting is the USGS gaging sta-

tion on the CSSC near Lemont, Illinois. As the quantification of withdrawal from Lake Michigan happens at this gaging station, it has become one of the highly scrutinized gauging station in the country. Any changes in the stream gauging practices at this gauging station is preceded by detailed analysis to ensure that the any change made will not adversely affect the ability of USGS to monitor flows.

In this research work index-velocity plot at the USGS gauging station [USGS-05536890] is constructed with the help of numerical models TELEMAC-2D and TELEMAC-3D. The aforementioned gauging station is equipped with AVM (Acoustic Velocity Meter) and H-ADCP (Horizontal Acoustic Doppler Current Profiler). The AVM measures the velocity profile in the transverse direction at the given section at three different vertical elevations beneath the water-surface. The H-ADCP also profiles the current along the transverse direction at a fixed vertical elevation beneath the water-surface elevation. The success of index velocity plot lies in the ability to relate, through an empirical relation between velocity at a point or a section within the channel, V_{index}, to the mean velocity of the rated cross-section defined as $V_{mean} = Q_{measured}/A_{rated}$, where A_{rated} is the rated area of the cross-section defined by the stage-area rating curve and $Q_{measured}$ is the measured discharge. The discharge at the pertinent gauging station is measured by USGS with the help of boat mounted-ADCP (BM-ADCP). In this research work V_{index} is computed with the 3D model (TELEMAC-3D). The average velocities along the three AVM paths were computed with the help of TELEMAC-3D. The arithmetic mean the average AVM velocities at three distinct elevation from the bed of the river finally formed the V_{index} for the AVM. Similar procedure was repeated for H-ADCP. As regards to V_{mean}, corresponding to the values taken by boat mounted ADCP, it is computed with the help of a depth-averaged model (TELEMAC-2D). Both 2D and 3D model were first validated with the help of real-time observed data for a given set of boundary conditions. A regression relationship between the AVM V_{index} and depth-averaged V_{mean} (obtained from TELEMAC-2D) is formulated. A similar formulation is also done for H-ADCP V_{index} and the numerically obtained V_{mean} values. The regression relationship thus obtained are compared with the similar relation ship based on the field data as reported in Jackson et al. (2012). Finally the impact of the changing upstream inflow boundary conditions are examined on the index-velocity plot obtained numerically,

which helps in testing the veracity and credibility on the index-velocity relation ship obtained from one set of boundary conditions. As mentioned before for the computation of discharge index-velocity relationship also needs stage-area rating, this rating for Lemont gauging station is given by the following relationship.

$$A_{CSSCL} = 139.83 G_{CSSCL} + 670.39 \tag{6.1}$$

In the above equation A_{CSSCL} is the rated area for the CSSC near Lemont and G_{CSSCL} is the gage height at CSSC near Lemont.

6.2 Domain Description and Modelling Methodology

The construction of the Chicago Sanitary and Ship Canal (CSSC) in the late 1800s and the subsequent reversal of the Chicago River in 1900 is considered as one of the marvel of civil and hydraulic engineering. It was due to this reversal that allowed Chicago to overcome its issues with wastewater and flourish as a city. But with the construction and subsequent flow reversal came scrutiny of the withdrawals from Lake Michigan and a U.S. Supreme Court decree limiting Illinois diversion of Great Lakes water. The Supreme Court decree established the need for diversion accounting and continuous measurement of the discharge of water out of Lake Michigan through the CSSC. This continuous monitoring of the flow of the diversion accounting has made the USGS gauging station at Lemont (shown as 1 in Figure 6.1) one of the most scrutinized gaging station in the US.

Although the CSSC is akin to prismatic channel in shape the flow in CSSC is highly unsteady and can be very three-dimensional in nature. The primary source of unsteadiness appears to be the controlling structures located at the end of the domain near Lockport, please see 6.1. Control changes and lockages at the downstream end of the flow at Lockport, Ill., cause changes in the stage and flow elsewhere on the system, and the disturbances propagate through the system in the form of flood waves and seiches, both of which can be identified in the discharge records near Lemont. Withdrawals and discharges from powerplants and industry on the canal and wastewater in-

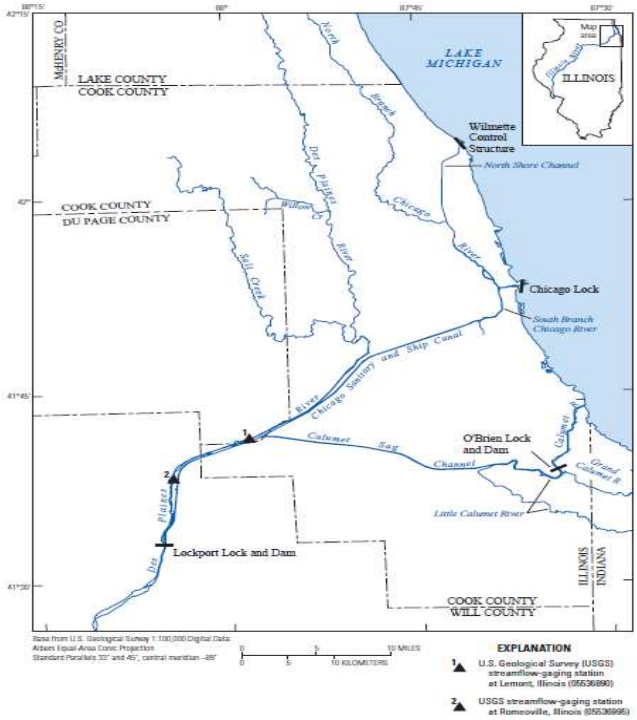

Figure 6.1: Chicago Area Waterway System

flows from three large water-reclamation plants further add variability to the flow. Storm-driven inflows from several tributaries on the Calumet Sag Channel and North Branch Chicago River and inflows from local runoff and combined-sewer overflows are yet other sources of flow variability, primarily during high flows. Localized and short-term flow variation near Lemont is caused by commercial water traffic, which can be heavy in the Lemont area. The various gates and lock structures located at the end of the domain near Lockport is shown in Figure

6.2.1 Shorter Domain

The computational domain for the three-dimensional modeling of CSSC extended from 7 kms upstream from the confluence of Calumet Sag Channel and CSSC along CSSC and Calumet Sag Channel. The downstream end of the domain was at Romeoville gaging station (Please see Figure 6.1). The downstream end of the domain was fixed at Romeoville (Figure 6.1) as the real time variation of the free surface was available at this location for the storm simulated. The area around the gaging station at Lemont is equipped

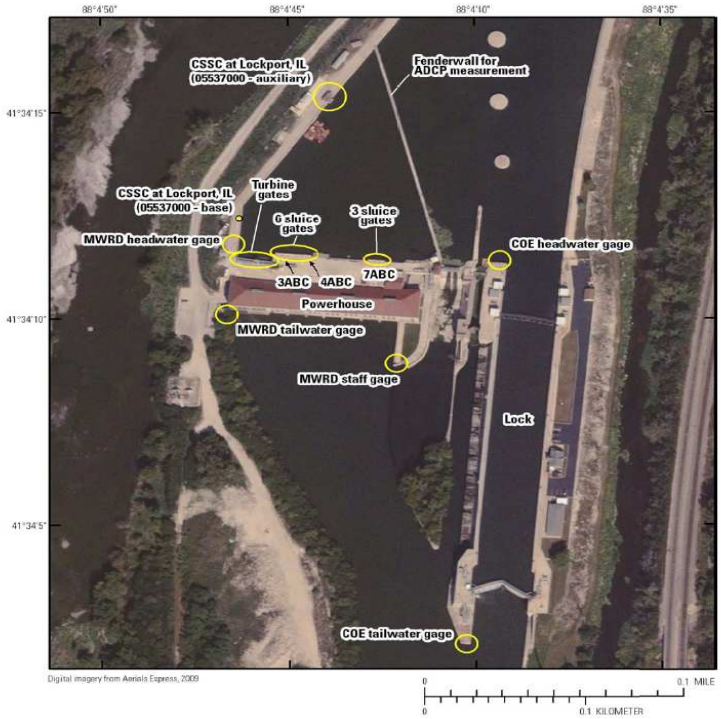

Figure 6.2: Lockport power house at the southern end of the domain

with AVM as well as H-ADCP. The location of these instruments and the transverse line along which they measure flow velocities are shown in Figure 6.3.

Also shown in Figures 6.4(a) and 6.4(b) are the vertical elevations along which the velocity values are extracted from the numerical model simulation.

6.2.2 Extended Domain

As explained before one of the most crucial factor affecting the flow structure in CAWS near Lemont and elsewhere are the controlling works at the downstream end of the domain at Lockport (please see Figure 6.2). In order to incorporate these structures in the numerical simulation and examine their impact on the flow structure the computational domain was extended to Lockport in an another set of simulation. Extending the domain all the way to Lockport was also helpful in the better validation of the model as now there were two calibration points inside the domain i.e. at Lemont and Romeoville. As the flow in CAWS is always subcritical the downstream boundary condition for setting up the numerical model is of utmost im-

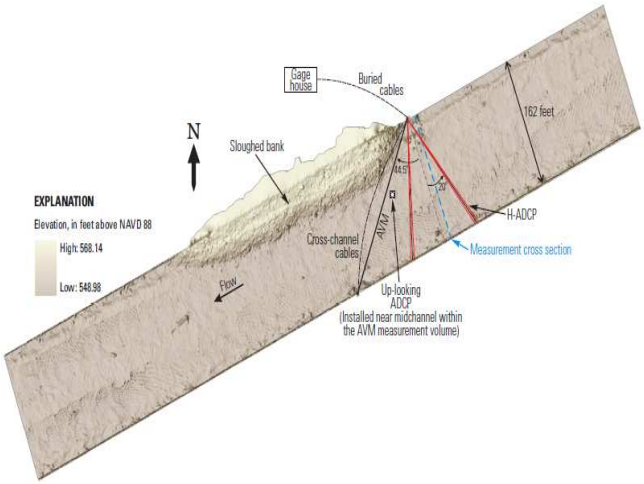

Figure 6.3: AVM and H-ADCP path near Lemont looking from top, adapted from Jackson et al. (2012)

portance. In the case of the extended domain considered here setting up the downstream boundary condition at Lockport is a very challenging task as the water surface elevation at Lockport is not always readily available. Keifer (1994), extended the pioneering work done by Tholin and Keifer (1959) for the flow routing algorithms developed for the overland and surface flow for the city of Chicago. Keifer (1994) came up with the mathematical expression for the lowering of water stage at Lockport in an event of the approaching storm. This relationship is given as follows.

$$Elv_{15} = Elv_0 + 0.45 * \left(54 - 2 * SJ - \frac{Q_L}{24000} - 0.893 - Elv_0\right) \qquad (6.2)$$

In the equation 6.2 Elv_{15} is the new stage elevation to which the Lokport levels should be decreased in next 15 minutes, Elv_0 is the initial water surface elevation at the Lockport controlling structures, SJ is the elevation at the Cal-Sag junction and Q_L is the flow through the Lockport gates and turbines. For the details of the algorithm behind the development of the equation 6.2,

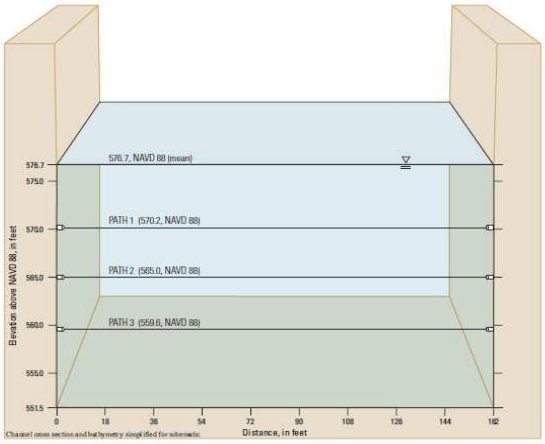

(a) Vertical elevation corresponding to AVM levels

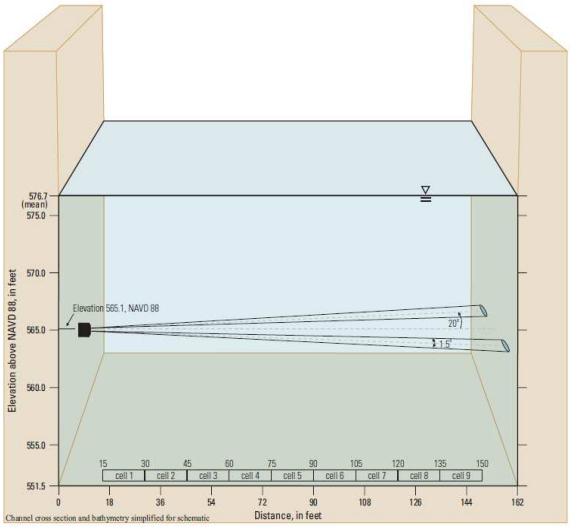

(b) Vertical elevation corresponding to H-ADCP level

Figure 6.4: Elevations from AVM and H-ADCP, adapted from Jackson et al. (2012)

please refer Keifer (1994). Although the equation 6.2 presents a good rule for the draw-down operation at the Lockport side, from the numerical modeling point of we still need the information about the stage variation at Cal-Sag junction which is again not so easily available.

6.3 Numerical Models Used

TELEMAC suite of models have been in continuous development since 1987 when the Telemac projct was launched by Research and Development department of Electricite de France (EDF). TELEMAC models are based on finite-element methodology and offers the ability to work with unstructured mesh. As explained before the numerical simulation presented in this chapter utilized both TELEMAC-2D and TELEMAC-3D models. Although the governing equations solved by TELEMAC-2D was presented in Chapter-3, for the sake of continuation and better readability they are presented here again. TELEMAC-2D model is based on the the finite element solution of two dimension Shallow Water Equations (SWE) presented here. Equations 6.3a to 6.3c denotes continuity, and momentum equations in x and y direction respectively.

$$\frac{\partial h}{\partial t} + \overrightarrow{u}\overrightarrow{\nabla}h + h\overrightarrow{\nabla}.\overrightarrow{u} = S_h \tag{6.3a}$$

$$\frac{\partial u}{\partial t} + \overrightarrow{u}.\overrightarrow{\nabla}\left(u\right) = -g\frac{\partial Z}{\partial x} + S_x + \frac{1}{h}\overrightarrow{\nabla}.\left(h\nu_t\overrightarrow{\nabla}u\right) \tag{6.3b}$$

$$\frac{\partial v}{\partial t} + \overrightarrow{u}.\overrightarrow{\nabla}\left(v\right) = -g\frac{\partial Z}{\partial y} + S_y + \frac{1}{h}\overrightarrow{\nabla}.\left(h\nu_t\overrightarrow{\nabla}v\right) \tag{6.3c}$$

In equations 6.3a to 6.3c h is the depth of the water (m), t is time (s), u and v the velocity components x and y direction respectively (m/s) and S_h is the source or sink of fluid. The numerical solution of these equations are obtained by adopting the fractional-step method. In the first step the advective part of the governing equations are solved by the method of characteristics. Due to the hyperbolic nature of the advection equation method of characteristics is a suitable choice. The variables solved for are depth-averaged velocity components (U and V) and water depth (h), also if $\kappa - \epsilon$ model is used for the eddy viscosity computation, they are also advected with the method of characteristics. In the second step the solution from the first step is used as the initial values for the hydrodynamic variables. In this step rest of terms

i.e. diffusion, source terms and propagation is considered. These terms are resolved with the help of finite-element methodology. Variational formulation and dicretization in space and time then transform continuous equations into discrete linear system whose unknown are the values of physical quantities, u, v and h at the nodes of the computational mesh. The linear system thus obtained is then resolved by an iterative method of the conjugate gradient type.

As regards to TELEMAC-3D , it has the capability of solving both hydrostatic and non-hydrostatic version of Navier-Stokes equation. The hydrostatic version of TELEMAC-3D, wherein the pressure along the water column is assumed hydrostatic, is also commonly know as three dimensional SWE. TELEMAC-3D solves the three-dimensional hydrodynamic equation with the following assumption.

- Model solves three-dimensional Navier-Stokes equations with a free surface changing in time
- Variation of density in the conservation of mass equation is ignored, hence its a case of incompressible flow
- Pressure is assumed to be hydrostatic along the water column, which implies that the pressure at any given depth is the sum of the air pressure at the fluid surface plus the weight of the overlying water body
- Boussinesq approximation for the momentum is assumed, which implied that the density variation is only considered in the gravity term

Based on aforementioned assumptions the equations solved by TELEMAC-3D are as follows.

$$\frac{\partial U}{\partial x} + \frac{\partial V}{\partial y} + \frac{\partial W}{\partial z} = 0 \tag{6.4a}$$

$$\frac{\partial U}{\partial t} + U\frac{\partial U}{\partial x} + V\frac{\partial U}{\partial y} + W\frac{\partial U}{\partial z} = -g\frac{\partial Z_s}{\partial x} + \nu\Delta\left(U\right) + F_x \tag{6.4b}$$

$$\frac{\partial V}{\partial t} + U\frac{\partial V}{\partial x} + V\frac{\partial V}{\partial y} + W\frac{\partial V}{\partial z} = -g\frac{\partial Z_s}{\partial y} + \nu\Delta\left(V\right) + F_y \tag{6.4c}$$

$$p = p_{atm} + \rho_o g\left(Z - z\right) + \rho_o g\int_z^{Z_s}\frac{\Delta\rho}{\rho_o}dz \tag{6.4d}$$

Equations 6.4a, 6.4b, 6.4c and 6.4d denotes continuity, momentum in x and y direction and pressure variation along the water column. In the aforementioned equations h (m) is the water depth, S (m) is the free surface elevation, U, V and W denotes the velocity components in x, y and z direction, p is the pressure, g is the acceleration due to gravity, ν (m^2/s) is the velocity and tracer diffusion coefficients, Z_f (m) is the bottom depth, ρ_o is the reference density and $\Delta\rho$ is the variation in density, t (s) denotes time, x and y (m) are horizontal space components, z(m) is the vertical space component, F_x and finally F_y (m/s^2) denotes the source terms. The source terms denoted by F_x and F_y encompasses the wind, the Coriolis force and the bottom friction (or any other process being modeled by the similar formulation).

As in the case of TELEMAC-2D the basic algorithm behind TELEMAC-3D can also be split in three distinct computational steps. The first step entails solving only the advection terms in the momentum equations. These advected values of the velocity components are then used in the second step wherein the diffusion term and the source terms in the momentum equations are solved. After the first two steps we obtain an intermediate velocity field. The third and the final step involves computing the water depth from the vertical integration of the continuity equation and the momentum equations only including the pressure-continuity terms (all the other terms are already accounted for in earlier two steps). By solving and obtaining the water depth it becomes possible to compute for the elevations of the various mesh points and then those of the free surface. Finally in the concluding steps the computation of U and V velocity is simply achieved through combination of equation linking the velocities. Finally, the vertical velocity W is computed from the continuity equation.

6.4 Computational Grid and Boundary Conditions for the Simulated Storm

In this chapter the aforementioned numerical models are used to simulate a five day storm of July-2010. The simulated storm started at 12:00 am July 22nd, 2010 and ended on 12:00 am July 27th, 2010. As mentioned before after doing some elementary water balance calculations, number of inflow boundary conditions were tried. Four inflow discharge combinations that were simulated as a part of this research is presented in Figure 6.5.

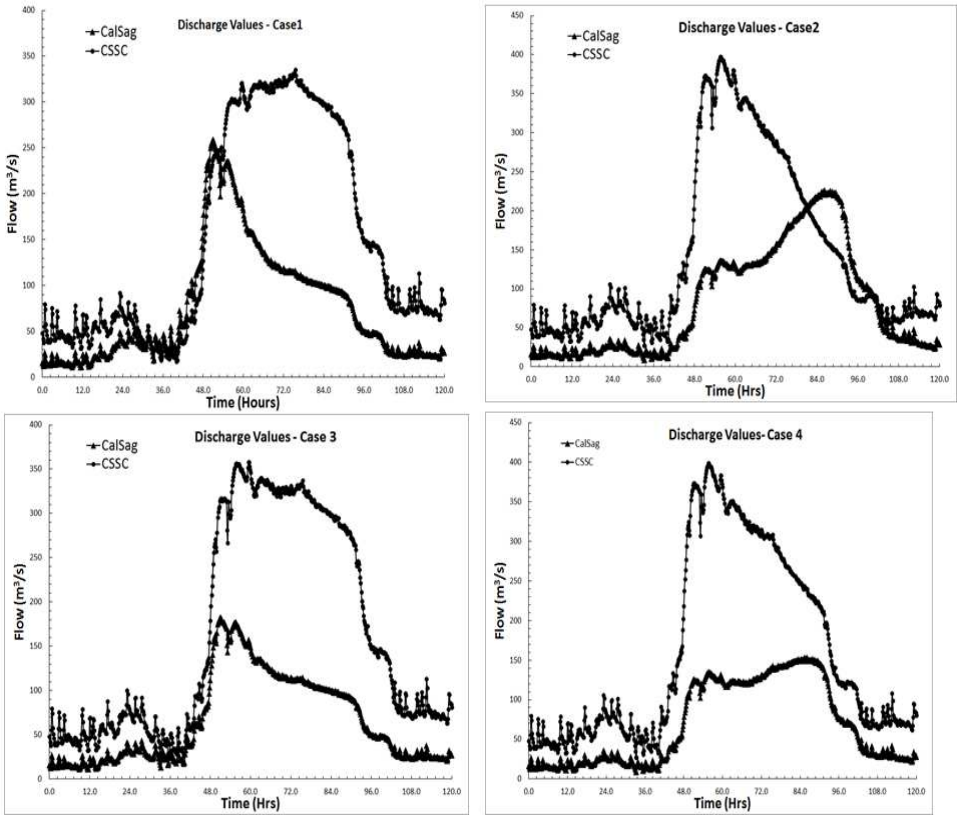

Figure 6.5: Combination of inflow conditions tried

The computational grid for both shorter and extended portion of the domain was constructed using freely downloadable mesh generator from Canadian Hydraulics Centre (CHC), Bluekenue. The mesh generated for the shorter portion of the domain along with the interface is presented in Figures 6.6(a) and 6.6(b). In order to capture the relevant flow physics at the confluence and at Lemont, where gaging station is located, the mesh resolution was kept at a value of 4 m. The computational mesh had 21000 nodes and

36000 elements. All the simulation conducted were ran on the hydrosystem cluster computer using 24 processors.

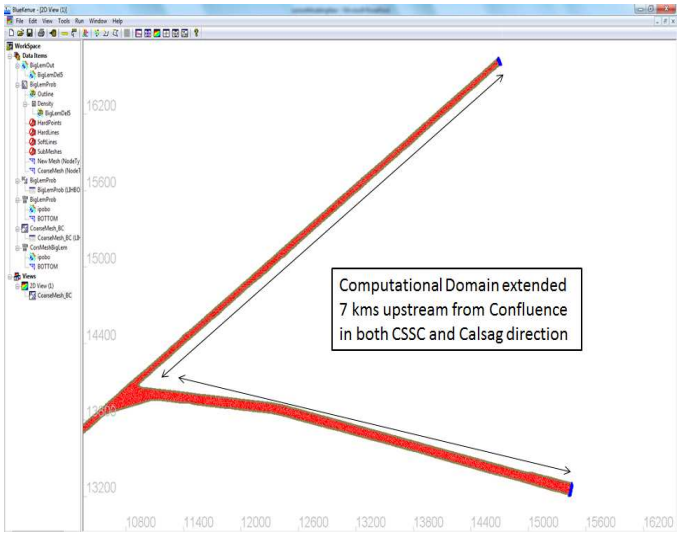

(a) Bluekenue software for mesh generation

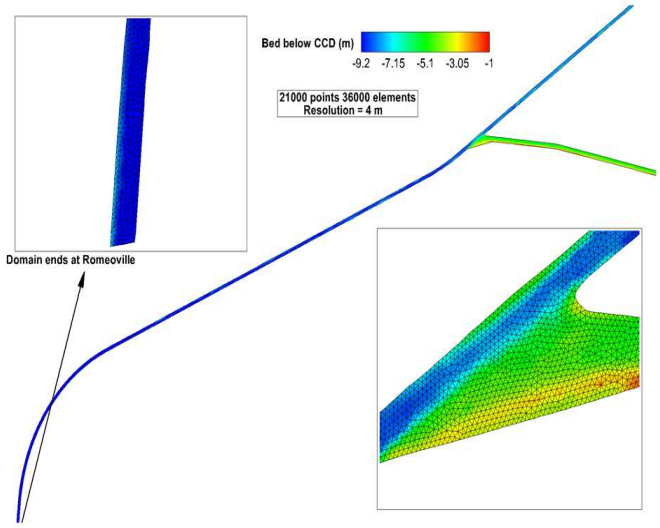

(b) Unstructured mesh for the shorter domain

Figure 6.6: Computational mesh generated through Bluekenue

As mentioned before the downstream boundary conditions was specified in form of time variation of stage elevation at Romeoville that came from USGS gaging station at Romeoville (please see Figure 6.1). The downstream boundary condition is presented in Figure 6.7. As far as the extended domain is concerned the same computational mesh was extended all the way till Lockport powerhouse and the same mesh generator Bluekenue was used. The same five day storm was simulated on the extended domain also. The

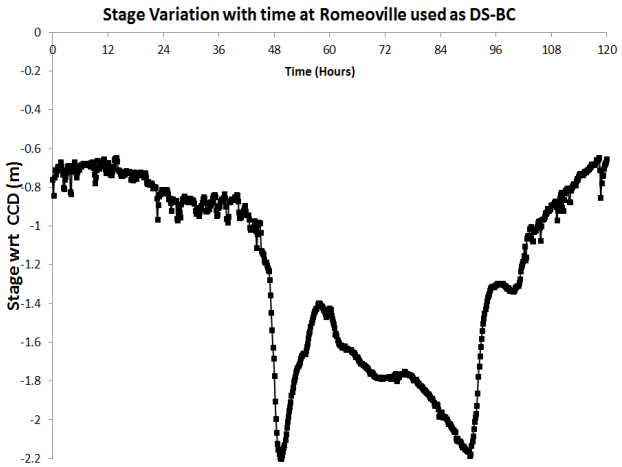

Figure 6.7: Stage variation at Romeoville for the period of simulated storm

mesh used for the extended domain is shown in Figure6.8. As far as the downstream boundary condition for the extended portion of the domain is concerned after doing some data analysis for the Romeoville stage and stage at Lockport it was decided to keep a differential of 35 cms between the stage at Romeoville and Lockport when the drawdown starts to occur. Incorporating this relationship, the downstream boundary condition at Lockport is shown in

6.5 Simulation Results and Discussion

6.5.1 Results from Simulation in the Shorter Domain

As explained both TELEMAC-2D and 3D were used for the simulated storm, the computational mesh for three-dimensional simulation was also constructed using Bluekenue. TELEMAC-3D as in many other surface flow model uses sigma grid in vertical. The three-dimensional mesh is obtained by stacking the constructed 2D mesh on top of one another in a layer wise manner. For the simulation presented here nine layers along the vertical direction was used. The three-dimensional mesh is shown in Figure 6.9.

For constructing the index velocity plot the, velocity information was extracted along the three-different AVM levels (Figure 6.4(a)) and H-ADCP levels (Figure 6.4(b)). Also along the boat-mounted ADCP path (please see

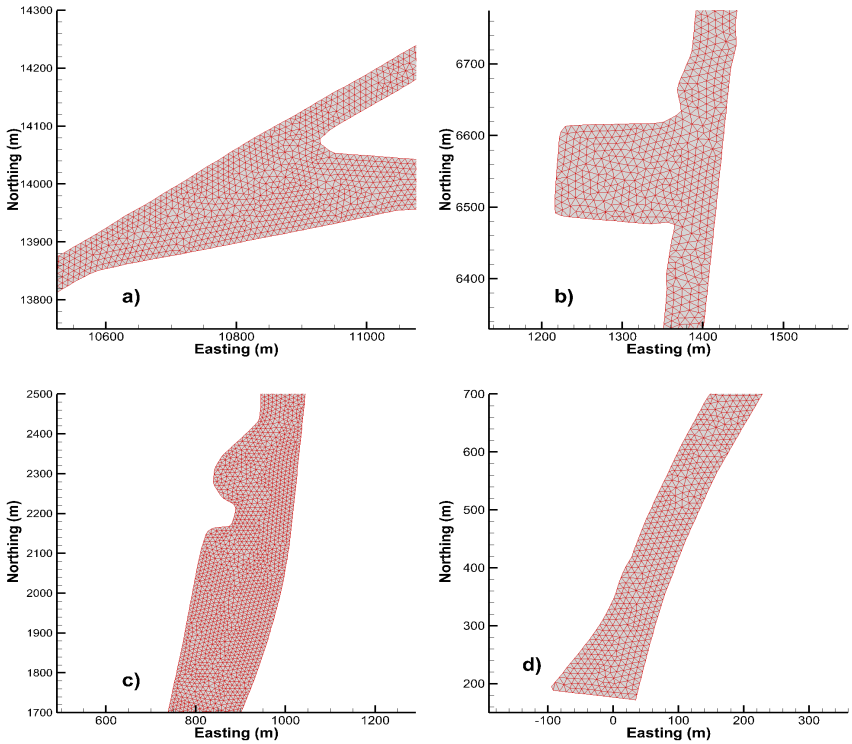

Figure 6.8: Computational mesh for the extended domain

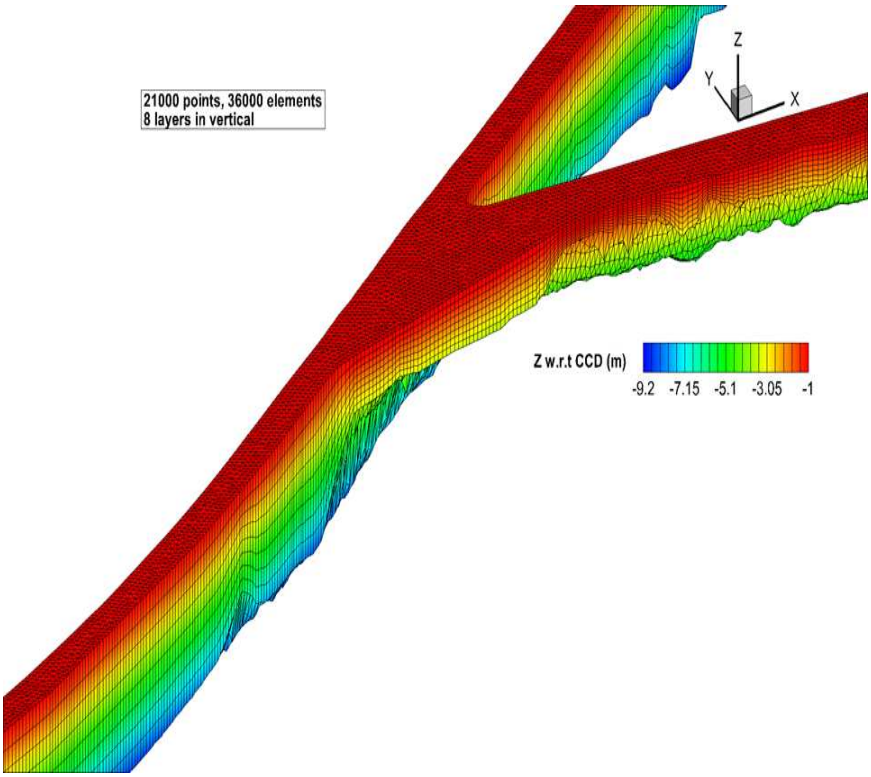

Figure 6.9: Computational mesh for the extended domain

Figure 6.3 the velocity values from TELEMAC-2D simulation were extracted. The depth-averaged velocity at different points in time during the simulated storm is presented in a series of plots here. Based on the various simulations conducted it was observed that the flow velocity near Lemont is guided by the two complementary factors namely the upstream inflow and the downstream stage elevation. At 9 hours after the start of the simulation the velocity near Lemont (Figure 6.10(a)) is around 0.22 m/s, this can be explained by the fact that inflow hydrograph from CSSC and Cal-Sag are at its lower value at this point in time. Also the downstream stage around 9 hrs after the start of the simulation (see Figure 6.7) is not significantly different from the initial stage elevation of -0.66 m with respect to Chicago City Datum (CCD). As the simulation progresses around 50 hours after the start of the simulation the velocity near Lemont reaches as high as 1.2 m/s, at this point in time it can be seen that both the inflow from CSSC and Cal-Sag are climbing up the rising limb of the hydrograph. The inflow from CalSag and CSSC are respectively of the order of 250 m^3/s. As far as the downstream boundary condition is concerned notice that (Figure 6.7) the water surface elevation at 50 hours after the start of the simulation is distinctly low at around -2.1 m with respect to CCD. Such low stage elevation implies that drawdown at Loport has already started and it is because of the head difference we notice the increased flow velocity at Lemont.

Also shown in Figures 6.11(a) and 6.11(b) are the velocity magnitude at 72 and 84 hours after the start of the simulation. Notice that the velocity magnitude at Lemont at these hours are still between 1 and 1.2 m/s. This is again due to the fact that we are still on the rising limb of the incoming flow hydrograph. Also the stage elevation at the downstream side is still significantly lower than its normal level of -0.66 m.

As we reach closer to the the end of the simulated storm we can see the velocity magnitude in the computational domain drastically subsiding, as shown in Figure 6.12(a) and 6.12(b) the velocity magnitude in the domain at these times are in the neighbourhood of 0.2 m/s. Furthermore velocity information corresponding to the vertical levels of installed AVM were extracted from TELEMAC-3D simulation. The results from the 3D simulation are presented here in a series of plots.

It is clearly noticeable, as in case of two dimensional simulation, when the flow is not very dominant from upstream and the downstream stage

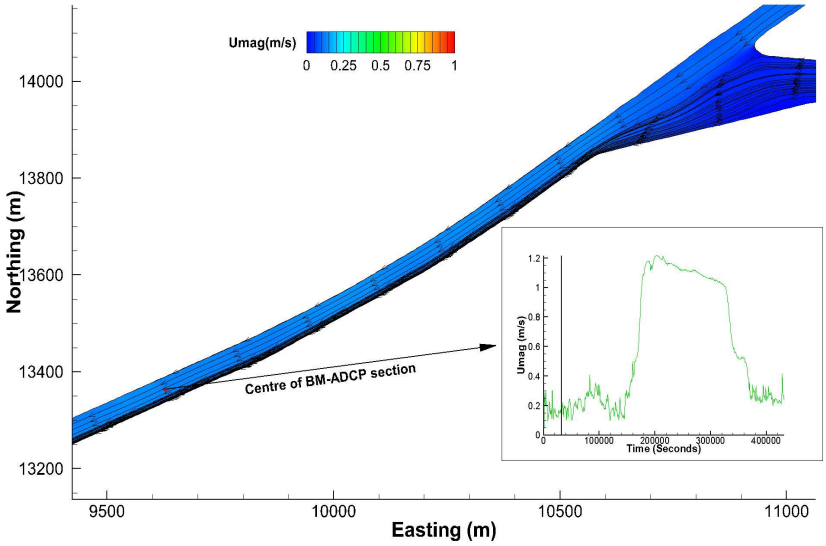

(a) Velocity plots 9 hrs after start of simulation

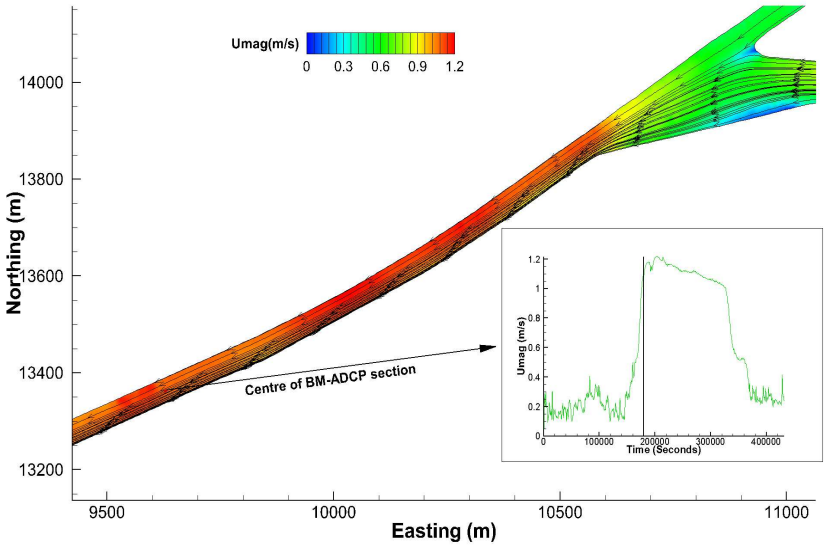

(b) Velocity plots 50 hrs after start of simulation

Figure 6.10: Depth averaged velocity plots from TELEMAC-2D after 9 and 50 hours start of the simulation

elevation is not very significant we can see that the velocity magnitude on all the AVM levels are in the area of 0.2 m/s (please see Figure 6.13). But as the simulation progresses in time and we start going through the rising limb of the inflow hydrograph, distinct increase in the velocity magnitude for all the AVM levels are noticed as shown in Figure 6.14. Also noticeable from the same figure is that the higher velocity corresponds to the AVM level-1 which

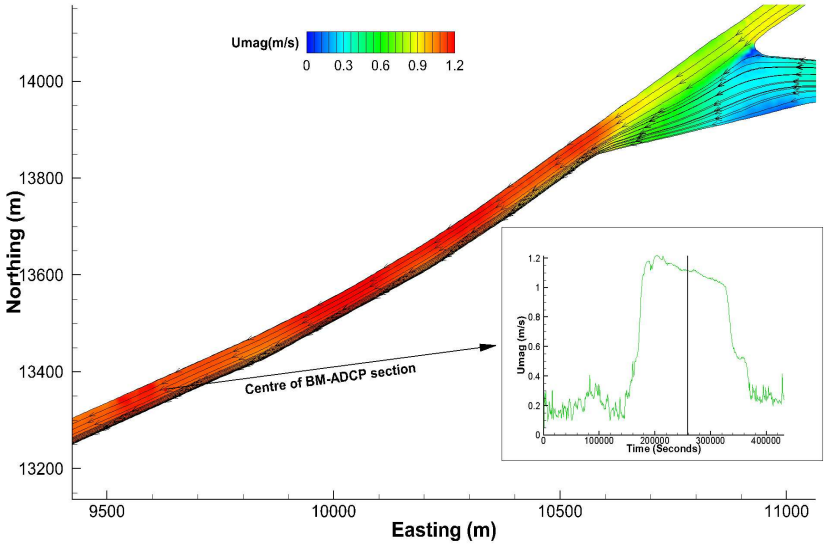

(a) Velocity plots 72 hrs after start of simulation

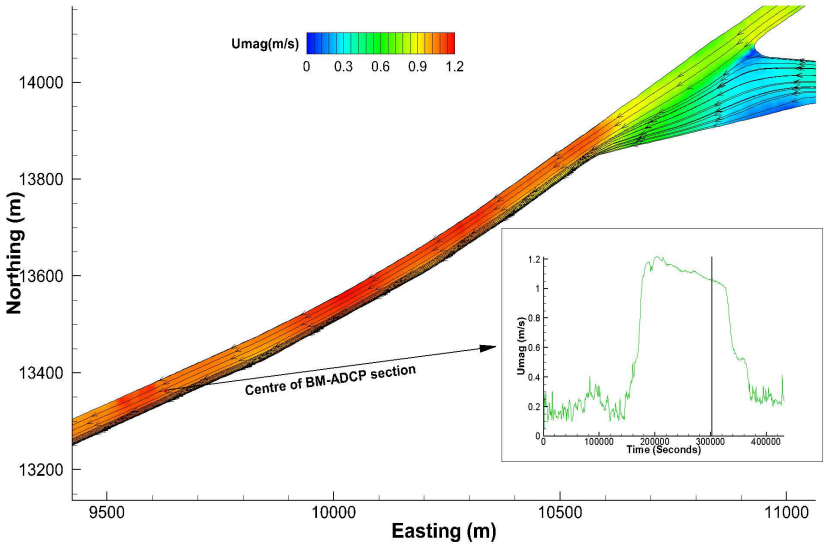

(b) Velocity plots 84 hrs after start of simulation

Figure 6.11: Depth averaged velocity plots from TELEMAC-2D after 72 and 84 hours start of the simulation

is closest to the free surface, this is in accordance with fundamental open channel theory where logarithmic velocity profile dictates higher velocities near the surface and reduced velocity near the bed as the flow feels enhanced bed friction near the bed. The same nature in the vertical variation of the velocity magnitude is noticed in plots presented here at other time steps.

As shown in Figures 6.15 and 6.16, it is at these times in the simulation

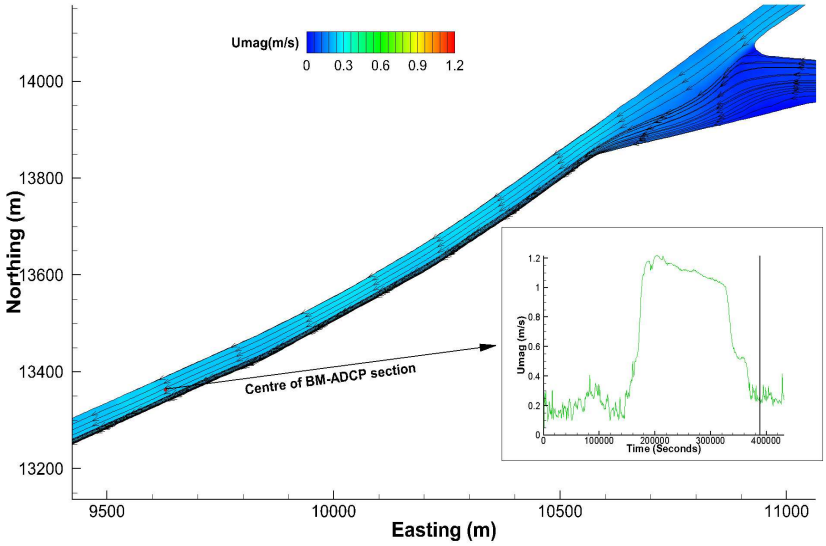

(a) Velocity plots 108 hrs after start of simulation

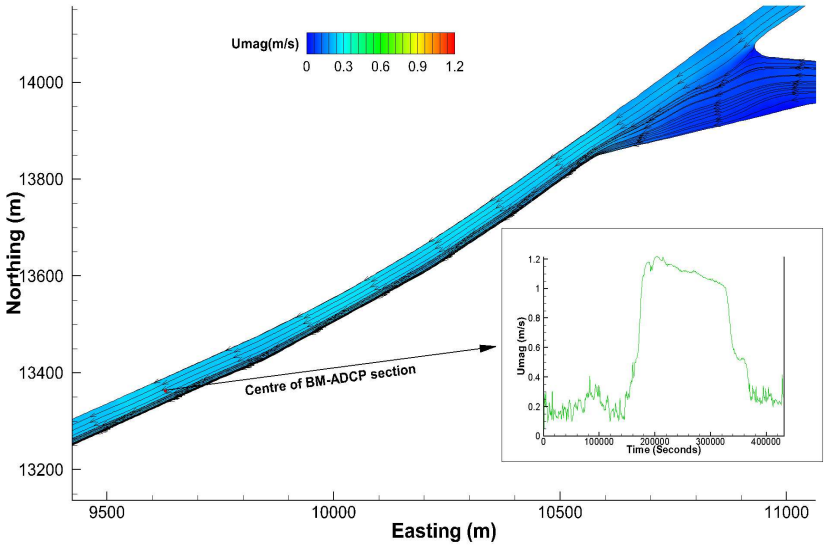

(b) Velocity plots 120 hrs after start of simulation

Figure 6.12: Depth averaged velocity plots from TELEMAC-2D after 108 and 120 hours start of the simulation

that the flow feels the peak of the incoming hydrograph and same is exhibited in the velocity plots at different AVM levels. Also as mentioned before the velocity magnitude corresponding to the AVM Level-1, nearest to the free surface is distinctly higher than the velocity magnitude at AVM leves that are vertically at the lower levels near the bed. Although due to the high flow coming from the upstream direction, combined with the draw-down which is

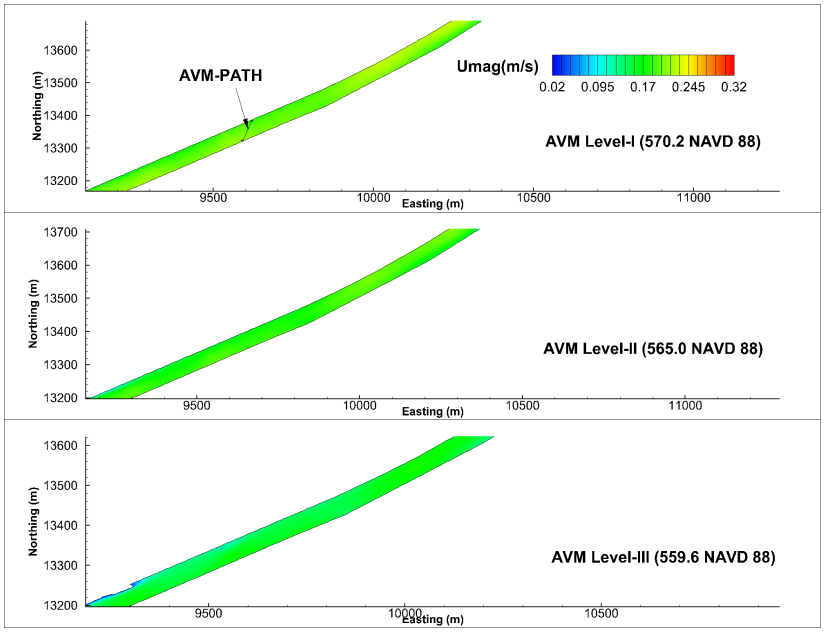

Figure 6.13: Results from TELEMAC-3D 12 hours after the start of the simulation

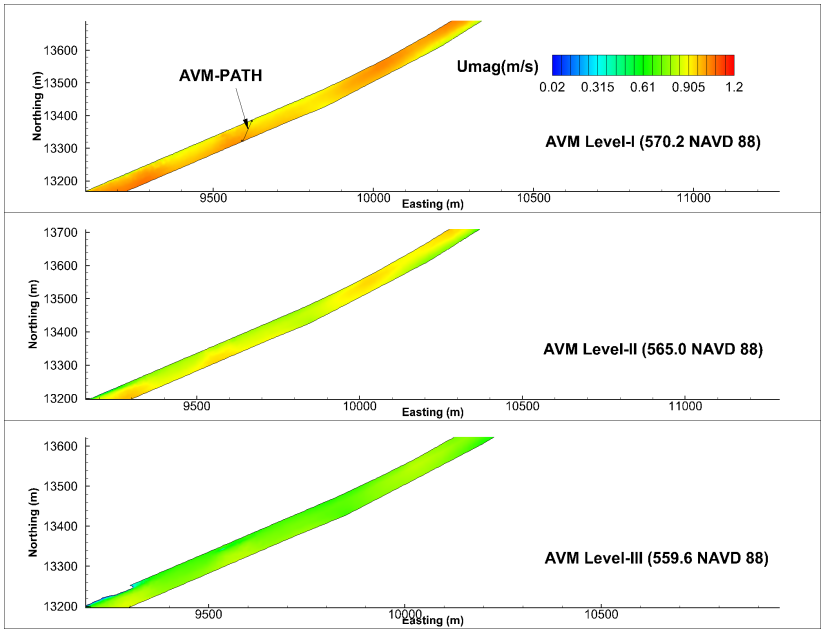

Figure 6.14: Results from TELEMAC-3D 48 hours after the start of the simulation

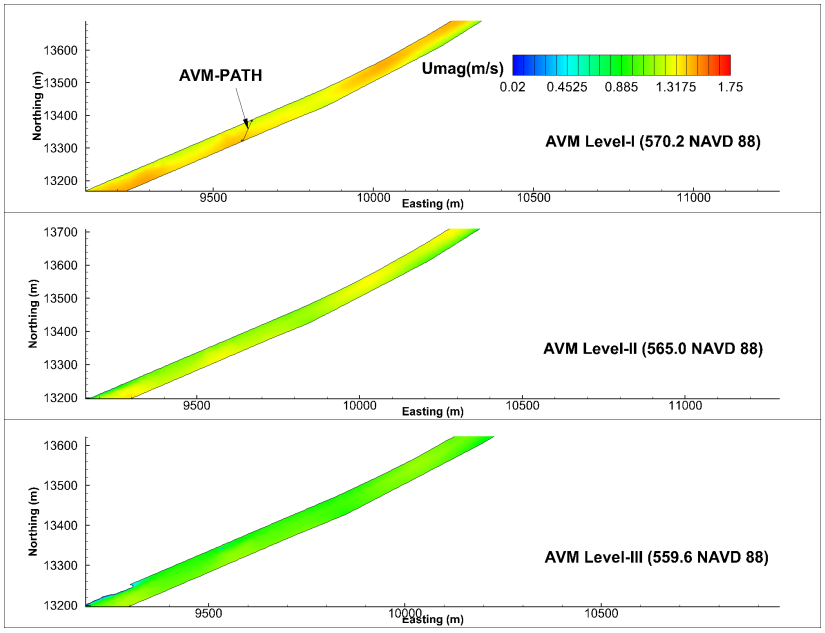

Figure 6.15: Results from TELEMAC-3D 72 hours after the start of the simulation

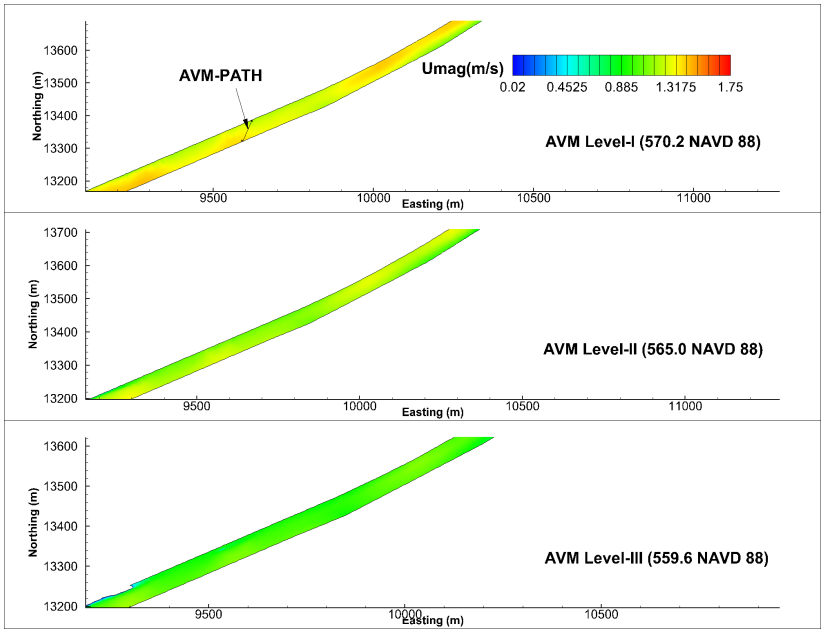

Figure 6.16: Results from TELEMAC-3D 84 hours after the start of the simulation

manifested as decreased stage elevation at Romeoville, results in distinctly higher velocities at all the AVM levels at these hours (please see Figures 6.15 and 6.14). Once again as we near towards the end of the simulation velocities in the whole domain reduces, this is shown in plots presented for 108 and 20 hours after the start of the simulation as shown in Figures 6.17 and 6.18.

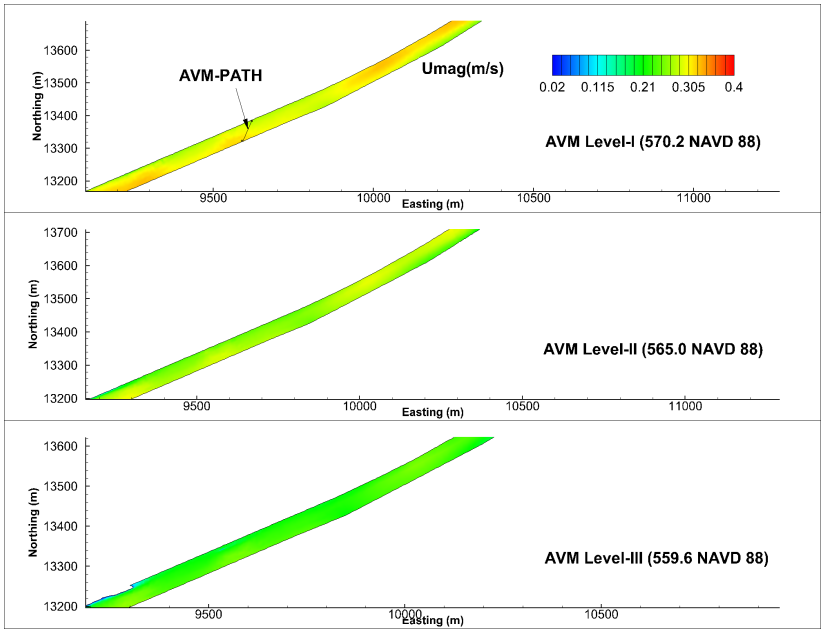

Figure 6.17: Results from TELEMAC-3D 108 hours after the start of the simulation

Notice the decrease in the velocity magnitude at all AVM levels in Figures 6.17 and 6.18. Although there is a decrease in the velocity magnitude but the logarithmic nature of velocity profile, higher velocity magnitude near the surface and less near the bed can be still seen in the presented plot. The velocity magnitude near the surface (AVM-Level-I) at 108 hours after the start of the simulation now is in the vicinity of 0.3 m/s, this is greater than what is observed at AVM level II and III. Also it must be stated that velocity magnitude at AVM level-I is greater than what is observed by the simulation results from TELEMAC-2D. This makes sense because two-dimensional simulation is based on depth-averaged equation where the characteristics of the vertical velocity profile is lost in the process of averaging.

The information extracted from two and three dimensional simulations finally aids in developing the index-velocity relationship at Lemont. The algorithm used for the construction of the index-velocity relationship comprise

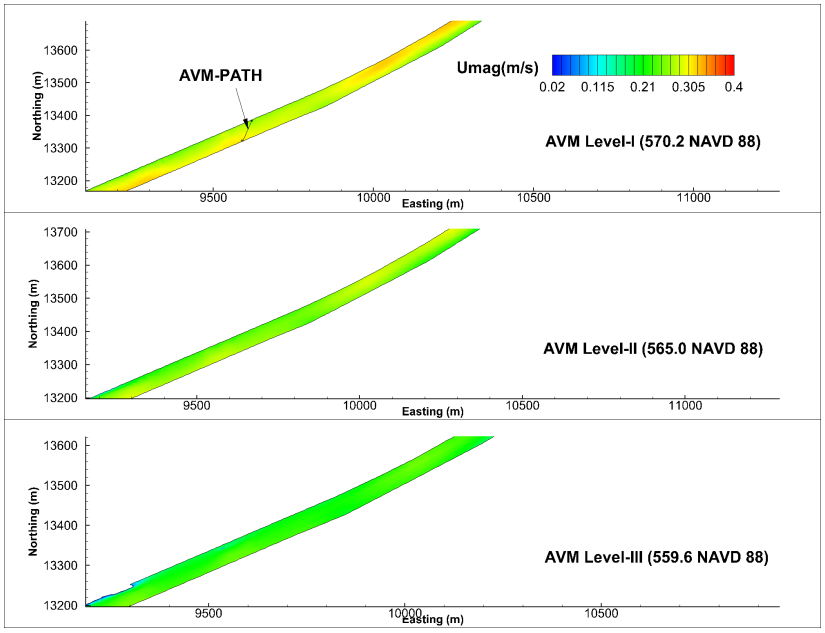

Figure 6.18: Results from TELEMAC-3D 120 hours after the start of the simulation

of following steps

- Take the average of velocity values along all three AVM levels at every hour of 120 hours storm simulated.
- Take arithmetic mean of the average velocities obtained in the previous step, these values can be categorised as $V_{AVM-Index}$
- Take the average of velocity values obtained along BM-ADCP (Boat mounted Acoustic Doppler Current Profiler) at every hour as obtained from TELEMAC-2D simulation, this is representative of the mean velocity (V_{mean}) and can be categorised as $V_{BM-ADCP}$
- Plot the values in $V_{BM-ADCP}$ and $V_{AVM-Index}$

The plots obtained by following the above steps is presented in Figure 6.19. Also presented in the same figure is a plot for V_{mean} as obtained by following the relation presented in Jackson et al. (2012), the relationship used for the same is $V_{mean} = 0.891V_{AVM-Index} - 0.0161$. As far as the relationship between V_{mean} and $V_{AVM-Index}$ as obtained by the numerical models it can be given by the following relationship $V_{mean} = 0.9297V_{AVM-Index} - 0.012$. Notice that

both field and index velocity plot tallies quite well with each other as shown in Figure 6.19.

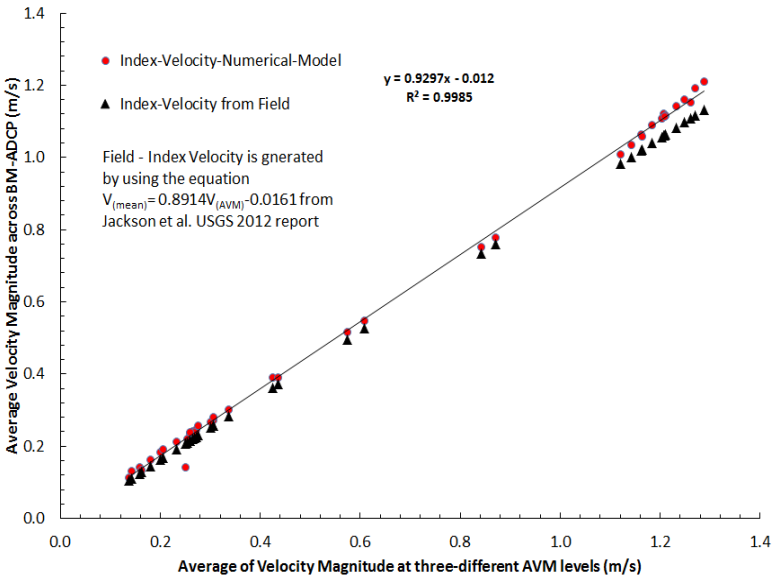

Figure 6.19: AVM Index velocity developed by numerical models

The same exercise was repeated for velocity corresponding H-ADCP level, the algorithm for developing index velocity for H-ADCP is almost same as AVM, the only difference in the algorithm is that now the velocity values are extracted along the H-ADCP path from TELEMAC-3D simulations and the average velocity values stored every hour of the simulation is categorised as $V_{HADCP-Index}$. These values are then plotted against the $V_{BM-ADCP}$, the results from this is presented in Figure 6.20. Once again the index-velocity relationship as developed by the field campaign (Jackson et al., 2012) was used to develop the comparative plot, the relationship used is $V_{mean} = 0.8866V_{H-ADCP} + 0.0239$. Notice that the values obtained from the field relationship tallies quite well with the index velocity plot developed by numerical models which can be given by the following relationship $V_{mean} = 0.9396V_{H-ADCP} - 0.0125$.

Also presented as a part of this exercise is velocity magnitude corresponding to H-ADCP level as obtained from TELEMAC-3D simulation at different times in simulation conducted at confluence of Cal-Sag junction and CSSC.

The velocity magnitudes as presented in Figures 6.21, 6.22 and 6.23 show the same trend as was seen with velocity magnitudes presented for AVM

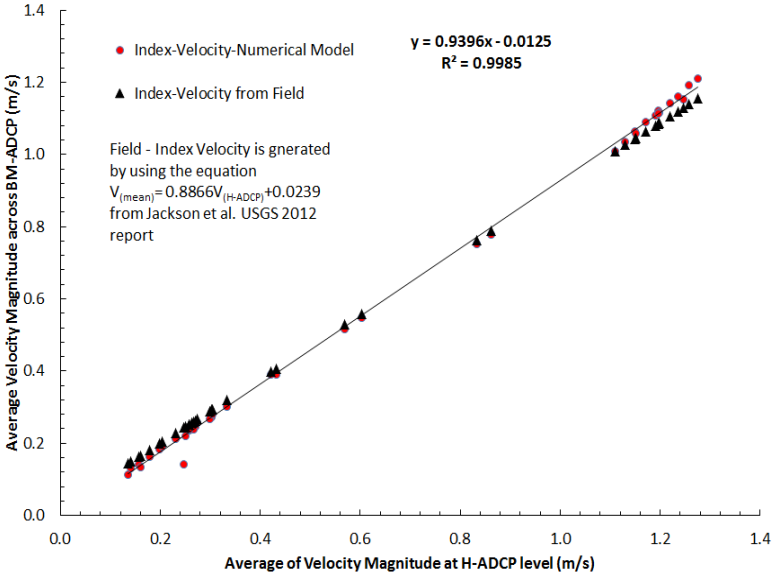

Figure 6.20: H-ADCP Index velocity developed by numerical models

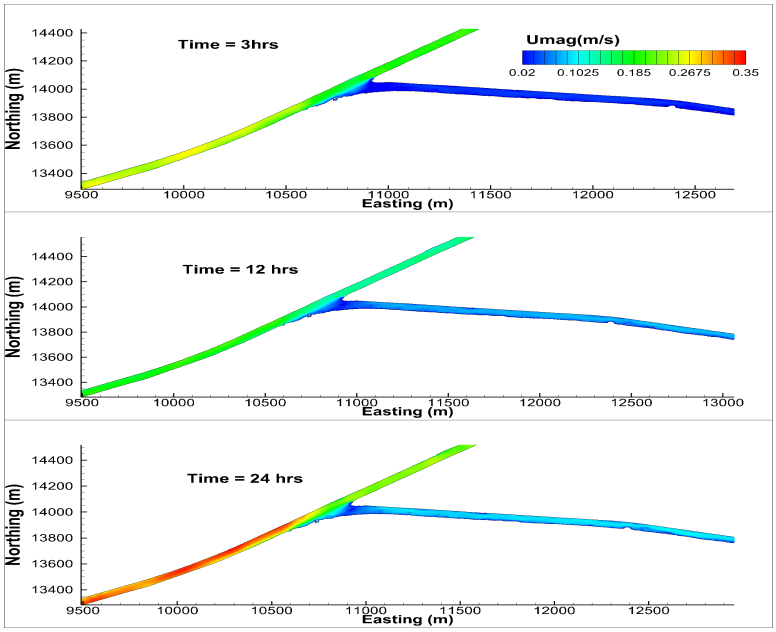

Figure 6.21: Velocity magnitude, 3, 12 and 24 hours after the start of the simulation

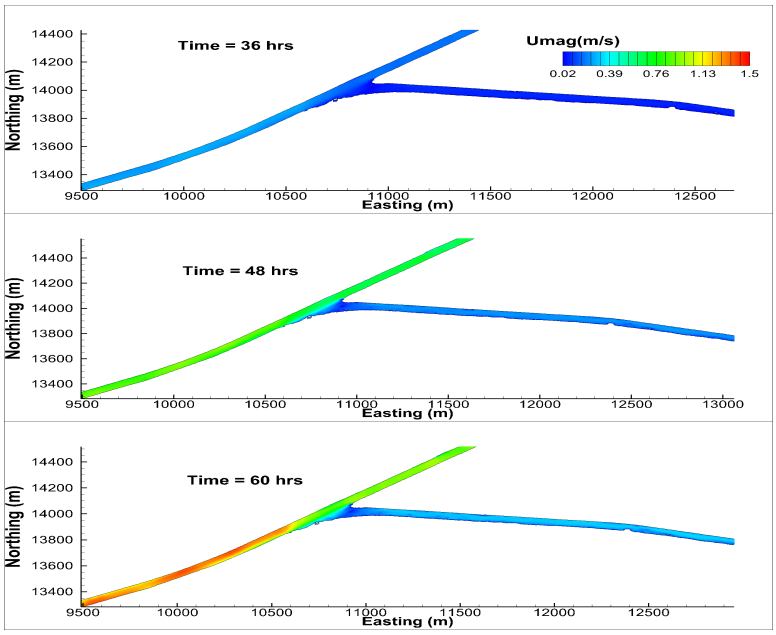

Figure 6.22: Velocity magnitude, 36, 48 and 60 hours after the start of the simulation

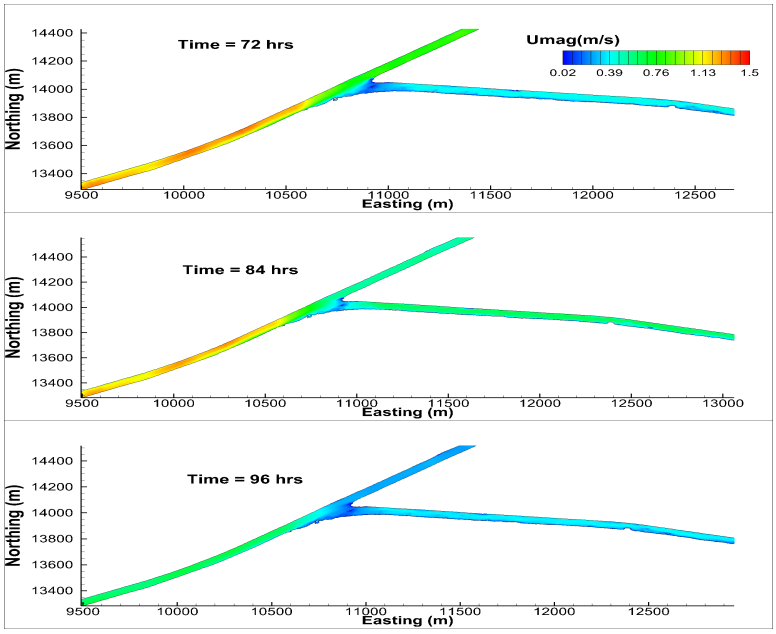

Figure 6.23: Velocity magnitude, 72, 84 and 96 hours after the start of the simulation

levels. Lower velocity magnitudes is observed at the start of the simulation as we progress further in the simulation, due to high flow from the upstream boundary combined with the draw-down happening at the downstream end, higher velocity magnitude is observed at 72 and 84 hours after the start of the simulation. Finally the model runs presented here is validated with the stage and discharge data at Lemont, these are presented in Figures 6.24 and 6.25. A very good match between the observed and modeled stage and discharge is obtained. Also worth mentioning is that time step used in both 3D and 2D simulation are 0.5 seconds. horizontal eddy viscosity was set at 0.001 m^2/s and in 3D simulation the vertical eddy viscosity was computed with the help of Prandtl mixing length model, in such a case the vertical eddy viscosity is given by the following formulation.

$$\nu = L_m^2 \sqrt{2 D_{ij} D_{ij}}; D_{ij} = \frac{1}{2}\left(\frac{\partial \bar{U}_i}{\partial x_j} + \frac{\partial \bar{U}_j}{\partial x_i}\right) \tag{6.5}$$

The standard Prandtl's model is suitable for the flows with strong barotropic component.

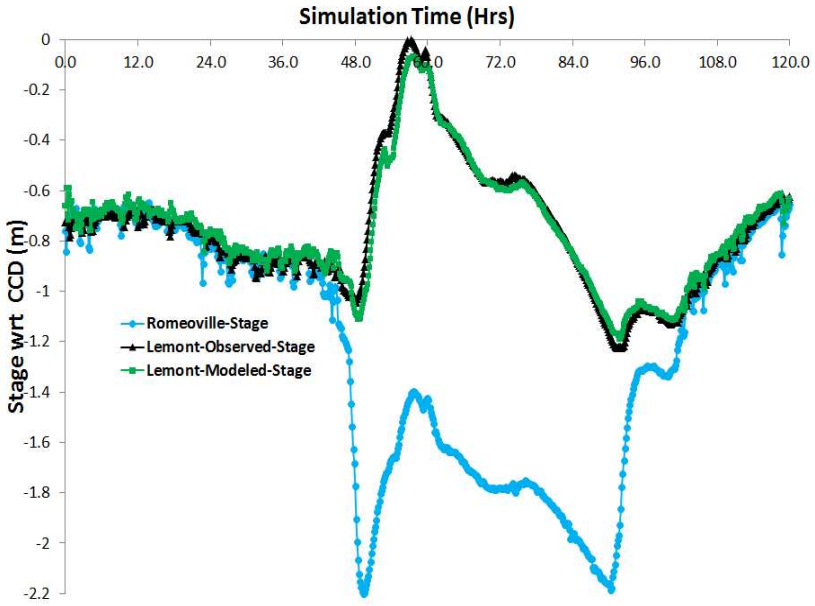

Figure 6.24: Comparison between modeled and observed stage at Lemont

Although the flow boundary condition simulated as a part of this chapter corresponds to high flow conditions, the flow conditions in the portion

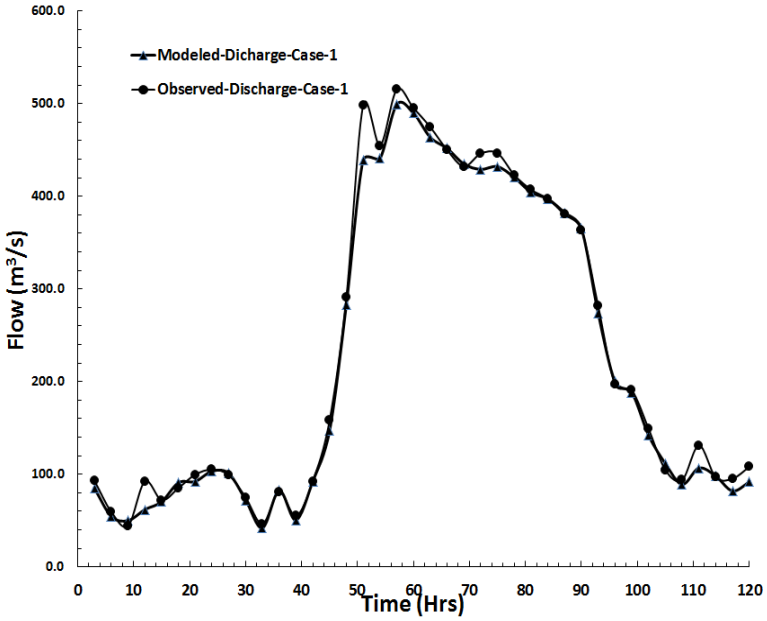

Figure 6.25: Comparison between modeled and observed discharge at Lemont

of CAWS simulated always stays sub-critical. As it is well known that in the simulation of sub-critical flow condition the characteristic information travel towards both upstream and downstream direction. In other words it can be said that in simulation of such a initial boundary value problem the downstream boundary condition is of utmost importance. This is further demonstrated by series of Froude No. plot presented here. Notice that the shape and value of Froude No. variation at a point near downstream boundary condition at Romeoville (Figure 6.26) and at a point near Lemont (Figure 6.26) are very identical in nature. This implies that flow dynamics at Lemont is to a large extent guided by the downstream boundary condition which is at Romeoville in this case. Also presented in the Figures 6.28 and 6.29 is the variation of Froude No. at points near upstream end at CSSC and Cal-Sag respectively. The shape and value of Forude No. in these plots are not at all similar to what is seen in Figures 6.26 and 6.27.

6.5.2 Results from Simulation in the Extended Domain

In this subsection the results from simulating the same storms for the extended portion of the domain is presented. As explained before this is done

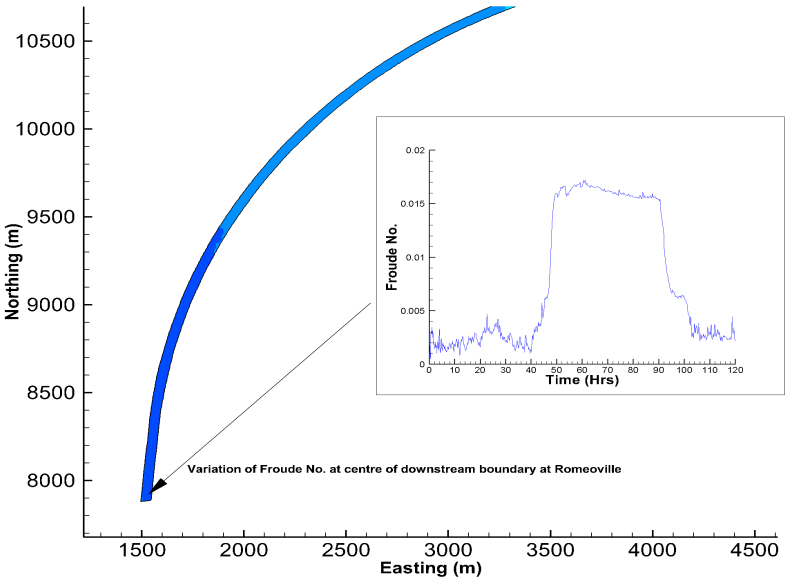

Figure 6.26: Froude number at Romeoville

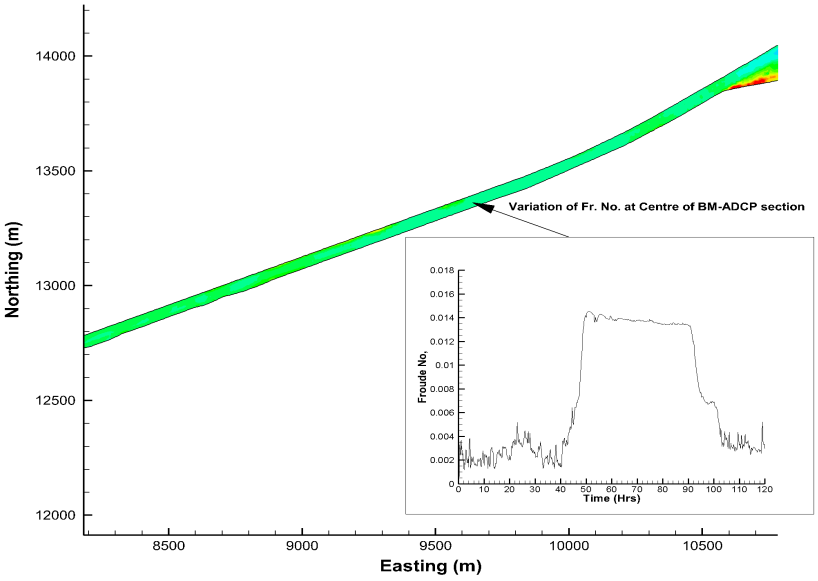

Figure 6.27: Froude number at Lemont

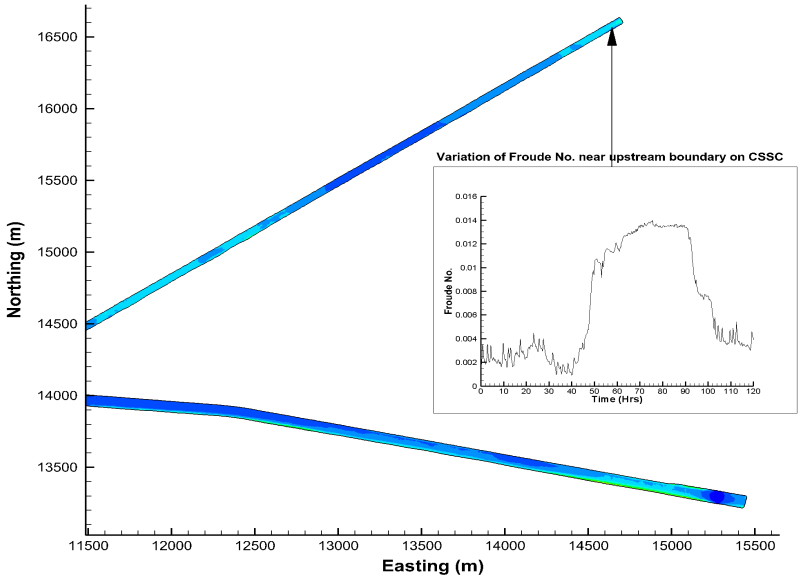

Figure 6.28: Froude number at the upstream end on CSSC stretch

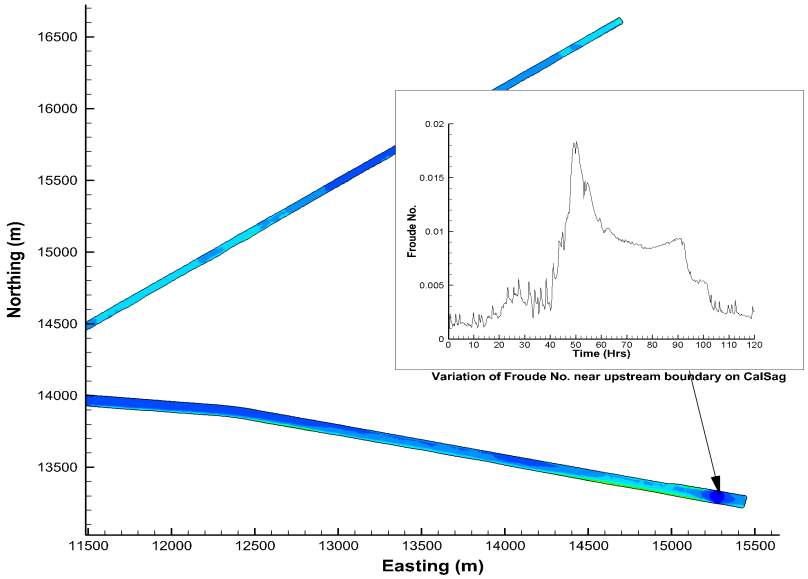

Figure 6.29: Froude number at the upstream end Cal-Sag stretch

in order to capture the and examine the impact of the downstream boundary condition on the flow structure inside the considered domain. The extended domain, along with controlling works and

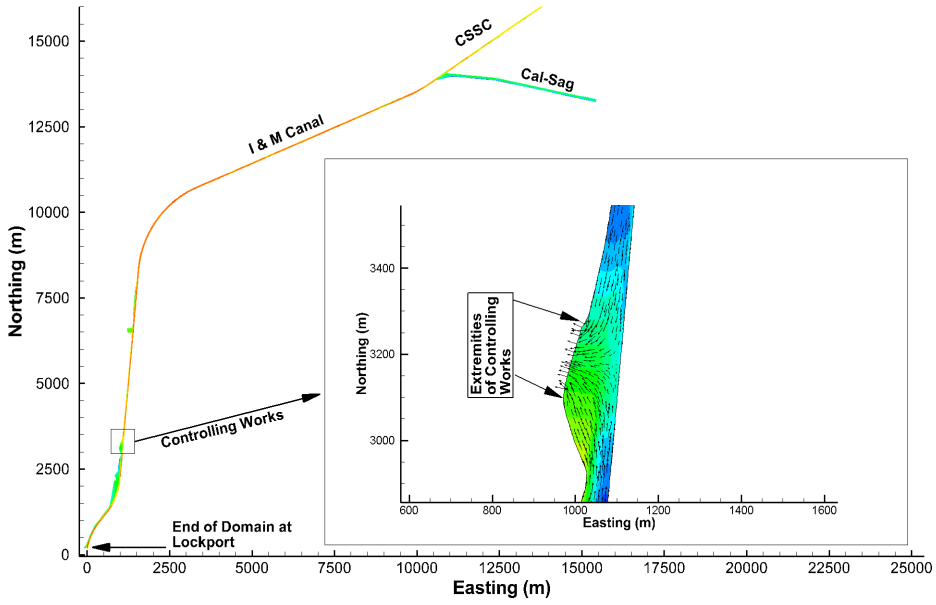

Figure 6.30: Extended domain ending at Lockport and including Controlling Works

As shown in Figure 6.30 because of an outlet at controlling works and lack of the outflow data through the controlling work the flow structure in the extended domain is further complicated. As far as the application of the numerical model for the extended domain is concerned, the outflow through the controlling work (please see Figure 6.30) is assigned a fixed value of 200 m^3/s. The downstream boundary condition is specified as the variation of free-surface, which is obtained by analysing the historical data and obtaining a relation between free-surface elevation at Lockport and Romeoville. On the basis of this data analysis a difference of 32 cms between the free-surface elevation at Romeoville and Lockport is assigned, the water level at Lockport is lower than that at Romeoville when the draw-down starts. Finally the downstream boundary condition utilized for the modeling of the extended domain is presented in Figure 6.31.

With the aforementioned downstream boundary-condition and the inflow condition being specified as the case-1 from Figure 6.5, the simulations were conducted again with both TELEMAC-3D and TELEMAC-2D. The man-

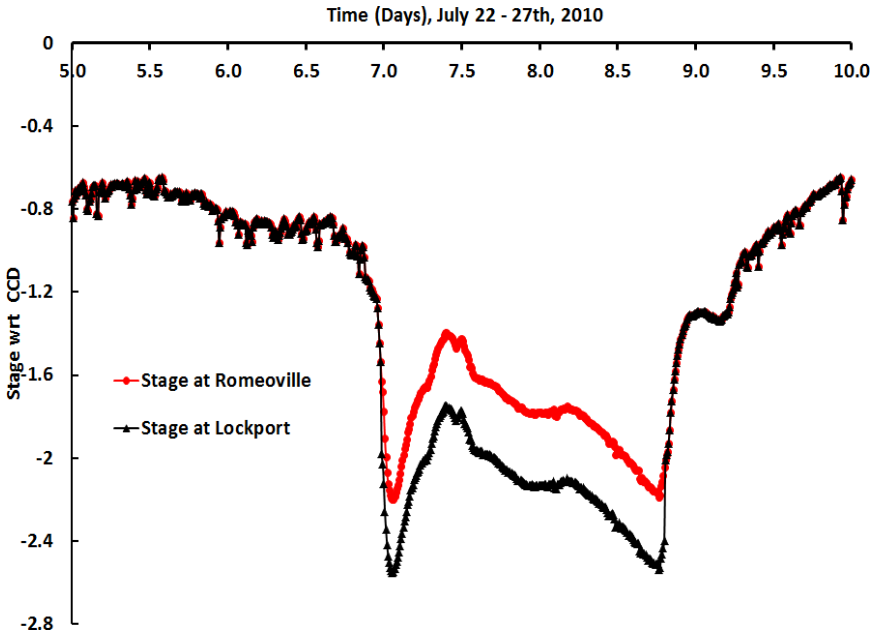

Figure 6.31: Free surface elevation between July, 22nd and 27th, 2010 at Romeoville and Lockport

ning's n for the extended domain was calibrated with a value of 0.032 and the comparison between observed and simulated stage is presented in Figure 6.31, very good agreement for the variation of free surface at Lemont is obtained. As regards to Romeoville although the shape the of observed free-surface is captured that match is far from satisfactory. This can also be attributed to the fact that Romeoville is closer to controlling works and Lockport and because of the addition of controlling work in the computational domain another variability is introduced.

A better agreement with the observed stage at Romeoville might be obtained by using the spatially varying mannin's n also the exact information about the amount of outflow from the controlling works might further improve the modeling results. As mentioned in the present simulation a constant outflow of $200m^3/s$ is assigned at the controlling works, this leads to an upstream propagating wave shown here in 6.33.

As there is too much of uncertainty with the amount of outflow through the controlling works for the duration simulated and also about the downstream boundary condition at Lockport the index velocity relation generated through the numerical model might not be entirely bankable.

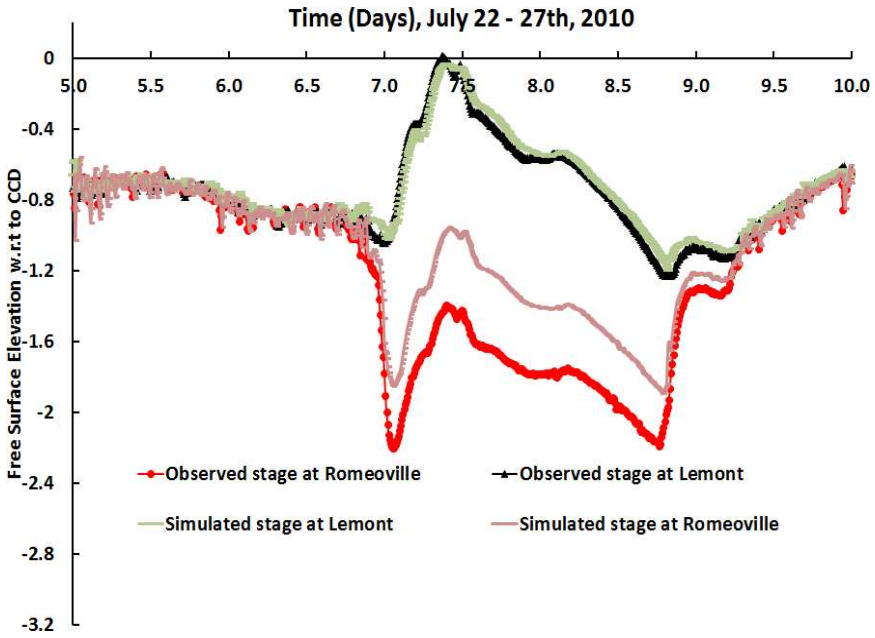

Figure 6.32: Simulated and observed stage at Romeoville and Lemont in the extended domain

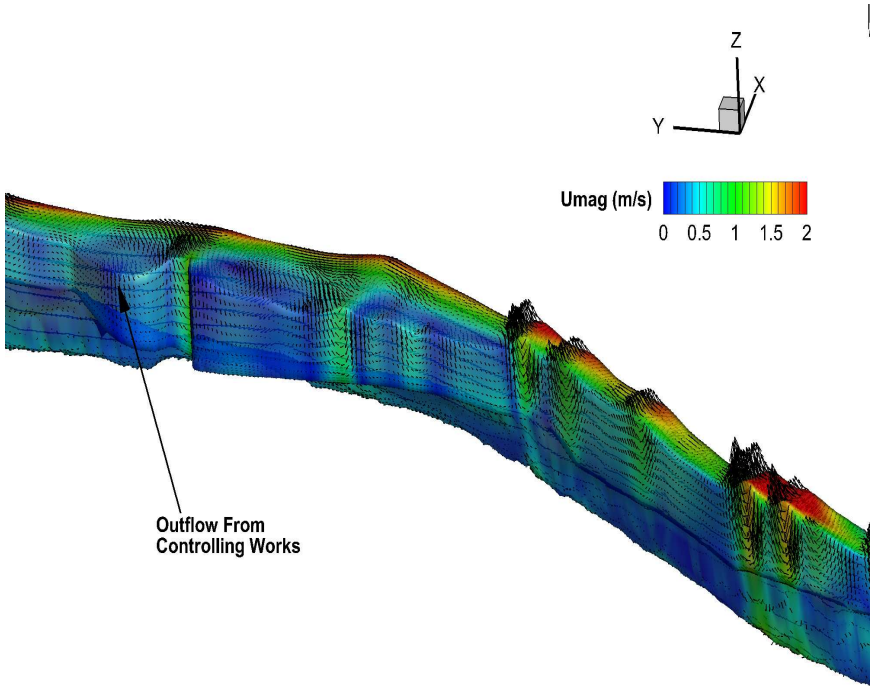

Figure 6.33: Upstream propagating surface wave near controlling works 2.25 hours after the start of the simulation

6.6 Conclusion

This chapter has dealt with the formulation of index velocity relationship at the Lemont gauging station with the help of TELEMAC2D an TELEMAC3D models. TELEMAC suite of models was chosen for the set of simulation presented in this chapter because of its ability to work with unstructured mesh and because of MPI implementation for the parallel version. It is because of this MPI implementation that it was possible to conduct number of simulations during the calibration runs to capture the stage variation at Lemont for the given ipstream boundary condition. For the sake of brevity the index velocity plots from only discharge case-1 and discharge case-4, please see Figure 6.5, is presented here. With the help of TELEMAC-2D and TELECMAC-3D it has been conclusively demonstrated that in the index-velocity plots (Figures 6.19 and 6.20) there is no loop present in the shorter portion of the domain simulated. The absence of loop in the index-velocity plot increases the confidence in the usage of index-velocity relationship at Lemont for accurate discharge computation. Moreover in absence of loop one can expect a single value function for the computation of discharge. Although very good results are obtained for the shorter portion of the domain modeled here, the complexity and variability involved in trying to model the extended portion of the domain increases by order of magnitude. The main source of variability in the extended domain comes from the gates located at Locport (Figure 6.2) this is further exacerbated by the existence of controlling works located 2.5 miles upstream of the Lockport gates. Although even in the longer domain considered here the stage elevation at Lemont is captured by TELEMAC-2D, it is near the downstream side that we don't obtain very good results, (please see Figure 6.32). Also due to lack of the outflow data through the controlling works an upstream promulgating surface wave, (please see Figure 6.33) is observed before the actual draw-down happens at the Lockport.

CHAPTER 7

PARALLELIZATION AND SCALE-UP OF I-EFDC MODEL

7.1 Introduction

The usage of cluster computers to in the field of surface flow modeling is becoming more and more common. Due to the large spatial and temporal scales most of the phenomenon to be simulated can lead to computationally intensive simulations some times to run large simulations even several days of CPU time might be needed. In the present day when multidimensional numerical models are commonly used for critical decision making tools, very long computational time on serial computer are plainly unacceptable. In regards with CAWS it might be of critical importance to predict which areas will experience flooding and over-topping of the river due to an approaching storm, during such circumstances optimized and parallized multidimensional hydrodynamic model can be of utmost importance. Furthermore it is a well known fact that for simulating water quality state variables usually long temporal simulations are conducted, on serial machines such simulation will take days if not months. Also as the number of state variables to be simulated increases and if one wants to implement higher order schemes for better accuracy of the modeling results the problem becomes constraint by memory size and is an additional motivation for the usage of cluster computers.

EFDC code has been parallelized using Open-MP paradigm leading to ***I-EFDC*** model, it is the purpose of this chapter to examine the speed up of ***I-EFDC*** model using different mesh resolution and by simulating them on multiple number of processors.

7.2 Domain Description

For examining and studying the speed-up of the parallelized EFDC model hereafter referred as I-EFDC, 22 kms of Phase-I domain was chosen. The domain extended from Grand avenue on the North branch to Stickney avenue on South branch, also included in the same domain in Bubbly creek and the Main branch of the Chicago river. The domain modeled is presented in Figure 7.1. This domain was chosen for examining the speed up of the I-EFDC as boundary conditions for the aforementioned domain is readily available from USGS gauging station conveniently located at the upstream end (Grand avenue) as well as the downstream end (Stickney avenue). Also available for the modeling purpose is the information about flow values at the Chicago River Controlling Works (CRCW) located on the Main branch of the Chicago River.

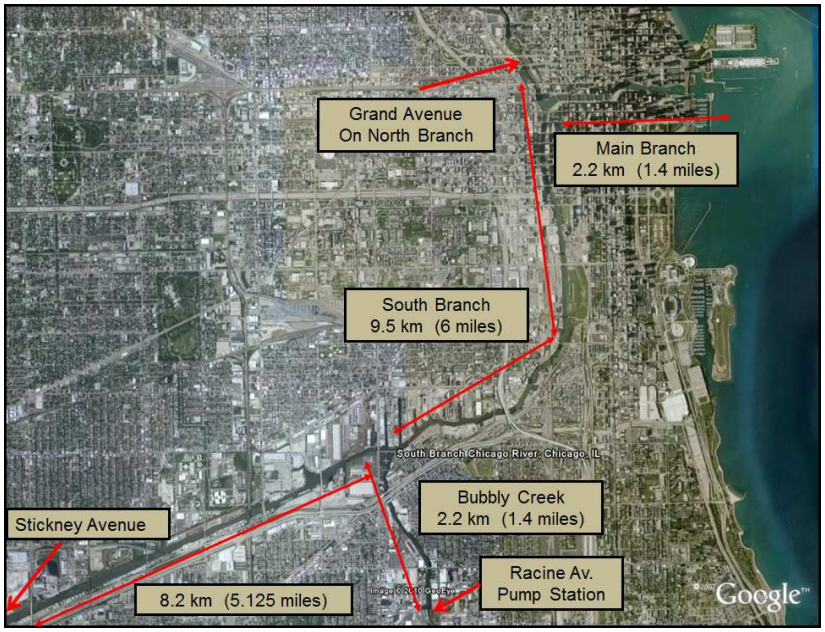

Figure 7.1: Domain for studying the parallel speed up of I-EFDC model

The aforementioned domain offers all the geographical complications of CAWS with confluence of slips and creeks along with the presence of controlling structures and pumping station. Sinha et al. (2012) simulated the same domain on one set of mesh and validated there hydrodynamic model. In this chapter the same domain will be simulated on different number of processors on different mesh resolution.

7.3 Numerical Discretization of the Governing Equations

As explained in chapter 4, EFDC model is based on three-dimensional shallow water equations. The numerical solution of these equations are accomplished by adopting the mode-splitting technique Madala. and Piacsek (1977). In mode splitting technique the fast moving gravity wave is separated from the slow moving three-dimensional flow. In regards with EFDC the governing momentum equations 4.3 and 4.4 are solved by a mix of finite-difference and finite volume techniques. It should be noted that in vertical (x,z) and (y,z) plane, the cells or control volumes are bounded by the same constant z surfaces which are referred as cell layers or layers. The momentum equations in x and y direction are integrated with respect to z over a cell layer assuming that the value at the cell center is constant in the control volume and the variable defined at the interface varies linearly through the cell control volume. The integrated form of momentum equations over cell layer is given by the following equations.

$$\begin{aligned} &\partial_t \left(mH\Delta_k u_k\right) + \partial_x \left(m_y H\Delta_k u_k u_k\right) + \partial_y \left(m_x H\Delta_k v_k u_k\right) \\ &+ \left(mwu\right)_k - \left(mwu\right)_{k-1} - \left(mf + v_k\partial_x m_y u_k \partial_y m_x\right)\Delta_k H v_k = \\ &-0.5 m_y H\Delta_k \partial_x \left(p_k + p_{k-1}\right) - m_y H\Delta_k g\partial_x \zeta m_y H\Delta_k g b_k \partial_x h - \\ &0.5 m_y H\Delta_k g b_k \left(z_k + z_{k-1}\right)\partial_y H + m\left(\tau_{xz}\right)_k - m\left(\tau_{xz}\right)_{k-1} + \left(\Delta Q_u\right)_k \end{aligned} \tag{7.1}$$

$$\begin{aligned} &\partial_t \left(mH\Delta_k v_k\right) + \partial_x \left(m_y H\Delta_k u_k v_k\right) + \partial_y \left(m_x H\Delta_k v_k v_k\right) \\ &+ \left(mwv\right)_k - \left(mwv\right)_{k-1} + \left(mf + v_k\partial_x m_y - u_k\partial_y m_x\right)\Delta_k H u_k = \\ &-0.5 m_x H\Delta_k \partial_y \left(p_k + p_{k-1}\right) - m_x H\Delta_k g\partial_y \zeta + m_x H\Delta_k g b_k \partial_y h - \\ &0.5 m_x H\Delta_k g b_k \left(z_k + z_{k-1}\right)\partial_y H + m\left(\tau_{yz}\right)_k - m\left(\tau_{yz}\right)_{k-1} + \left(\Delta Q_v\right)_k \end{aligned} \tag{7.2}$$

In the equations 7.1 and 7.2 Δ_k is the vertical cell layer thickness and the turbulent shear stresses at the cell layer interfaces are defined by the following equations.

$$\left(\tau_{xz}\right)_k = 2H^{-1}\left(A_v\right)_k \left(\Delta_{k+1} + \Delta_k\right)^{-1}\left(u_{k+1} - u_k\right) \tag{7.3}$$

$$(\tau_{xz})_k = 2H^{-1}(A_v)_k(\Delta_{k+1}+\Delta_k)^{-1}(v_{k+1}-v_k) \tag{7.4}$$

Finally also if there are K layers in vertical z direction, the hydrostatic pressure equation can be integrated from a cell layer interface to the surface to give the following expression.

$$p_k = gH\left(\Sigma_{j=k}^{K}\Delta_j b_j - \Delta_k b_k\right) + p_s \tag{7.5}$$

In equation 7.5 p_s is the physical pressure at the free surface divided by the reference density, subscript k denotes the layer number k and $b = (\rho-\rho_o)\rho_o^{-1}$ denotes the buoyancy term. The discretized equations presented in equations 7.1 and 7.2 are summed over k layers in the vertical to yield what is commonly known as the external mode equation. The discretized form of the external mode equations are given by the following expression.

$$\begin{aligned}\partial_t(mH\bar{u}) + \Sigma_{k=1}^{K}\partial_x(m_y H\Delta_k u_k u_k) + \partial_y(m_x H\Delta_k u_k v_k)\\ -H(mf + v_k\partial_x m_y - u_k\partial_y m_x)\Delta_k v_k = -m_y Hg\partial_x\zeta - m_y H\partial_x p_s +\\ m_y Hg\bar{b}\partial_x h - m_y Hg\left(\Sigma_{k=1}^{K}(\Delta_k\beta_k + 0.5\Delta_k(z_k+z_{k-1})b_k)\right)\partial_x H\\ -0.5m_y H^2\partial_x\left(\Sigma_{k=1}^{K}\Delta_k\beta_k\right) + m(\tau_{xz})_K - m(\tau_{xz})_0 + \bar{Q}_u\end{aligned} \tag{7.6}$$

$$\begin{aligned}\partial_t(mH\bar{v}) + \Sigma_{k=1}^{K}\partial_x(m_y H\Delta_k u_k v_k) + \partial_y(m_x H\Delta_k v_k v_k)\\ +H(mf + v_k\partial_x m_y - u_k\partial_y m_x)\Delta_k u_k = -m_x Hg\partial_y\zeta - m_x H\partial_y p_s +\\ m_x Hg\bar{b}\partial_y h - m_x Hg\left(\Sigma_{k=1}^{K}(\Delta_k\beta_k + 0.5\Delta_k(z_k+z_{k-1})b_k)\right)\partial_y H\\ -0.5m_x H^2\partial_y\left(\Sigma_{k=1}^{K}\Delta_k\beta_k\right) + m(\tau_{yz})_K - m(\tau_{yz})_0 + \bar{Q}_v\end{aligned} \tag{7.7}$$

$$\partial_t(m\zeta) + \partial_x(m_y H\bar{u}) + \partial_y(m_x H\bar{v}) = 0 \tag{7.8}$$

In the above equations the over bar denotes the depth-averaged values. The depth-averaged continuity equation stems from the equation 4.7 and imposes the continuity constraint for the external model equations. While

solving the external mode equations the state variables chosen are the free-surface displacement ζ and volumetric transport rates $m_y Hu$ and $m_x Hv$. To summarize the external mode equations 7.6, 7.7 and 7.8 presents the time rate of change of external or depth integrated volumetric transports to the pressure gradient associated with the free-surface slope, atmospheric pressure and buoyancy, the advective accelerations, the Coriolis and curvature accelerations, the free surface and the bottom tangential stresses and the general source and sink terms. As mentioned before the staggered arrangement of variables allows for second order central difference computation for all spatial derivatives. Finally the external mode equations are solved using semi-implicit three time level scheme (Madala. and Piacsek, 1977).

As far as the internal mode equations are considered they are formulated by dividing the equations 7.1 and 7.2 by the cell layer thickness Δ_k, subtracting the equations for cell layer k from the equations for cell layer k+1 and then dividing the results from the average thickness of the two cell layers to give the following expressions.

$$\begin{aligned}
&\partial_t(mH\Delta^{-1}_{k+1,k}(u_{k+1}-u_k)) + \partial_x(m_y H\Delta^{-1}_{k+1,k}(u_{k+1}u_{k+1}-u_k u_k)) \\
&\partial_y(m_x H\Delta^{-1}_{k+1,k}(v_{k+1}u_{k+1}-v_k u_k)) + m\Delta^{-1}_{k+1,k}\left(\Delta^{-1}_{k+1}\left((wu)_{k+1}-(wu)_k\right)\right) - \\
&m\Delta^{-1}_{k+1,k}\left(\Delta^{-1}_{k+1}\left((wu)_k-(wu)_{k-1}\right)\right) - \\
&\Delta^{-1}_{k+1,k}\left(mf+v_{k+1}\partial_x m_y - u_{k+1}\partial_y m_x\right)Hv_{k+1} - \\
&\Delta^{-1}_{k+1,k}\left(mf+v_{k+1}\partial_x m_y - u_{k+1}\partial_y m_x\right)Hv_{k+1} = \\
&m_y H\Delta^{-1}_{k+1,k} g\left(b_{k+1}-b_k\right)\left(\partial_x h - z_k\partial_x H\right) - \\
&0.5 m_y H^2\Delta^{-1}_{k+1,k} g\left(\Delta_{k+1}\partial_x b_{k+1} + \Delta_k\partial_x b_k\right) + \\
&m\Delta^{-1}_{k+1,k}\left(\Delta^{-1}_{k+1}\left((\tau_{xz})_{k+1}-(\tau_{xz})_k\right) - \Delta^{-1}_k\left((\tau_{xz})_k-(\tau_{xz})_{k-1}\right)\right) + \\
&\Delta^{-1}_{k+1,k}\left((Q_u)_{k+1}-(Q_u)_k\right)
\end{aligned} \tag{7.9}$$

$$\partial_t(mH\Delta^{-1}_{k+1,k}(v_{k+1}-v_k))+\partial_x(m_yH\Delta^{-1}_{k+1,k}(u_{k+1}v_{k+1}-u_kv_k))$$
$$\partial_y(m_xH\Delta^{-1}_{k+1,k}(v_{k+1}v_{k+1}-v_kv_k))+m\Delta^{-1}_{k+1,k}\left(\Delta^{-1}_{k+1}\left((wv)_{k+1}-(wv)_k\right)\right)-$$
$$m\Delta^{-1}_{k+1,k}\left(\Delta^{-1}_{k+1}\left((wv)_k-(wv)_{k-1}\right)\right)+$$
$$\Delta^{-1}_{k+1,k}\left(mf+v_{k+1}\partial_xm_y-u_{k+1}\partial_ym_x\right)Hu_{k+1}-$$
$$\Delta^{-1}_{k+1,k}\left(mf+v_k\partial_xm_y-u_k\partial_ym_x\right)Hu_k=$$
$$m_xH\Delta^{-1}_{k+1,k}g\left(b_{k+1}-b_k\right)\left(\partial_yh-z_k\partial_yH\right)-$$
$$0.5m_yH^2\Delta^{-1}_{k+1,k}g\left(\Delta_{k+1}\partial_yb_{k+1}+\Delta_k\partial_yb_k\right)+$$
$$m\Delta^{-1}_{k+1,k}\left(\Delta^{-1}_{k+1}\left((\tau_{yz})_{k+1}-(\tau_{yz})_k\right)-\Delta^{-1}_k\left((\tau_{yz})_k-(\tau_{tz})_{k-1}\right)\right)+$$
$$\Delta^{-1}_{k+1,k}\left((Q_u)_{k+1}-(Q_u)_k\right) \tag{7.10}$$

In the above equations $\Delta_{k+1,k} = 0.5\left(\Delta_{k+1}+\Delta_k\right)$. The internal model equations given by A.22 and 7.10 can be physically interpreted as K-1 inter-facial velocity differences or k-1 interior inter-facial shear stresses. The presented set of internal mode equations are solved using the fractional step scheme where the first step is explicit in nature and the second step being implicit. As far as the vertical velocity is concerned it is obtained by discretizing the continuity equations, the discretized form is given by the following equations.

$$w_k = w_{k-1}-m^{-1}\Delta_k\left(\partial_x\left(m_yH\left(u_k-\bar{u}\right)\right)\right)+m^{-1}\Delta_k\left(\partial_y\left(m_xH\left(v_k-\bar{v}\right)\right)\right) \tag{7.11}$$

Since the velocity at the bottom is taken as 0, the solution proceeds from the first cell layer (bottom-most) to the surface layer K. From the kinematic boundary condition the vertical velocity at the surface is also assigned 0 value.

7.4 Model Setup and Mesh Resolutions

For examining the parallel speed-up of I-EFDC model the wet-weather simulation of September 2008 presented in Chapter-5 is re-simulated. For the

sake of brevity the boundary conditions used for the simulation will not be presented here as it is already presented in Chapter 5. The storm simulated occurred on between September 10th and September 18th, 2008. The details about the various boundary conditions are presented in Chapter 5. The simulations presented in this chapter are conducted with the end purpose of examining the speed up of the I-EFDC model on different number of processors with different mesh resolution. In this part of the research two kind of mesh resolutions were tried. Mesh-1 had approximately 4000 cells in horizontal and 8 layers in vertical, Mesh-2 had approximately 8000 cells in horizontal and 8 layers in vertical. The snapshot of both the mesh, Mesh-1 and Mesh-2 are shown in Figure 7.2 and 7.3 respectively.

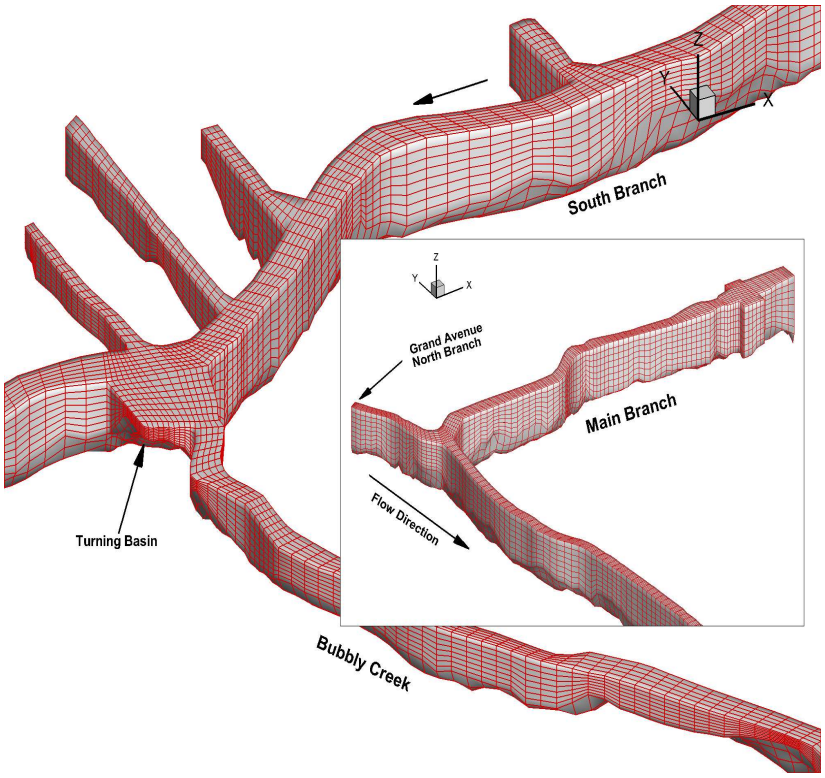

Figure 7.2: Mesh-1 with 4000 control volumes in horizontal and 8 layers in vertical

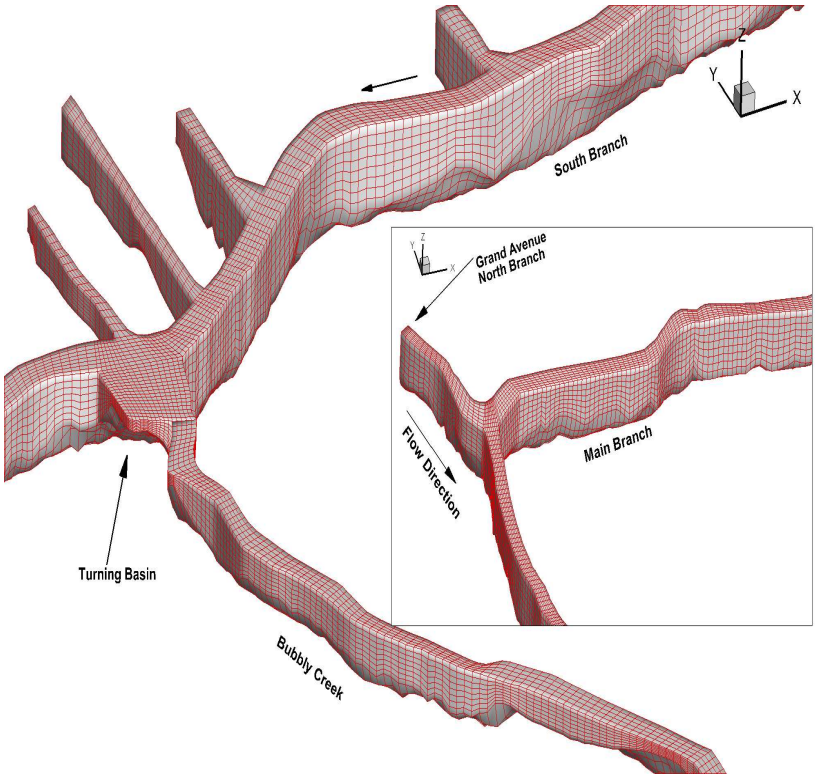

Figure 7.3: Mesh-2 with 8000 control volumes in horizontal and 8 layers in vertical

7.5 Results and Conclusion

For the parallelization of the EFDC kernel OpenMP methodology was chosen. OpenMP was the method of choice as it offers the advantage of parallelizing serial codes with minimal changes in the code structure. Open-MP technology draws its strength from what is commonly known as the loop level parallelization. A program that is written with OpenMP Fortran API (Application Programming Interface) begins execution as a single process called the master thread execution. The master thread executes sequentially until the first parallel construct is encountered. The parallel construct is defined by PARALLEL/END PARALLEL pair of directives. When a parallel construct is encountered, the master thread creates a team of threads and mater thread than becomes the mater of the team and all the constructs within the parallel constructs are executed in parallel by the team of threads. Number of threads spawned by each processor is usually implementation dependent, in case of Hydrosystem clusters each processor spawned a single thread. As mentioned before the same storm has been simulated with Mesh-1 in Chapter 5, the end purpose of the simulation presented in this Chapter is to examine the speed-up of the computational kernel of ***I-EFDC*** model. But before we draw conclusion about the speed up its essential to present the results from both the models in comparative manner. The comparison is done from examining the velocity plots from both the mesh resolution at different point in times. Presented here in series of plots are the velocity magnitude obtained in different portion of the simulated domain from both the mesh resolution.

The results obtained from both the mesh resolution is almost identical and upstream propagation of flow velocity in the South Branch exiting turning basin is observed. At the same instant in time the flow velocity in the Main Branch propagates towards Lake Michigan as the gates on Lake Michigan side is opened at this instant. The results on the Main Branch side is presented in Figures 7.6 and 7.7 respectively.

Notice once again that the velocity magnitude obtained by both the mesh resolutions are nearly same. As explained before in Chapter 5 that the normal flow direction in CAWS is from north to south, hence as we go ahead in time the flow velocity trend revert to its natural flow direction as shown in plots made at 120 hrs after the start of the simulation presented here in Figures 7.8 and 7.9 respectively.

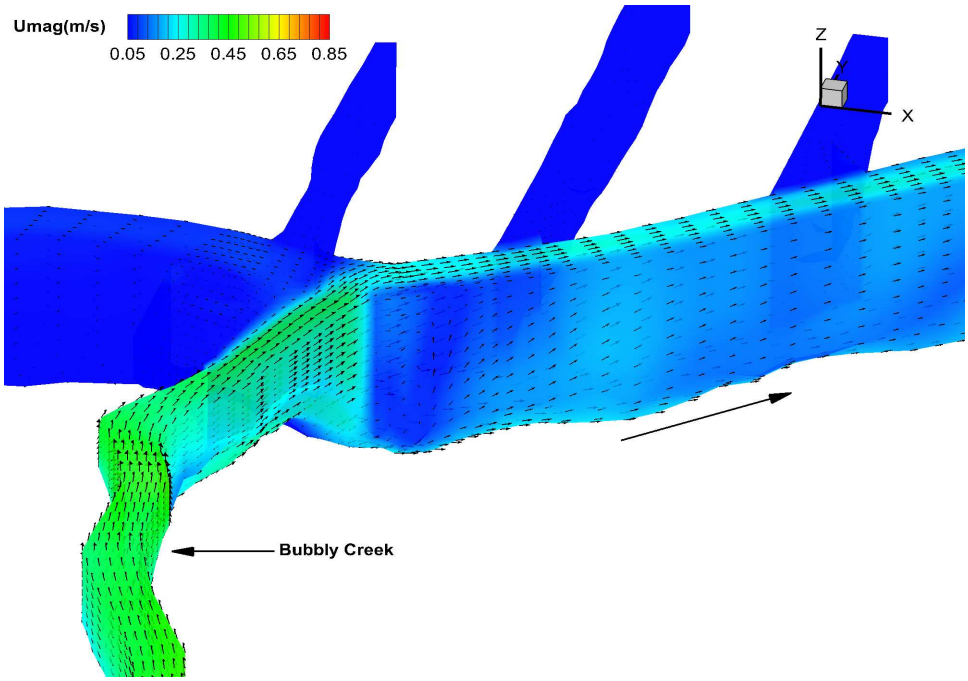

Figure 7.4: Velocity magnitude 114 hrs after the start of simulation on Mesh-1, near Turning Basin

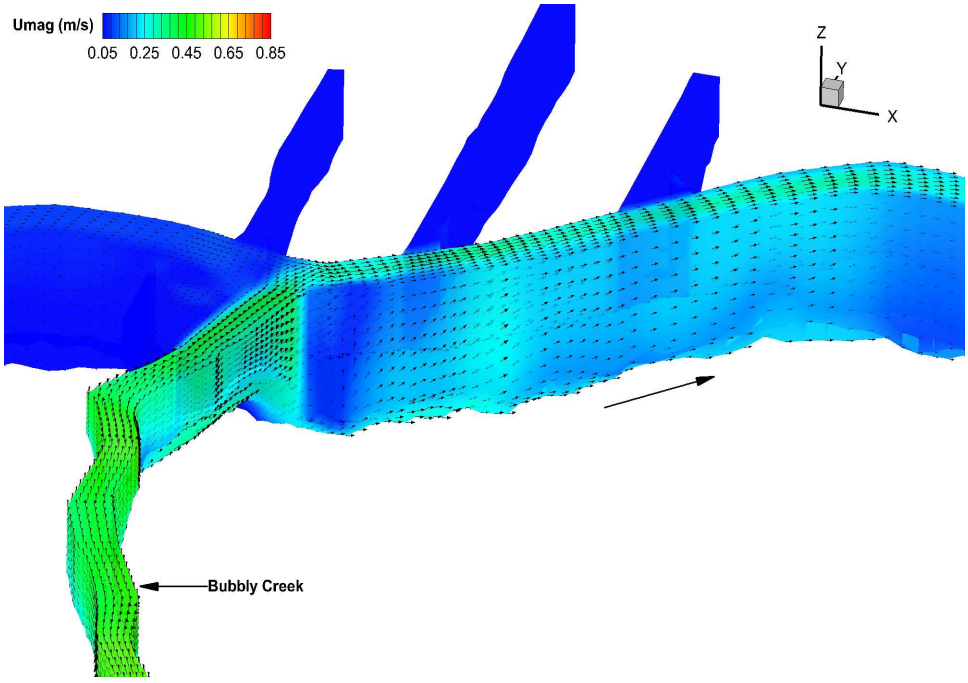

Figure 7.5: Velocity magnitude 114 hrs after the start of simulation on Mesh-2, near Turning Basin

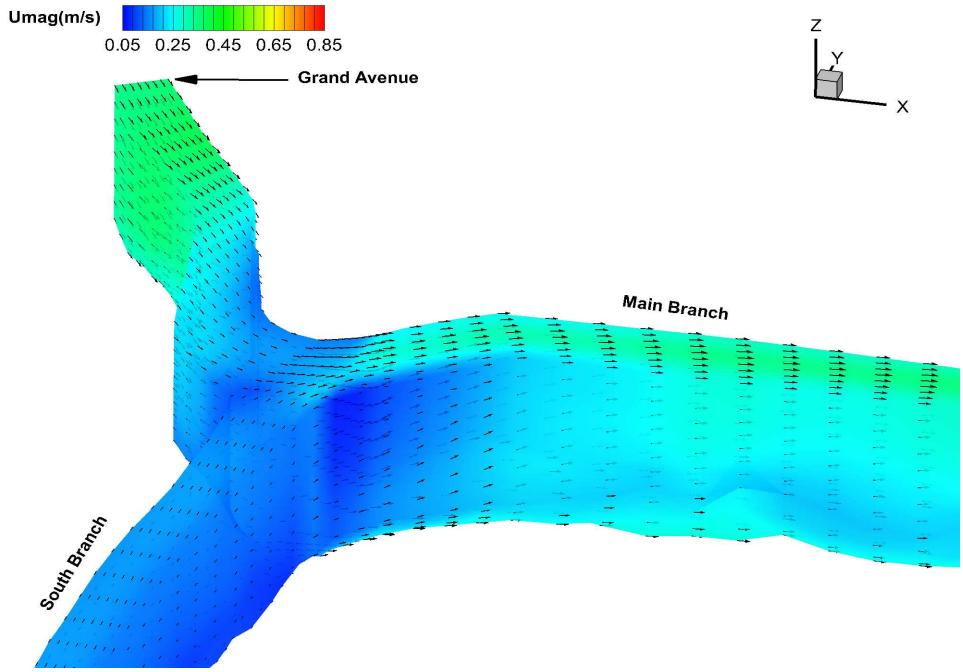

Figure 7.6: Velocity magnitude 114 hrs after the start of simulation on Mesh-1, on Main Branch

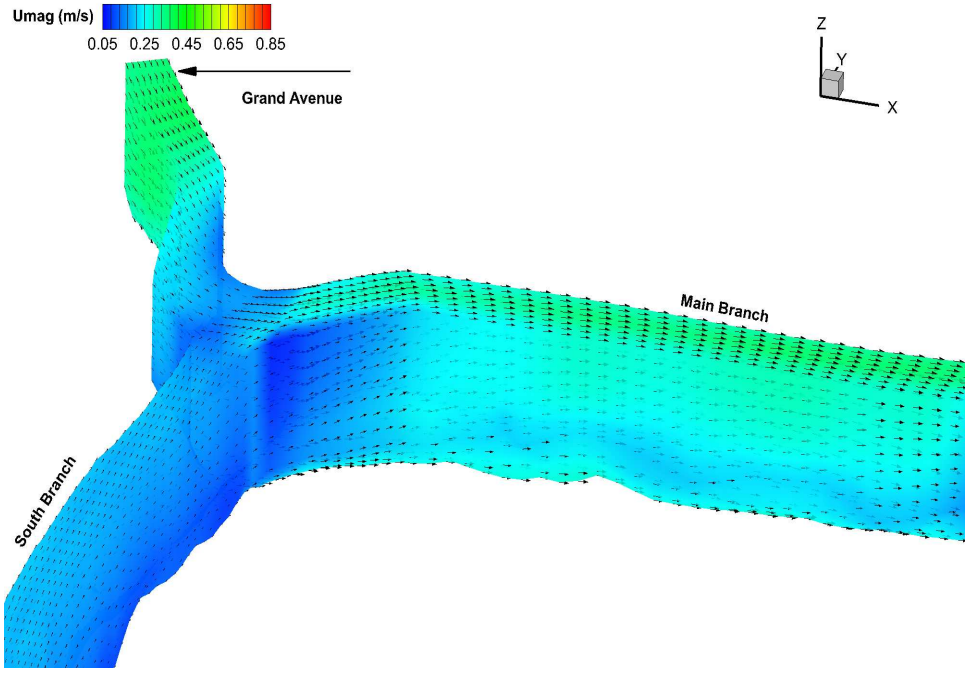

Figure 7.7: Velocity magnitude 114 hrs after the start of simulation on Mesh-2, on Main Branch

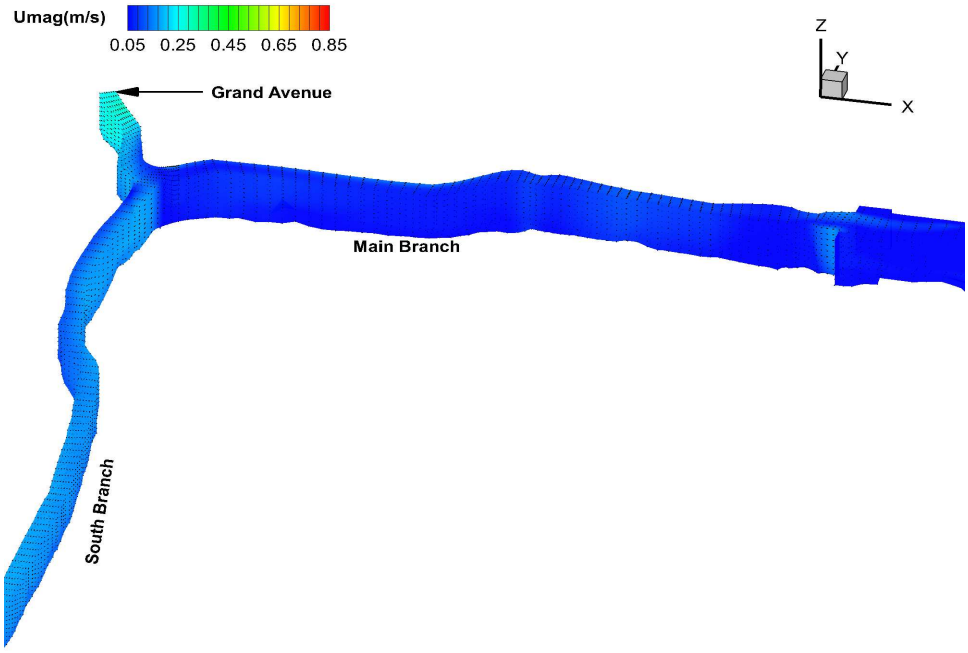

Figure 7.8: Velocity magnitude 120 hrs after the start of simulation on Mesh-1, on Main Branch

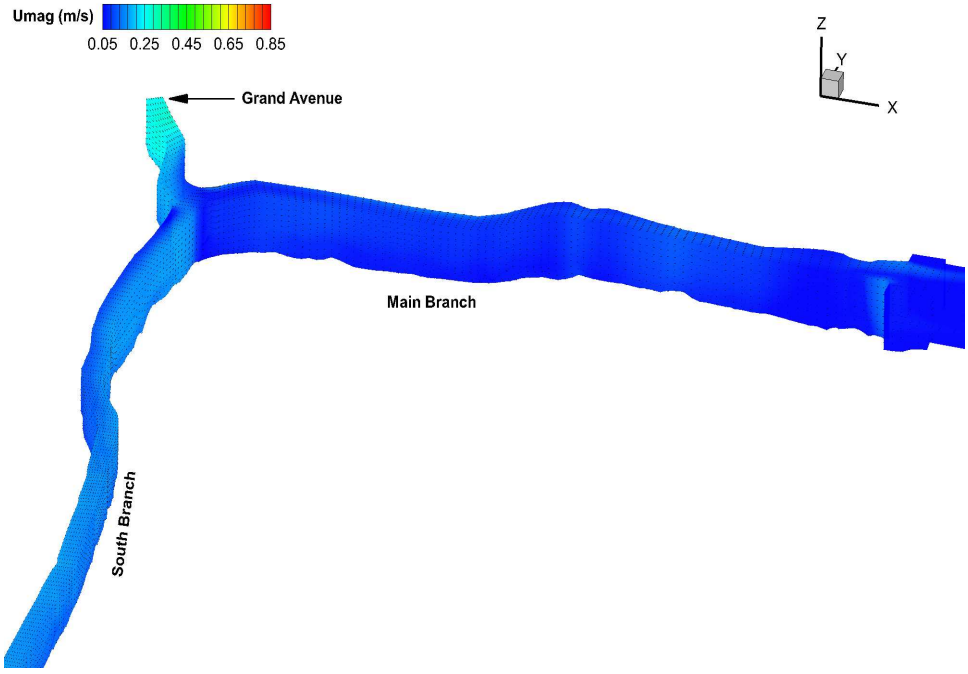

Figure 7.9: Velocity magnitude 120 hrs after the start of simulation on Mesh-2, on Main Branch

At the same time (120 hours after the start of the simulation) it can be seen that as the flow exits Bubbly Creek it flows south and no upstream intrusion of the flow is noticed. The results in that area of the domain is presented again in the following plots.

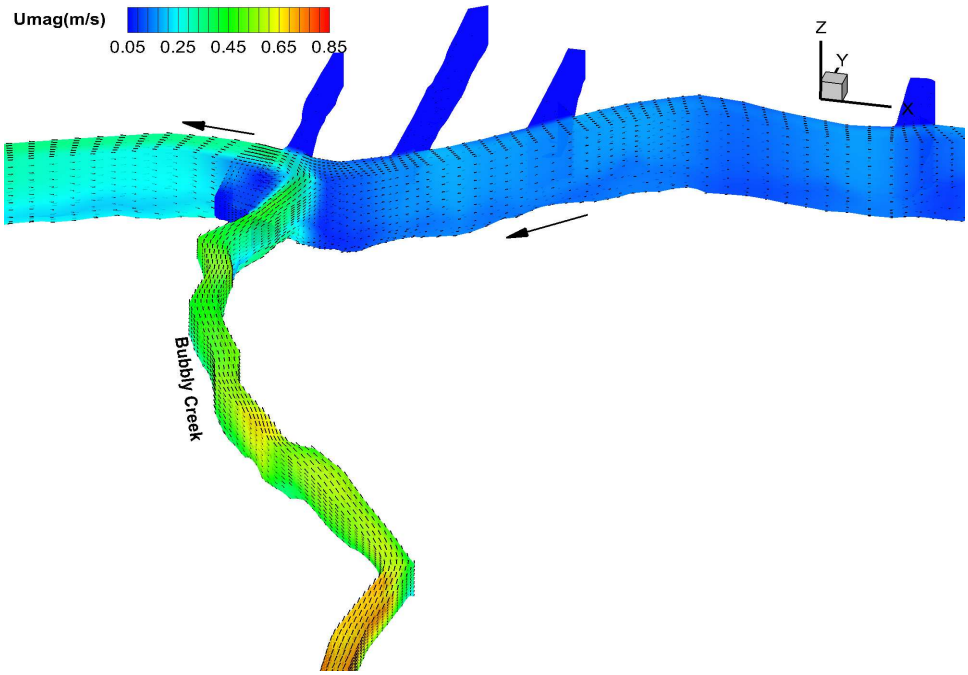

Figure 7.10: Velocity magnitude 120 hrs after the start of simulation on Mesh-1, in Bubbly Creek

Once again the simulation results obtained from both set of mesh are nearly same in terms of velocity magnitude. Furthermore as explained in Chapter 5 the validation point for this set of simulation comes from the gauging station located on the near Columbus drive on the Main Branch of the Chicago River [USGS 05536123]. The variation of free surface at this gauging station as recorded on both set of meshes is presented in Figure 7.14. Although both the mesh captures the free surface elevation at Columbus drive, what is worth noticing is that refining the mesh doesn't improve the result significantly.

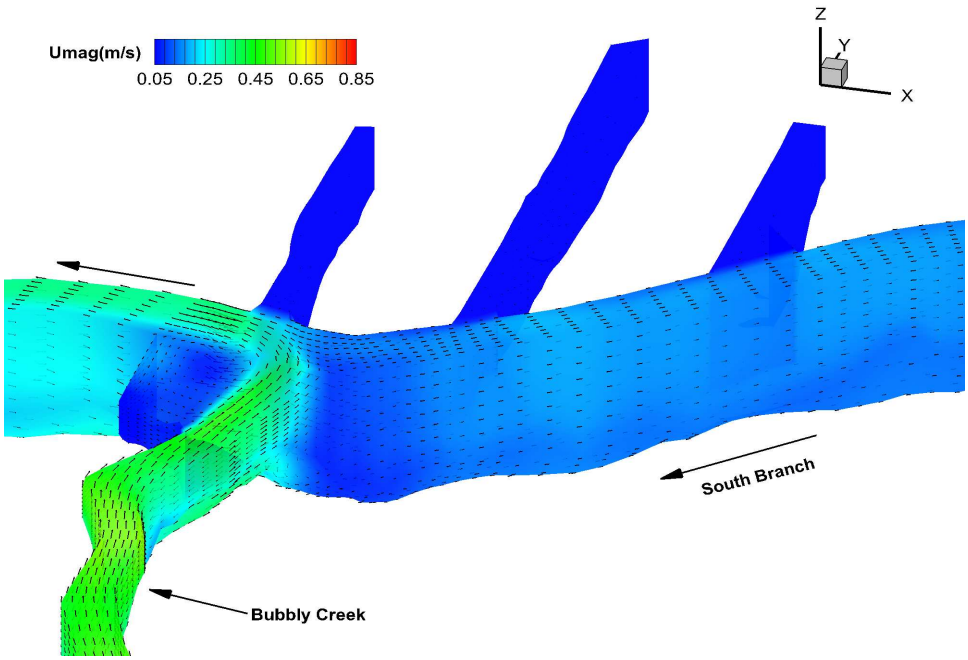

Figure 7.11: Velocity magnitude 120 hrs after the start of simulation on Mesh-1, near Turning Basin

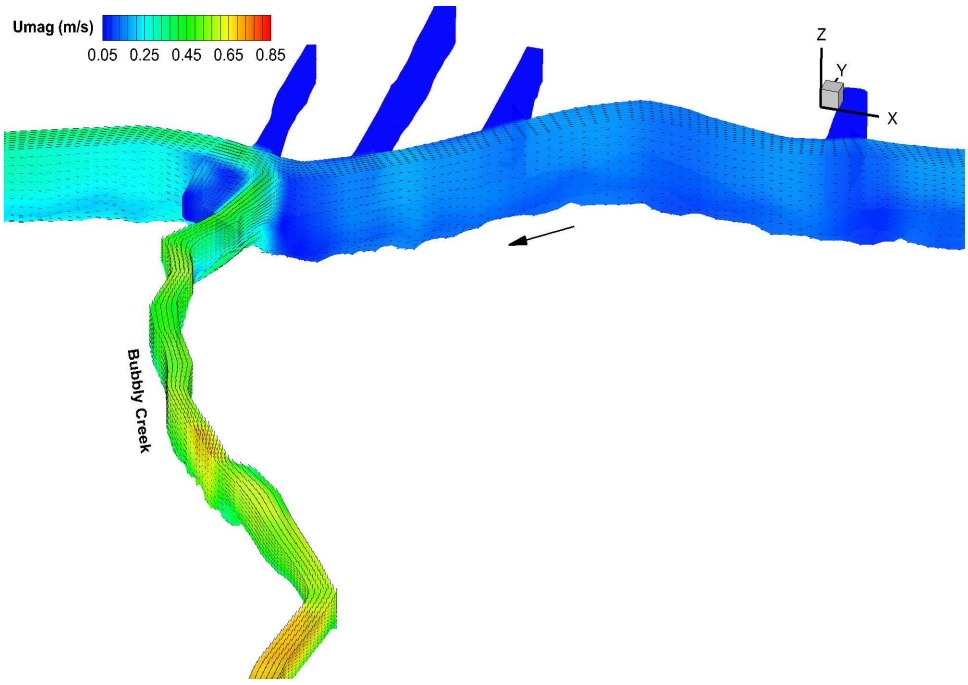

Figure 7.12: Velocity magnitude 120 hrs after the start of simulation on Mesh-2, in Bubbly Creek

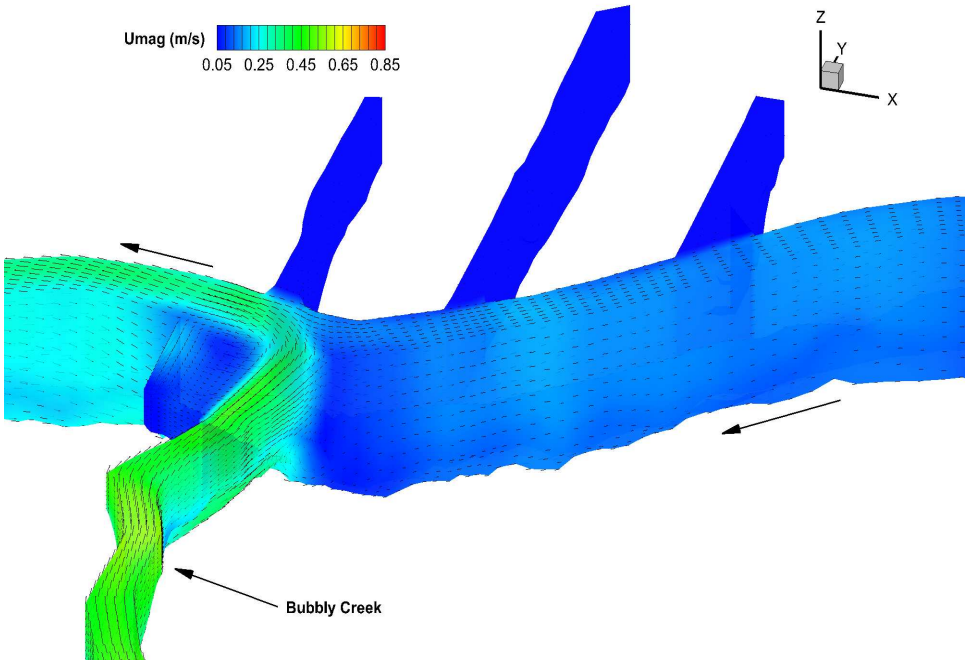

Figure 7.13: Velocity magnitude 120 hrs after the start of simulation on Mesh-2, near Turning Basin

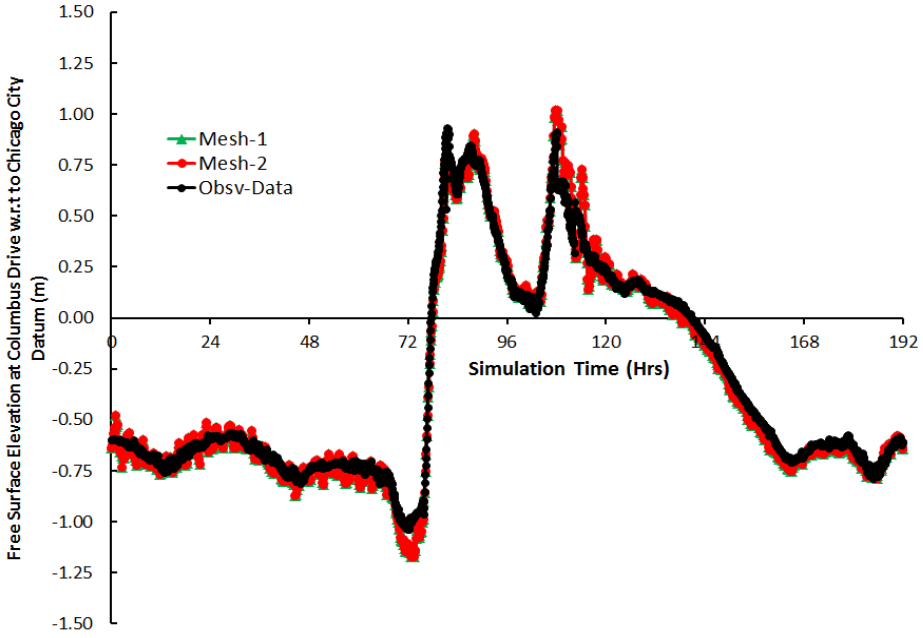

Figure 7.14: Free surface elevation with Mesh1 and Mesh2 near Columbus drive on Main Branch, Chicago River

Also examined as a part of this simulation exercise was the impact of increasing the number of layers in vertical on the accuracy of the solution. Three different vertical resolution was tested on the coarse mesh. The number of layers tried with coarse mesh were 4, 8 and 12. As refining the mesh in horizontal did not improve the results, to keep the computational time at an optimum level the impact of increasing and decreasing the vertical resolutions were conducted only on the coarse mesh. The velocity magnitude at three different times, obtained by using different number of layers in the vertical is presented here.

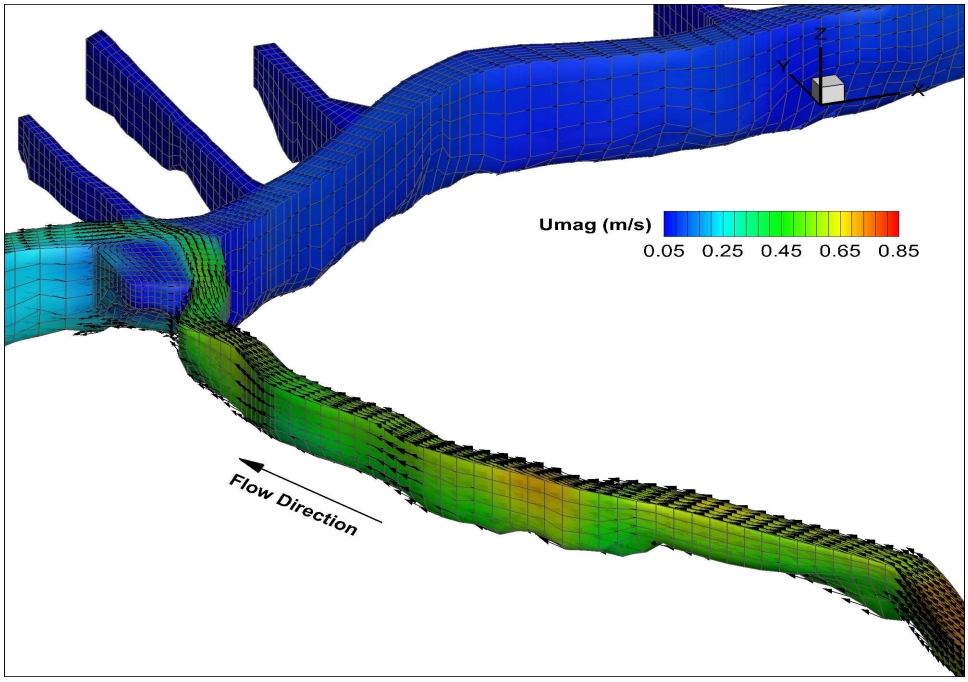

Figure 7.15: Velocity magnitude 102 hrs after the start of the simulation near Bubbly Creek with 4 layers in vertical on Mesh-1

As presented in series of Figures 7.15 to 7.20, increasing the numbers of layers in vertical doesn't change the velocity magnitude in a significant manner. Also presented here are the variation of velocity magnitude in the Main Branch of the Chicago River at the same points in time.

Once again it can be seen from the series of Figures presented above that changing the number of layers in vertical doesn't have a significant impact on changing the velocity magnitude. Also notice that in Figures 7.21, 7.22 and 7.23 the flow coming from Grand Avenue in North gets divided between the South Branch and the Main Branch. This is due to the fact that at this

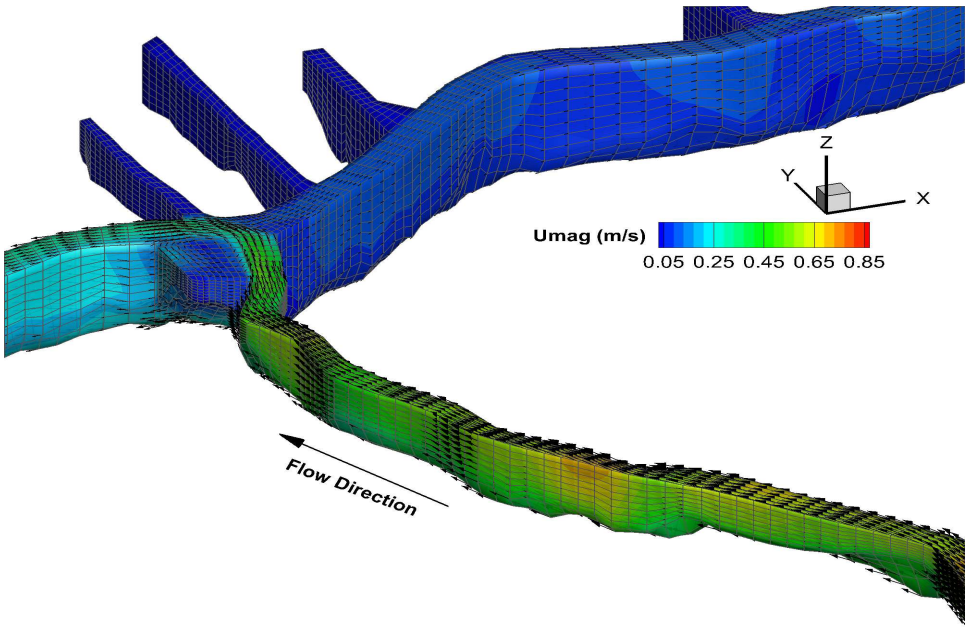

Figure 7.16: Velocity magnitude 102 hrs after the start of the simulation near Bubbly Creek with 8 layers in vertical on Mesh-1

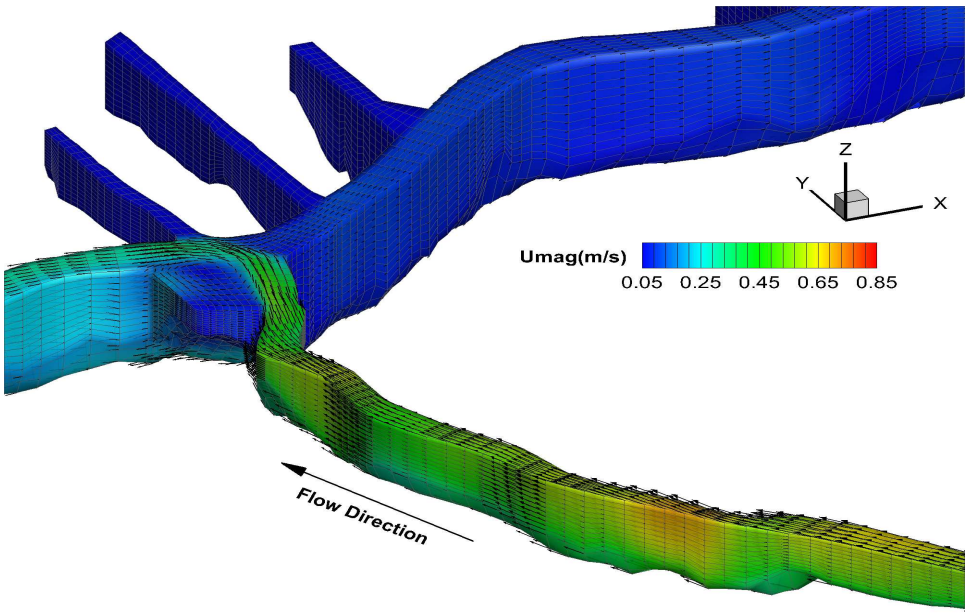

Figure 7.17: Velocity magnitude 102 hrs after the start of the simulation near Bubbly Creek with 12 layers in vertical on Mesh-1

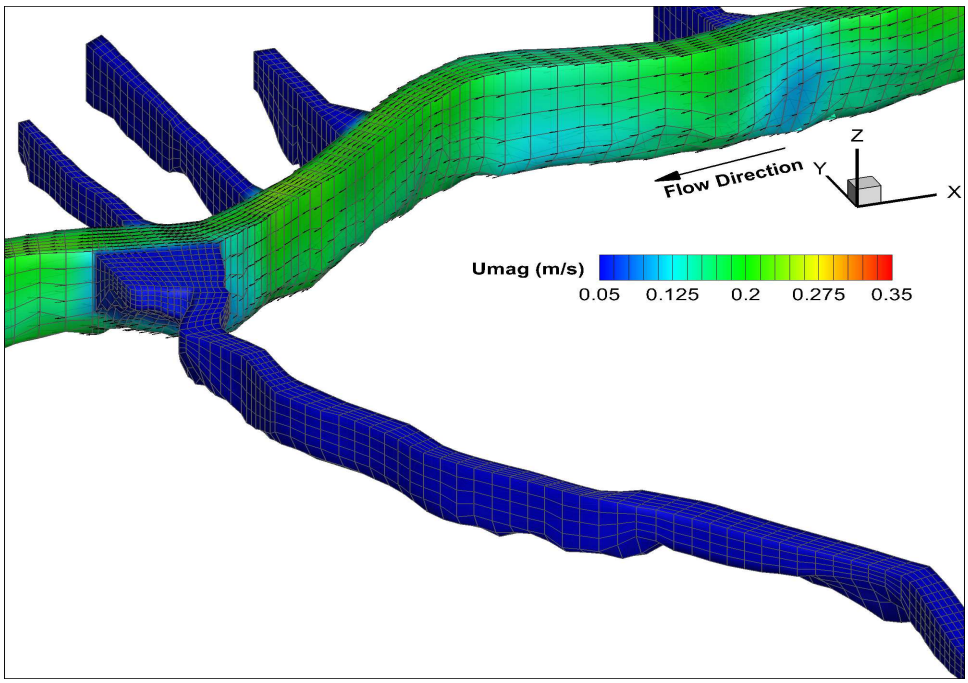

Figure 7.18: Velocity magnitude 144 hrs after the start of the simulation near Bubbly Creek with 4 layers in vertical on Mesh-1

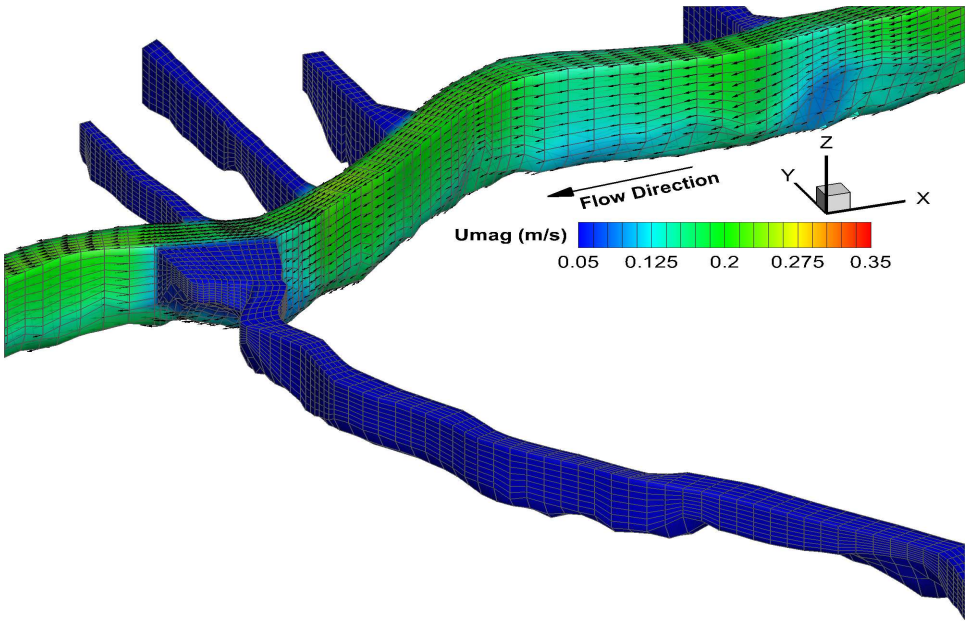

Figure 7.19: Velocity magnitude 144 hrs after the start of the simulation near Bubbly Creek with 8 layers in vertical on Mesh-1

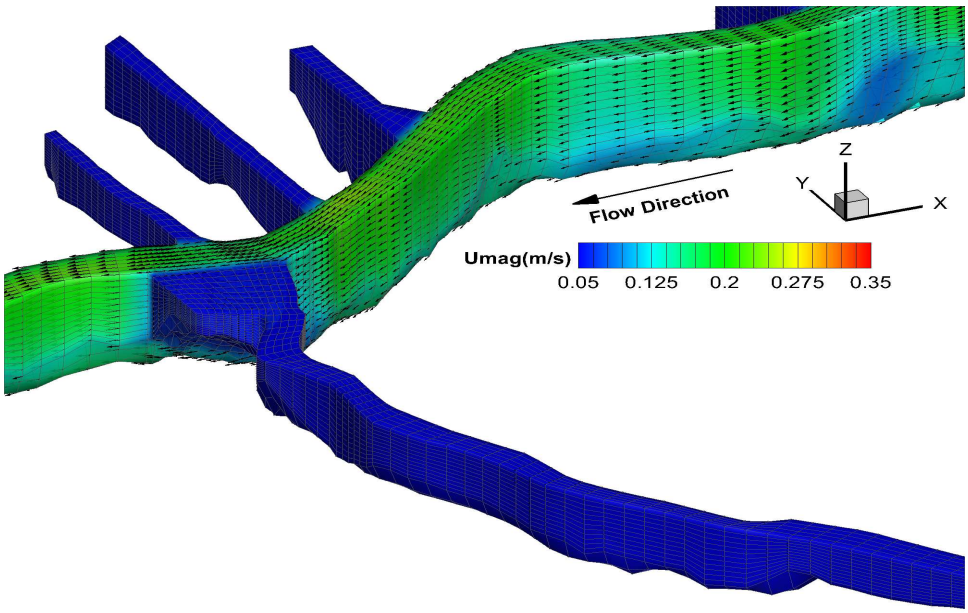

Figure 7.20: Velocity magnitude 144 hrs after the start of the simulation near Bubbly Creek with 12 layers in vertical on Mesh-1

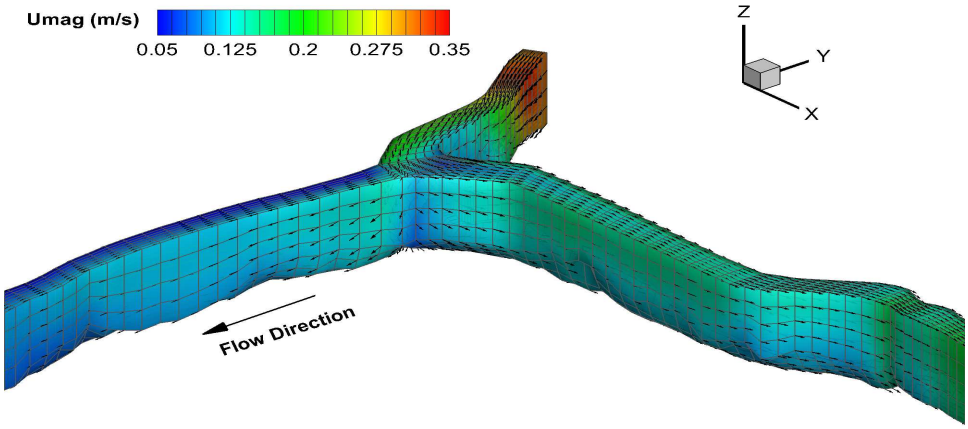

Figure 7.21: Velocity magnitude 102 hrs after the start of the simulation near Main Branch with 4 layers in vertical on Mesh-1

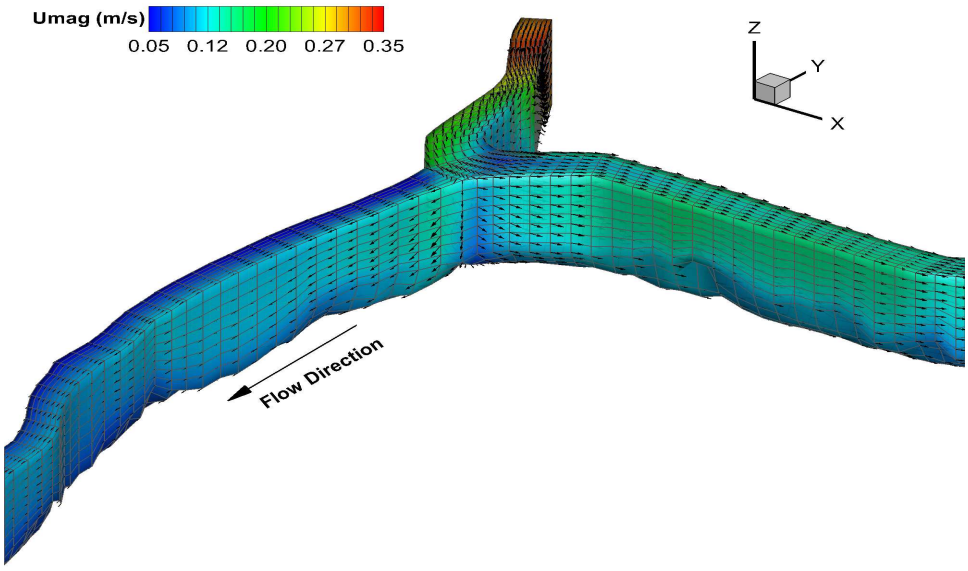

Figure 7.22: Velocity magnitude 102 hrs after the start of the simulation near Main Branch with 8 layers in vertical on Mesh-1

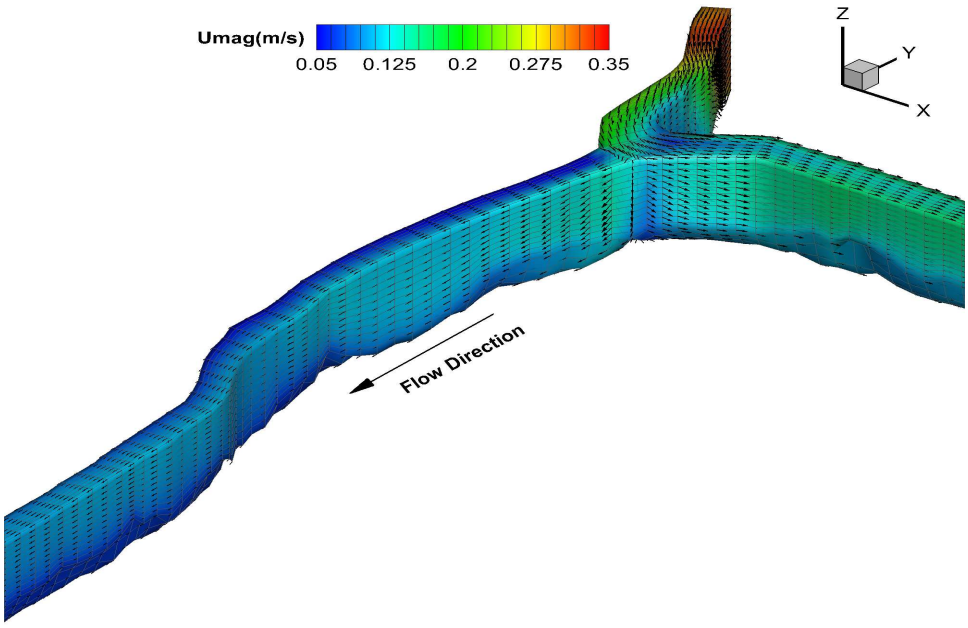

Figure 7.23: Velocity magnitude 102 hrs after the start of the simulation near Main Branch with 12 layers in vertical on Mesh-1

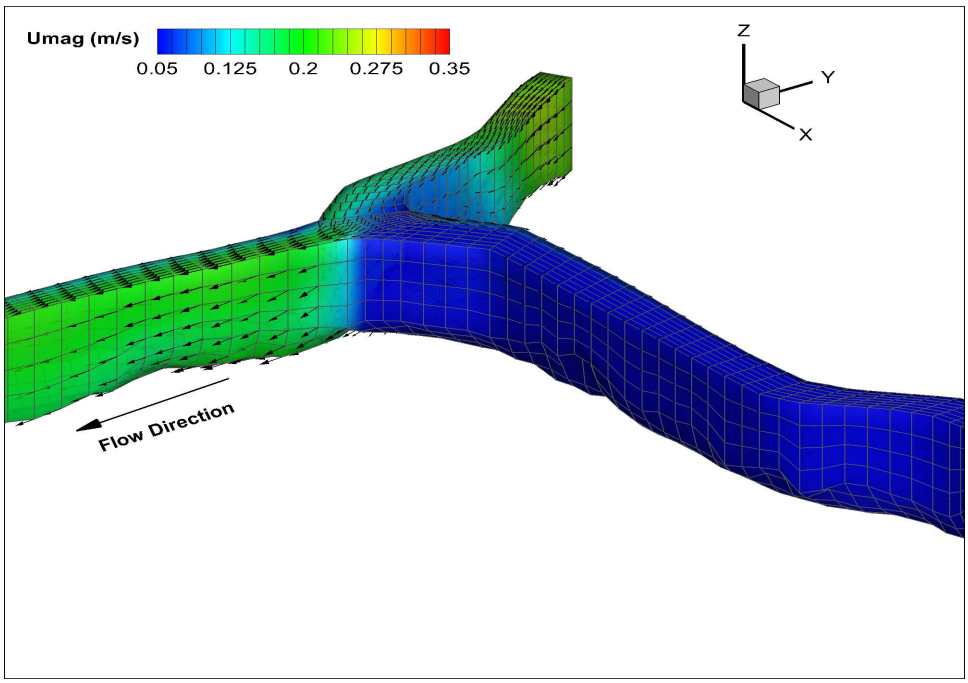

Figure 7.24: Velocity magnitude 144 hrs after the start of the simulation near Main Branch with 4 layers in vertical on Mesh-1

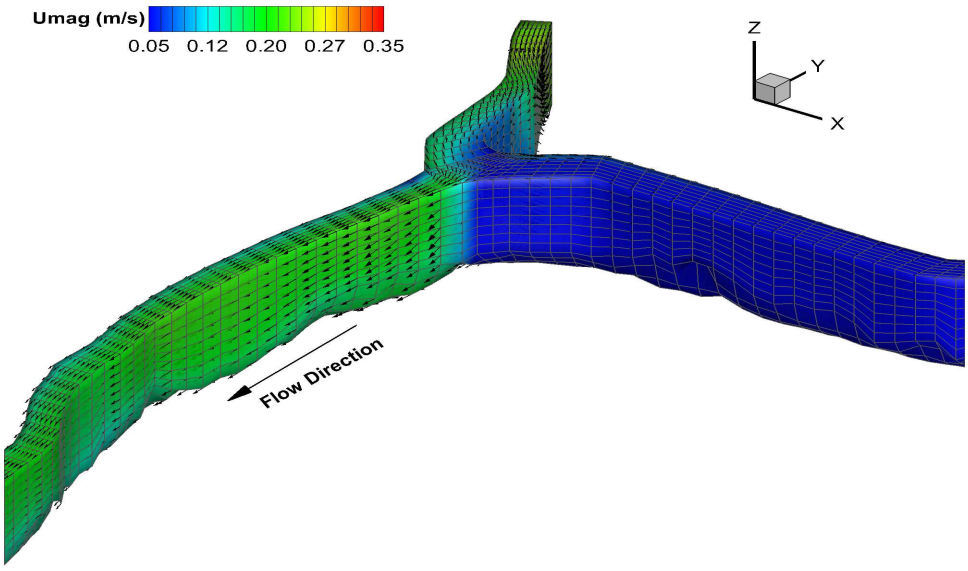

Figure 7.25: Velocity magnitude 144 hrs after the start of the simulation near Main Branch with 8 layers in vertical on Mesh-1

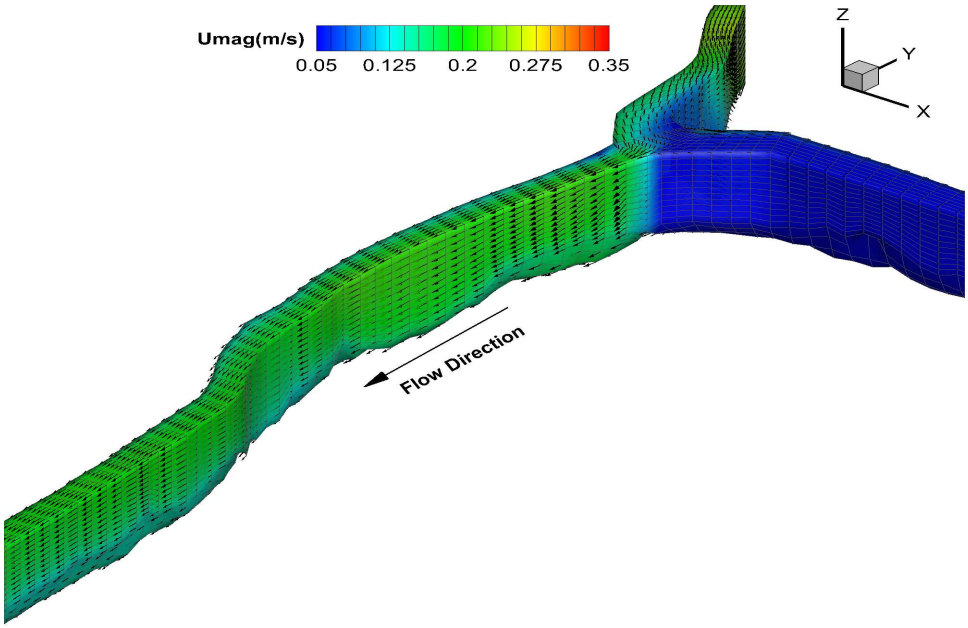

Figure 7.26: Velocity magnitude 144 hrs after the start of the simulation near Main Branch with 12 layers in vertical on Mesh-1

point in time, the gates associated with the Chicago River Controlling Works (CRCW) on the eastern end of the Main Branch are opened and as the water flows out of these gates it has a suction effect on the flow coming from Grand Avenue. Finally the water surface elevation recorded at Columbus drive on the Chicago River Main Branch for the simulation conducted with all the three different mesh resolution in the vertical.

As shown in Figure 7.27 by increasing the number of layers in the vertical from 4 to 8 improves the result, but as we increase the number of layers from 8 to 12 no further improvement in observed in comparison with the observed data. One of the main reasons for not so significant change in the velocity magnitude with increasing the number of layers in vertical is because of hydrostatic assumption for the pressure. As the numerical solution of the three-dimensional shallow water equations in EFDC model adopts mode-splitting technique, the external model solves the depth-averaged form of equations leading to the computation of water surface elevation, this water surface elevation is subsequently used in the internal model to compute the three-dimensional velocity structure. Also while computing the three-dimensional velocity structure in the internal mode the hydrodynamic state

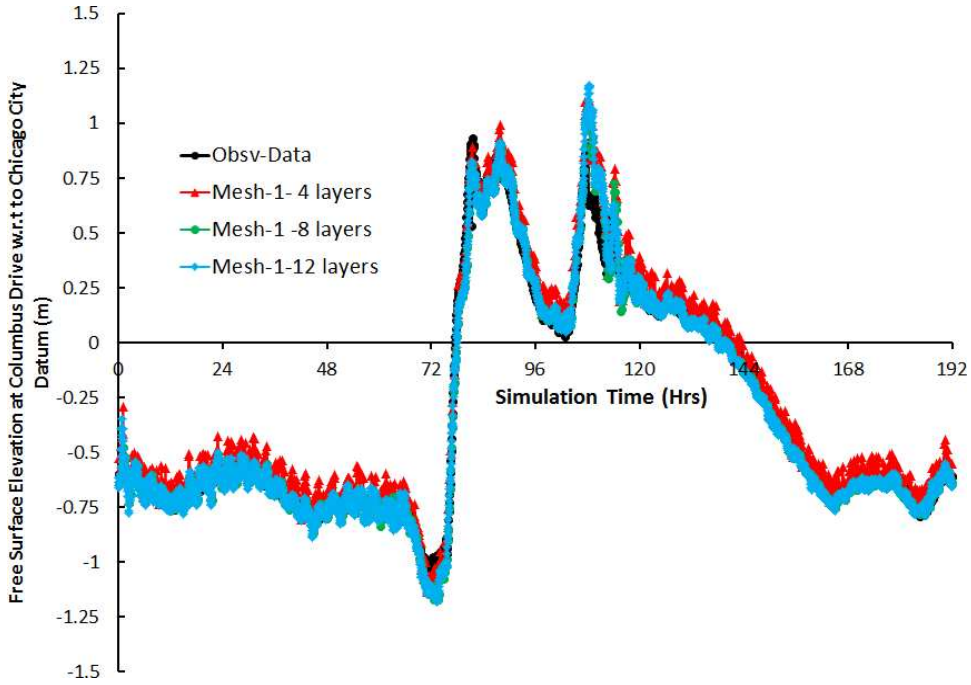

Figure 7.27: Variation of water surface elevation at Columbus Ave Mesh-1 with different numbers of layer in the vertical

variables care changed from three-dimensional velocity variables to the inter-layer turbulent shear stresses. The discretized equations expressed in terms of inter-layer shear stress are diagonally dominant and well conditioned and can be solved independently at each of the horizontal velocity locations, the details of the numerical procedure are presented in Hamrick (1992). The solution of internal-mode discretized equations expressed in terms of inter-layer turbulent shear stress requires the specification of bed shear stress at the bottom boundary and wind shear stress at the surface boundary. In EFDC model the bed shear stress is given by the quadratic law which also utilizes the depth-averged velocity computed by the external mode part of the computational kernel. As the starting point for the solution of the internal model comes from variables computed by the depth-averaged equations, increasing the number of layers doesn't have a significant impact in changing the three-dimensional velocity values as shown in series of plots from Figures 7.15 to 7.26. Finally in order to re-emphasize the minimal effect of increasing the number of layers in vertical, velocity magnitude through a cross-section in the turning basing near Bubbly Creek is presented in a series of plots here.

As shown in Figures 7.28 to 7.30 the velocity magnitude as shown in the

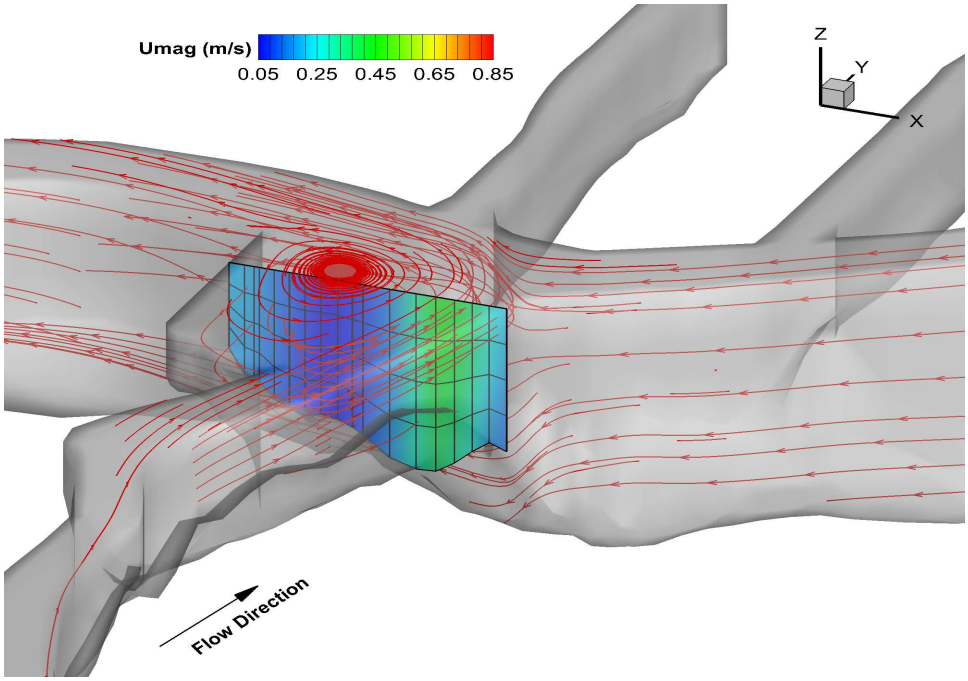

Figure 7.28: Velocity magnitude 102 hrs after the start of the simulation through a section in turning-basin near Bubbly Creek with 4 layers in vertical on Mesh-1

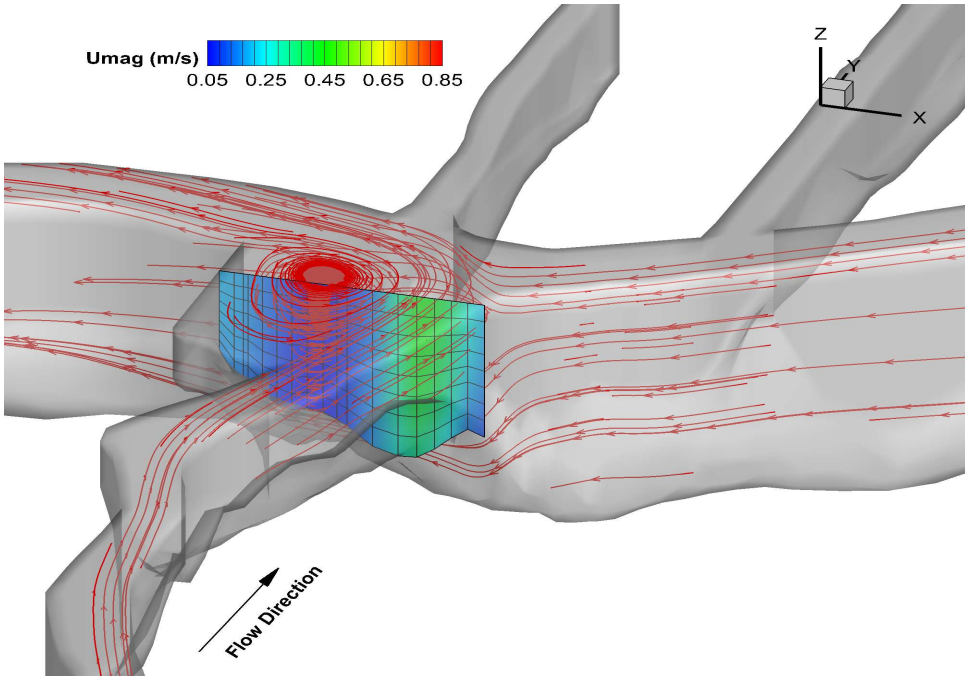

Figure 7.29: Velocity magnitude 102 hrs after the start of the simulation through a section in turning-basin near Bubbly Creek with 8 layers in vertical on Mesh-1

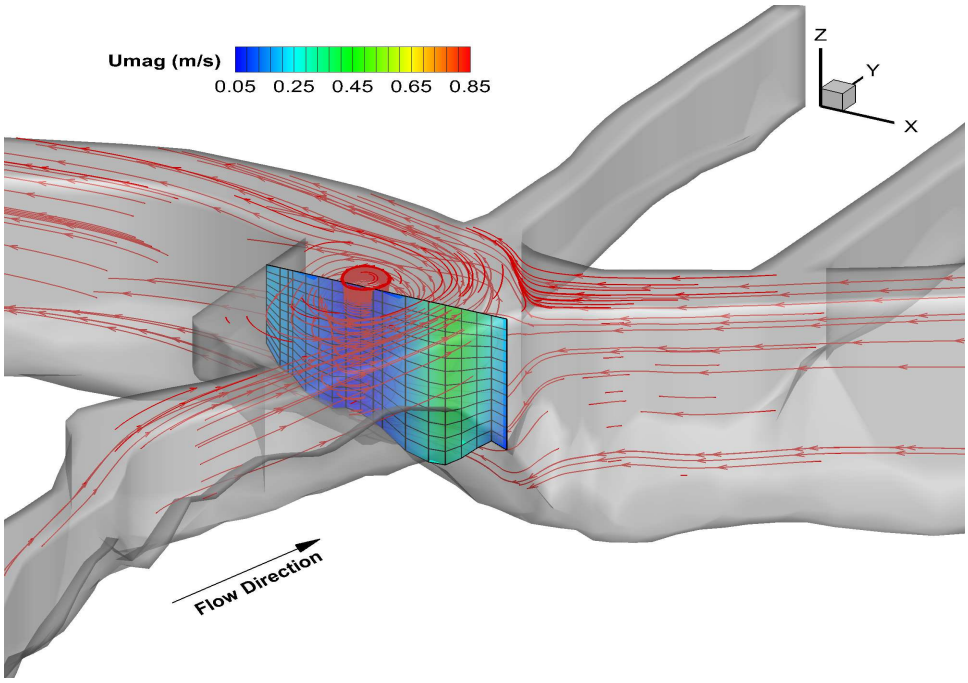

Figure 7.30: Velocity magnitude 102 hrs after the start of the simulation through a section in turning-basin near Bubbly Creek with 12 layers in vertical on Mesh-1

plotted cross-section does not change significantly as we increase the number of layers from 4 to 12.

As already explained the prime motivation of this chapter has been to examine the speed up of I-EFDC model, hence the time consumed by increasing the number of processors on both set of meshes has been recorded. The time consumed by different mesh resolution on increasingly number of processors is presented in the Figures 7.31 and 7.32. As shown in Figure7.31 the time taken by coarse mesh on 2 processors is about 3 hours, as we go on increasing the number of processors we do get some speed up but not significant and the time consumed for the same mesh is 2 hours with 8 processors. It is for the fine mesh that significant speed up is obtained. For the fine mesh the aforementioned simulation takes almost 22 hours on a single processor, 15 hours on 2 processors but as we go on increasing the number of processors the computational time keeps on reducing and is of the order of 7 hours with 8 processors as shown in Figure 7.32. One might argue against the refining of the mesh if not much improvement is obtained in the simulation results, but as mentioned before this exercise was undertaken to examine the speed-up of ***I-EFDC*** model. From that perspective it can be conclusively said that better speed up is obtained for higher resolution mesh for given set of boundary conditions. For further confirmation of the parallel performance of ***I-EFDC*** model speed-up plot is presented in Figure7.33. Speed-Up corresponding to n number of processors is defined as the ratio of computational time taken to finish the same job on a single processor by the time it takes to finish the job with n number of processors. These values are plotted on the y-axis in Figure 7.33, it is clearly seen that more linear speed up is obtained on the finer mesh (Mesh-2). Also in conclusion it must be stated that for another set of boundary conditions mesh refinement might improve the results, hence the extent of mesh resolution although very much dependent of boundary conditions and scale one is trying to resolve is also somewhat of an art which gets better as more experience is gained.

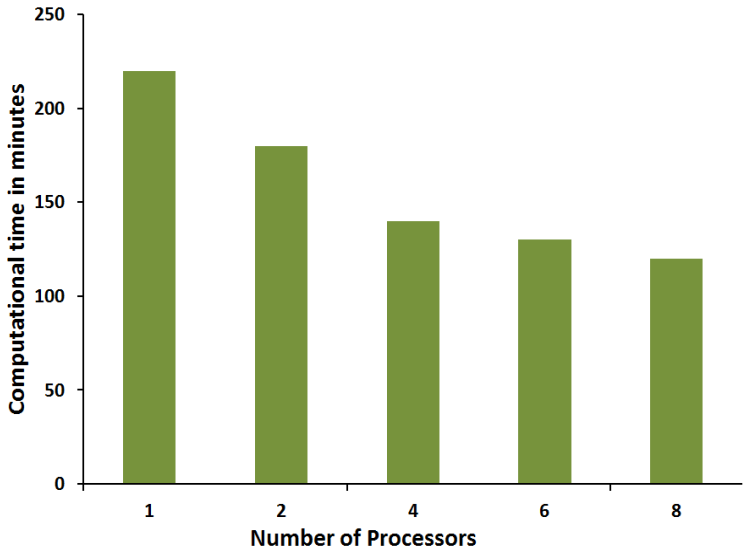

Figure 7.31: Computational time consumed by Mesh-1 with different number of processors

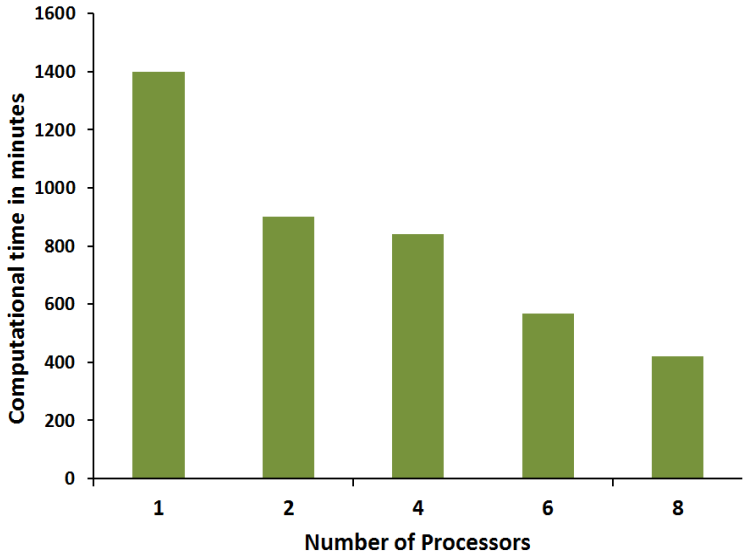

Figure 7.32: Computational time consumed by Mesh-2 with different number of processors

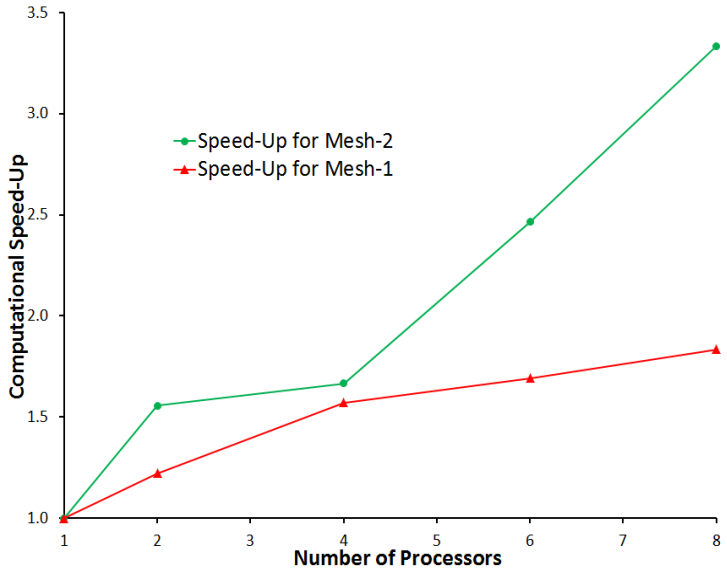

Figure 7.33: Speed-Up obtained on Mesh-1 and Mesh-2 with different number of processors

CHAPTER 8

CONCLUSION AND FUTURE WORK

8.1 Summary of Main Results

The overall aim of this research project was to develop a three-dimensional hydro-environmental model for the Chicago Area Waterway System (CAWS). A validated and calibrated three-dimensional hydrodynamic and water quality model explains and elucidates lot of phenomenon associated with the flow physics and water quality characteristics of the waterway system. A brief summary of major contribution from this research work is listed below.

- **A validated three-dimensional hydrodynamic model for Phase-I.** In the first part of this research project (Phase-I) as mentioned in Chapter 5, 22 kms of waterway was simulated. The Phase-I domain extended from Grand avenue on the north branch till Stickney avenue on the south branch. The domain modeled also included Bubbly Creek and the Main branch of the Chicago River. A high resolution computational model with 5000 cells in horizontal and 8 layers in vertical were put together for this portion of CAWS. The wet weather event of September 2008 was simulated on this model, the eight day event simulated with this model was validated with help of observed stage elevation obtained from USGS gauging station located near Columbus drive on the Main branch of the Chicago River. As a part of this simulation exercise it was also shown that due to the combine action of CSO (Combined Sewer Overflow) from RAPS and concomitant opening of gates at CRCW (Chicago River Controlling Works) the contaminated water that is pumped from RAPS has a potential to intrude upstream. As a result of this modeling exercise we have a calibrated hydrodynamic and water quality model for CAWS. Also a well calibrated three-dimensional hydrodynamic and water quality model can

be an extremely useful tool for the general upkeep and management of the CAWS.Finally, the 3D model presented herein provides a useful tool for the management of the waterways, in particular for the analysis of different alternatives currently being considered to reverse the Chicago River once again with the goal of separating the Great Lakes from the Mississippi River Basin and preventing the potential advance of invasive species such as the Asian carp into Lake Michigan.

- **A calibrated and validated three-dimensional hydro-environmental model for entire CAWS.** The three-dimensional hydro-environmental of CAWS was extended to cover 120 kms of waterway system. As presented in Chapter 5 long term simulation for the month of May-2009 was conducted on this model. The month of May-2009 was chosen as all the pertinent boundary conditions was available for this time duration. The model run was validated with the help free surface elevation data obtained from the gauging station present inside the modeled domain. The validated hydrodynamic model was further utilized for water quality simulation using simplistic DO-BOD model developed. The results of water quality simulation was validated with help of water quality probes maintained by MWRDGC at different points inside the domain.

- **Construction of Index-Velocity plot with help of two-dimensional and three-dimensional model.** On the $I\&M$ canal portion of CAWS, USGS maintains a gauging station near Lemont. Please refer to Figure 1.1 in Chapter 1. Following the flow reversal of the Chicago River, the amount of water that the State of Illinois withdraws from Lake Michigan is limited and restricted by US Supreme court decree. The flow accounting to that end is conducted at the Lemont gauging station, which makes this particular gauging station as one of the most scrutinized gauging station in the country. Also it is a well known fact that the gauging station located in unsteady flow field results in a loop phenomenon in stage-discharge rating curve. This loop or hystersis might lead to dubious discharge calculation, to obtain a single value discharge at a section in the river index-velocity technique has become popular, with help of 2D (TELEMAC-2D) and 3D (TELEMAC-3D) models index velocity plots were constructed for combination of upstream inflow

boundary conditions. These index velocity relation obtained from the numerical model was finally compared against the relationship available from the field campaign.

- **Development of two-dimensional shallow water equation model on generalised curvilinear coordinate.** Although host of flow phenomenon in CAWS are inherently three-dimensional to get an idea of flow structure in a depth-averaged mode two-dimensional shallow water equations model on a generalised curvilinear grid is developed (FinFlow-2D). A comparative study between three-dimensional (EFDC) and two-dimensional (FinFlow-2D) is conducted, the details of the simulation exercise and results is presented in Chapter 3. The process of code development is immensely helpful from the learning point of view as it enhances the understanding of how the numerical models work and why some times they crash.

8.2 Technical Contributions

- **Preprocessing program for making computational grid for EFDC.** As mentioned in Chapter 4 EFDC program is based on three-dimensional shallow water equations implemented in Orthogonal Curvilinear Coordinate eSystem (OCCS) in horizontal plane and sigma coordinate system in the vertical direction. In any kind of numerical simulation and modeling, a good quality grid is the first and a very crucial step in the entire modeling process. In regards with modeling of small and large portion of CAWS, the computational grid for the simulation was constructed using Gridgen (www.pointwise.com). An interface program was written in **Fortran-90** to convert the orthogonal grid constructed in Gridgen to EFDC format. Attention was paid that the grid constructed in Gridgen was as orthogonal as possible, given the irregular nature of the boundary of CAWS. Sankaranaryanan and Spauliding (1984) showed the adverse effect of grid non-orthogonality on the solution of shallow water equations in boundary fitted coordinate system, hence the importance of good quality grid can not be over emphasized.

- **Bathymetry processing program.** Corresponding to computational grid constructed it is necessary to extract bed elevation for each control volume in the constructed grid for setting up the simulation with EFDC model. An integrated bathymetry database containing 8.5 million data points was obtained and compiled from USGS. For various computational grid conducted bed level interpolation was done using the inverse interpolation technique. Lets suppose that we are interested in computing the depth at the center of a control volume denoted by x_c, y_c, the inverse interpolation technique is given by the following formulation.

$$Bed\,(x_c, y_c) = \frac{\sum_{p=1}^{p=5} \frac{Bed(x_p, y_p)}{d_p}}{\sum_{p=1}^{p=5} \frac{1}{d_p}} \tag{8.1}$$

  where $d_p = \sqrt{(x_c - x_p)^2 + (y_c - y_p)^2}$ is the distance from the grid point in question (x_c, y_c) to the five nearest depth point denoted by (x_p, y_p). To gain better insights into the flow physics of CAWS number of simulations on various portions of CAWS with varying mesh resolution was conducted. As stated above for the constructed grid the depth extraction algorithm was implemented in **Fortran-90**, to deal with number of grids this program was further parallelized using **MPI** (Message Passing Interface) methodology. The parallelized program was run on 32 and more processors which saved immense amount preprocessing time for the number of simulations conducted.

- **Implementing and examining the parallel speed-up of EFDC model using Open-MP paradigm.** As mentioned above the three-dimensional modeling of CAWS has progressed in a piecewise manner. For conducting simulation on larger spatial and extended temporal domain it was essential to parallelize the hydrodynamic and water quality kernel of EFDC. This was achieved by utilizing the Open-MP methodology. Open-MP paradigm was adopted as it offers the advantage of significant speed up without gigantic alteration in the source code. In Chapter-7 a detail study on the speed-up obtained by using the Open-MP paradigm on different mesh resolution is presented.

8.3 Future Work

As a result of this dissertation a three-dimensional hydro-environmental model for CAWS has been developed. Currently as the debate for the ecological separation of CAWS gains momentum, the hydrodynamic model developed can be used for studying flow physics associated with different boundary conditions resulting from ecological separation. For example if the physical separation is done just upstream of turning basin associated with Bubbly Creek on the South Branch of the Chicago River, the developed model can be used for studying the free-surface elevation in the Main Branch and examine the threat of flooding under extreme wet-weather condition. On the front of water quality modeling a simplistic DO-BOD model has been used for the simulation presented, perhaps it would be just to include the effect of Nitrogen and Phosphorus and study there effect on the variation of DO. Another important area where ***I-EFDC*** can be used is for studying the stratification effect in the Main Branch and its consequence on the discharge calculation in the South Branch of the Chicago River.

APPENDIX A

DERIVATION OF SHALLOW WATER EQUATIONS

Saint-Venant equations which are commonly known as Shallow Water Equations (SWE) are derived from the depth averaging of three-dimensional Reynolds-Averge-Navier-Stokes (RANS) equations. In the Cartesian coordinate system RANS equations is given by the following expression

$$\frac{\partial u}{\partial x}+\frac{\partial v}{\partial y}+\frac{\partial w}{\partial z}=0 \tag{A.1}$$

$$\frac{\partial u}{\partial t}+\frac{\partial\left(uu\right)}{\partial x}+\frac{\partial\left(uv\right)}{\partial y}+\frac{\partial\left(uw\right)}{\partial z}=\frac{1}{\rho}F_x-\frac{1}{\rho}\frac{\partial p}{\partial x}+\frac{1}{\rho}\frac{\partial\tau_{xx}}{\partial x}+\frac{1}{\rho}\frac{\partial\tau_{xy}}{\partial y}+\frac{1}{\rho}\frac{\partial\tau_{xz}}{\partial z} \tag{A.2}$$

$$\frac{\partial v}{\partial t}+\frac{\partial\left(vu\right)}{\partial x}+\frac{\partial\left(vv\right)}{\partial y}+\frac{\partial\left(vw\right)}{\partial z}=\frac{1}{\rho}F_y-\frac{1}{\rho}\frac{\partial p}{\partial y}+\frac{1}{\rho}\frac{\partial\tau_{yx}}{\partial x}+\frac{1}{\rho}\frac{\partial\tau_{yy}}{\partial y}+\frac{1}{\rho}\frac{\partial\tau_{yz}}{\partial z} \tag{A.3}$$

$$\frac{\partial w}{\partial t}+\frac{\partial\left(wu\right)}{\partial x}+\frac{\partial\left(wv\right)}{\partial y}+\frac{\partial\left(ww\right)}{\partial z}=\frac{1}{\rho}F_z-\frac{1}{\rho}\frac{\partial p}{\partial z}+\frac{1}{\rho}\frac{\partial\tau_{zx}}{\partial x}+\frac{1}{\rho}\frac{\partial\tau_{zy}}{\partial y}+\frac{1}{\rho}\frac{\partial\tau_{zz}}{\partial z} \tag{A.4}$$

Equations (A.1),(A.2),(A.3) and (A.4) represents Reynolds averaged continuity, and momentum equations in x, y and z directions respectively. The momentum equations can also be concisely written in tensorial form as shown in the equation (A.5)

$$\frac{\partial u_i}{\partial t}+\frac{\partial\left(u_iu_j\right)}{\partial x_j}=\frac{1}{\rho}F_i-\frac{1}{\rho}\frac{\partial p}{\partial x_i}+\frac{1}{\rho}\frac{\partial\tau_{ij}}{\partial x_j} \tag{A.5}$$

In the equation (A.5) u_i is the time-averaged velocity component in x_i

coordinate direction, p is the time-averaged pressure and τ_{ij} represents the fluid-deviatoric stresses action on plane i=constant in the direction j. These stresses are given by the following expressions.

$$\tau_{xx} = \mu\frac{\partial u}{\partial x} - \rho u'^2 \tag{A.6a}$$

$$\tau_{yy} = \mu\frac{\partial v}{\partial y} - \rho v'^2 \tag{A.6b}$$

$$\tau_{zz} = \mu\frac{\partial w}{\partial z} - \rho w'^2 \tag{A.6c}$$

$$\tau_{xy} = \tau_{yx} = \mu\left[\frac{\partial u}{\partial y} + \frac{\partial v}{\partial x}\right] - u'v' \tag{A.6d}$$

$$\tau_{xz} = \tau_{zx} = \mu\left[\frac{\partial u}{\partial z} + \frac{\partial w}{\partial x}\right] - u'w' \tag{A.6e}$$

$$\tau_{yz} = \tau_{zy} = \mu\left[\frac{\partial v}{\partial z} + \frac{\partial w}{\partial y}\right] - v'w' \tag{A.6f}$$

In the equation (A.6) μ represents the coefficient of dynamic viscosity and u', v' and w' are fluctuating turbulent velocity components. Although the momentum equation (A.5) and continuity equation (A.1) together depict the exact Navier-Stokes equation they no longer form a close set of equations. This is because the Reynolds averaging results in correlated fluctuating turbulent velocity components which are commonly known as Reynold stresses. These correlations when multiplied by the fluid density ρ represents the momentum transport due to the turbulent motion. It is the depth-averaging of these RANS equations, (A.1),(A.5) which leads to what is commonly known as Saint-Venant equation in two dimensions.

In any predominantly horizontal free-surface flow the vertical acceleration due to the hydrodynamic processes are inconsequentially smaller in comparison with gravitational effects. As a result of this the acceleration and shear stresses in the vertical direction is ignored resulting in hydrostatic pressure distribution which is given by the following expression.

$$\frac{\partial p}{\partial z} = -\rho g \tag{A.7}$$

We can integrate equation (A.7) and use the atmospheric pressure (p_a)

as the boundary condition at the surface of the water column, finally at a distance (z) from the surface of water column (ζ) the expression for pressure becomes:

$$p(z) = P_a + \int_z^{\zeta} \rho g dz \tag{A.8}$$

Having obtained the expression for pressure, equation (A.8), derivatives of the pressure in x and y direction can be expressed as

$$\frac{\partial p}{\partial x} = \frac{\partial P_a}{\partial x} + \frac{\partial}{\partial x}\int_z^{\zeta} \rho g dz \tag{A.9}$$

$$\frac{\partial p}{\partial y} = \frac{\partial P_a}{\partial y} + \frac{\partial}{\partial y}\int_z^{\zeta} \rho g dz \tag{A.10}$$

It should be kept in mind that in small scale simulations, atmospheric pressure gradients are assumed to have almost inconsequential effects on the hydrodynamic pressure gradients and can be eliminated from the equations (A.9) and (A.10). As regards to the rightmost terms in the equations (A.9) and (A.10) the integrals can be removed from with in the partial derivatives by using the Leibnitz rule which is given as

$$\int_a^b \frac{\partial f(x,y)}{\partial y} = \frac{\partial}{\partial y}\int_a^b f(x,y)dx - f(b,y)\frac{\partial b}{\partial y} + f(a,y)\frac{\partial a}{\partial y} \tag{A.11}$$

Using Leibnitz equation we can further reduce pressure derivatives as follows

$$\frac{\partial p}{\partial x} = g(\zeta - z)\frac{\partial \rho}{\partial x} + \rho g \frac{\partial \zeta}{\partial x} \tag{A.12}$$

$$\frac{\partial p}{\partial y} = g(\zeta - z)\frac{\partial \rho}{\partial y} + \rho g \frac{\partial \zeta}{\partial y} \tag{A.13}$$

As shown in the equations (A.12) and (A.13) the pressure derivative has been split into two separate terms; namely the baroclinic (density) and barotropic (surface) gradients. The depth-averaging of three-dimensional

Navier-Stokes equations requires invoking kinematic boundary conditions. The *free surface boundary condition* require that the vertical velocity at the free surface be equal to the total rate of change of surface elevation. Finally the vertical velocity at the surface is given by the following expression.

$$w_\zeta = \frac{d\zeta}{dt} = \frac{\partial \zeta}{\partial t} + u_\zeta \frac{\partial \zeta}{\partial x} + v_\zeta \frac{\partial \zeta}{\partial y} \tag{A.14}$$

In the above equation u_ζ, v_ζ and w_ζ denotes the time-averaged velocity components at the free surface. As regards to the bed-boundary condition, the condition imposed is that there can not be any flow through the bed.

$$w_{-h} = \frac{\partial(-h)}{\partial t} + u_{-h} \frac{\partial(-h)}{\partial x} + v_{-h} \frac{\partial(-h)}{\partial y} \tag{A.15}$$

Once again in equation (A.15) w_{-h}, u_{-h} and v_{-h} are the time averaged velocity components at the bed. The two-dimensional depth-averaged continuity equation is obtained by integrating equation (A.1) from bed ($z = -h$) to the free surface ($z = \zeta$). Hence the integral expression obtained is

$$\int_{-h}^{\zeta} \frac{\partial u}{\partial x} dz + \int_{-h}^{\zeta} \frac{\partial v}{\partial y} dz + \int_{-h}^{\zeta} \frac{\partial w}{\partial z} dz = 0 \tag{A.16}$$

In the above equation the partial derivative inside the integrals can be removed by using Leibnitz (equation (A.11)) and thus the continuity equation can be further reduce to the following expression.

$$\frac{\partial}{\partial x} \int_{-h}^{\zeta} u dz - u_\zeta \frac{\partial \zeta}{\partial x} + u_{-h} \frac{\partial(-h)}{\partial x} + \frac{\partial}{\partial y} \int_{-h}^{\zeta} v dz - v_\zeta \frac{\partial \zeta}{\partial y} + v_{-h} \frac{\partial(-h)}{\partial y} + w_\zeta - w_{-h} = 0 \tag{A.17}$$

Applying kinematic boundary conditions at the free-surface and bottom, equations (A.14) and (A.15), we get the following simplified expression

$$\frac{\partial}{\partial x} \int_{-h}^{\zeta} u dz + \frac{\partial}{\partial y} \int_{-h}^{\zeta} v dz + \frac{\partial \zeta}{\partial t} + \frac{\partial h}{\partial t} = 0.0 \tag{A.18}$$

At this point we can introduce the definition for the depth-averaged velocity as follows

$$U = \frac{1}{h+\zeta}\int_{-h}^{\zeta} u dz = \frac{1}{D}\int_{-h}^{\zeta} u dz \tag{A.19}$$

$$V = \frac{1}{h+\zeta}\int_{-h}^{\zeta} v dz = \frac{1}{D}\int_{-h}^{\zeta} v dz \tag{A.20}$$

In the above equations (A.19) and (A.20) denotes the depth-averaged velocities. Assuming that the bed level is not changing with time, we can rewrite the above equations in its final form of depth-averaged continuity equation which can be given as follows.

$$\frac{\partial \zeta}{\partial t} + \frac{\partial (UD)}{\partial x} + \frac{\partial (VD)}{\partial y} = 0 \tag{A.21}$$

As far as depth-averaged momentum equations are concerned they are obtained by integrating equations (A.2) and (A.3) between $z = -h$ and $z = \zeta$. By using Leibnitz rule, the equation for x direction momentum equation can be reduced to

$$\begin{aligned}
&\frac{\partial}{\partial t}\int_{-h}^{\zeta} u dz + \frac{\partial}{\partial x}\int_{-h}^{\zeta} u^2 dz + \frac{\partial}{\partial y}\int_{-h}^{\zeta} uv dz - \left[u_\zeta + \frac{\partial \zeta}{\partial t} + u_\zeta^2 \frac{\partial \zeta}{\partial x} + u_\zeta v_\zeta \frac{\partial \zeta}{\partial y} - u_\zeta w_\zeta\right] \\
&\qquad + \left[u_{-h} + \frac{\partial(-h)}{\partial t} + u_{-h}^2 \frac{\partial(-h)}{\partial x} + u_{-h} v_{-h} \frac{\partial(-h)}{\partial y} - u_{-h} w_{-h}\right] = f\int_{-h}^{\zeta} v dz \\
&\qquad -\frac{1}{\rho}\left[\int_{-h}^{\zeta} \rho g \frac{\partial \zeta}{\partial x} dz + \int_{-h}^{\zeta} g(\zeta - z)\frac{\partial \rho}{\partial x} dz\right] + \frac{1}{\rho}\frac{\partial}{\partial x}\int_{-h}^{\zeta} \tau_{xx} dz + \frac{1}{\rho}\frac{\partial}{\partial y}\int_{-h}^{\zeta} \tau_{yx} dz \\
&\qquad -\frac{1}{\rho}\left\{\tau_{xx_\zeta}\frac{\partial \zeta}{\partial x} + \tau_{yx_\zeta}\frac{\partial \zeta}{\partial y} - \tau_{zx_\zeta} - \tau_{xx_{-h}}\frac{\partial(-h)}{\partial x} - \tau_{yx_{-h}}\frac{\partial(-h)}{\partial y} + \tau_{zx_{-h}}\right\}
\end{aligned} \tag{A.22}$$

In the above equation the last term in curly brackets denotes the stress components on free-surface as well as bed. The wind and the bed shear stress can be denoted by the following expression.

$$\tau_{wx} = -\tau_{xx_\zeta}\frac{\partial \zeta}{\partial x} - -\tau_{yx_\zeta}\frac{\partial \zeta}{\partial y} + \tau_{zx_\zeta} \tag{A.23}$$

$$\tau_{bx} = -\tau_{xx_{-h}}\frac{\partial (-h)}{\partial x} - -\tau_{yx_\zeta}\frac{\partial (-h)}{\partial y} + \tau_{zx_{-h}} \tag{A.24}$$

As already defined $\int_{-h}^{\zeta} u dz = UD$ and $\int_{-h}^{\zeta} u dz = VD$, and applying the stress boundary condition on the bed and free-surface and assuming $u = U + (u - U)$ and $v = V + (v - V)$, equation (A.22) can be recast into the following form.

$$\frac{\partial (UD)}{\partial t} + \frac{\partial (U^2 D)}{\partial x} + \frac{\partial (UVD)}{\partial y} = fVD - gD\frac{\partial \zeta}{\partial x} - \frac{gD^2}{2\rho}\frac{\partial \rho}{\partial x} + \frac{\tau_{wx} - \tau_{bx}}{\rho}$$
$$\frac{1}{\rho}\left[\frac{\partial}{\partial x}\int_{-h}^{\zeta}\left[\tau_{xx} - \rho (u - U)^2\right] dz + \frac{\partial}{\partial y}\int_{-h}^{\zeta}\left[\tau_{yx} - \rho (u - U)(v - V)\right] dz\right] \tag{A.25}$$

The deviatoric stress in the fluid due to the velocity gradient as well as stress arising from the non-uniformity of the vertical velocity profile can be grouped together and defined as the effective stresses T_{xx}, T_{xy} and T_{yy}. After a little bit of manipulation the depth-averaged momentum equation in x and y direction can be recast in the following form.

$$\frac{\partial (UD)}{\partial t} + \frac{\partial (U^2 D)}{\partial x} + \frac{\partial (UVD)}{\partial y} =$$
$$fVD - gD\frac{\partial \zeta}{\partial x} - \frac{gD^2}{2\rho}\frac{\partial \rho}{\partial x} + \frac{\tau_{wx} - \tau_{bx}}{\rho} + \frac{1}{\rho}\left[\frac{\partial (DT_{xx})}{\partial x} + \frac{\partial (DT_{xy})}{\partial y}\right] \tag{A.26}$$

$$\frac{\partial (VD)}{\partial t} + \frac{\partial (UVD)}{\partial x} + \frac{\partial (V^2 D)}{\partial y} =$$
$$-fUD - gD\frac{\partial \zeta}{\partial y} - \frac{gD^2}{2\rho}\frac{\partial \rho}{\partial y} + \frac{\tau_{wy} - \tau_{by}}{\rho} + \frac{1}{\rho}\left[\frac{\partial (DT_{xy})}{\partial x} + \frac{\partial (DT_{yy})}{\partial y}\right] \tag{A.27}$$

The effective stresses in momentum equation in x and y direction is given

by the following formulation

$$T_{xx} = \frac{1}{D}\int_{-h}^{\zeta}\left[2\mu\frac{\partial u}{\partial x} - \rho u^{'2} - \rho\left(u-U\right)^2\right]dz \tag{A.28a}$$

$$T_{xy} = \frac{1}{D}\int_{-h}^{\zeta}\left[\mu\left[\frac{\partial u}{\partial y} + \frac{\partial v}{\partial x}\right] - \rho u^{'}v^{'} - \rho\left(u-U\right)\left(v-V\right)\right]dz \tag{A.28b}$$

$$T_{yy} = \frac{1}{D}\int_{-h}^{\zeta}\left[2\mu\frac{\partial v}{\partial y} - \rho v^{'2} - \rho\left(v-V\right)^2\right]dz \tag{A.28c}$$

The conservative form of SWE (equations A.26 and A.27) can be manipulated a bit with the help of the depth averaged continuity equation A.21 to give non-conservative form of SWE, which is given by the following expression.

$$\begin{aligned}\frac{\partial U}{\partial t} + U\frac{\partial U}{\partial x} + V\frac{\partial U}{\partial y} = \\ fV - g\frac{\partial \zeta}{\partial x} - \frac{gD}{2\rho}\frac{\partial \rho}{\partial x} + \frac{\tau_{wx}-\tau_{bx}}{\rho D} + \frac{1}{\rho D}\left[\frac{\partial\left(DT_{xx}\right)}{\partial x} + \frac{\partial\left(DT_{xy}\right)}{\partial y}\right]\end{aligned} \tag{A.29a}$$

$$\begin{aligned}\frac{\partial V}{\partial t} + U\frac{\partial V}{\partial x} + V\frac{\partial V}{\partial y} = \\ -fU - g\frac{\partial \zeta}{\partial x} - \frac{gD}{2\rho}\frac{\partial \rho}{\partial y} + \frac{\tau_{wy}-\tau_{by}}{\rho D} + \frac{1}{\rho D}\left[\frac{\partial\left(DT_{xy}\right)}{\partial x} + \frac{\partial\left(DT_{yy}\right)}{\partial y}\right]\end{aligned} \tag{A.29b}$$

Crowley (1968) conducted experiments on different form of SWE (conservative and non-conservative forms) and showed that non-conservative form SWE has a simpler computational molecule and easier to code. Although the argument in the favour of the conservative form of SWE is that it does a better job in numerically conserving the momentum equation. But this does not mean that the pertinent quantities will not be approximately conserved if one chooses to use non-conservative form of SWE. As the models developed and applied as a part of this research is of engineering importance the added

complexity posed by using the conservative scheme may not be well justified.

It can be clearly seen that the non-conservative form of SWE as presented in equations A.29a and A.29b do not form a close set of equations, therefore it is necessary to relate the effective stress terms to other quantities such as the mean velocity components in order to obtain a closed solution. Although in many large scale hydrodynamic simulations the depth-averaged turbulent stresses are negligible compared with the other terms and the only impact of turbulence in through the bottom shear stress. But to have a more physics based model the value of effective stress was incorporated in the two-dimensional model developed as a part of this research.

The effective stresses given by the equations A.28a to A.28c consist of three terms on the right hand side. The first term on the right hand side in each equation represents the viscous stresses acting on the vertical side of the fluid element. The second component is the Reynold stress and the final term describes the large scale transfer of momentum caused by the vertical non-uniformities of the mean flow, also commonly known as dispersion. The first term mentioned above is a laminar contribution and is usually negligible in the turbulent flow regime (Rastogi and Rodi, 1978). Also in well mixed system the dispersion term in generally smaller in comparison to the turbulent momentum transport. Finally incorporating only the term whose magnitude is significant and using Boussinesq eddy viscosity concept the effective stresses are given by the following relations.

$$T_{xx} = 2\rho\tilde{\nu_t}\frac{\partial U}{\partial x} - \frac{2}{3}\rho\tilde{k} \tag{A.30a}$$

$$T_{xy} = \rho\tilde{\nu_t}\left[\frac{\partial U}{\partial y} + \frac{\partial V}{\partial x}\right] \tag{A.30b}$$

$$T_{xy} = 2\rho\tilde{\nu_t}\frac{\partial V}{\partial y} - \frac{2}{3}\rho\tilde{k} \tag{A.30c}$$

In accordance with Prandtl mixing length theory , the depth-averaged

eddy viscosity is given by the following formulation.

$$\nu_t = \frac{\kappa\sqrt{U^2+V^2}D\sqrt{C_f}}{6} \tag{A.31}$$

where $C_f = \frac{n^2 g}{D^{1/3}}$. In the non-conservative form of SWE given by equations A.29a and A.29b the diffusive portion of the momentum equations can be expanded with chain rule concept and using the expression for effective stresses it reduces to the following expression.

$$\frac{1}{\rho D}\left[T_{xx}\frac{\partial D}{\partial x} + D\frac{\partial\left(T_{xx}\right)}{\partial x} + T_{xy}\frac{\partial D}{\partial y} + D\frac{\partial\left(T_{xy}\right)}{\partial y}\right] \tag{A.32}$$

Now assuming ∂D
$partialx$ and $\partial D\partial y$ to be negligible and also assuming the spatial variation of ν_t to be insignificant, we get the following expression for the diffusive portion of the momentum equations.

$$\nu_t\left[2\frac{\partial^2 U}{\partial x^2} + \frac{\partial^2 V}{\partial x\partial y} + \frac{\partial^2 U}{\partial y^2}\right] \tag{A.33}$$

Based on the above expression the final form of non-conservative form of SWE that formed the governing equation for the FinFlow-2D model developed as a part of this research is given by the following relationship.

$$\frac{\partial U}{\partial t} + U\frac{\partial U}{\partial x} + V\frac{\partial U}{\partial y} = fV - g\frac{\partial\zeta}{\partial x} - \frac{gD}{2\rho}\frac{\partial\rho}{\partial x} + \frac{\tau_{wx}-\tau_{bx}}{\rho D} + \nu_t\left[2\frac{\partial^2 U}{\partial x^2} + \frac{\partial^2 V}{\partial x\partial y} + \frac{\partial^2 U}{\partial y^2}\right] \tag{A.34}$$

$$\frac{\partial V}{\partial t} + U\frac{\partial V}{\partial x} + V\frac{\partial V}{\partial y} = -fU - g\frac{\partial\zeta}{\partial y} - \frac{gD}{2\rho}\frac{\partial\rho}{\partial y} + \frac{\tau_{wy}-\tau_{by}}{\rho D} + \nu_t\left[\frac{\partial^2 V}{\partial x^2} + \frac{\partial^2 U}{\partial x\partial y} + 2\frac{\partial^2 V}{\partial y^2}\right] \tag{A.35}$$

REFERENCES

Abad, J. D., Buscaglia, G. C., and García, M. H. (2008). 2d stream hydrodynamic, sediment transport and bed morphology model for engineering applications. *Hydrological Processes*, 22:1443–1459.

Abbott, M. B. (1979). *Computational Hydraulics: Elements of the theory of the free surface flows*. Pitman Publishing Limited, London, UK.

Akanbi, A. A. and Katapodes, N. (1988). Model for flood propagation on initially dry land. *Journal of Hydraulic Engineering*, 114:689–706.

Alcrudo, F., Garcia-Navarro, P., and Saviron, J. (1992). Flux difference splitting for 1d open channel flow equations. *International Journal of Numerical Method in Fluids*, 14:1009–1018.

Alp, E. and Melching, C. (2006). Calibration of a model for simulation of water quality during unsteady flow in the chicago waterway system and application to evaluate use attainability analysis and remedial actions. Technical Report Technical Rep. No. 18, Institute for Urban Environmental Risk Management.

Ambrossi, D. (1995). Approximation of shallow water equations by roe's riemann solver. *International Journal of Numerical Method in Fluids*, 20:157–168.

Anastasiou, K. and Chan, C. (1997). Solution of the 2d shallow water equations using finite volume method on unstructured triangular meshes. *International Journal of Numerical Method in Fluids*, 24:1225–1245.

Arakawa, A. and Lamb, V. R. (1977). Computational design of basic dynamical processes of the ucla general circulation model. *Methods in Cimputational Physics*, 17:173–265.

Asgeir, P. O. (2006). Modelling of stage-discharge relationships affected by hysteresis using jones formula and nonlinear regression. *Hydrological Sciences-Journal des Sciences Hydrologiques*, 51(3):365–388.

Aureli, F., Mingosa, P., and Tomirotti, M. (2000). Numerical-simulation and experimental verification of dam-break flows with shocks. *Journal of Hydraulic Research*, 38(3):197–206.

Bates, P. D. and Anderson, M. G. (1993). A two-dimensional finite-element model for river flow inundation. In *Proceedings of the Royal Society*.

Bates, P. D., Anderson, M. G., Baird, L., Walling, D., and Simm, D. (1992). Modelling flood plain flow with two-dimensional finite element scheme. *Earth Surface Processes and Landforms*, 17:575–588.

Bates, P. D. and DeRoo, A. P. J. (2000). A simple raster-based model for flood inundataion simulation. *Journal of Hydrology*, 236:54–77.

Bates, P. D., Wilson, C. A. M. E., Herouvet, J. M., and Stewart, M. D. (1999). Two-dimensional finite element modelling for flood plain flow. *La Houile Blanche*, (3/4):82–88.

Beam, R. M. and Warming, R. F. (1976). An implicit finite difference algorithm for hyperbolic systems in conservation form. *Journal of Computational Physics*, 22:87–110.

Beffa, C. and Connel, R. J. (2001). Two-dimensional flood plain flow. i: model description. *Journal of Hydrological Engineering*, 6(5):397–405.

Berger, R. C. and Stockstill, R. L. (1995). Finite element model for high velocity channels. *Journal of Hydraulic Engineering*, 121(10):710–716.

Blumberg, A. F. and Mellor, G. L. (1987). A description of a three-dimensional coastal ocean circulation model. *Three-Dimensional Coastal Ocean Models, Coastal and Estuarine Science*, 4:1–19.

Brufau, P., Vazquez-Cendon, M. E., and Garcia-Navarro, P. (2002). A numerical model for flooding and drying of irregular domains. *International Journal for Numerical Methods in Fluids*, 37:209–248.

Brunner, G. W. (2001). *HEC-RAS river analysis system user's manual: version 4.0*. U.S. Army Corps of Engineers, Hydrologic Engineer Center Davis California.

Casulli, V. and Cattani, E. (1994). Stability, accuracy and efficiency of a semi-implicit method for three-dimensional shallow water flow. *Computers and Mathematics with Applications*, 27(4):99–112.

Casulli, V. and Cheng, R. (1992). Semi-implicit finite difference methods for three-dimensional shallow water flow. *International Journal for Numerical Methods in Fluids*, 15:629–648.

Casulli, V., Cheng, R., and Gartner, J. (1993). Tidal, residual, intertidal mudflat (trim) model and its application to san francisco bay, california. *Estuarine Coastal and Shelf Science*, 36:235–280.

Cerco, C. F. and Cole, T. (1995). *User's quide to the CE-QUAL-ICM three dimensional eutrophication model*. U.S. Army Engineer Waterways Experiment Station, Vicksburg, Mississippi.

Chapra, S. (1997). *Surface Water Quality Modeling*. Mcgraw-Hill Series.

Chaudhry, M. H. (1994). *Open-Channel Flow*. Prentice Hall of India Pvt. Ltd.

Chow, V. T. (1973). *Open Channel Hydraulics*. Mcgraw-Hill, New York.

Chow, V. T. and Ben-Zvi, A. (1973). Hydrodynamic modeling of two dimensional watershed flow. *Journal of Hydr. Div.*, 99(11):2023–2040.

Crowley, W. P. (1968). Numerical advection experiments. *Monthly Weather Review*, V 96, No. 1:1–11.

Cunge, J. A., Holly, F., and Verwey, A. (1980). *Practical Aspects of Computational River Hydraulics*. Pitman Publishing Limited, London, UK.

Deardoff, J. (1970). A numerical study of three-dimensional turbulent channel flow at large reynolds numbers. *Journal of Fluid Mechanics*, 41(2):453–480.

Delis, A. I. and Skeels, C. P. (1998). Tvd schemes for open channel flow. *International Journal of Numerical Method in Fluids*, 26:791–809.

DHI (2005). *Mike 11, A modelling system for rivers and channels, short introduction and tutorial*. Danish Hydraulic Institute.

Fennema, R. J. and Chaudhry, M. H. (1990). Explicit methods for 2d transient free surface flows. *Journal of Hydraulic Engineering*, 116(8):1013–1034.

Fenton, J. D. and Keller, R. J. (2001). The calculation of streamflow from measurements of stage. Technical report, Center for Catchment Hydrology, Melbourne, Australia.

Fread, D. L. (1975). Computation of stage-discharge relationships affected by unsteady flow. *Water Resources Bulletin*, 11(1):213–228.

Gabutti, B. (1983). On two finite element schemes for hyperbolic equations in nonconservative form. *Computational Fluids*, 11:207–230.

Galperin, B., Kantha, L. H., Hassid, S., and Rosati, A. (1988). A quasi-equilibrium turbulent energy model for geophysical flows. *Journal of the Atmospheric Sciences*, 45 (1):55–62.

Glaister, P. (1988). Approximate riemann solution of the shallow water equations. *Journal of Hydraulic Research*, 26(3):293–306.

Goutal, N. and Maurel, F. (2002). A finite volume solver for 1d shallow-water equations appled to an actual river. *International Journal of Numerical Method in Fluids*, 38:1–19.

Hamrick, J. M. (1992). A three-dimensional environmental fluid dynamics computer code: Theoretical and computational aspects. Technical Report Special Report 328, Virginia Institute of Marine Science.

Henderson, F. M. (1966). *Open Channel Flow*. MacMillan, New York.

Hervouet, J. M. (2007). *Hydrodynamics of free surface flows*. Wiley.

Hervouet, J. M. and Petitjean, A. (1999). Malpasset dam-break revisited with 2-dimensional computations. *Journal of Hydraulic Research*, 37(6):777–788.

Hicks, F. E. and Steffler, P. M. (1992). Characteristic dissipative galerkin scheme for open channel flow. *Journal of Hydraulic Engineering*, 118:337–351.

Hirsch, C. (1988). *Numerical computation of internal and external flows. Vol. 1.* John Wiley & Sons.

Hirt, C. W. and Nichols, B. D. (1981). Volume of fluid (vof) method for the dynamics of free boundaries. *Journal of Computational Physics*, 29:201–220.

Horritt, M. S. and Bates, P. D. (2001). Predicting floodplain inundataion: raster-based modelling versus the finite element approach. *Hydrological Processes*, 15:825–842.

Hydraulics, D. (1999). *Delft3D-Flow manual*. Delft.

Hydroqual (1991). A primer for ecom-3d. Technical Report Technical Rep. No. 18, HydroQual, Inc., Mahwah NJ.

Hydroqual (1995). A primer for sedzl-3d. Technical Report Technical Rep. No. 18, HydroQual, Inc., Mahwah NJ.

Jackson, D. H., Garcia, M. C., Oberg, K. A., Johnson, K. K., and García, M. H. (2008). Density currents in chicago river: Characterization, effects on water quality, and potential sources. *Science of the Total Environment*, 401:130–143.

Jackson, P. R., Johnson, K. K., and Duncker, J. J. (2012). Compairsion of index velocity measurements made with a horizontal acoustic doppler current profiler and three-path acoustic velocity meter for the computation of discharge in the chicago sanitary and ship canal near lemont, il. Technical report, U.S. Geological Survey.

Katapodes, N. D. (1984). Two-dimensional surges and shocks in open channel. *Journal of Hydraulic Engineering*, 110:794–812.

Keifer, C. J. (1994). *Operation and Description of KIM PROGRAMS*. Keifer Engineering Inc.

Keuning, D. H. (1976). Application of finite element method to open channel flow. *Journal of Hyrdraulic Engineering*, 102:459–468.

Lai, Y. G. (2010). Two-dimensional depth-averaged flow modeling with an unstructured hybrid mesh. *Journal of Hydraulic Engineering*, 136(1):12–23.

Lax, P. D. and Wendroff, B. (1960). System of conservation laws. *Comm. Pure Appl. Math.*, 13:217–237.

MacCormack, R. W. (1969). The effect of viscosity in hyperbolicity impact catering. In *American Institute of Aeronautics and Astronautics*.

MacCormack, R. W. and Paullay, A. J. (1972). Computational efficiency achieved by time splitting of finite difference operators. In *American Institute of Aeronautics and Astronautics*.

Madala., R. V. and Piacsek, S. A. (1977). A semi-implicit numerical model for baroclinic oceans. *Journal of Computational Physics*, 23:167–178.

Mander, R. J. (1978). *Aspects of unsteady flow and vraiable backwater, In: Hydrometry: Principles and Practice*. John Wiley and Sons, Chichester, UK.

McDonald, P. W. (1971). The computation of transonic flow through two-dimensional gas turbine cascades. In *ASME Paper 71-GT-89*.

Mellor, G. and Yamada, T. (1982). Development of a turbulence closure model for geophysical fluid problems. *Review of Geophysical Space Physics*, 20:851–875.

Mellor, G. L. (1988). *User's Guide for a Three-Dimensional, Primitive Equation, Numerical Ocean Model*. Atmospheric and Ocean Sciences Program, Princeton University.

Molls, T. and Chaudhry, M. H. (1995). Depth averaged open channel flow model. *Journal of Hydraulic Engineering*, 121(6):453–465.

Moretti, G. (1979). The lambda scheme. *Computational Fluids*, 7:191–205.

Morlock, S. E., Nguyen, H. T., and Ross, J. H. (2001). Feasibility of acoustic doppler velocity meters for production of discharge records from u.s. geologiocal survey stream-gaging stations. Technical report, U.S. Geological Survey.

Motta, D., Abad, J. D., and García, M. H. (2010). Modeling framework for organic sediment resuspension and oxygen demand: Case of bubbly creek in chicago. *Journal of Environmental Engineering*, 136(9):952–964.

Moyeed, R. A. and Clarke, R. T. (2005). The use of bayesian methods for fitting rating curves, with case studies. *Advances in Water Resources*, 28:807–818.

O'Connor, D. J. and Dobbins, W. E. (1958). Mechanism of reaeration in natural streams. *ASCE Transactions*, 86(SA3):35–55.

Orlanski, I. (1976). A simple boundary conditions for unbounded hyperbolic flows. *J. Comput. Phys.*, 21:251–269.

Preissmann, A. (1961). Propagation des intumescences dans les canaux et rivieries. In *First Congress of the French Association for Computation, Grenoble*.

Rastogi, A. and Rodi, W. (1978). Predictions of heat and mass transfer in open channels. *Journal of Hydr. Div.*, 104:397–420.

Rouse, H. and Ince, S. (1957). *History of Hydraulics*. Iowa Institute of Hydraulic Research.

Sankaranaryanan, S. and Spauliding, S. (1984). A study of the effects of the grid non-orthogonality on the solution of shallow water equations in boundary-fitted coordinate system. *Journal of Computational Physics*, 184:299–320.

Shettar, A. S. and Muruthy, K. K. (1997). A numerical study of division of flow in open channels. *Journal of Hydraulic Research*, 34(5):651–675.

Simpson, M. and Rodger, B. (1999). Techniques for accurate estimation of net discharge in a tidal channel. In *Proceedings of the Institute of Electrical and Electronics Engineers Sixth Working Conference on Current Measurements, Airlie, Virginia*.

Sinha, P. A., Sotiropoulos, F., and Odgaard, A. J. (1998). Three-dimensional numerical for flow through natural rivers. *Journal of Hydraulic Engineering*, 124(1):479–508.

Sinha, S., Liu, X., and Garcia, M. H. (2010). Three-dimensional hydrodynamic and water quality modeling of a cso (combined sewer overflow) event in bubbly creek, il. In *proceedings of Riverflow2010 conference, Braunschweig, Germany*.

Sinha, S., Liu, X., and Garcia, M. H. (2012). Three-dimensional hydrodynamic modeling of the chicago river, illinois. *Environmental Fluid Mechanics*.

Smagorinsky, J. (1963). General circulation experiments with the primitive equations. *Monthly Weather Review*, 91 (3):100–164.

Smith, J. and McLean, S. (1977). Spatially averaged flow over a wavy surface. *Journal of Geophysical Research*, 83:1734–1746.

Sommerfeld, A. (1949). *Partial differential equations. Lecture notes on Theoretical Physics*, volume 6. Academic Press., San Diego, CA.

Stoker, J. J. (1957). *Water Waves: Mathematical Theory with Application*. John Wiley & Sons.

Tholin, A. J. and Keifer, C. J. (1959). The hydrology of urban runoff. *Journal of Sanitary Engineering Divison*, SA 2:47–105.

Tucciarelli, T. and Termini, D. (2000). Finite element modelling of flood plain flow. *Journal of Hydraulic Engineering*, 126(6):416–424.

USACE (2001). Lake michigan diversion accounting, water year 2001. Technical report, US Army Corp of Engineers.

Vreugdenhil, C. B. (1973). Computational methods for channel flow. *Journal of Water Resources Planning and Management*, 116:803–819.

Vukovic and Sopta (2002). Eno and weno schemes with exact conservation property for one-dimensional shallow water equations. *Journal of Computational Physics*, 148:497–526.

Waterman, D., Wartuke, A., Motta, D., Catano-Lopera, Y., and Garcia, M. (2009). Bubbly creek sediment oxygen demand (sod) study with the u of i hydrodynamic sod sampler. Technical report, Ven Te Chow Hydrosystems Labrotary, University of Illinois Urbana-Champaign.

Waterman, D. M., Waratuke, A. R., Motta, D., Catano-Lopera, Y. A., Zhang, Y. A., and Garcia, M. H. (2011). In situ characterization of resuspended-sediment oxygen demand in bubbly creek, chicago, illinois. *Journal of Environmental Engineering*, 137(8):717–730.

Welch, J. E., Harlow, F. H., Shannon, J. P., and Daly, B. J. (1966). The mac method. Technical report, Los Almos National Library.

Wu, W. and Vieira, D. A. (2001). *One-dimensional channel network model CCHE1D version 3.0-technical manual*. National Center for Computational Hydroscience and Engineering, University of Mississippi Oxford Mississippi.

Ye, J. and McCorquodale, J. A. (1998). Simulation of open channel flows by 3d hydrodynamic model. *Journal of Hydraulic Engineering*, 124(7):687–698.

Yen, B. C., Jackson, T. J., Schmugge, T. J., and Lai, C. (1986). *Advances in Hydrosciences*. Academic Press.

Zhao, D. H., Shen, H. W., Tabois, G. Q., Lai, J. S., and Tan, W. Y. (1994). Finite-volume two-dimensional unsteady-flow model for river basins. *Journal of Hyrdraulic Engineering*, 120(7):863–883.